

## **8.10 THREE-DIMENSIONAL NUMERICAL MODELING OF THE UNSATURATED ZONE AT YUCCA MOUNTAIN**

As described in Sections 8.1 to 8.8, the unsaturated zone at Yucca Mountain has been studied extensively and many types of data have been collected and analyzed. These data include detailed geologic framework, spatial estimates of net infiltration, core-sample saturations, in situ and core-sample water potentials, saturated conductivities and moisture-retention curves, core-sample bulk-property measurements, and results of pneumatic and temperature monitoring in deep boreholes, air permeability tests, geochemical analysis, and perched-water testing (Bodvarsson et al. 1999, p. 20). Data from the Exploratory Studies Facility (ESF) include fracture and fault mapping, environmental isotope and hydrochemical data, fracture coating data, bulk properties from in situ and core-sample measurements, ambient characterization of the Thermal Test Facility, and results of various hydrologic studies of drift seepage and percolation flux. These data have been used to develop the conceptual models of flow and transport described in Section 8.9 and the numerical models described in this section. The numerical models of hydrologic behavior of the site are intended to simulate ambient conditions and perform predictive studies of potential changes in the unsaturated zone at various scales caused by climate-related, thermal, and geochemical perturbations. The comprehensive three-dimensional site-scale model of unsaturated zone flow and transport integrates all pertinent data from the unsaturated zone at Yucca Mountain to quantify the flow of gas, moisture, chemical solutes, and heat (Bodvarsson et al. 1999, p. 5).

The primary objectives of the unsaturated zone flow and transport model (CRWMS M&O 2000d, Section 6, p. 29; Bodvarsson et al. 1999, pp. 18 to 20) are as follows:

- Integrate available data from the unsaturated zone into a single, comprehensive, and calibrated three-dimensional model simulating ambient conditions and predicting system response to future climate conditions
- Quantify the flow of moisture, heat, and gas through the unsaturated zone under present-day and hypothesized future climates
- Create a number of submodels using boundary and initial conditions from the site-scale model for detailed studies of perched water, percolation through the Paintbrush nonwelded (PTn) unit, flow through the Calico Hills nonwelded (CHn) zeolitic units, sorption of radionuclides, and thermal effects of heat from the potential repository after waste emplacement
- Evaluate the effects of thermal loading on moisture, gas, and heat flow within the mountain, as well as study the combined thermo-mechanical-chemical effects of waste emplacement
- Simulate the ambient geochemistry as well as predict the migration of radioactive isotope releases after waste emplacement
- Contribute model parameters and boundary conditions for drift seepage studies

- Provide a defensible and credible model of all relevant unsaturated zone processes for use in performance assessment and repository design.

In addition, the unsaturated zone hydrologic models provide estimates for important parameters and processes, such as the following:

- Spatially and temporally averaged values of the percolation flux at the potential repository horizon
- Components of fracture and matrix flow within and below the potential repository horizon
- Probable flow paths from the potential repository to the water table
- Liquid water travel/radionuclide transport times, radionuclide migration paths from the potential repository to the water table, and breakthrough curves at the water table for tracers and radioactive isotopes.

The total system performance assessment (TSPA) will use the unsaturated zone flow simulations to provide input to other models such as ambient and thermal drift-scale models, the mountain-scale thermohydrological model, and the unsaturated zone transport model. The relationships among these various models are shown schematically in Figure 8.10-1.

The description of the site-scale unsaturated zone flow and transport model and submodels is divided into the following sections:

- History of the development of the site-scale unsaturated zone model (Section 8.10.2)
- Numerical approaches and their applicability (Section 8.10.3)
- Development of numerical grids for flow and transport modeling (Section 8.10.4)
- Calibrated properties model (Section 8.10.5)
- Calibration and application of the three-dimensional site-scale flow and transport model (Section 8.10.6)
- Seepage model for performance assessment (Section 8.10.7)
- Mountain-scale coupled thermohydrologic model (Section 8.10.8)
- Drift-scale coupled thermohydrologic-chemical seepage models (Section 8.10.9)
- Radionuclide-transport models under ambient conditions (Section 8.10.10).

### 8.10.1 Data Sources

Because of the large quantity and diversity of data used as input to the various unsaturated zone modeling efforts, the sources and interpretations are described individually in the sections below. For each investigation, the data sources are addressed in the introduction to each major section.

### 8.10.2 History of the Development of the Site-Scale Unsaturated Zone Model

The unsaturated zone model of Yucca Mountain has evolved from simple one- and two-dimensional models that included little geological or hydrological detail, to a fully coupled three-dimensional model that incorporates much of the known geologic, hydrologic, chemical, and thermal complexity of Yucca Mountain. The earliest versions of the unsaturated zone model were constructed with the TOUGH code (Transport of Unsaturated Groundwater and Heat) (Pruess 1987), which is a numerical computer program that simulates the transport of water, air, and heat in an unsaturated porous medium. Later versions of the model used TOUGH2 (Pruess 1991), which is an enhanced version of TOUGH that contains additional capabilities such as solute transport. All versions of the TOUGH codes use the method of integral finite difference (Narasimhan and Witherspoon 1976) to represent the equations of conservation of mass and conservation of energy in an algebraic form. These algebraic equations are solved by various numerical techniques, such as Gaussian elimination or the conjugate gradient method (Moridis and Pruess 1995). The ability of the TOUGH2 code to accurately simulate unsaturated flow processes has been documented by Pruess and Antunez (1995).

An important early step in the development of an unsaturated zone model of Yucca Mountain was a set of cross-sectional models to investigate various important flow processes, such as lateral flow within the PTn and flow partitioning between fractures and the rock matrix (Rulon et al. 1986). In the early 1990s, the first complex, three-dimensional hydrologic model was developed (Wittwer et al. 1995). The model incorporated many geologic and hydrologic complexities, such as geologic layering, degree of welding of the rock layers, fault offsets, and differing matrix and fracture properties. This model analysis addressed many processes and hydrological issues and showed complex moisture flow patterns caused by dipping hydrologic units and the offsets of the faults. Ahlers, Bandurraga et al. (1995a, 1995b) continued the development of the three-dimensional unsaturated zone model by incorporating greater spatial resolution and consideration of processes such as gas pressures and gas flow, and temperature and heat flow analyses. Inverse modeling, in many cases performed with the ITOUGH2 code (Finsterle 1993), was used to estimate rock-property values by varying the physical properties until an optimal fit was achieved between computed and measured values of parameters such as liquid saturation and water potential.

Development and improvement of the site-scale unsaturated zone model continued with intensive calibration against site data (Bodvarsson and Bandurraga 1996). Calibration exercises conducted with the model included matching saturation and water potential data, gas pressures and gas flow rates, ambient temperature and heat-flow data, locations of perched-water bodies, and concentrations of environmental isotopes. Preliminary work began on model calibrations with respect to percolation fluxes inferred from fracture-coating data. Coupled calibrations of various state variables (e.g., liquid potentials, liquid saturations) were also started, providing tighter parameter constraints. In addition to model calibration, considerable effort was devoted

to parameter uncertainties and sensitivity studies for fracture and matrix properties, infiltration patterns, fault properties, and percolation fluxes. Studies of the various numerical approaches (e.g., effective-continuum method, dual-porosity method, dual-permeability method) and their appropriate use for different processes such as moisture flow, gas flow, heat flow, and chemical transport also were presented. Bodvarsson et al. (1997) describe further model refinement and calibration, incorporation of ESF data, development of hydrologic properties data, evaluation of the spatial distribution of the percolation flux, and evaluation of the impact of potential future climate changes at Yucca Mountain.

The most recent improvements and advances in the site-scale unsaturated zone flow and transport model are described in a series of analysis and modeling reports. These analysis and modeling reports encompass the complete range of technical topics necessary to document the current status of the unsaturated zone model. These topics include numerical grids, numerical methods, calibrated properties model, the primary unsaturated zone models and submodels, seepage model for performance assessment, radionuclide transport models, mountain-scale coupled thermohydrologic models, and drift-scale coupled thermohydrologic-chemical seepage models. These topics are summarized, according to the content of the analysis and modeling reports, in Sections 8.10.3 to 8.10.10.

### **8.10.3 Numerical Approaches and Their Applicability to Yucca Mountain**

In this section, currently available numerical approaches that can be used for modeling flow and transport in unsaturated fractured rocks are reviewed briefly. The appropriateness of these approaches for use in the unsaturated zone flow and transport model of Yucca Mountain is discussed.

A variety of numerical approaches have been proposed in literature about flow and transport processes in fractured media at the field scale (CRWMS M&O 2000m, Section 6.4.1, p. 35). When classified according to the manner in which fracture networks are treated in the model structure, the approaches fall into one of three groups: continuum approaches, discrete-fracture network approaches, and other approaches.

#### **8.10.3.1 Continuum Approaches**

In continuum approaches, fractures are considered to be sufficiently ubiquitous and distributed in such a manner that they can be described statistically in a meaningful way (CRWMS M&O 2000m, Section 6.4.1.1, p. 35). The role of individual fractures in fractured media is considered to be similar to that of individual pores in porous media. Therefore, one can describe average fracture properties as macroscopic and those associated with individual fractures as microscopic. Theoretically, the macroscopic scale is related to the representative elementary volume. A physical property value at a "point" in the fracture or matrix continuum is defined as that averaged over the corresponding representative elementary volume. When the continuum approaches are valid, the size of a representative elementary volume must be much larger than the scale of microscopic heterogeneity and much smaller than the scale of whole flow and/or transport domain.

In continuum approaches, connected fractures and rock matrix are viewed as two or more overlapping, interacting continua (CRWMS M&O 2000m, Section 6.4.1.1, pp. 35 and 36). In this case, the continuum mechanics formulations, such as those used for porous media, can be used to describe flow and transport in each continuum. Coupling of processes between different continua is determined by interaction mechanisms at a subgrid scale. Depending on the number of continua and methodologies used to treat fracture-matrix interaction, continuum approaches can be further classified as effective-continuum, dual-continua, and multiple-interacting-continua approaches.

In the effective-continuum approach, fractures and rock matrix are replaced with a single effective continuum (CRWMS M&O 2000m, Section 6.4.1.1.2, p. 36). In the traditional effective continuum, nonzero liquid saturation in the fracture does not occur until the matrix is fully saturated, which occurs at the threshold saturation. Composite characteristic curves are constructed that embody matrix behavior when the saturation of the effective continuum is less than the threshold saturation and fracture behavior when the saturation is greater than the threshold saturation. In the generalized effective continuum (Wu et al. 1999b, p. 194), the concept of threshold saturation is not invoked. Instead, liquid saturation is partitioned into the matrix and fracture in accordance with the principle of local thermodynamic equilibrium, which requires capillary pressure in the matrix and equal fracture components in the grid block. Thus, in the generalized effective-continuum formulation, fracture flow occurs at all saturations, although small fracture flow is computed at low saturations. Effective continuum also assumes fractures and matrix with the same chemical concentration and temperature. The effective-continuum approach provides a substantial simplification for describing flow and transport in fractured porous media and is computationally efficient in handling a large model grid. However, the assumptions on which the effective continuum is based may break down when long times are needed to reach local conditions of equilibrium between the fracture and matrix continua. This is especially true for a very tight and low-permeability rock matrix with rapid fracture flow (Wu et al. 1999b, p. 195).

In dual-continua approaches, fractures and matrix are treated as two separate, yet interacting continua, and each grid block is subdivided into one fracture block and one matrix block (CRWMS M&O 2000m, Section 6.4.1.1.3, p. 37). The fracture-matrix flow and transport are approximated as quasi-steady. If global flow occurs only between fracture grid blocks, the approach is known as a dual-porosity approach because fractures alone control large-scale fluid flow and the matrix contributes only an additional storage term. If global flow occurs within both fracture and matrix continua, the scheme is known as a dual-permeability approach (Doughty 1999, p. 76). Compared to the effective-continuum approach, dual-continua approaches can more accurately predict flow and transport because nonequilibrium is allowed between fracture and matrix continua. The dual-porosity approach is valid only when matrix flow is not important. When both fracture flow and matrix flow are important, the dual-permeability scheme is more accurate. On the other hand, since only one matrix block is used for each grid block and a quasi-steady fracture matrix flow assumption is employed, gradients of matrix capillary pressures, temperature, and concentration near a fracture-matrix interface may be poorly predicted using dual-continua schemes. This is especially true during a rapid, transient flow or transport period of a system with large-size and low-permeability matrix blocks. Therefore, the dual-continua approach could give rise to poor solutions to fracture-matrix flow for rapid, transient flow and transport. Under steady-state conditions, however, the gradients

near the matrix surface become minimal, and dual-continua approaches are expected to produce acceptable solutions.

A more general and rigorous approach, the multiple-interacting-continua approach, was developed to overcome the limitations of the effective-continuum approach (CRWMS M&O 2000m, Section 6.4.1.1.4, p. 38). Specifically, the multiple-interacting-continua approach is based on the notion that changes in fluid pressures, temperature, and phase compositions will propagate rapidly through the fracture system, while invading the tight matrix blocks slowly. Therefore, changes in matrix conditions will be locally controlled by the distance from the fractures. In the multiple-interacting-continua approach, all fractures are lumped into one continuum; all matrix materials within a certain (small) distance from the fractures are lumped into a second continuum; matrix materials at a larger distance from the fractures become a third continuum, and so on. Therefore, the multiple-interacting-continua approach can be considered a generalization of the dual-continua approach. Compared with dual-continua approaches, the multiple-interacting-continua approach can more accurately predict flow and transport in fractured media, but it has larger computational requirements.

### **8.10.3.2 Discrete-Fracture Network Approaches**

Discrete-fracture network approaches are based on an assumption that flow and transport behavior can be predicted from knowledge of the fracture geometry and data on hydraulic properties of individual fractures (CRWMS M&O 2000m, Section 6.4.1.2, p. 38). These approaches involve computational generation of synthetic fracture networks and subsequent modeling of flow and transport in each individual fracture. These approaches have been extensively used for single-phase flow and transport, with deterministic, stochastic, artificial, or site-specific fracture networks in two or three dimensions. Recently, the same approaches also have been applied to unsaturated conditions (Kwicklis and Healey 1993; Kwicklis et al. 1998; Anna 1998b).

While discrete-fracture network approaches are useful tools for concept evaluation or model-based process studies, they have several limitations (CRWMS M&O 2000m, Section 6.4.1.2, p. 38). First, the approaches require geometric parameters that may strongly impact flow and transport, such as fracture apertures and conductivity, but typically cannot be well constrained from field observations (Pruess et al. 1999, p. 308). Second, it is difficult to separate the conductive fracture geometry from the nonconductive fracture geometry. Third, flow and transport models based on these approaches can be complex and computationally intensive for realistic fracture densities. Fourth, to date, the studies based on discrete-fracture network approaches have rarely considered fracture-matrix interaction because of computational complexity (Pruess et al. 1999, p. 308). The fracture-matrix interaction has important effects on flow and transport in unsaturated fractured rocks.

### **8.10.3.3 Assessment of Numerical Approaches**

The appropriateness of the numerical approaches currently available for the unsaturated zone flow and transport model depends on several important factors, including flow and transport behavior at the Yucca Mountain site, scale of the problem, data availability, and computational feasibility (CRWMS M&O 2000m, Section 6.4.2, p. 39). The overall flow and transport

behavior in the unsaturated zone at Yucca Mountain has two important features that constitute the critical basis for assessing numerical approaches for fracture flow and transport:

- Coexistence of a few isolated, transient, fast-flow paths and relatively uniform flow and transport within the majority of fractures, making continuum approaches reasonable choices
- Coexistence of matrix-dominant flow and transport in nonwelded units and fracture-dominant flow and transport in welded units, which can be handled easily by continuum approaches.

Scale of the problem is an important factor for assessing the appropriateness of numerical schemes for the unsaturated zone flow and transport model. Because continuum approaches are relatively simple and straightforward to implement, they are preferred for most applications that are encountered in practice (CRWMS M&O 2000m, Section 6.4.2, p. 39). There are estimated to be about 1 billion fractures at Yucca Mountain (Doughty 1999, p. 77), making it practically impossible to construct and calibrate a discrete fracture network site-scale model, considering data availability and computational feasibility. Based on the above considerations, continuum approaches have been considered appropriate for use in the unsaturated zone model. As a compromise between accuracy and feasibility, the dual-permeability method has become the primary modeling approach currently used in the unsaturated zone model and submodels to simulate water flow, heat transfer, and chemical transport.

#### **8.10.3.4 Heterogeneity and Parameterization**

Heterogeneities exist at different scales within both the fracture and matrix continua in the unsaturated zone at Yucca Mountain (CRWMS M&O 2000m, Section 6.4.3, pp. 39 and 40). Parameterization refers to the use of a number of parameters to represent the heterogeneous distribution. Treatment of subsurface heterogeneity and parameterization are important for modeling flow and transport processes. For modeling flow and transport in the unsaturated zone at Yucca Mountain, subsurface heterogeneity has been treated using a geology-based, deterministic approach in which an entire model layer is assigned uniform properties. The geology-based deterministic approach is based on the following considerations:

- Overall behavior of site-scale flow and transport processes is determined primarily by relatively large-scale heterogeneities associated with the geological structures of the mountain.
- The complexity of a heterogeneity model needs to be consistent with the availability of the data. More complicated models introduce larger degrees of uncertainties in rock-property estimations when data are limited because they invoke larger numbers of variables.
- The layered approach is supported by field observations, such as similarities in distribution of matrix water saturation for a given geologic unit, indicating that matrix flow behavior and effective hydraulic properties should be similar within the unit.

- A flow and transport model based on a layered approach can be relatively easily calibrated with multiple data sets and provides a means to incorporate a significant amount of the available site data.
- Upscaling issues can be dealt with in a straightforward manner using inverse modeling when a layered approach is employed because effective parameters can be inferred directly by matching the large-scale simulation results with grid-block-scale observations averaged from small-scale measurements.

### 8.10.3.5 Considerations for Modeling Chemical Transport

In general, there are two kinds of numerical algorithms for modeling chemical transport in the subsurface, the conventional algorithm based on finite difference and/or finite element methods and the particle-tracking algorithm (CRWMS M&O 2000m, Section 6.4.4, p. 41). In the particle-tracking algorithm, chemical mass is divided into a large number of particles and chemical transport is simulated by calculating particle movement, which is determined by velocity fields, dispersion/diffusion coefficients, and fracture-matrix interaction formulations. Compared with the conventional approaches, particle tracking has the following two advantages:

- Particle tracking can significantly reduce or eliminate numerical dispersion, which artificially smears concentration fronts in many coarse-grid simulations of chemical transport.
- Particle-tracking algorithms can be computationally more efficient.

One shortcoming of particle-tracking algorithms is that they can be used only for chemical transport with simple chemical reactions like linear sorption and decay. These considerations suggest that particle-tracking algorithms are appropriate for modeling chemical transport with simple reactions, and conventional algorithms are appropriate for transport with complex reactions. Both particle-tracking and conventional algorithms should yield similar results for transport with simple reactions when numerical dispersion is insignificant.

Although it is generally recognized that dispersion in a fractured medium is physically different from dispersion in a porous medium, the porous medium form of the dispersion tensor generally is used for lack of a more appropriate expression (CRWMS M&O 2000m, Section 6.4.4, pp. 41 and 42). Dispersion may not be a major transport mechanism for the unsaturated zone at Yucca Mountain because for a dual-continua system, chemical transport is determined primarily by the largest heterogeneity, the property difference between the matrix and fracture continua. In this case, heterogeneity in each continuum, resulting in the corresponding macroscopic dispersion process, becomes secondary. Therefore, more accurate description of the fracture dispersion may not significantly improve the accuracy of transport simulations. This is supported by a tracer-transport simulation study conducted in ESF Alcove 1 (Section 8.10.6.10.1).

Because radionuclide transport is a transient process, the use of a dual-continua approach may result in some modeling errors for chemical transfer between fractures and the matrix (CRWMS M&O 2000m, Section 6.4.4, pp. 41 and 42). This is particularly true when the chemical transfer occurs only within a portion of the matrix close to the fracture-matrix interface. Generally, the dual-continua approach may underestimate the chemical concentration gradient at the fracture-

matrix interface and, therefore may underestimate chemical transfer from fractures to matrix under certain conditions. This is confirmed by the modeling study of Doughty (1999, pp. 94 and 95), which showed that the dual-continua approach yields shorter travel times than the multiple-interacting-continua approach. Because matrix transport processes correspond to relatively long travel times to the water table compared with those in fractures, the dual-continua approach is expected to give conservative predictions of radionuclide transport in the unsaturated zone.

#### **8.10.3.6 Active-Fracture Model**

In a dual-continua approach, the treatment of fracture-matrix interaction is important for accurate modeling flow and transport, and the active-fracture model accounts for this interaction in a realistic manner (CRWMS M&O 2000m, Section 6.4.5, p. 42). Although a number of mechanisms exist, fingering flow at a fracture network scale is considered to be a key mechanism for limiting fracture-matrix interaction and is more important than that at a single-fracture scale (CRWMS M&O 2000m, Section 6.4.5.1, p. 42). For unsaturated fractured rock, the pattern of water flow is expected to exhibit significant preferential (fingering) flow at a fracture-network scale because of the large nonlinearity involved in an unsaturated system and heterogeneities of fracture structure at different scales. The active-fracture concept is based on the reasoning that as a result of fingering flow, only a portion of fractures in a connected, unsaturated fracture network contribute to liquid water flow, while others are simply bypassed. It is hypothesized that the number of active fractures in the unsaturated zone at Yucca Mountain is small compared to the total number of connected fractures. Therefore, active fractures, rather than total connected fractures, must be used in numerical models. Further, it is hypothesized that the number of active fractures within a grid block is large, such that a continuum approach is still valid for describing fracture flow. These hypotheses are consistent with the consideration that flowing fractures in the unsaturated zone are many and highly dispersed.

To use the active-fracture concept to model flow and transport in fractures, active fractures are treated as a portion of the homogeneous fracture continuum for a given grid block (CRWMS M&O 2000m, Section 6.4.5.1, pp. 42 and 43). It is important to note differences between the active-fracture model and the conventional, capillary-equilibrium-based fracture-water distribution model. The latter assumes that liquid water occupies fractures with small apertures first, followed by fractures with relatively large apertures as water potential (or water saturation) increases. In contrast, the active-fracture model presumes gravity-dominated, nonequilibrium, preferential liquid water flow in fractures, which is expected to be similar to fingering flow in unsaturated porous media. A liquid finger can bypass a large portion of a porous medium; which does not necessarily correspond to large pores. It is also consistent with the numerical study results of Kwicklis and Healey (1993, pp. 4097 to 4099), which showed that the distribution of liquid water in a connected fracture network is not necessarily determined by fracture apertures.

Flow and transport conditions and fractured rock properties should determine the fraction of active fractures in a connected-fracture network (CRWMS M&O 2000m, Section 6.4.5.1, p. 43). All connected fractures are active if the system is fully saturated with liquid, and all fractures are inactive if the system is at residual saturation. Thus, the fraction of active fractures should be related to water flux in fractures. It is generally believed that more fractures are conducive to larger water flux. The water flux in fractures is considered to be dependent mainly on fracture saturation because fracture-water flow is gravity dominated. Liu et al. (1998, pp. 2633 to 2646)

have developed a mathematical expression that describes these conditions and includes a single parameter ( $\infty$ ) that is a power function of effective water saturation in the connected fractures. The expression accounts for all the ramifications of the active-fracture hypothesis (modified fracture capillarity, relative permeability, and fracture-matrix interaction reduction) in an integrated manner. The expression also is roughly consistent with the simulation results for a simple-fracture network (Kwicklis and Healey 1993, pp. 4098 to 4099). Their results indicated that fracture flow generally occurs in a smaller number of fracture segments when the characteristic capillary pressure of the fracture network is reduced. An increase in the magnitude of the capillary pressure corresponds to a decrease in the fracture saturation.

In the active-fracture model, only the active-fracture continuum, a portion of the total fracture continuum, contributes to flow and transport in fractures and fracture-matrix interaction (CRWMS M&O 2000m, Section 6.4.5.2, pp. 43 to 45). Therefore, fracture hydraulic properties should be defined for active fractures. The effective water saturation of active fractures is related to the effective water saturation in connected fractures and should be less than or equal to 1. The effective water saturation of active fractures is related to the actual water saturation in active fractures. If all connected fractures are considered to be active in conducting water, as assumed in previous studies, the water capillary pressure for the fracture continuum may be described by the well-known van Genuchten relation. In the active-fracture model, however, the van Genuchten capillary pressure relation is considered to be relevant for the active-fracture continuum rather than for the whole fracture continuum. For a given effective water saturation in connected fractures, a larger effective water saturation in active fractures corresponds to a lower absolute value for capillary pressure. The liquid-phase relative permeability for the active-fracture continuum is determined directly by the effective water saturation of active fractures. However, because only some of the fractures are active, the relative permeability of the entire fracture continuum should be the relative permeability of active fractures multiplied by the portion of active fractures in the fracture network (Liu et al. 1998, p. 2636).

In the active-fracture model, the reduction factor for fracture-matrix interface area results from three aspects (CRWMS M&O 2000m, Section 6.4.5.2, p. 46):

- The average interface area between mobile water (saturated liquid-water segments) in an active fracture and the surrounding matrix is smaller than the geometric interface area.
- The number of active fractures is smaller than that of connected fractures.
- Average spacing of active fractures is much larger than that of connected fractures.

Under the quasi-steady-state condition, flow and transport between fractures and surrounding matrix is inversely proportional to the corresponding fracture spacing. Based on these considerations, Liu et al. (1998, pp. 2636 to 2638) derived an expression for the reduction factor.

The active-fracture model uses a combination of the volume averaged method and a simple filter to deal with fracture flow and transport (CRWMS M&O 2000m, Section 6.4.5.2, p. 47). Inactive fractures are filtered out in modeling fracture-matrix interaction, flow, and transport in the fracture continuum. It is believed that use of the filtering method could add to continuum approaches the capability of capturing dispersed fingering flow at a subgrid scale. A major

limitation of continuum approaches was considered to be their inability to represent subgrid-scale fingering flow.

#### **8.10.4 Development of Numerical Grids for Flow and Transport Modeling**

Numerical grid generation is an integral part of the development of a complex, three-dimensional model, such as the unsaturated zone flow and transport model of Yucca Mountain (CRWMS M&O 2000e, Section 1, p. 11). The resulting numerical grids, developed using current geologic, hydrogeologic, and mineralogical data, provide the necessary framework for the following:

- Developing calibrated hydrogeologic property sets and flow fields
- Testing conceptual hypotheses of flow and transport
- Predicting flow and transport behavior under a variety of climatic and thermal-loading conditions.

The steps involved in numerical grid development include the following:

- Defining the location of important calibration features
- Determining model grid layers and fault geometry based on the geologic framework model, the integrated site model, and definition of hydrogeologic units
- Analyzing and extracting from the geologic framework model and the integrated site model data pertaining to layer contacts and property distributions
- Discretizing and refining the two-dimensional (planview) numerical grid
- Generating the three-dimensional grid with finer resolution at the potential repository horizon and within the CHn hydrogeologic unit
- Formulating the dual-permeability mesh.

The products of grid development include a set of one-dimensional vertical columns of grid blocks for inversions of the hydrogeologic property set (see Section 8.10.5 for a description of these inverse-modeling simulations), a two-dimensional unsaturated zone flow and transport model vertical cross-sectional grid for calibrations of fault hydrogeologic properties, a three-dimensional unsaturated zone flow and transport model grid for additional model calibrations, and a three-dimensional unsaturated zone flow and transport model grid for generating flow fields for performance assessment. These four sets of model grids are described in CRWMS M&O (2000e, Section 6.1, p. 29, Table 6).

Numerical grid generation is an iterative process that must achieve a proper balance between desired numerical accuracy in terms of grid block size and computational time controlled by the total number of grid blocks (CRWMS M&O 2000e, Section 1, p. 11). Grid block size should reflect the scale of the process to be modeled. For example, in order to capture flow and transport phenomena along individual waste-emplacement drifts, grid block thickness and width

should not exceed the drift diameter or the drift spacing. For large models, such as the site-scale unsaturated zone flow and transport model of Yucca Mountain, flow and transport phenomena occurring on scales of less than a few meters cannot be captured. Rather, the model is intended to provide an overview of key unsaturated zone characteristics and processes potentially affecting repository performance. Grids also must be adapted to the particular needs of the processes to be modeled because sharp gradients may occur in different domains for different flow processes. At Yucca Mountain, the heterogeneous, variably fractured layers are best represented by a dual-continua (matrix and fracture) model, rather than a single-continuum approach (Section 8.10.3). Once developed, the numerical grids for the unsaturated zone flow and transport model are evaluated for appropriate resolution, representation of important features, and proper grid block connections.

#### **8.10.4.1 Data Sources for Development of Numerical Grids**

The primary source of data for the development of numerical grids for unsaturated zone flow and transport modeling is the geologic framework model, version 3.1, which is a representation of lithostratigraphic layering and major fault geometry in the Yucca Mountain area (CRWMS M&O 2000e, Section 4.1, pp. 17 and 18). The model contains information about layer thickness and layer contact elevation and defines major fault orientation and displacement. The data for each layer and each fault within the geologic framework model are available on a regular horizontal grid spacing of 60 by 60 m (200 by 200 ft) over the model's domain. A total of 48 geologic units and 42 faults are represented in the geologic framework model. Approximately 40 of these units and 18 faults (those that lie within the unsaturated zone flow and transport model domain) were incorporated into the three-dimensional unsaturated zone flow and transport model grids.

Data pertaining to hydrogeologic rock properties also were used in the development of numerical grids for the unsaturated zone flow and transport model (CRWMS M&O 2000e, Section 4.1, p. 42). Based on analyses of several thousand rock samples, 30 hydrogeologic units have been identified (Flint L.E. 1998, pp. 1 and 3 to 4). Because the hydrogeologic property sets to be calculated with the model grid used, to a large extent, the matrix properties data collected and analyzed by Flint, L.E. (1998), layering within the numerical grid was chosen to correspond as closely as possible to hydrogeologic units, in order to facilitate data usage. The boundaries of hydrogeologic units are not defined by regularly spaced data, but are more qualitative in nature. The qualitative descriptions given in Flint L.E. (1998, pp. 21 to 32), when correlated with the geologic framework model, version 3.1, data, are used to develop a set of hydrogeologic layers (thickness and elevation are described by regularly spaced data) for the unsaturated zone flow and transport model.

Because of the importance of mineral (especially zeolitic) alteration on flow and transport calculations, boundaries between vitric and zeolitic areas were defined within certain unsaturated zone flow and transport model grid layers below the repository horizon (CRWMS M&O 2000e, Section 4.1, p. 18). Data used in numerical grid development for defining low-permeability, zeolitic volumes of rock are obtained from the rock properties model of the integrated site model, version 3.0 (Section 4.8).

The repository layout configuration is used during numerical grid generation to locate areas where a finer grid mesh was needed to enhance numerical resolution (CRWMS M&O 2000e, Section 4.1, p. 18). The lower boundary of the unsaturated zone flow and transport model was defined by the most recent (1993) water-table elevations given in the Yucca Mountain Site Characterization Project (YMP) Reference Information Base. In addition, perched-water elevations for two boreholes north of the site area, USW G-2 and USW WT-24, were used to define the lower boundary of the model. Fracture hydrogeologic properties describing unsaturated zone flow and transport model layers were used to formulate the dual-permeability meshes for one-dimensional hydrogeologic property set inversions, for two-dimensional fault property calibration, for three-dimensional unsaturated zone flow and transport model calibration, and for generating three-dimensional flow fields for performance assessment.

#### **8.10.4.2 Computer Software Used for Development of Numerical Grids**

The software used for development of numerical grids for the unsaturated zone flow and transport model and submodels are described in CRWMS M&O (2000e, Section 3 and Table 1). EARTHVISION was used to evaluate and extract data from the geologic framework model, version 3.1, and the integrated site model, version 3.0 (CRWMS M&O 2000e, Section 3, p. 15). The software program "ESF4\_XYZ V.03.XLS" was used to calculate easting and northing coordinates for alcoves and niches within the ESF, given their linear distance in meters from the North Portal. The WinGridder software program was used to generate one-, two-, and three-dimensional grid-block element and connection information in a TOUGH2 format (the primary mesh is an effective-continuum mesh). The software macro DKMgenerator generates a dual-permeability mesh from a primary effective-continuum mesh. The software macro ExportProp exports information on rock properties from the integrated site model, version 3.0.

#### **8.10.4.3 Overview of Numerical Grid Development**

Data extracted from the geologic framework model, version 3.1, and the integrated site model, version 3.0 (Section 4.8), form the basis for numerical grid development (CRWMS M&O 2000e, Section 6.1, p. 30). With these data, an initial two-dimensional (plan view) grid was developed defining locations of boreholes, faults, the ESF, the Enhanced Characterization of the Repository Block (ECRB), and potential repository columns, where appropriate. Using the two-dimensional grid as the basis for column locations, a three-dimensional effective-continuum grid was constructed using layer horizon and thickness data from the geologic framework model, version 3.1. Initial grid generation was followed by an iterative process of grid evaluation and modification in order to achieve appropriate spatial resolution and representation of important features and to ensure proper connections between the various elements of the grid. Revisions were made accordingly until these criteria were met. Next, the three-dimensional effective-continuum grid was modified to allow for dual-continua processes (matrix and fracture flow) using a dual-permeability mesh maker, DKMgenerator. The DKMgenerator incorporates information from fracture data analyses (i.e., fracture porosity, spacing, aperture, and fracture-matrix interaction area) into the grids.

The computer code WinGridder was used to generate one-, two-, and three-dimensional integral finite difference grids for the unsaturated zone flow and transport model domain (CRWMS M&O 2000e, Section 6.1, pp. 30 and 31). The type of grid generated by WinGridder version 1.0

was consistent with the computational requirements of the TOUGH2 simulator. TOUGH2 and the inverse modeling code ITOUGH2 use cells or grid blocks, and connections between those grid blocks to represent the flow system without requiring the global location of each grid block or connection. This approach provides great flexibility in describing complex flow geometry and relationships between individual objects within the system. Unlike other gridding software, WinGridder has the capability of designing complex, irregular grids with large numbers of cells and connections, and it can handle incorporation of nonvertical faults and other embedded refinements, such as spacing of waste-emplacement drifts within the potential repository area.

The methods used to develop numerical grids for inversions of hydrogeologic property sets, model calibration, and calculation of unsaturated zone flow fields are summarized in Sections 8.10.4.4 to 8.10.4.9.

#### **8.10.4.4 Boundaries and Calibration Features**

The areal domain of the unsaturated zone flow and transport model encompasses approximately 40 km<sup>2</sup> (15 mi.<sup>2</sup>) of the Yucca Mountain area (CRWMS M&O 2000e, Section 6.2, pp. 31 to 33). Figure 8.10-2 is a map view of the model domain, including the potential repository boundary, the paths of the ESF and ECRB Cross Drift, major faults defined in the geologic framework model, version 3.1, and selected boreholes. Yucca Wash marks the northern model boundary, while the approximate latitude of borehole USW G-3 defines the southern boundary. The eastern model boundary coincides with the Exile Hill, "Toe," and Bow Ridge faults, and the western boundary lies approximately 1 km (0.6 mi.) west of the Solitario Canyon fault. These boundaries encompass many of the existing hydrology wells for which extensive moisture tension data were used as calibration points for determining layer properties (Section 8.10.4.5). One important objective of selecting these boundaries was to minimize potential boundary effects on numerical simulation results within the repository footprint. The upper boundary of the unsaturated zone flow and transport model is the bedrock surface (topography minus alluvium), which is defined by the geologic framework model, version 3.1. The lower boundary is located coincident with the water table (potentiometric surface derived from water level elevation data described in the YMP Reference Information Base). Borehole water level elevations beneath Yucca Mountain suggest the water table can be separated into three zones. East of the Solitario Canyon fault and below the potential repository, the water level elevations are approximately flat at 730 m (2,395 ft) above mean sea level. West of the Solitario Canyon fault, the water level elevations are approximately flat at 776 m (2,546 ft) above mean sea level. Well north of the potential repository, water level elevations in boreholes G-2, WT#6, and WT-24 are observed at approximately 1,000 m (3,281 ft) above mean sea level, significantly above the flat water levels observed to the south. Two explanations have been proposed for these observations. Either there is a steep hydraulic gradient in the water table in the northern portion of the mountain, or perched or semiperched water is responsible for the high water level observations. For the purposes of developing unsaturated zone flow and transport model grids, the second alternative is assumed. Consequently, east of the Solitario Canyon fault, the water table was treated as a flat, stable surface at an elevation of about 730 m (2,390 ft) above mean sea level. West of the Solitario Canyon fault, the water table was treated as a flat surface at an elevation of about 776 m (2,540 ft) above sea level (CRWMS M&O 2000q, p. 149).

Unsaturated zone flow and transport model calibration features represented as column centers in the one-dimensional inversion and three-dimensional calibration grids include the following (CRWMS M&O 2000e, Section 6.2, p. 34):

- The vertical boreholes indicated in Figure 8.10-2 (some pairs of closely spaced boreholes are represented by a single vertical column)
- ESF Alcoves 3, 5, 6, and 7 (Figures 8.3-33 and 8.8-1) (Alcove 4 and borehole UE-25 NRG#4 were represented by a single vertical column.)
- ESF Niches 3107 (Niche No. 3), 3566 (Niche No. 1), 3650 (Niche No. 2), and 4788 (Niche No. 4) (Figure 8.8-1)
- ESF/ECRB Cross Drift centerline locations in plan view.

Boreholes, alcoves, niches, the ESF, and the ECRB Cross Drift are important for hydrogeologic property set inversions and calibration (Section 8.10.6) because they are key data collection points. In addition, their locations are reference points for shallow infiltration, which is the upper boundary condition for the unsaturated zone flow and transport model (CRWMS M&O 2000e, Section 6.2, p. 34). The spatial relationships among boreholes, alcoves, niches, faults and ESF/ECRB Cross Drift locations are such that these features may intersect or overlap in the 30-m (98-ft) resolution distance of the grid. Consequently, locations of certain features with respect to column centers were prioritized based on the following hierarchy: boreholes (highest priority), alcoves and niches, faults, ESF, ECRB Cross Drift, other domain nodes (lowest priority).

#### **8.10.4.5 Unsaturated Zone Model Layers and Fault Geometries**

Layering within the unsaturated zone flow and transport model grid was configured to correspond as closely as possible to hydrogeologic units in order to facilitate usage of rock-properties data (CRWMS M&O 2000e, Section 6.3, p. 36). Table 8.10-1 indicates the correlation among major hydrogeologic units, the geologic framework model version 3.1 lithostratigraphic units, unsaturated zone flow and transport model layers, and detailed hydrogeologic units (Flint L.E. 1998, Table 1). In many cases, detailed hydrogeologic units correlate directly to or are simple combinations of geologic framework model version 3.1 layers. In a few instances, multiple detailed hydrogeologic units are present within one geologic framework model version 3.1 layer, such as the Yucca Mountain Tuff (Tpy), the lower nonlithophysal zone of the Topopah Spring Tuff (Tptpln), or the Calico Hills Formation (Tac). Using the information in Table 8.10-1 as a basis for unsaturated zone flow and transport model layering, geologic framework model, version 3.1, layer-thickness (isochore) grid files were combined or subdivided, as appropriate, to correspond to the detailed hydrogeologic units (Section 8.10.4.6).

Faults are important features to include in the unsaturated zone flow and transport model grids because they may either provide fast pathways for flow or serve as barriers to flow (CRWMS M&O 2000e, Section 6.3, p. 38). A fault can be a surface with arbitrary shape in the three-dimensional unsaturated zone flow and transport model domain and is represented as a surface (defined by a set of x, y, z data on a regular grid spacing) in the geologic framework model,

version 3.1. In unsaturated zone flow and transport model grids, fault surfaces are represented by a series of connected columns of grid blocks. Faults can be represented in the grid as either vertical or nonvertical features. Many of the faults at Yucca Mountain are steeply dipping, particularly within the unsaturated zone. For unsaturated zone flow and transport modeling studies of Yucca Mountain, it is believed that flow through faults is much more sensitive to the rock properties assigned to fault zones than to slight variations in fault dip. Because large numbers of grid blocks are needed to discretize nonvertical fault zones, certain criteria have been developed to reduce the total number of grid blocks along faults in order to simplify the unsaturated zone flow and transport model grids. Faults are modeled as vertical if they meet any of the following criteria:

- Have an average dip exceeding 85°
- Have an average dip exceeding 80° and lie greater than 1 km from the potential repository layout area (do not significantly affect flow and transport calculations)
- Are located west of the Solitario Canyon fault
- Coincide with unsaturated zone flow and transport model boundaries.

The faults included within the domain of the unsaturated zone flow and transport model are shown in Figure 8.10-2 and listed in CRWMS M&O (2000e, Table 11). The average slopes of all faults were evaluated to determine which could be approximated by vertical columns of grid blocks in the model grids (CRWMS M&O 2000e, Section 6.3, p. 39). The following faults were represented by vertical columns of grid blocks in the unsaturated zone flow and transport model grids: Solitario Canyon (west), "SolJFat," Sundance, "Toe," Sever Wash, Pagany Wash, Drill Hole Wash, Ghost Dance, Ghost Dance (west), "Imbricate," and Exile Hill faults. The remaining faults (Solitario Canyon, Splay "S," Dune Wash, Dune Wash "X," and Dune Wash (west 1), were represented by nonvertical columns of grid blocks in the three-dimensional model grids. Splay faults "N" and "G" lie close to the Solitario Canyon fault and intersect it at relatively shallow depth. Thus, these two splay faults are considered part of the Solitario Canyon fault zone and are not explicitly defined. However, after grid generation, fault properties can be assigned to the grid blocks closest to the location of these faults, as needed. Faults represented as vertical features in the unsaturated zone model grids use fault-trace information at an arbitrary elevation of 1,100 m (3,600 ft) above mean sea level. During grid generation, vertical columns of grid blocks are assigned along each fault trace. Faults represented with nonvertical columns of grid blocks use fault-trace information at three elevations—near the land surface, near the water table, and approximately midway between them—to capture variations in dip. The unsaturated zone flow and transport model gridding process interpolates the location of each nonvertical fault using data points at the three prescribed elevations. With this approach, the dip of a fault within a given fault column is uniform in each of the upper and lower intervals, but can be different in each interval, which may occur if the fault surface is curved, rather than planar. Furthermore, dip angles within the same vertical interval can be different in different columns (i.e., laterally along a fault). Thus, even a fault with variable dip along its trace can be represented with this method.

#### **8.10.4.6 Extraction of Lithostratigraphic Data from the Geologic Framework Model, Version 3.1, and the Integrated Site Model, Version 3.0**

Geologic layers were correlated with detailed hydrogeologic units as shown in Table 8.10-1, and unsaturated zone flow and transport model layers were determined based on this correlation (CRWMS M&O 2000e, Section 6.4.1, p. 41). Based on the relationships in Table 8.10-1, certain geologic framework model version 3.1 layers (represented by isochore grids) were combined, while others were subdivided, to create hydrogeologic model layers for the unsaturated zone model grids. Geologic framework model version 3.1 isochore grids used in fiscal year 1999 unsaturated zone model grid development include those lying between the upper Tpcpv3 contact and the lower Trambt contact. Layers with the following features were combined:

- They have similar hydraulic properties.
- They are very thin across Yucca Mountain.
- Property data are very limited for the rock units.

Geologic framework model version 3.1 isochores were subdivided if rock-property data suggest two or more distinct hydrogeologic layers within a geologic unit.

Based on the detailed hydrogeologic units defined by Flint, L.E. (1998, Table 1), geologic framework model version 3.1 layer Tpy (Yucca Mountain Tuff) was subdivided vertically into three layers of equal proportional thickness (CRWMS M&O 2000e, Section 6.4.1, p. 42). Because the densely welded Tptrv1 (Topopah Spring Tuff upper vitrophyre) is relatively thin (0 to 2 m [0 to 6.6 ft] thick, typically less than 0.5 m [1.6 ft]) across Yucca Mountain, geologic framework model version 3.1 layers Tptrv1 and Tptrn (Topopah Spring Tuff upper nonlithophysal unit) were combined to capture within the vertical resolution of the model this potentially important flow unit at the interface of PTn and Topopah Spring welded (TSw). The upper 2 m (6.6 ft) of the combined unit was assigned a distinct model layer name corresponding to the detailed hydrogeologic unit "TC," and the remaining thickness of the combined unit corresponds to detailed hydrogeologic unit "TR." Geologic framework model version 3.1 layer Tptpln (Topopah Spring lower nonlithophysal) was subdivided vertically into two model layers to correspond with detailed hydrogeologic units "TM2" and "TM1" (Table 8.10-1). Geologic framework model version 3.1 layer Tac (Calico Hills Formation) was subdivided vertically into four layers of equal proportional thickness throughout the domain of the unsaturated zone flow and transport model because of its large thickness beneath northern Yucca Mountain.

In addition to defining the discretization of vertical grid blocks based on hydrogeologic units, elevations of three major horizons were defined in the unsaturated zone flow and transport model grids using the program WinGridder (CRWMS M&O 2000e, Section 6.4.2, p. 43). These horizons are a top boundary equivalent to the bedrock surface, a structural reference horizon that identifies faults and their associated offsets, and a bottom boundary equivalent to the water table. The reference horizons are surfaces from which elevations of all hydrogeologic unit interfaces were calculated by stacking layer thicknesses above or below them based on their stratigraphic position. All offsets resulting from faulting were described by the reference horizon data.

#### 8.10.4.7 Two-Dimensional Grid Generation

The two-dimensional (map view) grid defined the structure of columns and segments that provide the basis for projecting the three-dimensional grid (CRWMS M&O 2000e, Section 6.5, p. 44). Each column was represented by a node in map view that indicated the column's position in the x-y plane. Additionally, the shape of each column is a polygon in the x-y plane whose boundaries consist of segments that were defined prior to three-dimensional grid generation. Grid development began with the assignment of nodes in map view for each object (e.g., domain nodes, fault nodes, and repository nodes) with specified orientation and density. Based on the location of these nodes, a primary two-dimensional grid was generated using the WinGridder program. The two-dimensional grid was then improved systematically and interactively by deleting physically incorrect or unnecessary connections. A few iterations of these steps, including adding, moving, and deleting certain nodes, were necessary to create the final two-dimensional grid, that served as the basis for generating the vertical component of the unsaturated zone flow and transport model grid.

Two-dimensional grid generation for the unsaturated zone flow and transport model considered the location of domain and repository boundaries; borehole, alcove, and niche locations; and map-view traces of the ESF, ECRB Cross Drift, and major faults (CRWMS M&O 2000e, Section 6.5, p. 44). Various subsets of these features were included in the different unsaturated zone flow and transport model grids depending on their intended use. Because the one-dimensional hydrogeologic property-set inversions considered rock properties data only from vertical boreholes, only borehole locations are relevant when generating this particular grid. In contrast, the two-dimensional grid used for calibration of the unsaturated zone flow and transport model (Figure 8.10-3) contains nodes for all data sources (boreholes, alcoves, niches, ESF, and ECRB cross drift) and along faults within the site-scale model domain. The unsaturated zone flow and transport model calibration grid contains 1,434 vertical columns, and when the grid is projected vertically downward through the model layers, it encompasses 53,512 grid blocks in the effective-continuum formulation for the site-scale model (CRWMS M&O 2000e, Attachment V, Table V-1). The number of grid blocks nearly doubles for the dual-permeability formulation (see Section 8.10.3.1 for a discussion of the dual-permeability approach). The grid designed for flow-field calculations (Figure 8.10-4) and used mainly for performance assessment studies, contains nodes only for fault traces and borehole locations, but has a denser grid mesh within the potential repository area.

Grid resolution (node spacing) was a compromise between computational efficiency and a need to capture spatial variability in rock properties and boundary conditions such as infiltration rate (CRWMS M&O 2000e, Section 6.5, p. 44). In the case of model calibration, the goal was to generate a two-dimensional grid that was as computationally efficient as possible, while capturing the level of detail necessary to perform reasonably accurate calibrations. The result was a fairly coarse two-dimensional grid with refinement added only in the location of calibration features (boreholes, alcoves, niches, ESF, and ECRB Cross Drift) and along faults. In doing this, the grid captured the needed spatial variability in the infiltration rate at the bedrock surface. Unlike the calibration grid, the grid for performance assessment activities contains greater numerical resolution within the potential repository boundary, the area most important to predictive studies.

#### 8.10.4.8 Three-Dimensional Grid Generation

Model-layer contact elevations were determined for each vertical column within the grid based on the value of the closest geologic framework model version 3.1 isochore or surface-horizon data point (CRWMS M&O 2000e, Section 6.6, p. 45). The estimated maximum error in layer contact elevations at unsaturated zone flow and transport model column centers is about 5 m, assuming that the hydrogeologic layers dip 10°. The three-dimensional grid describes the location, rock material name, and connection information for each three-dimensional grid block in the unsaturated zone flow and transport model domain. All three-dimensional grid blocks (cells) were generated column by column with WinGridder based on the plan-view grid design to ensure that each vertical connection occurs between adjacent grid blocks and that each grid block has at least one vertical connection. Lateral connections were then generated segment by segment within a model layer, with each segment joining two neighboring columns. This ensures that only grid blocks in two adjacent columns have lateral connections and that no connections between two adjacent columns are missing.

The maximum thickness of any cell within the unsaturated zone model grids was 60 m (200 ft) (CRWMS M&O 2000e, Section 6.6, pp. 45 and 46). If the thickness of a model layer within a column exceeded 60 m (200 ft), the layer was subdivided equally into two layers. The minimum vertical grid resolution was 1.5 m (4.9 ft). If the thickness of a hydrogeologic layer was less than 1.5 m (4.9 ft) within a column, the layer was considered absent and no grid block was generated for the layer at this location. To conserve the total thickness of the unsaturated zone, layer thicknesses less than 1.5 m (4.9 ft) were added to the overlying layer if they were above the structural reference horizon (top of Tpbt4), or were added to the underlying layer if they were below the reference horizon.

A finer mesh grid was developed to increase vertical resolution within and below the potential repository horizon (CRWMS M&O 2000e, Section 6.6, p. 46). The potential repository volume encompasses five grid layers, each 5 m thick. Below the highest elevation of the potential repository horizon (1,111 m [3,645 ft] above sea level) and in the area lying south of N 236,000 m and east of E 170,000 m (Figure 8.10-4), model layers were subdivided if their thickness exceeded 20 m (66 ft). The additional vertical resolution was added to enhance modeling of flow and transport between the potential repository horizon and the water table and any potential downgradient areas outside the potential repository footprint. Consistent with current repository design, all model columns representing the potential repository (Figure 8.10-4) were aligned, in plan view, along the direction of the planned configuration of the emplacement drifts (CRWMS M&O 2000e, Section 6.6.2, p. 48). Each column of grid blocks (except those corresponding to borehole locations) has four sides to facilitate the representation of a drift with a series of connected three-dimensional grid blocks. For the interfaces between repository grid blocks, lateral connections were established if two adjacent grid blocks belong to the same layer within the five-layer grid structure of the potential repository horizon. For interfaces between a repository grid block and a nonrepository grid block, the connection was built based on the similarity of their hydrogeologic layer.

Material properties were assigned to grid blocks depending on the hydrogeologic layer to which the grid block corresponds (CRWMS M&O 2000e, Section 6.6, p. 46). For layers with multiple properties, such as the vitric and zeolitic zones within the Calico Hills Formation, polygons

defining the areal extent of these zones were created so that the assignment of material properties to model grid blocks could be confined to the appropriate polygon.

Although faults may occur as displacement surfaces only or as deformation zones of variable width, each fault within the current unsaturated zone flow and transport model domain is represented by columns of grid blocks with an arbitrary width of 30 m (98 ft) (CRWMS M&O 2000e, Section 6.6.1). Nevertheless, adjustments were made within the grid to assign appropriate rock properties and to ensure accurate representation of various fault configurations. The three most important fault configurations are the following:

- A discontinuity of geological layers that may result in a structural barrier to lateral flow
- A continuous zone that may serve as a fast path for flow depending on hydraulic properties
- A nonvertical fault whose angle of inclination may vary spatially.

To implement these features in the unsaturated zone flow and transport model grids, three parallel rows of fault-related columns were constructed for each fault (CRWMS M&O 2000e, Section 6.6.1). Each section of a fault in map view consists of three connected columns, with the fault column located in the middle. The inclination of the fault was represented by a series of connected grid blocks whose x and y locations vary with elevation. The fault-related grid blocks were connected vertically, if they belong to the same column, regardless of the fault angle. Additional vertical resolution was added to fault-related grid blocks based on the elevation of hydrogeologic layer contacts on both sides of the fault. Consequently, vertical grid discretization in each set of the three fault-related columns is identical, and all interfaces between hydrogeologic units in both side columns correspond to the interfaces between grid blocks. The layer and rock properties of fault grid blocks were then assigned according to the stratigraphy of the fault column. Fault-related lateral connections are of two types: fault-fault grid block connections and fault-side cell connections. In either case, lateral connections were assigned between grid blocks that share the same interface; and the interface area was determined based on the contact area between the two grid blocks.

Special care was taken in construction of the unsaturated zone flow and transport model grid to accurately represent the vitric-zeolitic boundary in the CHn. The distribution of low-permeability zeolites is of great importance in modeling unsaturated zone flow and transport of Yucca Mountain because zeolites have the potential to significantly alter flow paths and radionuclide transport from the potential repository horizon to the water table (CRWMS M&O 2000e, Section 6.6.3). At high matrix saturations, liquid water flow within the CHn seems to be diverted around zeolitic volumes of rock and only a low percentage of the total percolation flux is expected to travel through significantly zeolitized tuffs (Section 8.9.1.2). Therefore, high- and low-permeability regions were defined within certain unsaturated zone flow and transport model layers corresponding to the tuffs of the upper CHn (above lithostratigraphic unit Tactb). Lateral boundaries between high- and low-permeability tuffs within the CHn were determined using results from the geostatistical rock properties model contained in the integrated site model, version 3.0. The net result was the vertical subdivision of the lithostratigraphic unit Tac into four

grid layers, each containing separate but laterally contiguous vitric and zeolitic regions to which separate hydrogeologic and sorptive properties were assigned.

As indicated in Table 8.10-1, the vertical grid used for calibration of the site-scale unsaturated zone flow and transport model contains 32 layers. These layers, along with selected columns from the unsaturated zone flow and transport model calibration grid and the geologic framework model version 3.1 stratigraphy are shown in Figure 8.10-5. The figure also shows how the offset and dip angle of faults is represented by the sets of three connected columns of grid blocks. In the potential repository footprint (Figure 8.10-2), the number of layers was increased to 44 (about 15 above, 5 within, and about 24 below the potential repository horizon) (CRWMS M&O 2000e, Section 6.8) to provide greater vertical resolution of flow and transport calculations for use in performance assessment. Overall results from the development of numerical grids for the unsaturated zone flow and transport model of Yucca Mountain include the following:

- One primary mesh and four dual-permeability meshes consisting of one-dimensional columns at borehole locations for developing calibrated hydrogeologic property sets
- One primary mesh and two dual-permeability meshes consisting of a two-dimensional cross section through Yucca Mountain to calibrate fault hydrogeologic properties
- One primary mesh and two dual-permeability meshes for three-dimensional unsaturated zone flow and transport model calibration
- One primary mesh and three dual-permeability meshes to generate three-dimensional, unsaturated zone flow fields for performance assessment.

#### **8.10.5 Calibrated Properties Model**

The calibrated properties model provides calibrated parameter sets (interpreted input data) for unsaturated zone flow and transport process models for the YMP (CRWMS M&O 2000f, Section 1). These calibrated property sets include matrix and fracture hydrologic-property values for the unsaturated zone flow and transport model, drift seepage models, drift-scale and mountain-scale coupled-process models, and TSPA models. These process models provide the necessary framework to test conceptual hypotheses of flow and transport at different scales and predict flow and transport behavior under a variety of possible climatic and thermal loading conditions for the potential repository. The principal outputs or products from the calibrated properties model are the following calibrated property sets:

- Mountain-scale calibrated parameter sets based on one-dimensional inversions for base-case, upper-bound, and lower-bound infiltration rates
- Drift-scale calibrated parameter sets based on one-dimensional inversions for base-case, upper-bound, and lower-bound infiltration rates
- Calibrated fault parameters based on two-dimensional inversions for base-case, upper-bound, and lower-bound infiltration rates.

The properties-calibration process involved a series of inverse-modeling simulations (inversions) using the computer code ITOUGH2 (Finsterle 1993, 1999). Property sets were generated corresponding to maps of the best estimate of current net infiltration as well as maps representing the upper and lower bounds of net infiltration (Section 8.2.10).

Calibration of the unsaturated zone flow and transport model was necessary in order to refine the property estimates derived from laboratory and field data so that they were suitable for use in the unsaturated zone flow and transport model and so that the model accurately depicts hydrologic conditions in the mountain (CRWMS M&O 2000f, Section 6). Because the unsaturated zone flow and transport model considers hydrologic processes on a mountain scale and properties are scale-dependent, upscaling is an inherent part of the calibration process. The calibration process also reduces the uncertainty and bias associated with property estimation. Because property estimates from laboratory and field data collected at Yucca Mountain have uncertainty associated with them, data inversion was used to calibrate some of the numerical model parameters (properties). Inversion is an iterative process in which predictions from a numerical model are compared to data, and the numerical model parameters are adjusted (calibrated) to improve the match between the model prediction and the data. For the unsaturated zone flow and transport model, the data that were inverted to provide the calibrated properties include saturation in the rock matrix, water potential in the rock matrix, and pneumatic pressure in the fractures. Estimates of hydrologic properties from laboratory and field measurements, which provide initial guesses for model parameters, also were included as data in the inversions.

Model parameters that were estimated through the inversion process are fracture and matrix permeability, van Genuchten parameters for the fractures and matrix, and a fracture activity parameter described in Section 8.10.3.6 (CRWMS M&O 2000f, Section 6, p. 31). These parameters were estimated for 32 model layers (Table 8.10-1), although in some cases a common parameter value was estimated for groups of layers, and for 3 of the 4 layers in faults zones. Also, it should be noted that the five layers of the Calico Hills Formation (Tac) were reconstituted into four layers for property inversion: vitric ch1, zeolitic ch1, vitric ch2-ch5, and zeolitic ch2-ch5 (CRWMS M&O 2000f, Section 6.1). A total of 199 rock parameters were estimated through inverse calibration because they represent the smallest set that uniquely represents ambient conditions in the unsaturated zone. Fracture and matrix porosity were not calibrated in the liquid flow simulations because the steady-state simulations are insensitive to porosity variations. Similarly, in the pneumatic simulations, diffusivity, which is proportional to the ratio of permeability to porosity, is the sensitive parameter. Permeability was chosen for calibration because it is already needed for the liquid flow portion of the calibration. Further, matrix porosity is a well-constrained property because the techniques used to measure it are simple and measurement error was low. Fracture porosity, though not well constrained, would not alone provide sufficient range to calibrate the pneumatic simulations to the data. Residual and saturated saturation were not calibrated because they do not influence the calibration to ambient data as strongly as the van Genuchten parameters. In addition, like matrix porosity, matrix residual saturation is simple to measure with low error.

Calibration of properties for the unsaturated zone flow and transport model through inversion was carried out in a series of steps (CRWMS M&O 2000f, Section 6, p 32). One-dimensional vertical column submodels were used for the calibration of the nonfaulted formation rock parameters for the mountain-scale and drift-scale conceptual models. The one-dimensional

submodels correspond to 11 surface-based boreholes in which saturation, water potential, and pneumatic pressure have been measured. Water flow (or gas flow in the pneumatic simulations) was simulated simultaneously in all columns. An effective average value of each parameter was estimated for each geologic layer in all 11 columns. A two-dimensional model, consisting of an east-west, vertical cross section through borehole USW UZ-7a, was used to calibrate parameters for the faults. Data from USW UZ-7a (location shown in Figure 8.10-2) are the most comprehensive with respect to faults. This is because saturation, water potential, and pneumatic pressure data are available within the Ghost Dance fault zone from the surface down through the upper layers of the TSw (Sections 8.3.2.2, 8.4.2.1, 8.4.2.2, and 8.5.1.2). Because data on faults are so limited (one borehole that only partially penetrates the unsaturated zone), the data were separated into four layers (Tiva Canyon welded [TCw], PTn, TSw, and CHn/Crater Flat undifferentiated [CFu]) to reduce the number of parameters used to characterize the fault zones. Data for inversion were available for only the first three layers because borehole USW UZ-7a bottoms out in the TSw; therefore, only the parameters of these layers were calibrated.

The software ITOUGH2 version 3.2 (Finsterle 1999) was used to carry out the automatic portion of the inversion process (CRWMS M&O 2000f, Section 6, p. 34). The software was used to minimize the sum of the squared, weighted residuals by iteratively adjusting (calibrating) selected model parameters. When the residuals reached a minimum, the resulting parameter set was considered to be the best estimate. Because some important aspects of the conceptual model and some data could not be easily integrated into the format of ITOUGH2 version 3.2 code, some manual adjustments to parameters were made. For example, to ensure that matrix flow was dominant in the PTn and the vitric portion of the CHn, proportions of matrix and fracture flow through each column were checked and appropriate manual adjustment to parameters were made. Another example is the manual adjustment of fracture permeability of the TSw layers to ensure consistency with pneumatic pressure data from boreholes that indicate minimal attenuation of the atmospheric pressure signal through the entire thickness of the TSw (CRWMS M&O 2000f, Section 6, p. 34).

#### **8.10.5.1 Data Sources for the Calibrated Properties Model**

The sources of data for the calibrated properties model are documented in the analysis and modeling report titled *Calibrated Properties Model* (CRWMS M&O 2000f, Table 2).

Developed data used by the calibrated properties model include spatially variable shallow infiltration rates (Section 8.2.10) and several numerical model grids (Section 8.10.4). Uncalibrated matrix and fracture properties and property-estimate uncertainty data used as input to the calibration also are listed in CRWMS M&O (2000f, Tables 3 and 4). Matrix porosity, residual saturation, and saturated saturation were not calibrated (CRWMS M&O 2000f, Section 4.1.1). All other properties and uncertainty data were used as initial guesses and/or to constrain the calibration.

Acquired data used by the calibrated properties model include saturation, water potential, and pneumatic pressure from surface-based boreholes and the ESF/ECRB Cross Drift (CRWMS M&O 2000f, Section 4.1.2, p. 16), and are listed in CRWMS M&O (2000f, Table 2).

Saturation data measured on rock cores (Section 8.3.2.2) from boreholes USW SD-6, USW SD-7, USW SD-9, USW SD-12, USW UZ-14, UE-25 UZ#16, and USW WT-24 (locations shown in Figure 8.10-2) were used for the one-dimensional property inversions (CRWMS M&O 2000f, Section 4.1.2.1, p. 17). Because these boreholes do not intersect large faults, the saturation data are representative of the formation rock of Yucca Mountain. Because borehole USW UZ-7a intersects the Ghost Dance fault, saturation data measured on rock core from this borehole were used for the two-dimensional inversions as representative of the faulted rock of Yucca Mountain. Saturation data measured on rock cores from boreholes USW NRG-6 and USW NRG-7a were not used because excessive drying of the cores occurred prior to analysis (Rousseau et al. 1999, p. 125). Further, saturation data measured on rock cores from the neutron boreholes (Section 8.3.2.2) were not used because these boreholes do not penetrate significant portions of the unsaturated zone and thus would be of limited usefulness. Similarly, saturation data measured on rock cores from the ESF/ECRB Cross Drift, alcoves, and niches were not used because they represent only one layer at any one column of unsaturated zone flow and transport model grid.

Water potential data measured in situ in boreholes USW NRG-6, USW NRG-7a, UE-25 UZ#4, and USW SD-12 (Section 8.5.1) were used in the one-dimensional inversions (CRWMS M&O 2000f, Section 4.1.2.2, p. 18). Because these boreholes do not intersect large faults, the water potential data were considered representative of the formation rock of Yucca Mountain. Some water potential data measured in situ in the ECRB also were used in the one-dimensional inversions. Because borehole USW UZ-7a intersects the Ghost Dance fault, water potential data from this borehole were used for the two-dimensional inversions to determine the properties of fault zones. Water potential data measured on rock cores were not used because drying during drilling and/or handling may have substantially changed the water potential.

Pneumatic pressure data measured in situ in boreholes UE-25 NRG#5, USW NRG-6, USW NRG-7a, USW SD-7, and USW SD-12 (Section 8.4.2) were used in the one-dimensional inversions to represent nonfaulted formation rock. In situ pneumatic pressure data from borehole USW UZ-7a were used in the two-dimensional inversions as representative of the faulted rock.

#### **8.10.5.2 Computer Software Used for the Calibrated Properties Model**

Computer software used for the calibrated-properties model is described in CRWMS M&O (2000f, Section 3 and Table 1). The primary software code used for the calibrated-properties model was ITOUGH2, version 3.2 (Finsterle 1999).

#### **8.10.5.3 One-Dimensional Mountain-Scale Calibration**

Saturation, water potential, and pneumatic pressure data from 11 boreholes at Yucca Mountain were used to calibrate the parameters for the 32 model layers regrouped from those listed in Table 8.10-1 (CRWMS M&O 2000f, Section 6.1). The focus of the one-dimensional inversions is the 11 columns of the numerical grid that correspond to the 11 boreholes (Figure 8.10-3) for which field data are available (CRWMS M&O 2000f, Section 6.1.1, p. 36, Table 9). Three calibrated parameter sets were produced, one for each present-day infiltration case: the base case, the lower bound, and the upper bound (Section 8.2.10.1). The calibrated parameter sets were produced using the present-day infiltration rates corresponding to the calibration boreholes.

The saturation, water potential, and gas pressure data were transformed so that they could be compared with simulated values within the framework of the numerical grid. Because the rock core saturation data were collected at much smaller intervals than those contained in the vertical grid of the numerical model, the field data were averaged. Because the in situ water potential and pneumatic pressure data were measured on depth intervals equal to or greater than the spacing of the vertical numerical grid, these data did not need to be averaged.

One-dimensional data inversion was carried out in a series of steps (CRWMS M&O 2000f, Section 6.1.3, p. 43). First, the parameters were calibrated by inversion of saturation and water potential data. Second, the calibrated parameters from the first step were used as initial guesses for further parameter calibration by inversion of the pneumatic data. Third, the calibrated parameter set from the second step was checked against the saturation and water potential data and further calibrated if needed. If further calibration was carried out in the third step, then the new parameter set was checked against the pneumatic data. In general, this iterative approach was continued until satisfactory matches to the saturation, water potential, and pneumatic pressure data were achieved.

In the saturation and water potential inversions, the Richards' equation module (EOS9) of the ITOUGH2 code was used to calibrate moisture flow (CRWMS M&O 2000f, Section 6.1.3.1, p. 44). For both upper-bound and lower-bound infiltrations, two inversion runs were performed. In the first run, reasonable matches were obtained between the simulated and observed matrix saturation and water potential profiles in the calibration boreholes. Then the output parameters from the first run were modified as the new initial guesses for the second run. The objective of the modification was to ensure the model was simulating matrix flow in the PTn and the vitric part of the CHn. Results of the one-dimensional inversions for saturation and water potential for borehole USW SD-12 are shown in Figures 8.10-6 and 8.10-7, respectively.

In the pneumatic inversions, the EOS3 module of the ITOUGH2 code was used for both gas-phase and liquid-phase flow calculations (CRWMS M&O 2000f, Section 6.1.3.2). The pneumatic inversions were carried out in two steps. First, the fracture permeabilities for layers tew11 through ptn26 in the TCw and PTn (Table 8.10-1) were calibrated; then the permeabilities for layers tsw31 through tsw37 in the TSw were calibrated. Trial inversions showed that the calibrated fracture permeabilities resulting from inversion of pneumatic data for the TCw and PTn were higher than the field data, probably because of scale effects. Inversions of pneumatic data for all three infiltration scenarios result in calibrated parameters that provide nearly identical matches to the data. Because the gas pressure data from the TSw are limited as a result of the almost insignificant amount of attenuation and lag between the uppermost and lowermost sensors, the fracture permeabilities for different model layers in this unit could not be independently estimated in a reliable manner. Therefore, the ratios of the permeabilities of layers tsw31 through tsw37 were held constant in the inversions and the field permeability values were multiplied by a single factor. The permeability values resulting from the inversions for the TSw were almost 100 times the field values, probably because of scale effects. Figure 8.10-8 shows simulated and measured pneumatic pressure at borehole USW SD-12 for the one-dimensional mountain-scale inversion for base-case present-day infiltration.

The layer-averaged, calibrated parameter set for base-case present-day infiltration resulting from the one-dimensional inversions for nonfaulted rock is presented in Table 8.10-2.

#### **8.10.5.4 One-Dimensional Drift-Scale Calibration**

As a result of the pneumatic inversion, the site-scale fracture permeabilities in most of the TSw model layers were almost 100 times greater than the field data from air-injection tests (CRWMS M&O 2000f, Section 6.2, p. 58). This is because the pneumatic pressure data result from the mountain-scale gas-flow processes, while air-injection tests correspond to scales on an order of several meters or less. It is well documented in the literature that large-scale effective permeabilities are generally larger than smaller-scale ones. An intuitive explanation for this scale-dependent behavior is that a large observation scale, in an average sense, corresponds to a larger opportunity to encounter more permeable zones or paths when observations are made, which considerably increases values of the observed permeability. Because of the scale difference, mountain-scale fracture permeabilities, determined from the pneumatic data inversion, cannot be applied to drift-scale modeling. Therefore, development of drift-scale properties was needed.

Although it is expected that estimated large-scale matrix permeabilities should be larger than those measured on a core scale, no evidence exists to indicate that the matrix properties should be very different between the site and drift scales, which are much larger than the scale characterized by the fracture spacing (CRWMS M&O 2000f, Section 6.2). Therefore, only fracture permeabilities for the drift-scale property sets were recalibrated while other properties remain the same as those in the corresponding site-scale properties. Because the drifts are located within the TSw units, the calibration was limited to model layers tsw32 through tsw37. Data used for the calibration were the same as those used for the site-scale property calibration, except that the pneumatic data are excluded. Unlike the mountain-scale property calibration, the permeabilities for each of the layers are estimated independently, except that a single value is estimated for layers tsw36 and tsw37.

The calibrated results are given in Table 8.10-3 for the base-case, upper-bound, and lower-bound infiltration rates. As expected, the calibrated fracture permeabilities are much lower than those corresponding to the site scale and are closer to the field values (CRWMS M&O 2000f, Section 6.2, p. 59). Except in two cases (upper-bound infiltration scenario permeabilities for layers tsw32 and tsw35), all the estimated permeabilities are within a factor of two of the field values. Note that the fracture permeabilities for the upper-bound infiltration rates are generally higher than those for the base-case and lower-bound infiltration rates. This is because relatively large fracture fluxes occur for upper-bound infiltration and permeabilities of some layers may need to be adjusted upward to accommodate the increased liquid flow. For the base-case and lower-bound infiltration scenarios, fracture permeabilities are more than enough to carry the small amount of liquid flow, so the inversions were not very sensitive to the estimated fracture permeabilities.

#### **8.10.5.5 Two-Dimensional Fault Calibration**

Saturation, water potential, and pneumatic pressure data from borehole USW UZ-7a, located in the Ghost Dance fault zone, were inverted to calibrate the properties of fault zones in three of the four fault layers in the unsaturated zone flow and transport model (CRWMS M&O 2000f, Section 6.3, p. 60). Because only core data and no in situ data are available for the lowest fault layer in the CHn/CFu, the fault parameters for this layer were not included in the calibration.

Because geologic layering data from USW UZ-7a were not included in the geologic model used to develop the numerical grid, there was no one-to-one correlation between the grid layer elevations and the geology of USW UZ-7a. Therefore, saturation, water potential, and pneumatic pressure data had to be interpolated onto the vertical grid for comparison with results of the inversion (CRWMS M&O 2000f, Section 6.3.2, p. 61). For the pneumatic inversion, monitoring data were taken from the lowest TCw instrument station and all instrument stations in the PTn and in the TSw within the fault zone. Data from three instrument stations in the footwall of the fault were not included in the inversion because they represent interactions at the edge of the fault on a subgrid block scale not captured by the unsaturated zone flow and transport model.

The data inversion for calibration of fault parameters was carried out in the same sequence of steps used for the one-dimensional mountain-scale inversion for nonfaulted properties (CRWMS M&O 2000f, Section 6.3.3, p. 62). As with the one-dimensional mountain-scale inversion, fracture permeabilities were fixed during the saturation and water potential inversion, and were then the only parameters calibrated to the pneumatic data. At several points during the trial-and-error process, automated inversion of the saturation and water potential data was attempted, but was not successful at significantly improving the match to the measured data. However, using the parameter set from the initial calibration step, automated inversion successfully improved the fracture permeabilities and provided an excellent match to the measured pneumatic data. Further, using the parameter set from the pneumatic calibration step, automated inversion of the saturation and water potential data resulted in a slight improvement to the match.

Because the nonfaulted parameters were assumed to have a significant effect on the behavior in the fault zone, the fault parameters calibrated for the base-case infiltration scenario were checked to determine whether they were satisfactory for the other two infiltration scenarios (CRWMS M&O 2000f, Section 6.3.4). Saturation and water potential matches were slightly affected, but not significantly enough to warrant separate fault parameter sets for each of the infiltration scenarios. The calibrated fault parameter set is presented in Table 8.10-4. Comparison of the parameter values for faulted rock in Table 8.10-4 with parameter values for nonfaulted rock in Table 8.10-2 indicates some significant differences in the properties of faulted and nonfaulted rocks. For example, although the matrix permeability of faulted TCw rocks falls in the lower range of matrix permeability for nonfaulted TCw rocks, the fracture permeability of faulted TCw rocks falls in the upper range of fracture permeability for nonfaulted TCw rocks. For the PTn, there seems to be little difference between faulted and nonfaulted matrix permeability, but the fracture permeability of faulted PTn rocks seems to fall in the upper range of fracture permeability of nonfaulted PTn rocks. For the TSw, the matrix permeability of faulted TSw rocks is significantly greater than the matrix permeability of nonfaulted TSw rocks. However, there seems to be little difference between faulted and nonfaulted fracture permeability of TSw rocks, although the fracture activity parameter for faulted TSw rocks is greater than the fracture activity parameter for nonfaulted TSw rocks.

#### **8.10.6 Calibration and Application of the Site-Scale Flow and Transport Model**

The site-scale unsaturated zone flow and transport model and its submodels are important tools for evaluation of hydrogeologic and geochemical processes in the unsaturated zone at Yucca Mountain (CRWMS M&O 2000d, Section 1). These models provide the necessary framework to test conceptual hypotheses of flow and transport at different scales and predict flow and

transport behavior under a variety of climatic conditions. The primary purpose of the unsaturated zone flow and transport model is to generate flow fields in the unsaturated zone for direct use by the TSPA model. These flow fields also are used by other performance assessment activities, including abstractions, particle-tracking transport simulations, and the unsaturated zone radionuclide transport model. By incorporating the hydrologic parameter sets from the calibrated properties model (Section 8.10.5) and other site data, the unsaturated zone flow and transport model has been used to generate flow fields for spatially varying mean, lower-bound, and upper-bound net infiltration for the current climate, a postulated future monsoon climate, and a postulated future glacial transition climate (Section 8.2.10). Each net infiltration case scenario was evaluated using two different perched-water models, resulting in a total of 18 flow fields. Additionally, three-dimensional flow fields were generated to evaluate the uncertainty and sensitivity of the unsaturated zone flow and transport model relative to fracture-matrix parameters and infiltration rates over the mountain by using three sets of model parameters and the nine infiltration scenarios (CRWMS M&O 2000d, Section 6).

The unsaturated zone flow and transport model encompasses several flow-process submodels, including geothermal, geochemistry, and liquid water flow and tracer/radionuclide transport (CRWMS M&O 2000d, Section 6, p. 29). The geothermal submodel was used to characterize ambient geothermal conditions with temperature data for use in the unsaturated zone flow and transport model. The geochemical submodel included two submodels of the specific constituents chloride and strontium. The chloride submodel was constructed to represent the conceptual model for the spatial and temporal variations in chloride chemistry, and its results were compared with pore-water concentrations measured in samples from boreholes and the ESF. The strontium submodel incorporated the effects of rate-limited dissolution and precipitation on the concentration of a solute, in addition to dispersion, radioactive decay, and linear equilibrium sorption.

The discussion of calibration and application of the site-scale unsaturated zone flow and transport model and its submodels encompasses the following topics:

- Data sources for the three-dimensional site-scale flow and transport model
- Computer software used for the site-scale flow and transport model
- Unsaturated zone flow and transport model boundary conditions
- Calibration of three-dimensional unsaturated zone flow model
- Simulation of temperature in the unsaturated zone
- Analysis and modeling of pore-water chemical data
- Simulation of calcite deposition
- Simulation of three-dimensional flow fields for TSPA
- Liquid water travel times and tracer/radionuclide transport
- Model validation.

#### **8.10.6.1 Data Sources for the Three-Dimensional Site-Scale Flow and Transport Model**

The sources of data for the site-scale flow and transport model are documented in CRWMS M&O (2000d, Table 4-1).

A wide variety of acquired and developed data were used to construct and calibrate the unsaturated zone flow and transport model and its submodels, including the following (CRWMS M&O 2000d, Section 4, p. 22):

- Matrix-property data from the ESF and boreholes
- Stratigraphy data from borehole logs
- Infiltration maps
- Calibrated fracture and matrix properties
- Hydrologic property data for the CHn unit
- Geochemistry data from the ESF and boreholes
- Unsaturated zone flow and transport model grids
- Temperature data for boreholes
- Pneumatic pressure data from boreholes
- Locations and elevations of perched water in boreholes
- Uncalibrated fracture and matrix properties
- Water potential data from boreholes and the ESF
- Matrix liquid-saturation data.

The key input data used in the unsaturated zone flow and transport model and its submodels include parameters from the analysis of hydrologic properties data (CRWMS M&O 2000g) and the calibrated properties model (CRWMS M&O 2000f) as follows (CRWMS M&O 2000d, Section 4.1):

- Fracture properties (frequency, permeability, van Genuchten parameters, aperture, porosity, interface area, and residual and saturated saturations) for each unsaturated zone flow and transport model layer
- Matrix properties (porosity, permeability, van Genuchten parameters, and residual and saturated saturations) for each unsaturated zone flow and transport model layer
- Thermal properties (grain density, wet and dry thermal conductivity, grain specific heat, and tortuosity coefficients) for each unsaturated zone flow and transport model layer
- Fault properties (matrix and fracture parameters) for each major hydrogeologic unit.

The calibrated parameter sets also included an estimate of the active-fracture parameter for each model layer that accounts for the reduction in interaction between matrix and fracture flow resulting from flow fingering and channelization (Section 8.10.3.6).

#### **8.10.6.2 Computer Software Used for the Site-Scale Flow and Transport Model**

The software items used for development and application of the site-scale flow and transport model and associated submodels are described and documented by software tracking number in CRWMS M&O (2000d, Section 3, Table 3-1). The principal computer codes used for the site-scale flow model were TOUGH2, T2R3D, TOUGHREACT9, and Infil2grid. TOUGH2 was used to generate flow fields and conduct flow model calibrations. T2R3D was used to simulate tracer/radionuclide transport, to estimate liquid water travel times, and to model pore-water chemistry. TOUGHREACT9 was used to model calcite geochemistry. Infil2grid was used to

interpolate infiltration maps onto the numerical grids used for simulating flow and chemical transport.

### **8.10.6.3 Unsaturated Zone Model Boundary Conditions**

The ground surface of the mountain, or the tuff-alluvium contact in areas of significant alluvial cover, was taken as the upper model boundary, and the water table was treated as the lower model boundary (CRWMS M&O 2000d, Section 6.1.3). Both the upper and lower boundaries of the model were treated as Dirichlet-type conditions with specified constant but spatially distributed temperature, gas pressure, and liquid saturation values along these surfaces. For liquid-flow simulations, only pressure or saturation values were needed along the upper and lower model boundaries. Surface infiltration was applied using a source term in the grid blocks within the second grid layer from the top. This method was adopted because the first layer was treated as a Dirichlet-type boundary with constant pressure, saturation, and temperature to represent average atmospheric conditions.

All lateral boundaries (Figure 8.10-2) were treated as no-flow (closed) boundaries (CRWMS M&O 2000d, Section 6.1.3, p. 38). This treatment was considered reasonable for the eastern boundary, which is along the Bow Ridge fault, "Toe" fault, and Exile Hill fault, because faults tend to have high or vertical permeability and lower capillary forces (Section 8.10.5.5). For the southern, western, and northern lateral boundaries, no-flow boundaries were expected to have little effect on moisture flow within and near the potential repository areas because these boundaries are far away from the repository and liquid water flow is mostly vertically downward.

The spatially distributed values of temperatures along the upper and lower boundaries were calculated based on field observations (CRWMS M&O 2000d, Section 6.1.3, p. 38). Pressure conditions at the lower boundary of the model were calculated using observed gas pressure values. The water table, which is the bottom boundary of the unsaturated zone flow and transport model, was observed and assumed to be a flat, stable surface. East of the Solitario Canyon fault, water table elevations are about 730 m (2,400 ft) above sea level. However, the water table elevation increases by 46 m (150 ft) west of the Solitario Canyon fault. The gas pressures at the water table were estimated using a pressure value of 92 kPa (0.92 bars) at an elevation of 730 m (2,400 ft). Surface gas pressures were determined by running the TOUGH2 code to steady state under given temperature, lower-boundary pressure, and surface infiltration conditions. This was necessary to generate a steady-state, equilibrated gas-pressure boundary to avoid artificial air flow or circulation, which may occur if nonequilibrated pressures are imposed on the ground surface boundary.

Net infiltration of water resulting from precipitation penetrating the surface of Yucca Mountain is the most important factor affecting the overall hydrological and thermohydrologic behavior of the unsaturated zone (CRWMS M&O 2000d, Section 6.1.3, p. 38). Net water infiltration is the ultimate source of percolation through the unsaturated zone and saturated-zone recharge, which may cause advective transport of radionuclides from the potential repository to the water table. A total of nine net infiltration scenarios were simulated with the unsaturated zone flow and transport model and its submodels, including lower-bound, mean, and upper-bound rates for present-day, monsoon, and glacial transition climatic scenarios. These distributions of net

infiltration were derived from the results of net infiltration modeling (USGS 2000b, Section 6.7) described in Section 8.2.10. Although percolation fluxes were estimated using other methods (Section 8.7), these analyses were conducted in order to test the validity of the net infiltration model. Because none of the results of these analyses suggested that the infiltration model was invalid and a continuous spatial distribution of infiltration flux was required over the domain of the site-scale unsaturated zone flow model (rather than point estimates), the results of the net infiltration model were adopted for use. Average values of net infiltration over the domain of the unsaturated zone flow and transport model for all nine infiltration scenarios are indicated in Table 8.10-5 as they were interpolated onto the unsaturated zone flow and transport model flow-field grid (Figure 8.10-4). The mean infiltration rate for each climate scenario is considered the base case, whereas the lower-bound and upper-bound infiltration values are intended to represent the uncertainties associated with estimating both present-day and future precipitation and net infiltration (Section 8.2.10). The average infiltration rates in Table 8.10-5 are very similar but not identified to the infiltration rates indicated in Tables 8.2-11, 8.2-14, and 8.2-17 because of slight differences in the spatial resolution of the grids used to construct the infiltration model and the unsaturated zone flow and transport model.

A plan view of the spatial distribution of present-day mean infiltration, as interpolated onto the unsaturated zone flow and transport model flow-field grid (CRWMS M&O 2000d, Section 6.1.3), is shown in Figure 8.10-9. In this figure, infiltration rates equal to and greater than 20 mm/yr. are encompassed by the darkest color band. However, in the northwestern corner of the unsaturated zone flow and transport model area, infiltration rates actually exceed 100 mm/yr. in relatively small, isolated areas (Section 8.2.10.1) (Figure 8.2-32). Similarly, along the western edge of the potential repository area, infiltration rates actually exceed 50 mm/yr. in small, isolated areas just east of the Solitario Canyon fault. Analogous distributions of mean net infiltration for the monsoon and glacial transition climate scenarios also were developed for the unsaturated zone flow and transport model flow-field grid (CRWMS M&O 2000d, Figures 6-4 and 6-5). Although the magnitudes of flux differ, the three climate scenarios show similar distributions of infiltration flux, with the highest rates in the northern part of the model domain and along the crest of the mountain ridge east of the Solitario Canyon fault.

#### **8.10.6.4 Three-Dimensional Unsaturated Zone Flow Model Calibration**

A critical step in developing the three-dimensional unsaturated zone flow model was the use of field-measured liquid saturation, water potential, and perched-water data for calibration (CRWMS M&O 2000d, Section 6.2). This additional calibration step was important because it increased confidence in model predictions for site conditions. Although the one-dimensional inversions performed with the calibrated properties model (Section 8.10.5) produced a valid and appropriately scaled set of parameters on which to base the three-dimensional unsaturated zone flow and transport model, the one-dimensional models, in general, did not predict perched water in several hydrogeologic units below the level of the potential repository. Therefore, the three-dimensional calibration effort focused on reproducing perched water observed in the field by using core-scale matrix liquid saturation data, in situ matrix water potential data, and perched-water elevations from surface-based boreholes and the ECRB Cross Drift. Two perched-water models were investigated in which rock properties were modified locally in several grid layers of the lower basal vitrophyre of the TSw unit and upper zeolites in the CHn unit. The objectives of investigating these two different models were the following:

- Accurately simulate the various perched water occurrences observed at the site
- Investigate the differences in groundwater flow paths, fluxes, travel times, and radionuclide transport resulting from varying the simulated percentage of water flowing through or bypassing perched water bodies because of permeability barriers in the lower TSw and upper CHn units.

#### 8.10.6.4.1 Simulation of Perched Water

A numerical representation of a permeability-barrier conceptual model, called the flow-through model for perched water, was developed for the perched water bodies in the vicinity of the ESF North Ramp. In this area (near boreholes USW UZ-14, USW SD-9, USW NRG-7a, USW G-2, and USW WT-24), perched water occurs above the base of the TSw and is underlain by a zone of low-permeability, zeolitized rock (CRWMS M&O 2000d, Section 6.2.2). Although these perched water bodies in the northern area of the potential repository may be interconnected, the perched-water zones farther south at boreholes USW SD-7 and USW SD-12 are considered to be local, isolated bodies. In this conceptual model, both vertical and lateral water movement in the vicinity of the perched zones is controlled mainly by the fracture permeability and matrix permeability distributions. The major aspects of the permeability-barrier conceptual model are the following:

- No large-scale vertically connected fractures transect the underlying low-permeability units.
- Both vertical and horizontal permeabilities within and below the perched-water zone are small compared with permeabilities outside perched-water zones.
- Sufficient percolation flux (more than 1 mm/yr.) exists.

Previous modeling studies (Wu et al. 1999a) concluded that this conceptual model of perched water is able to match the observed data for perched water in the unsaturated zone of Yucca Mountain.

Another perched-water conceptual model, called the bypassing model, considers the zeolitic rocks of the CHn to be unfractured (CRWMS M&O 2000d, Section 6.2.2, p. 45). Similar to the permeability-barrier model, in the numerical representation of this model it is presumed that the occurrence of perched water at Yucca Mountain results mainly from the lack of globally connected fractures within zeolitic rocks of the CHn. This model is a special case of the permeability-barrier model in which only the low-permeability zeolitic matrix controls water perching because, presumably, fractures are not present in the perching layers. The concept of unfractured zeolitic rocks in the CHn is partially supported by the analysis of fracture data in CRWMS M&O (2000g, Section 6.1.2.3, Table 6), which suggests a very small fracture frequency within the zeolitic units.

In current numerical modeling studies, perched water bodies are formed as a result of permeability-barrier effects in accordance with either of the two conceptual models: permeability-barrier and unfractured zeolites (CRWMS M&O 2000d, Section 6.2.2). Current modeling studies also consider a nonperching conceptual model that represents an extreme case

in which maximum flow through the zeolites occurs. This nonperching model was used for sensitivity analyses and for comparison with the two perched-water models.

To calibrate the three-dimensional unsaturated zone flow model against observed perched-water conditions at Yucca Mountain, some local modification of rock properties was necessary (CRWMS M&O 2000d, Section 6.2.3, p. 46). In general, permeability was adjusted only within the model layers associated with the perched-water occurrences. In several locations at Yucca Mountain, perched water caused by a permeability barrier involves the highly fractured basal vitrophyre of the TSw unit overlying bedded units of low permeability.

For the flow-through conceptual model, calibrated parameters of fracture and matrix permeabilities within perched zones resulted from a series of three-dimensional modeling simulations (CRWMS M&O 2000d, Section 6.2.3, p. 47). Matrix permeabilities of potential perched layers/zones are based on average values of the measured matrix permeabilities, while fracture permeabilities used for the northern perched zones are 10 times higher than matrix permeabilities under the mean and upper-bound infiltration scenarios. In the lower-bound infiltration case, the same permeability values were used for both fractures and matrix for perched zones near boreholes USW SD-7 and USW SD-12. Van Genuchten parameters and residual saturations for matrix blocks within perched zones were identical to parameters estimated from the one-dimensional inversions (Section 8.10.5.3). The active-fracture parameter was set to zero for all the perched zones because they are saturated. For the bypassing perched-water conceptual model, rock properties of all the fractures within the potential perched layers/zones were replaced by the corresponding matrix properties from the one-dimensional inversions (Section 8.10.5.3). In addition, properties of the grid blocks adjacent to borehole USW SD-12 and the borehole column itself were adjusted.

A series of seven three-dimensional calibration simulations was performed in order to test the effects of the perched-water conceptual models on liquid water flow in the unsaturated zone below the potential repository horizon (CRWMS M&O 2000d, Section 6.2.5, p. 49). One simulation was of the nonperching model with present-day mean infiltration. The other six simulations were of the flow-through and bypassing perched-water conceptual models, each coupled with lower-bound, mean, and upper-bound present-day infiltration. The adjusted, layer-averaged parameter sets resulting from all seven simulations are documented in CRWMS M&O (2000d, Attachment II). Six out of the seven simulations, all except the nonperching one, were calibrated primarily against the field-observed data for perched water. The objectives of these model calibration efforts were to estimate rock parameters in perched zones and to develop a more realistic model representation of the three-dimensional moisture-flow system in the unsaturated zone.

The results of the three-dimensional calibration simulations were compared with measured data of matrix liquid saturation, water potential, and perched-water elevations from seven boreholes where perched water had been observed (USW NRG-7a, USW SD-7, USW SD-9, USW SD-12, USW UZ-14, USW WT-24, and USW G-2) and two boreholes where perched water had not been observed (USW SD-6 and UE-25 UZ#16) (CRWMS M&O 2000d, Section 6.2.5, p. 52). The locations of all nine of these boreholes are shown in Figure 8.10-2. Comparisons of simulated and observed matrix liquid saturations and perched-water elevations for boreholes USW UZ-14 and USW SD-12 are shown in Figures 8.10-10 and 8.10-11, respectively, for the

two perched-water conceptual models under present-day mean infiltration. Comparison of simulated and observed in situ water potential and perched-water elevation for borehole USW SD-12 is shown in Figure 8.10-12 for the two perched-water conceptual models under present-day mean infiltration. In general, simulated saturations and water potentials were in reasonable agreement with the measured data. These three figures also indicate fairly good agreement between simulated and observed perched-water elevations at the two boreholes. However, for borehole USW UZ-14 (Figure 8.10-10) under the bypassing model, the simulated perched-water elevation is a little lower than what was observed. In addition, each of the six simulations was compared to perched-water data for the other boreholes, with the following results:

- Under the present-day mean infiltration scenario, both perched-water simulations generally matched perched-water conditions within the unsaturated zone flow and transport model domain.
- Under the present-day upper-bound infiltration scenario, both perched-water simulations generally reproduced all perched-water conditions within the unsaturated zone flow and transport model domain.
- Under the present-day lower-bound infiltration scenario, the perched-water simulations reproduced perched-water conditions only at boreholes USW G-2, USW NRG-7a, USW SD-12, and USW WT-24. The simulations could not adequately reproduce perched-water conditions at boreholes USW SD-7, USW SD-9, and USW UZ-14 because of low percolation fluxes (0.01, 0.01, and 0.005 mm/yr., respectively).

Perspective views of simulated three-dimensional perched water bodies within the unsaturated zone flow and transport model domain for the two conceptual models under present-day mean infiltration are shown in Figures 8.10-13 and 8.10-14. Figure 8.10-13 depicts simulated water saturation in fractures along the base of the TSw (lowest basal vitrophyre model layer) for the flow-through perched-water model (CRWMS M&O 2000d, Section 6.2.5, p. 54). In the dark blue areas on the figure, fractures have liquid saturations of 100 percent (perched-water zones), whereas in the green areas, fractures have liquid saturations of less than 100 percent. Figure 8.10-13 clearly shows several extensive perched water bodies predicted in the northern part of the model domain, near the basal vitrophyre of the TSw and separated by faults. These simulated perched water bodies correspond well with those observed in boreholes USW G-2, USW WT-24, USW UZ-14, USW NRG-7a, USW SD-9, and USW SD-12.

Figure 8.10-14 shows perched water bodies along the upper zeolitic layer of the CHn simulated using the bypassing conceptual model (CRWMS M&O 2000d, Section 6.2.5, p. 54). The areal extent of the perched-water zones on Figure 8.10-14 is quite similar to that shown on Figure 8.10-13 (flow-through model), but slightly larger overall.

#### **8.10.6.4.2 Simulation of Flow at and below the Potential Repository Horizon for the Flow-Through and Bypassing Perched-Water Conceptual Models**

Percolation flux through the unsaturated zone is one of the most critical factors affecting repository performance calculations (CRWMS M&O 2000d, Section 6.2.5, p. 55). The quantity and spatial and temporal variations in percolation flux directly affect the following:

- The amount of water that may flow into drifts of the potential repository
- Moisture conditions and the corrosion environment of canisters within the drifts
- Waste mobilization from the potential repository
- Radionuclide migration through the unsaturated zone to the water table underneath the potential repository.

However, because percolation fluxes through the unsaturated zone cannot be readily measured in the field, they must be estimated using indirect data and numerical models. Model studies (Wu et al. 1999a, 1999b) indicate that accuracy of model predictions of percolation fluxes at Yucca Mountain depends on many factors. The most important factors are the following:

- Net infiltration rates over the surface boundary
- Representative geological and conceptual models
- Reliable distributed rock-property values of fractures and matrix blocks
- Treatment of fracture-matrix flow and interactions.

The seven simulations of perched-water conceptual models (Section 8.10.6.4.1) were used to analyze percolation fluxes at the potential repository horizon and flow beneath the potential repository (CRWMS M&O 2000d, Section 6.2.5). (Percolation flux, which is defined as total vertical liquid mass flux through both fractures and matrix, was converted to millimeters per year per unit area using a constant water density.) Percolation fluxes at the repository horizon were calculated for both the flow-through and bypassing perched-water conceptual models under all three present-day infiltration scenarios: lower bound, mean, and upper bound (CRWMS M&O 2000d, Figures 6-11 through 6-13). In each case, the distribution of percolation flux at the repository horizon was nearly the same as the distribution of net infiltration used as the upper-boundary condition, regardless of which perched-water conceptual model was simulated. The reasons for the similar distribution are as follows: (1) lateral diversion of flow between the land surface and the repository horizon, which occurs in the middle of the model domain where higher fluxes seem to be moving down the faults, is minimal, and (2) the perched-water conceptual models differ only in the rock properties used in the bottom layers of the TSw and zeolitic units of the CHn, which have little effect on flow at and above the repository horizon. Thus, the distribution of percolation flux at the repository horizon for both the flow-through and bypassing conceptual models under present-day mean infiltration is very similar to the distribution of present-day surface infiltration shown in Figure 8.10-9. Percolation flux at the repository horizon exhibits the same non-uniform pattern as surface infiltration, with the highest percolation fluxes located primarily north of the potential repository area and along the Solitario Canyon fault in the middle portion of the model domain.

The seven simulations of perched-water conceptual models also were analyzed to determine the fracture and matrix components of percolation flux at the repository horizon and at the water table beneath the potential repository (CRWMS M&O 2000d, Section 6.2.5, Table 6-11). The simulation results indicate that fracture flow is dominant both at the repository horizon and at the water table. At the repository horizon, fracture flow is more than 80 percent of the total percolation flux, with virtually no difference between the two conceptual models. Fracture flow

at the water table ranges from 70 to 90 percent of the total flow, with the bypassing model consistently predicting lower fracture-flow components at the water table for all three infiltration scenarios than those predicted by the flow-through model. For the present-day mean infiltration scenario, the flow-through model predicts that about 87 percent of the flow at the water table is fracture flow, whereas the bypassing model predicts about 73 percent fracture flow.

The percentage of water flowing through or bypassing perched water bodies below the potential repository may have an effect on the flow paths and travel times of liquid water (CRWMS M&O 2000d, Section 6.2.5, p. 60). This may in turn affect the amount of radionuclides potentially released from the repository that would be adsorbed onto zeolitic and vitric rocks, directly affecting the repository performance. The percentage of flow through and bypassing flow was analyzed using the seven perched-water calibration simulations. Simulation results were analyzed at the locations of two boreholes in the vicinity of the potential repository: USW SD-6 in the southern part and USW UZ-14 in the northern part of the repository area (Figure 8.10-2). The results indicate that at borehole USW SD-6 under present-day mean net infiltration, the flow-through model predicts a much higher percentage (nearly 100 percent) of flow through the CHn unit than does the bypassing model (Figure 8.10-15a). At borehole USW UZ-14 (Figure 8.10-15b), the flow through model also predicts a higher percentage (about 50 percent) of flow through the perched-water layers than does the bypassing model (about 10 percent flow through). Obviously, the nonperching model predicts the highest, most complete flow through. Overall, the results of these simulations indicate the following:

- Perched-water zones may only partially block vertical water flow; a certain percentage of the vertical water flux flows downward through the perching layers regardless of which conceptual model or infiltration scenario is simulated.
- The higher the infiltration rate, the higher the percentage of bypassing flow.
- The flow-through conceptual model results in consistently higher percentages of flow-through than the bypassing model.
- The nonperching model predicts nearly complete flow through the zeolites in the CHn.

#### **8.10.6.5 Simulation of Temperature in the Unsaturated Zone**

For thermohydrologic studies, distributions of saturation and steady-state ambient temperature were needed as initial conditions for unsaturated zone flow and transport model simulations of thermal load and infiltration scenarios at Yucca Mountain (CRWMS M&O 2000d, Section 6.3, p. 63). Field temperature data were required to specify upper- and lower-boundary conditions so that a steady-state ambient temperature distribution for the unsaturated zone could be calculated using the TOUGH2 numerical code. To account for differences in temperature at the surface of the mountain caused by variations in elevation, a standard equation was used to extrapolate mean measured surface temperatures at specific locations to the entire surface of the mountain (CRWMS M&O 2000d, Section 6.3.1, p. 63). Surface temperatures measured at boreholes USW NRG-6 and USW NRG-7a, with several years of continuous temperature data (Section 8.5.3), were used as reference temperatures for these calculations. The reference temperature used in this model was 18.23° C at an elevation of 1,231.0 m (4,038.7 ft) above mean sea level,

measured at borehole USW NRG-6. The measured mean temperature at USW NRG-7a at an elevation 1,282.2 m (4,026.7 ft) was 17.78° C. The calculated mean lapse rate, based on these field measurements, is 0.009° C/m, which was in close agreement with published data.

For the lower boundary at the water table, temperatures were interpolated from borehole temperature profiles reported in Sass et al. (1988). Because several of these boreholes do not actually extend to the water table, temperatures at the water table were obtained by linear extrapolation of the measured profiles, resulting in a temperature distribution that was interpolated over the entire model domain. This interpolated temperature distribution was calibrated against temperature data recently acquired from boreholes USW NRG-6, USW NRG-7a, USW SD-12, UE-25 UZ#4, UE-25 UZ#5, and USW UZ-7a. To obtain accurate lower-boundary temperature conditions for use in thermohydrologic simulations, the initial distribution of boundary temperature was adjusted so that the computed steady-state temperature profiles matched measured temperature profiles in the six boreholes with temperature data. Several measured temperature profiles (Sass et al. 1988) were used as corroborative data.

The temperature profiles in these boreholes are controlled by the thermal conductivity of the rock mass, the geothermal gradient, and ambient infiltration, all of which need to be calibrated together to determine the ambient temperature distribution (CRWMS M&O 2000d, Section 6.3.3, p. 64). The ambient temperature condition was calibrated using the effective-continuum formulation of the three-dimensional unsaturated zone flow and transport model and the calibration grid (Figure 8.10-3). The simulations were performed using the EOS3 module of the TOUGH2 code with matrix and fracture hydrologic properties from the one-dimensional mountain-scale inversions (Section 8.10.5.3) and appropriate thermal properties, for the base-case present-day mean infiltration scenario. The resulting simulated temperature profiles for the six boreholes match the measured temperature data reasonably well (Figure 8.10-16), except near the ground surface where significant seasonal variations in temperature are apparent. However, these seasonal changes in surface temperature have little impact on steady-state heat flow deeper (more than 20 m deep [66 ft]) in the unsaturated zone. The calibrated temperature distribution (CRWMS M&O 2000d, Figure 6-17) indicates that mean temperatures at the water table (elevation 730 m [2,400 ft]) range from 28° to 32°C over the model domain.

Although the mountain-scale ambient temperature distribution for the unsaturated zone was simulated with a steady-state effective-continuum formulation of the unsaturated zone flow and transport model, it should be applicable under different steady-state model formulations, such as steady-temperature distribution with the dual-permeability approach (CRWMS M&O 2000d, Section 6.3.4, p. 67). This is because ambient heat flow is controlled by mountain-scale steady-state heat-conduction and fluid-flow processes, which can be simulated equally well using either an effective-continuum or dual-permeability approach (Section 8.10.3).

#### **8.10.6.6 Analysis and Modeling of Pore-Water Chloride Data**

Geochemical data from the unsaturated zone at Yucca Mountain have been analyzed and modeled in order to evaluate the hydrologic system and assess the spatial and temporal distribution of surface net infiltration (CRWMS M&O 2000d, Section 6.4.1, p. 67). Percolation flux through the unsaturated zone strongly depends on the spatial distribution of infiltration rates, and much work has been done to calculate the infiltration flux based on various water-balance

and evapotranspiration models (Section 8.2). Geochemical data provide additional information to analyze the unsaturated zone system. Pore-water chemical concentration data have been used to calibrate the unsaturated zone flow and transport model and to bound the infiltration flux, flow pathways, and transport time. Distribution of chemical constituents in both liquid and solid phases of the unsaturated zone depends on many factors, such as hydrologic and geochemical processes of surface precipitation, evapotranspiration, the fracture-matrix interactions of flow and transport, large-scale mixing during lateral transport, and history of climate changes and recharge. A dual-permeability transient model was necessary to investigate fluid flow and chemical transport phenomena and to represent the large spatial and temporal chemical variations at Yucca Mountain. Chemical concentration data were analyzed and modeled using three-dimensional chemical transport codes and analytical methods, and water infiltration rates were calibrated using pore-water chloride concentrations. Model results for chloride distributions more closely matched the observed data when the chloride-based infiltration rates were used.

Geochemical data include chloride concentrations in pore-water from eight boreholes (USW NRG-6, USW NRG-7a, USW SD-7, USW SD-9, USW SD-12, UE-25 UZ-14, UE-25 UZ#4, and UE-25 UZ#16) and the ESF tunnel, including the South Ramp, North Ramp, and Main Drift, and the ECRB Cross Drift (CRWMS M&O 2000d, Section 6.4.2.1, p. 68). The initial infiltration flux used in the geochemical model was the distribution of present-day mean infiltration derived from the numerical water-balance model (Section 8.2.10.1) and shown in Figure 8.10-9. To reflect possible future climate changes, a glacial infiltration scenario was devised for geochemical modeling by multiplying the present-day mean infiltration rate by a factor of five to ensure the same distribution pattern. The glacial infiltration scenario that multiplied the infiltration rate by a factor of five was a scenario with the purpose of matching the glacial maxima 18 ka. The glacial transition model is in Section 8.2.10.3. Surface chloride flux included dissolved material in rain, particulate in snow, and a contribution from windblown dusts. Either chloride concentration in infiltrating water or total surface chloride flux could be used as input for the geochemical model. Surface chloride flux was obtained by applying a mean chloride concentration of 0.62 mg/L to precipitated water, which is a combination of infiltrating water in the form of precipitation, run-on, and runoff. The same mean chloride concentration was applied to glacial total water precipitation to derive a chloride flux for the glacial infiltration scenario.

In the geochemical modeling, the unsaturated zone was assumed to be a two-phase system (water and air) under isothermal conditions (CRWMS M&O 2000d, Section 6.4.3.1, p. 68). Major chemical-transport processes taken into account were molecular diffusion, mechanic dispersion, and first-order radioactive decay. A three-dimensional dual-permeability model was developed using the T2R3D code. The steady-state liquid-flow fields were obtained using the EOS9 module of T2R3D. Chemical distributions were then computed from transport equations using the decoupled T2R3D module. The flow boundary conditions, simulation grids, basic hydrologic properties of rock matrix and fractures were the same as those used in the three dimensional unsaturated zone flow and transport model for the nonperched conceptual model simulations (Section 8.10.6.4.1). Boundary conditions for chemical components were treated similarly to those for flow simulations, with mass fluxes simulated at the upper boundary and no-flow and water table conditions simulated at the lateral and lower boundaries, respectively. The dispersivities for both fracture and matrix continua in the simulation were

assumed to be zero. Diffusion coefficients used were those for chemical ions at 25° C and infinite dilution in water. The tortuosity was set to 0.7 for the fracture medium and 0.2 for the matrix medium, respectively. Transient transport modeling was analyzed using an analytical solution for a one-dimensional semi-infinite chemical-transport system (CRWMS M&O 2000d, Section 6.4.3.2, p. 69).

A base-case simulation was conducted using the present-day (modern) mean infiltration rate from the water-balance model (Figure 8.10-9) to compare the uncalibrated geochemical model with observed chloride data (CRWMS M&O 2000d, Section 6.4.4.1, p. 69). Chloride concentrations predicted by the steady-state transport simulation were compared with measured pore-water chloride concentration data from the ESF, the ECRB Cross Drift, and borehole UE-25 UZ#16. Figure 8.10-17 indicates that simulated chloride concentrations were higher than measured concentrations in the North Ramp (Stations 00+00 to 20+00) and the South Ramp (Stations 64+00 to 80+00). Similar differences between simulated and measured chloride concentrations were observed for the ECRB Cross Drift and borehole UE-25 UZ#16. These differences seem to be proportional to spatially variable infiltration rates, in that high simulated chloride concentrations correspond to very low infiltration rates and high infiltration rates correspond to lower simulated chloride concentrations. Consequently, infiltration rates were calibrated based on the observed chloride concentrations and a modified spatial distribution of net infiltration was developed (Figure 8.10-18). The domain of the chloride-based infiltration distribution was divided into nine regions based on the range of measured chloride concentrations. A comparison between water-balance-model infiltration rates and the chloride-based infiltration rates in different regions of the model domain is given in Table 8.10-6. Simulation results using the chloride-based infiltration distribution for the ESF are shown in Figure 8.10-19. It is apparent from these results that the chloride-based infiltration analysis has effectively smoothed out the very low and very high values of infiltration from the water-balance model that would have resulted in chloride concentrations much higher or lower than observed. However, the data in Table 8.10-6 indicate that within each of the regions and for the entire domain of the unsaturated zone flow and transport model, average infiltration rates and volumes for the water-balance model and the chloride-based model are very similar.

#### **8.10.6.7 Simulation of Calcite Deposition**

Past percolation flux through the unsaturated zone has been estimated based on the characteristics and composition of hydrogenic calcite deposits in fractures and lithophysal cavities in the rocks at Yucca Mountain (Section 8.11.2). These deposits may provide important information for understanding the current and possible future percolation through the unsaturated zone, given that direct measurements of percolation fluxes over thousands of years are not possible (CRWMS M&O 2000d, Section 6.5.1, p. 80). Thus, several factors that influence calcite deposition in the rocks were investigated using reaction-transport modeling. Calcite deposition in the unsaturated fractured rock system occurs through a complex interplay of fluid flow, chemical transport, and reaction processes. The reaction-transport simulations considered the following important processes:

- Fracture-matrix interaction (dual-permeability) for water flow and chemical constituents
- Gaseous CO<sub>2</sub> diffusive transport and partitioning in liquid and gas phases

- Ambient geothermal gradient for geochemical calculations
- Kinetic interactions between fluids and rock chemicals.

A large number of simulations were performed using a range of infiltration rates, water and gas chemistry (at the upper boundary), reaction rates, and initial mineralogical conditions.

#### 8.10.6.7.1 Description of the Geochemical Model

The numerical analysis of calcite deposition in the unsaturated zone at Yucca Mountain was performed using the reactive-transport computer codes TOUGHREACTE9 and TOUGHREACT (CRWMS M&O 2000d, Table 3.1), which were developed by introducing reactive chemistry into the framework of the existing multiphase fluid-flow code TOUGH2 (CRWMS M&O 2000d, Section 6.5.2, p. 81). TOUGHREACTE9 uses a sequential iteration approach that solves the transport and reaction equations separately, as described by Xu and Pruess (1998). Water flow was solved using the EOS9 flow module of TOUGH2, which considers only saturated-unsaturated liquid-phase water flow (Richards' equation). For the purpose of solving water flow, the gas phase was held at a constant (atmospheric) pressure. Under ambient steady-state conditions, the effects of heat and gas-phase flow on water flow were assumed to be insignificant. To test this assumption, two flow simulations were performed using a one-dimensional column model representative of borehole USW WT-24, which was used later for analysis of the calcite deposition. One simulation considered only moisture flow at a constant temperature of 25° C for the entire column, whereas the second simulation considered both liquid water flow, gas-phase flow, and heat transfer with an upper-boundary temperature of 15.6° C and a lower-boundary temperature of 30° C (Section 8.10.6.5). Because a similar water saturation distribution was obtained from both simulations, subsequent hydrochemical-transport simulations were based on the single-phase water flow module EOS9.

Advective and diffusive transport of aqueous chemical species were considered in the liquid phase and molecular diffusive transport of gaseous species (CO<sub>2</sub>) was considered in the gas phase (CRWMS M&O 2000d, Section 6.5.2, p. 81). Although atmospheric-pumping effects on CO<sub>2</sub> transport change daily, they were not considered a significant influence on CO<sub>2</sub> transport and calcite deposition in the deep units such as the TSw. Aqueous chemical complexation and gas dissolution/exsolution were considered under the local-equilibrium assumption and mineral dissolution/precipitation was considered according to kinetic conditions. Temperature effects were considered for calculations of geochemical reactions because equilibrium and kinetic data are functions of temperature, even though the effects were not considered for calculations of water flow. Two one-dimensional columns (representing boreholes USW NRG-7a and USW WT-24) were used for the analysis of the calcite deposition in the unsaturated zone at Yucca Mountain (CRWMS M&O 2000d, Section 6.5.3, p. 81). The modeling mesh (Figure 8.10-3), hydrogeologic parameters, and flow conditions were all adopted from the one-dimensional column inversions conducted for the calibrated properties model (Section 8.10.5.3). Borehole USW NRG-7a was selected initially for analysis of calcite deposition under ambient conditions; however, because no calcite deposition data were available from USW NRG-7a, the USW NRG-7a model was used for sensitivity analysis. Borehole USW WT-24 was chosen for analysis of calcite deposition because calcite deposition data had been collected and interpreted.

A dual-permeability model was employed for water flow and chemical transport, and the active-fracture model (Section 8.10.3.6) was used to describe gravity-dominated and preferential liquid flow in fractures (CRWMS M&O 2000d, Section 6.5.3). One-dimensional vertical water flow was assumed, but local fracture-matrix interaction was considered. Each simulation used a constant infiltration rate over the entire simulation time. The established steady-state water-flow condition was used for chemical transport and fluid-rock interactions. Because a constant infiltration and steady-state water flow were considered, percolation through the entire column was equal to the infiltration rate applied at the surface. The temperature distribution and ambient geothermal gradient obtained from the TOUGHREACT simulation (using the EOS3 flow module) were used for geochemical calculations.

In the geochemical column models, two sets of initial mineralogical conditions were evaluated (CRWMS M&O 2000d, Section 6.5.3). The first set, called simple mineralogy, included only calcite, quartz, cristobalite- $\alpha$  (similar to opal, thermodynamically), and amorphous silica, which are the most relevant to the calcite deposition. The second set, called complex mineralogy, included microcline, albite, anorthite, calcium-smectite, sodium-smectite, magnesium-smectite, potassium-smectite, illite, tridymite, cristobalite- $\alpha$ , amorphous silica, quartz, glass, hematite, calcite, stellerite, heulandite, mordenite, clinoptilolite, kaolinite, sepiolite, and fluorite. Each model layer was assumed to have two mineralogical compositions, one for the fracture block and the other for the rock matrix block. The CHn unit was not considered in the geochemical simulations for the following reasons:

- Lateral flow may occur in the CHn (Section 8.10.6.4.1).
- The CHn has complicated mineralogy that is not yet well known.
- The primary interest is calcite deposition in the TSw, where the potential repository may be located.
- The exclusion of the CHn unit does not affect the results on upper units because flow is predominantly gravity-driven and backward diffusion can be neglected.

Four water types with different chemical compositions were used for the upper boundary of the hydrochemical-transport simulations (CRWMS M&O 2000d, Section 6.5.3, Table 6-14):

- Average Topopah Spring Tuff water calculated from several samples
- Water sampled from the PTn in borehole USW UZ-14 at a depth of 13.8 m (45.3 ft)
- Water sampled from the PTn in borehole USW NRG-7a at a depth of 50.6 m (166 ft) with higher CO<sub>2</sub> partial pressure and lower pH
- Water sampled from the TSw with a higher calcium concentration.

The water applied at the upper boundary was the water after transformation by soil-zone processes, which does not affect the hydrochemical evolution and calcite deposition in the deeper model layers. For the purpose of determining model sensitivity, a range of water types from different locations and depths was used. Although the TSw waters were sampled from greater

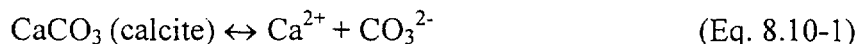
depths, it was considered that these waters may preserve the chemical composition of upper-boundary waters over a longer period of time. The average TSw water was used as the initial chemical compositions in the geochemical models and was used uniformly throughout the column for both the fracture and matrix blocks. In addition to aqueous-species transport and reactions in water, diffusive transport of CO<sub>2</sub> in the gas phase and CO<sub>2</sub> equilibration with pore water were considered. The CO<sub>2</sub> gas partial pressure used for initial and upper-boundary conditions was in equilibrium with the corresponding aqueous chemical composition.

Two groups of geochemical simulations were performed with one-dimensional column models (CRWMS M&O 2000d, Section 6.5.3, p. 83). The first group of 18 sensitivity simulations was designed to analyze calcite deposition affected by percolation rate, upper-boundary water and gas chemistry, and reaction rate. These simulations were based on the USW NRG-7a borehole column with the simple mineralogy. The second group of nine mineralogy simulations was based on the borehole USW WT-24 column, where measured calcite-deposition data were available for comparison. Both sets of simple and complex mineralogy were used in the second group of simulations. All simulations were run for 10 m.y. because mineral growth seems to have remained approximately constant over the past 8 m.y. and because all outer mineral surfaces appear young compared to the 12.7 m.y. age of the tuffs (Section 8.11.2).

#### 8.10.6.7.2 Results of Geochemical Modeling

The sensitivity simulations of calcite deposition (CRWMS M&O 2000d, Section 6.5.4) were performed with the base-case percolation rate of 0.2119 mm/yr. at borehole USW NRG-7a and two additional percolation rates of 2 and 10 mm/yr. A total of 18 simulations were performed using different percolation rates, upper-boundary water and gas chemistry, and reactive surface area as an indicator of reaction rate. The simulated change in calcite volume fraction was expressed as the average among the matrix and the fractures (calculated by calcite volume in the matrix and fractures divided by the total matrix and fracture solid volume). Simulation results indicated that calcite precipitation generally increased as the percolation rate increased, especially in the TSw unit. However, an increase in percolation resulted in only a slight change in the amount of calcite at the bottom of the PTn unit.

Calcite precipitation also was sensitive to upper-boundary water chemical composition, as represented by CO<sub>2</sub> partial pressure (CRWMS M&O 2000d, Section 6.5.4, p. 85). The higher the CO<sub>2</sub> partial pressure, the lower the calcite precipitation because the higher partial pressure causes higher concentrations of hydronium ion (H<sup>+</sup>), which associates with carbonate (CO<sub>3</sub><sup>2-</sup>) to form bicarbonate (HCO<sub>3</sub><sup>-</sup>), lowering the concentration of carbonate available to form calcite. The lower calcite precipitation (potential dissolution) can be clearly seen from the equation that governs calcite formation:



The calcite distribution was also dependent on reaction rate, which was simulated by changing the reactive surface area (CRWMS M&O 2000d, Section 6.5.4, p. 86). For the TCw unit close to the land surface, the higher the reaction rate, the higher the calcite precipitation. For the deeper TSw unit, the highest surface areas (estimated) resulted in the lowest calcite precipitation. The shift of the calcite precipitation in the TSw from the TCw mainly resulted from the proximity of

the TCw to the upper boundary, where percolation water and reactants of calcite were applied. Therefore, much more calcite precipitation occurred in the TCw than in the TSw. Increasing the reactive surface areas by a factor of 100 resulted in the same general trend as the initial estimated areas. Decreasing the reactive surface areas by a factor of 10 from the initial estimated data resulted in the most favorable conditions for calcite formation in the TSw unit.

In the mineralogy simulations, two different sets of mineralogy (simple and complex) were analyzed to investigate how the mineralogy affects calcite deposition (CRWMS M&O 2000d, Section 6.5.5, p. 87). The mineralogy simulations were based on the borehole USW WT-24 column. Three percolation rates were simulated: the base-case rate of 5.92 mm/yr., a lower rate of 2 mm/yr., and a higher rate of 20 mm/yr. Two of the four water types were applied to the upper boundary: average TSw water and measured TSw water. A total of nine simulations were performed using different percolation rates, upper-boundary water input and gas chemistry, and reactive surface areas. Three of the simulations used the average TSw water, simple mineralogy, and reactive surface areas reduced by a factor of 10 for the TCw and TSw units and reduced by a factor of 100 for the PTn. A different infiltration rate was employed for each simulation. Figure 8.10-20 shows the changes of calcite volume fraction resulting from the simulation together with measured calcite deposition data from borehole USW WT-24.

In general, simulations using complex mineralogy or the lower percolation rates resulted in much smaller volumes of calcite precipitation (CRWMS M&O 2000d, Section 6.5.5, pp. 89 to 91). The only exception was one model layer at the bottom of the PTn unit. At the higher percolation rate (20 mm/yr.) under the complex-mineralogy conditions, calcite precipitation increased in the TCw and TSw units. However, under the complex mineralogy, most of the calcite precipitated in the rock matrix, especially in the TCw unit, whereas under the simple-mineralogy condition almost all calcite precipitation occurred in the fractures of the TCw and PTn units. Some calcite precipitation in the matrix of the TSw unit has been observed, but its density was much lower than that in the fractures. The results indicate that chemical interaction of fractures and matrix has a more significant effect on calcite deposition under the complex-mineralogy conditions than under the simple mineralogy conditions. Under simple mineralogy, the reactant calcium for calcite precipitation is only from percolation water and, therefore, calcite precipitation occurs mostly in the preferential water-flow paths in the fractures.

Overall, simulation results indicate that calcite precipitation values for the TCw unit obtained using simple mineralogy and average TSw water (Figure 8.10-20) are closer to the measured data than those obtained using complex mineralogy and measured TSw water. The simple-mineralogy simulations also reproduced the calcite deposition in the PTn unit reasonably better, except for the bottom layer. Improved agreement for the PTn unit was achieved by reducing the reactive surface area, which is consistent with the lower fracture density in this unit. The simulated calcite precipitation values at the bottom of PTn unit, especially those from the complex-mineralogy simulation, may be overestimated for the borehole USW WT-24 column. However, high calcite concentrations in this layer have been observed at several other locations. Simulation results for the TSw unit from both mineralogy conditions generally fall in the wide range of measured calcite data. However, the simple-mineralogy simulations (Figure 8.10-20) better represent the field observation that calcite coatings are frequently found on fractures and lithophysal cavities in the TCw and TSw tuffs. This is especially true for the TCw unit close to

the land surface, in which reactants of calcite deposition come primarily from percolation water, and calcite precipitation occurs mostly in the preferential water-flow paths in the fractures.

The results of simulated calcite deposition (Figure 8.10-20) were sensitive to percolation flux in that calcite deposition values obtained from the highest percolation simulated rate (20 mm/yr.) were close to the high bound of the measurements (CRWMS M&O 2000d, Section 6.5.6). Results from the base case (5.92 mm/yr.) and lower percolation rate (2 mm/yr.) fall in the middle of the range of measured data for the TSw. This may imply that the 20 mm/yr. percolation rate is an upper bound for the borehole USW WT-24 location, whereas the base-case percolation (5.92 mm/yr.) may be a median value. Because the reactive surface area for calcite deposition was reduced by a factor of 10 from the initial estimation to provide the most favorable condition for calcite formation in the deeper TSw unit, the simulated values of calcite deposition for borehole USW WT-24 may be slightly overestimated.

The simulations of calcite deposition for borehole USW WT-24 provide some constraints on percolation flux, but cannot provide a definite value or a narrow range of values because calcite precipitation also depends on other factors, such as water and gas chemistry, reaction rate, and mineralogy (CRWMS M&O 2000d, Section 6.5.6, p. 94). Also, additional uncertainty could arise from climate and percolation variations over time, transient water-flow conditions, and possible lateral flow. Furthermore, measured calcite deposition varies significantly laterally and vertically in the unsaturated zone at Yucca Mountain. For example, the peak values observed in borehole USW WT-24 are in contrast with calcite deposition in the ESF, where calcite abundance decreases with depth in the TSw unit. The mean calcite abundance in the ESF is 0.034 percent, which is close to the lower bound of calcite observed in borehole USW WT-24.

#### **8.10.6.8 Simulation of Three-Dimensional Flow Fields for Input to Total System Performance Assessment**

A series of 18 simulations was made using the calibrated three-dimensional unsaturated zone flow model in order to produce flow fields needed as input to TSPA modeling (CRWMS M&O 2000d, Sections 6.6, 6.6.1). The 18 simulations encompassed all nine infiltration scenarios (lower-bound, mean, and upper-bound infiltration rates for present-day, monsoon, and glacial transition climates) for each of the two perched-water conceptual models: flow-through and bypassing (Section 8.10.6.4.1). Three simulations also were performed for the nonperching conceptual model for the mean present-day, monsoon, and glacial transition infiltration scenarios. All 21 simulations were performed using the dual-permeability formulation of the unsaturated zone flow and transport model, the numerical grid shown in Figure 8.10-4, and the calibrated parameter sets derived from the hydrologic-property and perched-water calibration exercises described in Sections 8.10.5 and 8.10.6, respectively.

Mass-balance calculations for these simulations indicate there was virtually no difference in total steady-state flow through the model domain between the simulations of the flow-through and bypassing perched-water conceptual models (CRWMS M&O 2000d, Section 6.6.2). For the mean present-day infiltration scenario, total flow through the domain was about 5.64 kg/s, whereas the total flows were about 1.47 kg/s and 13.80 kg/s for the lower-bound present-day scenario and the upper-bound present-day scenario respectively (CRWMS M&O 2000d, Table 6-19, p. 99). Total flow through the model was about 15.17 kg/s for the mean monsoon

infiltration scenario (CRWMS M&O 2000d, Table 6-20, p. 99) and about 22.05 kg/s for the mean glacial transition infiltration scenario (CRWMS M&O 2000d, Table 6-21, p. 99).

#### **8.10.6.8.1 Percolation Flux at the Potential Repository Horizon**

As described in Section 8.10.6.4.2, simulations of percolation flux at the potential repository horizon were not affected by the particular perched-water conceptual model that was used. In addition, because model simulations indicate that little lateral diversion occurs during flow from surface to repository horizon, the distribution of percolation flux at the repository horizon was very similar to the distribution of net infiltration used for the upper-boundary condition (CRWMS M&O 2000d, Section 6.6.3, p. 101). Figures 8.10-21, 8.10-22, and 8.10-23 show the distribution of simulated percolation flux at the potential repository horizon for the mean present-day, mean monsoon, and mean glacial transition infiltration scenarios, respectively. All three of these distributions of percolation flux were calculated using the unsaturated zone flow and transport model numerical grid that had a greater density of grid blocks in the area of the potential repository.

Figure 8.10-21 indicates that for mean present-day infiltration, percolation flux at the repository horizon equals or exceeds 15 mm/yr. in relatively small areas in the northern part of the unsaturated zone flow and transport model domain. In addition, percolation flux equals or exceeds 15 mm/yr. in a small area along the Solitario Canyon fault just west of the potential repository area and in a small area of the southwestern quadrant of the repository area. However, percolation flux is less than about 10 mm/yr. over most of the repository area. For the mean monsoon infiltration scenario (Figure 8.10-22), the highest percolation fluxes occur in about the same places as for the present-day scenario, but the highest percolation flux equals or exceeds 40 mm/yr. Over most of the repository area, percolation flux is less than 15 mm/yr., but in small parts of the repository area percolation flux equals or exceeds about 40 mm/yr. For the mean glacial transition infiltration scenario (Figure 8.10-23), the areas where percolation flux equals or exceeds 40 mm/yr. are significantly larger than for the monsoon scenario. Percolation flux equals or exceeds 40 mm/yr. over much of the northern one-third of the unsaturated zone flow and transport model area and over about one-third of the potential repository area.

#### **8.10.6.8.2 Percolation Flux at the Water Table**

Comparison of the distributions of simulated percolation flux at the water table reveals some important differences between the flow-through and the bypassing perched-water conceptual models (CRWMS M&O 2000d, Section 6.6.3, p. 105). Figures 8.10-24 and 8.10-25 show simulated percolation fluxes at the water table for the mean present-day infiltration scenario for the flow-through and the bypassing perched-water conceptual models, respectively. With the flow-through simulation (Figure 8.10-24), percolation fluxes at the water table under the northern part of the potential repository area are less than about 1.5 mm/yr., they are between about 1.5 and 15 mm/yr. under the southern part and are highest near the Ghost Dance fault. This probably reflects, in part, the lower permeability of the thick zeolitic CHn under the northern part of the repository area compared to the higher permeability of the vitric CHn under the southern part. With the bypassing simulation (Figure 8.10-25), percolation fluxes at the water table still are less than about 1.5 mm/yr. under the northern part of the repository area. Under the southern part, fluxes generally are less than 3 mm/yr., except near the Ghost Dance

(west) fault, where they exceed 15 mm/yr. Comparison of Figures 8.10-24 and 8.10-25 with Figure 8.10-21 (percolation flux at the repository horizon) indicates the degree of lateral diversion and bypassing of the perching layers that has occurred by the time water reaches the water table. Although the flow-through model predicts large lateral diversion under the northern part of the potential repository where thick, low-permeability zeolitic layers are located, overall there is much greater vertical flow and much less lateral flow than predicted by the bypassing model. Furthermore, the bypassing model predicts greater bypassing of the perching layers and the zeolitic rocks of the CHn. The lateral flow simulated by both perched-water conceptual models results in concentrations of high percolation flux in the major faults, as seen in Figures 8.10-24 and 8.10-25.

Simulations of the mean monsoon infiltration scenario for the two perched-water conceptual models resulted in patterns of percolation flux at the water table (Figures 8.10-26 and 8.10-27) similar to the simulations of present-day infiltration, but with higher fluxes. For the simulated mean monsoon scenario for the flow-through model, percolation fluxes are less than about 4 mm/yr. under the northern part of the potential repository area and between 4 and 35 mm/yr. under the southern part. For the bypassing model, fluxes generally are less than 4 mm/yr. under most of the repository area but are close to 40 mm/yr. near the Ghost Dance (west) fault.

For simulations of the mean glacial transition infiltration scenario for the flow-through model (Figure 8.10-28), percolation fluxes at the water table still are less than 4 mm/yr. under the northern part of the potential repository. However, the areas where fluxes equal or exceed 35 mm/yr. are larger under the southern part of the repository than they were with the monsoon scenario. For the mean glacial transition infiltration scenario simulated with the bypassing model (Figure 8.10-29), percolation fluxes at the water table remain less than 4 mm/yr. under most of the repository area, but are close to 40 mm/yr. near the Ghost Dance (west) fault. The fact that the simulated distributions of percolation flux at the water table do not change very much as the climate gets wetter (compare Figures 8.10-27 and 8.10-29) is further evidence of the strong lateral flow that occurs above the perching layers under the bypassing model.

#### **8.10.6.8.3 Fracture and Matrix Flow Components of Percolation Flux**

The unsaturated zone flow and transport model simulations made to produce flow fields for input to the TSPA also were analyzed to determine the matrix and fracture components of percolation flux at the potential repository horizon and at the water table (CRWMS M&O 2000d, Section 6.6.3, p. 115). Table 8.10-7 indicates that fracture flow is dominant both at the potential repository horizon and at the water table for all infiltration scenarios simulated with both perched-water conceptual models. Simulated fracture and matrix flow components for the present-day mean infiltration scenario using the flow-field grid (Figure 8.10-4) are similar to those simulated using the calibration grid (Figure 8.10-3) and described in Section 8.10.6.4.2. At the repository horizon, fracture flow accounts for more than 80 percent of the total flow and, at the water table, fracture flow accounts for 70 to 90 percent of total flow.

The data in Table 8.10-7 also show that the percentage of fracture flow for both perched-water conceptual models is progressively greater for the monsoon and glacial transition infiltration scenarios compared to the present-day scenario (CRWMS M&O 2000d, Section 6.6.3, p. 115, Tables 6-22 to 6-24). The results of these simulations also indicate that the bypassing conceptual

model predicts consistently lower fracture-flow components at the water table than does the flow-through model.

#### **8.10.6.9 Liquid Water Travel Times and Tracer/Radionuclide Transport**

The three-dimensional flow fields developed for the TSPA using the unsaturated zone flow and transport model also were used to investigate liquid water travel times and tracer/radionuclide transport (CRWMS M&O 2000d, Section 6.7, p. 116). Processes that control radionuclide transport processes from the potential repository to the water table (saturated zone) were investigated, including the effects of the perched-water conceptual models, infiltration scenarios, and sorption (CRWMS M&O 2000d, Section 6.7.1). Simulation results and analyses were based on transport studies of conservative and reactive tracers using a version of the code T2R3D, which used as direct input the flow fields from the dual-permeability steady-state simulations described in Section 8.10.6.8. Tracers, or radionuclides, were treated as conservative (nonsorbing) and reactive (sorbing) components transported through the unsaturated zone. For both cases, the hydrodynamic-dispersion effect through the fracture-matrix system was ignored. A constant molecular diffusion coefficient of  $3.2 \times 10^{-11}$  (m<sup>2</sup>/s) was used for matrix diffusion of the conservative component (such as <sup>99</sup>Tc), and  $1.6 \times 10^{-10}$  (m<sup>2</sup>/s) was used for the reactive component. In the case of a reactive (sorbing) tracer, several sorption coefficients ( $K_d$  values) were used to approximate those for <sup>237</sup>Np transport. The zeolitic matrix of the CHn was assigned a  $K_d$  of 4.0 mL/g, whereas the vitric matrix of the CHn, the matrix of the TSw, and the fault matrix of the CHn were assigned a  $K_d$  of 1.0 mL/g. The fracture and matrix of the remaining hydrogeologic units were assigned a  $K_d$  of 0.0 mL/g. For a conservative (nonsorbing) tracer,  $K_d$  was set to 0.0 mL/g. Diffusion coefficients and sorption coefficients ( $K_d$ ) were the same as the values used in the TSPA radionuclide-transport simulations conducted for the Viability Assessment (DOE 1998b, Section 3.6.2.3 and Table 3-18). All transport simulations were run to 1 m.y. with a constant infiltration and an initial constant source concentration condition at the repository fracture blocks, under the assumption that the tracer/radionuclide was released at the start of each simulation.

##### **8.10.6.9.1 Liquid Water Travel and Tracer-Transport Times**

A total of 42 transport simulations were conducted to encompass all nine infiltration scenarios, both perched-water and nonperching conceptual models, and conservative (nonsorbing) and reactive (sorbing) transport types (CRWMS M&O 2000d, Section 6.7.2, p. 117). Liquid water travel times from the potential repository to the water table were analyzed as cumulative or fractional breakthroughs (CRWMS M&O 2000d, Section 6.7.3, p. 121). The fractional mass breakthrough was defined as the cumulative mass of a tracer, or radionuclide, arriving at the water table over the entire lower model boundary at a time, normalized by the total mass of the component initially introduced at the repository. The simulations yielded a wide range of liquid water travel or tracer-transport times for different infiltration rates, tracers, and perched-water conceptual models. The predominant factors affecting liquid water travel times or tracer transport were net-infiltration rates and sorption effects, depending upon whether the tracer was conservative or reactive. To a certain extent, perched-water conceptual models also affected liquid water travel/transport times. However, the overall impact of the perched-water conceptual models on tracer breakthrough at the water table was secondary compared to the effects of infiltration and sorption.

Results for simulations of nonsorbing (conservative) and sorbing (reactive) tracers, or radionuclides, for the two perched-water conceptual models and mean infiltration for each of the three climate states are given in Table 8.10-8. Several conclusions about liquid water travel times from the potential repository to the water table can be drawn from these results:

- Nonsorbing tracers migrate about 100 times faster from the potential repository to the water table than sorbing tracers under the same infiltration scenario.
- For both nonsorbing and sorbing tracers, there are differences in travel times from the potential repository to the water table between the two perched-water conceptual models, with the bypassing model producing shorter travel times in the majority of cases (see CRWMS M&O [2000k] for results of an alternative model). However, the differences in travel times between sorbing and non-sorbing tracers are much more significant than the differences between perched-water models.
- Liquid-water travel or tracer-transport times are inversely proportional to the average net-infiltration rate over the model domain (CRWMS M&O 2000d, p. 124, Figure 6-57). As average net infiltration increases from 5 to 35 mm/yr., average liquid-water travel times for the 50 percent breakthrough of nonsorbing tracers decrease by a factor of 100 to approximately 1,000.

#### **8.10.6.9.2 Potential Locations of Tracer/Radionuclide Breakthrough at the Water Table**

The tracer-transport simulations also were used to estimate potential locations where radionuclides are most likely to break through at the water table (CRWMS M&O 2000d, Section 6.7.3, p. 126). Figures 8.10-30 and 8.10-31 show mass-fraction contours at 1 k.y. after release from the potential repository for conservative tracer transport under present-day, mean infiltration for the flow-through and bypassing perched-water conceptual models, respectively. The two figures clearly indicate a significant difference in distributions of tracer mass fraction (or concentration) at the water table. The flow-through model (Figure 8.10-30) predicts a large area of high concentration covering the entire area directly below the potential repository, indicating that transport is predominantly vertical for this case. In contrast, the bypassing model (Figure 8.10-31) shows only three high-concentration areas, which are associated primarily with faults, indicating significant lateral diversion of flow in the perched water bodies below the potential repository area and subsequent flow down faults to the water table (Section 8.10.6.4.2). Results of the mass fraction for reactive tracer transport (CRWMS M&O 2000d, Figures 6-60 and 6-61) show similar distribution patterns, but with lower concentrations in smaller areas.

#### **8.10.6.10 Model Validation**

Several validation exercises have been conducted with the unsaturated zone flow and transport model and its submodels in order to assess their accuracy and reliability in describing and predicting flow and transport processes in the unsaturated zone at Yucca Mountain (CRWMS M&O 2000d, Section 7.7, p. 149). These activities include simulation studies of the following:

- Alcove 1 infiltration and tracer-transport test
- ECRB Cross Drift moisture measurements
- Boreholes USW SD-6 and USW WT-24 saturation and perched-water data

- Three-dimensional gas-flow simulation using pneumatic data.

These validation exercises are significant because they involve field data that were not used for development and calibration of the unsaturated zone flow and transport model. In all cases, unsaturated zone flow and transport model simulations reasonably match different types of data, such as water potentials, liquid saturation, seepage rate, breakthrough concentrations, and pneumatic pressures, as observed at Yucca Mountain.

#### **8.10.6.10.1 Simulation of Alcove 1 Infiltration and Tracer-Transport Test**

Recently, an infiltration and tracer-transport test was performed in ESF Alcove 1, which is located near the North Portal of the ESF in the upper lithophysal zone of the Tiva Canyon Tuff (CRWMS M&O 2000d, Section 6.8.1, p. 132). The infiltration test involved applying water at the ground surface directly over the end of Alcove 1, which is approximately 30 m (98 ft) below the ground surface. At a late stage of the test, a conservative tracer bromide was introduced into the infiltrating water. Seepage into the alcove and tracer arrival time were recorded throughout the duration of the test. Because the experimental observations were directly related to the flow and transport processes in the unsaturated fractured rocks, the test provided a useful data set for evaluating the continuum approaches used in the unsaturated zone flow and transport model. The test consisted of two phases. Phase I was performed from March to August 1998 and had a relatively large degree of temporal variability in infiltration rate. Phase II was performed from January to June 1999.

A cylindrical two-dimensional grid was constructed for simulation of the Alcove 1 infiltration and tracer test, as described in CRWMS M&O (2000d, Section 6.8.1.1, p. 132). The active-fracture model (Section 8.10.3.6) was employed to describe flow and transport within fractures and between fractures and the matrix. Because of the highly transient nature of the infiltration test, the multiple-interacting-continua approach was used (Section 8.10.3.1). Inverse modeling with ITOUGH2 version 3.2 was used to calibrate the model to the Phase I test data (CRWMS M&O 2000d, Section 6.8.1.2, p. 134). Although the calibration matched the timing and duration of infiltration episodes reasonably well, the calibration underestimated peak infiltration rates because vapor-phase flow and hysteresis (wetting and drying) were not accounted for by the simplified model. However, the calibrated model simulation of the Phase II infiltration test was much more successful than the Phase I simulation, primarily because Phase II took place during the cooler part of the year when vapor-phase flow was not a significant factor.

The tracer-transport component of the Alcove 1 seepage test was simulated using the T2R3D code (CRWMS M&O 2000d, Section 6.8.1.2, p. 137). Tracer arrival time was found to be insensitive to fracture dispersivity. A molecular diffusion coefficient for bromide was assigned and a range of representative values of matrix tortuosity was considered based on the literature. Because pore velocities in the matrix generally are small, mechanical dispersion was ignored for the matrix. The calibrated hydrologic properties based on both Phase I and Phase II seepage data were used in the simulation. The simulated breakthrough curve (CRWMS M&O 2000d, Figure 6-65) closely matched the tracer concentration data for a tortuosity value of 0.75, which was close to the representative value of 0.7 from the literature. The results indicate that the model correctly predicted the tracer-transport behavior of the Alcove 1 test without calibration of transport parameters, which validates the continuum approach and shows that the unsaturated

zone flow and transport model can capture important features of unsaturated zone transport processes. An important finding from the tracer simulations was that the breakthrough curve was considerably sensitive to the matrix molecular diffusion coefficient and tortuosity, suggesting that matrix diffusion is an important mechanism for transport. This sensitivity also implies that flow and transport between the two continua (fracture-matrix interaction) was correctly simulated with the active-fracture model, although complex fingering flow and transport occurred in the fracture networks during the Alcove 1 test. On the other hand, the simulation result was not sensitive to the fracture dispersivity, possibly because in a dual-continua system the chemical transport is mainly determined by the largest heterogeneity, the property difference between the matrix and fracture continua. In this case, heterogeneity in each continuum, resulting in the corresponding macroscopic dispersion process, becomes secondary.

#### **8.10.6.10.2 Simulation of Enhanced Characterization of the Repository Block Cross Drift Moisture Measurements**

As the Cross Drift was constructed in 1997 as part of the ECRB program (Figure 8.10-2), water-potential data were collected from heat-dissipation probes installed in the tunnel walls. Unsaturated zone flow and transport model results were compared to the moisture data collected from the walls of the Cross Drift to check the accuracy of the model simulations. The model simulation used for the comparison included the calibration grid (Figure 8.10-3) and the flow-through perched-water conceptual model for the mean present-day infiltration scenarios. The hydrologic properties used for the simulation were those developed with the calibrated properties model (Section 8.10.5). Most of the water-potential measurements from the walls of the Cross Drift are distributed between -10 to -100 kPa (-0.1 and -1 bar), with a minimum of -340 kPa (-3.4 bar) (CRWMS M&O 2000d, Figure 6-66). The model-simulated water potential for the same section of the Cross Drift averaged about -100 kPa (-1 bar) and ranged from -10 and -330 kPa (-.1 and -3.3 bars). Although the model-simulated water-potential values are lower than most of the observed data, the unsaturated zone flow and transport model generally simulates the range of the measured water-potential data from the Cross Drift.

#### **8.10.6.10.3 Simulation of Saturation and Perched-Water Data from Boreholes USW SD-6 and USW WT-24**

Boreholes USW WT-24 and USW SD-6 (Figure 8.10-2) were drilled in 1997 as part of the ECRB program, and saturation measurements were made on rock cores from both boreholes (CRWMS M&O 2000d, Section 6.8.3, p. 140). Perched water was not detected in borehole USW SD-6, but was detected within the basal vitrophyre of the TSw in borehole USW WT-24 (Section 8.5.2.7). As part of the model validation process, model-simulated saturations were compared to the field data. The model simulation used for the comparison included the calibration grid (Figure 8.10-3) and the flow-through perched-water conceptual model for the mean present-day infiltration scenario. The hydrologic properties used for the simulation were those developed with the calibrated properties model (Section 8.10.5). The simulated saturation profile for borehole USW SD-6 (CRWMS M&O 2000d, Figure 6-67) indicates that simulated saturations generally were consistent with the field measurements. In particular, the model correctly simulated no perched water at this borehole, which is consistent with field observations. There was, however, some discrepancy between model-simulated and

measured saturations in the CHn zeolitic unit. The model simulated fairly high saturation values in this CHn unit, whereas the field measurements indicate fairly dry conditions.

For borehole USW WT-24, measurements of saturation on drill core were limited to the deeper section of the borehole, mostly in the CHn unit (CRWMS M&O 2000d, Section 6.8.3, p. 141, Figure 6-68). The unsaturated zone flow and transport model accurately simulated the location of perched water in borehole USW WT-24 and, in general, simulated the measured saturation profile. However, as with borehole USW SD-6, the measured data indicate a low-saturation layer within the CHn unit about 70 m (230 ft) below the contact with the TSw that was not simulated by the model. This may be due to the inaccuracy and uncertainty of the three-dimensional geological framework model version 3.1 at certain locations. The accuracy of the unsaturated zone flow and transport model depends largely on the accuracy of the geological framework model. While the degree of lateral continuity of layers represented in the geological framework model version 3.1 is a valid interpretation, the impact of a more heterogeneous structure on flow could be significant, especially in areas where little or no information has been collected. The spatial heterogeneity of low-permeability alteration minerals, such as zeolites, has a profound impact on flow and transport calculations, yet the nature of their distribution is not fully understood.

#### **8.10.6.10.4 Three-Dimensional Gas-Flow Simulation**

As part of the validation of the calibrated properties sets documented in Section 8.10.5, a fully three-dimensional gas-flow (pneumatic) simulation was performed (CRWMS M&O 2000d, Section 6.8.4, p. 142). The three-dimensional numerical mesh for the flow-field calculations (Figure 8.10-4) without perched-water adjustments was used for the pneumatic simulation. The calibrated properties used for the pneumatic simulation were those developed by inversion of saturation, water potential, and pneumatic data using one-dimensional and two-dimensional models for the present-day base-case infiltration scenario (Section 8.10.5). Pneumatic boundary conditions were developed using the TBgas3D routine and atmospheric pressure data from boreholes USW NRG-6 and USW NRG-7a.

The results of this simulation were compared to both the pneumatic data used for the one-dimensional and two-dimensional calibrations (Section 8.10.5) and the pneumatic data for the 30 days immediately following the calibration period. The three-dimensional pneumatic simulation was compared to pneumatic data from 27 instrument stations in six boreholes UE-25 NRG#5, USW NRG-6, USW NRG-7a, USW SD-7, USW SD-12, and USW UZ-7a (CRWMS M&O 2000d, Section 6.8.4, Table 6-35). Simulated pneumatic pressures closely matched those measured in all boreholes for both the calibration period and the following 30-day period. The matches between simulated and measured pneumatic pressure for borehole USW SD-12 were especially significant because USW SD-12 has more instrument stations spread over a greater range of depths and hydrogeologic units than the other instrumented boreholes (Section 8.4.2.1). For borehole USW SD-12, good matches between simulated and measured pneumatic pressure were obtained in all four major hydrogeologic units: TCw, PTn, TSw, and CHn (CRWMS M&O 2000d, Figure 6-69). In addition, the three-dimensional simulation resulted in slightly larger and more accurate amplitude responses in the TSw to atmospheric pressure changes than the calibrated one-dimensional simulation. This difference can be attributed to the presence of the

nearby Ghost Dance fault, which has a higher permeability through the PTn than does the unfaulted rock at borehole USW SD-12.

The good match between the three-dimensional pneumatic simulation and the pneumatic data from boreholes validates the base-case infiltration-scenario calibrated properties for gas-flow simulations. The simulations using the upper-bound and lower-bound infiltration-scenario calibrated properties produced results that were virtually identical to those from simulations using the base-case infiltration-scenario calibrated properties model (Section 8.10.5). This is not expected to change for the three-dimensional simulations and, thus, the upper-bound and lower-bound infiltration-scenario calibrated properties also are expected to be applicable for gas-flow simulations. The comparisons of the three-dimensional pneumatic simulations with the one dimensional and two-dimensional calibrated pneumatic simulations showed that the assumptions of one-dimensional and two-dimensional flow were not completely accurate. However, the comparisons also demonstrated that the initial assumptions of one-dimensional and two-dimensional flow were adequate for providing reasonable estimates of fracture permeability for the three-dimensional unsaturated zone flow and transport model.

#### **8.10.7 Drift Seepage Model for Performance Assessment**

Two critical models have been developed that provide quantitative descriptions of potential water seepage into drifts of the potential repository at Yucca Mountain: the seepage model for performance assessment and the disturbed drift seepage submodel (CRWMS M&O 2000h, Section 1, p. 11). The results from these models will be used in performance assessment to develop the probability distributions of water seepage into waste-emplacement drifts in the potential repository. These models were used to perform numerical simulations of drift seepage with stochastic representations of hydrological properties and to evaluate the effects of a partially collapsed drift on drift seepage. (Note: An evaluation of the seepage threshold in potential repository drifts was discussed in Section 8.8.5.2 and a drift seepage calibration model was described in Section 8.8.5.3.)

Seepage into drifts was evaluated by applying numerical models with stochastic representations of hydrological properties and performing multiple realizations of the permeability field around the drift (CRWMS M&O 2000h, Section 1, p. 11). The seepage model uses the distribution of permeabilities derived from testing in the ESF niches (Section 8.8.5) to stochastically simulate the three-dimensional flow of water in the fractured host rock in the vicinity of potential emplacement drifts under ambient conditions. The disturbed drift submodel was developed to evaluate the impact of the partial collapse of a drift on seepage. Drainage in rock below a potential emplacement drift also was evaluated.

Specifically, the scope of the development and application of the seepage model and the disturbed drift model involved the following:

- Evaluation of percolation flux calculated by the site-scale unsaturated zone flow and transport model for use in establishing a range of flux rates to be applied at the upper boundary of the drift seepage model
- Use of the calibrated parameter sets developed using the seepage calibration model

- Design of a set of simulations for evaluating drift seepage
- Performance of multiple realizations of heterogeneous rock properties and subsequent simulations of drift seepage and development of input for the evaluation of the distribution probability of water dripping onto waste packages
- Evaluation of the dependence of predictions on the effective local correlation length and the degree of heterogeneity of hydrologic parameters
- Evaluation of existing models of tunnel or drift collapse for representation as an alternative drift geometry and development of a simplified representation of partial drift collapse
- Performance of simulations using the distributed drift model
- Use of the seepage model to evaluate drainage of water through the rocks below a drift.

The drift seepage analysis was limited to the current repository design and available site data, including drift configuration, available hydrologic properties data from the site, and consideration of seepage under ambient conditions only. Thus, thermohydrologic and thermohydronechanical effects of waste emplacement were not considered. Also, because the primary seepage-related data were available for the Topopah Spring middle nonlithophysal geological unit (Tptpmn) at Yucca Mountain, the evaluation was primarily for this unit.

The primary purpose of the drift seepage analysis was to provide input to performance assessment and not to draw any conclusions on final performance assessment predictions (CRWMS M&O 2000h, Section 1, p. 12). Thus, this analysis forms a vital link between the field data and calibrated model parameters and the performance assessment effort.

#### **8.10.7.1 Data Sources and Software for the Drift Seepage Models**

Data sources for the development of the drift seepage models are described in CRWMS M&O (2000h, Section 4, pp. 17 and 18, and Table 2). Input data for model development included the following:

- Proposed drift configuration
- Calibrated drift-scale properties to establish parameter ranges
- Calibrated fracture properties (frequency and van Genuchten  $\alpha$  and  $n$  parameters) for the potential repository host rock to establish parameter ranges
- Fracture permeabilities from air permeability tests in ESF niches to corroborate the choice of permeability range
- Air permeability measurements from the Single Heater Test and Drift Scale Test areas to corroborate the choice of parameter ranges

- Detailed line survey of fractures in the Topopah Spring middle nonlithophysal geologic unit along the ESF Main Drift (Stations 27+20 to 37+80) to corroborate the use of the fracture-continuum approach
- General drift shape from drift degradation analysis of the engineered barrier system.

The software items used for development and application of the drift seepage models are described in CRWMS M&O (2000h, Section 3, pp. 15 and 16, and Table 1). The three principal computer codes used were ITOUGH2 V3.2\_drift, the SISIM module of the GSLIB version 2.0 package, and AMESH version 1.0. ITOUGH2 V3.2\_drift was used to perform forward simulations of multiphase fluid flow and calibration inversions during the analyses. The SISIM module of GSLIB was used to generate stochastic representations of the permeability fields in the host rock surrounding the drifts using the air permeability test data obtained from ESF niche studies. The AMESH version 1.0 code was used in the analysis to generate numerical grids for modeling simulations of the undisturbed and partially collapsed drifts. A number of software routines also were used to preprocess model input and postprocess model output.

#### 8.10.7.2 Model Description and Selection of Cases

The drift seepage model was based primarily on the model of Birkholzer et al. (1999, pp. 358 to 362) (CRWMS M&O 2000h, Section 6.3, p. 22). The conceptual model was a heterogeneous permeability field for the fracture continuum generated with parameters discussed below using the code GSLIB version 2.0. The three-dimensional field was 20 m (66 ft) high, 15 m (49 ft) wide normal to drift axis, and 5.23 m long along the drift axis. Inside the permeability field, the drift was 5.5 m (18 ft) in diameter with a distance to either side boundary of 4.75 m (15.6 ft). With this geometry, it was expected that a vertical cross section through the permeability field would be of sufficient size to capture the flow features around the drift. The distance along the drift axis was defined by the waste package length of 5.13 m (16.8 ft) with 0.1 m (0.33 ft) between the waste packages. The side boundary conditions of the model were assigned as no-flow and the lower-boundary condition was assigned as gravity drainage. The upper-boundary surface was simulated by an extra grid cell with constant percolation flux connected to all the grid cells in the upper boundary so that flow was free to move into these cells according to local property parameters.

The model mesh was generated using the AMESH version 1.0 code and the grid cell used was a cube 0.5 m (1.6 ft) on a side (CRWMS M&O 2000h, Section 6.3, p. 22). This cell size was chosen as a compromise between being fine enough to include the main flow features and being coarse enough to allow about 1,000 three-dimensional stochastic simulations. A more detailed numerical study demonstrated that 0.5 m (1.6 ft) was an adequate grid size for the flow calculations.

Flow calculation was performed using ITOUGH2 V3.2\_drift code. The model considered a drift that is in the Topopah Spring middle nonlithophysal unit (CRWMS M&O 2000h, Section 6.3, p. 22), which is unsaturated zone flow and transport model layer tsw34 or the lithostratigraphic unit Tptpmn (Table 8.10-1). Thus, parameter values considered during model development for the rock surrounding the drift were for the Tptpmn unit. The three parameters to which drift seepage is most sensitive are the fracture-continuum permeability ( $k_{FC}$ ), the van Genuchten

$\alpha$  value, and the standard deviation in the natural log of  $k_{FC}$  ( $\sigma$ ), which is a measure of heterogeneity of the permeability field. For each combination of these three parameters in each grid cell, seepage model calculations were made for three realizations, using a range of values for percolation flux at the repository level. This resulted in more than 1,000 simulations. Choices of parameter ranges on which seepage calculations were performed were based on the best available field data. However, the data values were not used directly to produce a single set of simulation results, but were used as references to establish parameter ranges.

The range of permeability chosen for the fracture continuum ( $k_{FC}$ ) was from  $0.9 \times 10^{-14}$  to  $0.9 \times 10^{-11} \text{ m}^2$  (CRWMS M&O 2000h, Section 6.3.2, p. 24), based on results from air permeability tests conducted in the ESF niches (both pre-excavation and post-excavation), the ESF Single Heater Test area, and surface-based boreholes. For the standard deviation in the natural log of  $k_{FC}$  ( $\sigma$ ), values of 1.66, 1.93, and 2.5 were evaluated based on earlier studies (CRWMS M&O 2000h, Section 6.3.3, p. 25). For the van Genuchten  $n$  parameter, a single value of 2.7 was used based on previous studies and fracture information in the ESF (CRWMS M&O 2000h, Section 6.3.4, p. 25). A sensitivity study performed by running several cases with an  $n$  of 2.55 demonstrated that the differences in seepage results were not significant. For the van Genuchten  $\alpha$  value, four values of  $1/\alpha$  (0.03, 0.1, 0.3, and 1.0 kPa) were simulated in the model, with the largest and smallest values being derived from recent studies (CRWMS M&O 2000h, Section 6.3.4). Because field data suggest that fracture permeability of the Tptpmn is random without a spatial correlation length ( $\lambda$ ), a  $\lambda$  equivalent to the grid size (0.5 m [1.6 ft]) was used in the main set of calculations (CRWMS M&O 2000h, Section 6.3.5, p. 26). However, a sensitivity analysis was performed with values of  $\lambda$  equal to 1 m and 4 m. Finally, percolation flux was varied over a range from 5 to 500 mm/yr. to account for the fracture component of percolation flux at the potential repository horizon (Section 8.10.6.8.1) and the associated uncertainty (CRWMS M&O 2000h, Section 6.3.6, p. 27).

### 8.10.7.3 Calculation of Seepage into a Drift

Seepage percentage was defined as the model-simulated liquid that seeped into the drift divided by the total liquid arriving on a cross-sectional area corresponding to the footprint of the drift (CRWMS M&O 2000h, Section 6.6, p. 29). Model results indicate that seepage percentage decreases with increasing van Genuchten  $1/\alpha$  or fracture-continuum permeability ( $k_{FC}$ ) (CRWMS M&O 2000h, Section 6.6.1, p. 30). At a percolation flux of 5 mm/yr., the seepage percentage was 0 or very near 0 for  $k_{FC}$  values greater than  $0.9 \times 10^{-14} \text{ m}^2$  and  $1/\alpha$  values greater than 0.1 kPa, regardless of the value of the standard deviation in the natural log of  $k_{FC}$  ( $\sigma$ ) (CRWMS M&O 2000h, Table 4). The highest seepage percentages for a percolation flux of 5 mm/yr. occur at the lowest fracture permeability when  $1/\alpha$  equals 0.03 kPa, and they range from 33 to 38 percent. At a percolation flux of 14.6 mm/yr., the seepage percentage might be 0 for  $k_{FC}$  values greater than  $0.9 \times 10^{-13} \text{ m}^2$ , regardless of the values of  $1/\alpha$  or  $\sigma$  (CRWMS M&O 2000h, Table 5). When  $k_{FC}$  is equal to  $0.9 \times 10^{-13} \text{ m}^2$ , seepage percentages generally are less than 10 percent, regardless of the values of  $1/\alpha$  or  $\sigma$ . The highest seepage percentages for a percolation flux of 14.6 mm/yr. occur at the lowest fracture permeability when  $1/\alpha$  equals 0.03 kPa, and they range from 58 to 68 percent. At a percolation flux of 73.2 mm/yr., seepage percentages were less than 5 percent when  $k_{FC}$  is equal to  $0.9 \times 10^{-12} \text{ m}^2$ , regardless of the values of  $1/\alpha$  or  $\sigma$  (CRWMS M&O 2000h, Table 6). At the lowest permeability and operation rate of

73.2 mm/yr. seepage percentages were 80 percent or greater when  $1/\alpha$  was equal to 0.03 kPa and about 70 percent or greater when  $1/\alpha$  was equal to 0.1 kPa.

A sensitivity analysis for the spatial correlation length ( $\lambda$ ) of fracture permeability was conducted with simulations of nonrandom  $\lambda$  of 1 m and 4 m (CRWMS M&O 2000h, Section 6.6.2, p. 38). These simulations indicated that the seepage percentage was as high as 8.3 percent for  $k_{FC}$  equal to  $0.9 \times 10^{-13} \text{ m}^2$ ,  $1/\alpha$  equal to 1 kPa,  $\sigma$  equal to 1.93, and percolation flux equal to 73.2 mm/yr. (CRWMS M&O 2000h, Table 9), whereas with the random fracture permeability ( $\lambda$  equal to grid size) the seepage percentage was 0 for these same properties.

Cases considering correlation between  $k_{FC}$  and  $\alpha$  also were examined as an “alternative approach” (CRWMS M&O 2000h, Section 6.6.4, Figures 3 and 4). These simulations indicated that with the correlated  $\alpha$  condition, seepage into a drift was 0 to 10 percent higher than with the uncorrelated cases.

#### 8.10.7.4 Effects of Drift Degradation on Seepage

Drift degradation may occur in three ways (CRWMS M&O 2000h, Section 6.4, p. 27):

- Loosening of rock blocks and hence wider fracture aperture (fracture dilation)
- Rockfall from the ceiling of the drift
- Extended rock failure in drift roof.

Based on these possibilities, a drift degradation submodel was designed to evaluate the impact of drift degradation on seepage.

Because of excavation, stress is relieved at the drift and fractures are expected to dilate in certain areas around the drift (CRWMS M&O 2000h, Section 6.4.1, p. 28). Such fracture dilation depends on the orientation of the fracture set and generally occurs within one drift radius. An increase in fracture aperture due to dilation generally causes an increase in fracture permeability and a decrease in van Genuchten  $1/\alpha$  value. The increase in permeability from the pre-excavation to the post-excavation values (Section 8.8.5.1.1) is a result of this effect. The effect on seepage due to increase in permeability and decrease in  $1/\alpha$  has already been accounted for in the simulations described in Section 8.10.7.3.

Rockfall from the ceiling of the potential repository drift has been quantified using the key block theory and fracture maps in the ESF (CRWMS M&O 2000h, Section 6.4.2, p. 29). For the Topopah Spring Tuff middle nonlithophysal zone, it has been estimated that 39 key blocks per kilometer of the drift will fall, equaling  $19 \text{ m}^3$  ( $671 \text{ ft}^3$ ) of total rockfall per kilometer. This implies that rockfall occurs on an average of one block every 25 m (82 ft) and that the mean size of the block is about  $0.5 \text{ m}^3$  ( $18 \text{ ft}^3$ ). It also has been estimated that 90 percent of the blocks have sizes less than  $1.18 \text{ m}^3$  ( $41.7 \text{ ft}^3$ ). In another study, a two-dimensional discrete-element method was used to conclude that rockfall is most likely to occur at the spring line of the drift and the size of the block depends on the assumed fracture spacing. To study the effect of rockfall on seepage, a parameter set ( $k_{FC} = 0.9 \times 10^{-12} \text{ m}^2$ ,  $1/\alpha = 0.1 \text{ kPa}$ ,  $\sigma = 1.66$ , and  $\lambda = 0.5 \text{ m}$ ) was used that is closest to the parameter values obtained with the seepage calibration model described in Section 8.8.5.3. Two calculations were performed, one in which a  $1\text{-m}^3$  ( $35 \text{ ft}^3$ ) block was taken

out from the crown of the drift and the second in which the 1-m<sup>3</sup> (35 ft<sup>3</sup>) block was taken out at the spring line.

Over time, extended rock failure may also occur at the roof of the drift (CRWMS M&O 2000h, Section 6.4.3, p. 29). It has been estimated that the failure at the roof would be 0.1 to 1 m (0.33 to 3.3 ft) in depth, and it would be 0.4 to 1.2 m (1.3 to 3.9 ft) in depth if seismic effects were included. It was expected that stress-induced failure at the drift crown would occur over a distance of one-half the drift radius, or about 1.25 m (4.10 ft) into the rock. Another study using a discrete region key block analysis indicated a more extended failure region of up to one drift diameter above the drift roof. In the seepage model, a case was designed in which an extended cavity developed in the drift roof with a step shape of 0.5 m (1.6 ft) at the crown, 1-m (3.3 ft) depth at 0.5 m (1.6 ft) to one side, and so on, reaching a 3-m (9.8-ft) depth at 2 m (6.6 ft) laterally from the drift crown. Further, the step-shaped failure was 1 m thick. For these simulations, a parameter set was used that is closest to the parameter values obtained with the seepage calibration model described in Section 8.8.5.3 ( $k_{FC} = 0.9 \times 10^{-12} \text{ m}^2$ ,  $1/\alpha = 0.1 \text{ kPa}$ ,  $\sigma = 1.66$ , and  $\lambda = 0.5 \text{ m}$ ).

Using these parameters and a percolation flux of 73.2 mm/yr. or less, model simulations indicated that all seepage percentages were 0, as they were for the nondegraded case (CRWMS M&O 2000h, Section 6.6.5, p. 39). For a percolation flux of 500 mm/yr., model results indicated that the effect of a single rockfall does not significantly alter drift seepage from the nondegraded case. A deeper rock failure in the drift roof (3 m [9.8 ft]) increases seepage but only by 1 to 3 percent, with the calculated seepage remaining 10 percent or less of percolation flux (CRWMS M&O 2000h, Table 12).

#### **8.10.8 Mountain-Scale Coupled Thermohydrologic Model**

The mountain-scale thermohydrologic model was developed to evaluate the effects of coupled thermohydrologic processes on mountain-scale conditions in the unsaturated zone at Yucca Mountain (CRWMS M&O 2000i, Section 1, p. 13). The mountain-scale thermohydrologic model and associated submodels provide the necessary framework to test conceptual hypotheses of flow and predict flow behavior under thermal-loading conditions that may occur if the potential repository actually is filled with high-level radioactive wastes. The mountain-scale thermohydrologic model numerically simulates the potential impact of repository decay heat on the natural hydrogeologic system, including a representation of heat-driven processes occurring in the far field some distance from the potential repository drifts. The thermohydrologic model was used to determine the effect of thermal loading in the potential repository on mountain-scale liquid and gas fluxes as well as temperature and moisture distribution in the unsaturated zone. Of particular interest is the impact of thermal loading due to waste emplacement on percolation at and near the repository host rock and the potential flow-barrier effects in the basal vitrophyre underlying the repository horizon.

The mountain-scale thermohydrologic flow fields were developed using the unsaturated zone flow and transport model (Section 8.10.6) with input parameters based on the calibrated properties set (Section 8.10.5) (CRWMS M&O 2000i, Section 1, p. 13). The flow fields were simulated with the spatially varying mean infiltration rates for the three climate states that are

likely to occur during the thermal-loading period. The simulations were performed using the average thermal load of 72.7 kW/acre and a ventilation efficiency of 70 percent for 50 yr.

Prediction of the thermal-loading effects requires prior establishment and acceptance of mathematical models that accurately represent the physics of heat and fluid transport in the unsaturated zone (CRWMS M&O 2000i, Section 1, p. 13). The mountain-scale thermohydrologic model used the mathematical formulation in the TOUGH2 family of codes, the continuum modeling approaches, and the van Genuchten capillary-pressure and relative-permeability relationships to adequately describe the behavior of the unsaturated zone under thermal-loading conditions. This formulation is based on the traditional energy-conservation and mass-conservation relationships, together with the constitutive equations. During the development of the mountain-scale thermohydrologic model, the accuracy and validity of model results were evaluated based on scientific principles and current understanding of fracture-matrix interactions, heat transport, and two-phase flow in the unsaturated zone. Calibration of modeled temperature provided a basis for assessing the effectiveness of the model in capturing mountain-scale processes.

#### **8.10.8.1 Data Sources and Software for the Mountain-Scale Coupled Thermohydrologic Model**

Data sources for development and application of the thermohydrologic model and associated submodels are documented in CRWMS M&O (2000i, Section 4.1, p. 19, and Table 2). Primary input data used for the thermohydrologic model include the following:

- Fracture properties (frequency, permeability, van Genuchten parameters, aperture, porosity, and interface area) for each model layer
- Matrix properties (porosity, permeability, van Genuchten parameters) for each model layer
- Thermal properties (grain density, wet and dry thermal conductivity, grain specific heat, and tortuosity coefficients) for each model layer
- Fault properties (matrix and fracture) for each hydrogeologic unit
- Potential repository thermal load and ventilation efficiency.

The calibrated parameter sets (Section 8.10.5) also include estimates of the active-fracture parameters (Section 8.10.3.6) for each model layer, which accounts for the reduced interaction between matrix and fracture flow resulting from flow fingering and channeling.

Computer software items used in the development of the thermohydrologic model and associated submodels are described in CRWMS M&O (2000i, Section 3, p. 17, Table 1). To simulate the nonisothermal effects of thermal loading on the unsaturated zone, the computer program TOUGH2 version 1.4 was used with the equation-of-state-module EOS3. The post processor code EXT version 1.0 was used to process the TOUGH2 output for plotting and display. The code Infil2grid version 1.6 was used to interpolate net-infiltration flux from the infiltration model (Section 8.2.10) onto the numerical grid for the thermohydrologic model numerical grid. The

code WinGridder version 1.0 was used to generate numerical grids used for the thermohydrologic model.

### **8.10.8.2 Description of the Mountain-Scale Coupled Thermohydrologic Model and Associated Submodels**

In the thermohydrologic model and submodels, heat and fluid flow were simulated using both the effective-continuum and dual-permeability numerical formulations (CRWMS M&O 2000i, Section 6.1.2, p. 28). These formulations are described in detail in Section 8.10.3. For thermal-loading simulations, the dual-permeability formulation was used, with a single fracture element and single matrix element representing each discrete block. This formulation allows matrix-to-matrix and fracture-to-fracture flow, as well as fracture-matrix interactions.

#### **8.10.8.2.1 Numerical Grids**

The following numerical grids were used in the thermohydrologic model and submodels (CRWMS M&O 2000i, Section 6.2, p. 29):

- A three-dimensional potential repository submodel grid derived from the flow-field grid for the unsaturated zone flow and transport model (Figures 8.10-4), with the finer mesh grid in the potential repository area to increase vertical resolution (Section 8.10.4.8)
- Two two-dimensional cross-section model grids (NS#1 and NS#2).

The first cross-section grid (NS#1) was extracted directly from the flow-field grid for the unsaturated zone flow and transport model, whereas the second grid (NS#2) is a refined north-south cross section also based on the geological framework model version 3.1. Figure 8.10-32 shows a plan view of the thermohydrologic model grid, the location of the potential repository submodel domain, and the locations of the two cross sections. The layering scheme for the thermohydrologic model is shown along cross sections NS#1 and NS#2 in Figures 8.10-33 and 8.10-34, respectively.

The thermohydrologic repository submodel domain is bounded by the Solitario Canyon fault to the west, the Pagany Wash fault to the north, the Imbricate fault to the east, and the unsaturated zone flow and transport model boundary to the south (CRWMS M&O 2000i, Section 6.2.1) (Figure 8.10-32). The submodel domain consists of 62,884 elements and 249,813 connections in a dual-permeability formulation. The thermohydrologic model grids (both three-dimensional and two-dimensional) and model input were not configured to simulate perched-water zones because perched water was assumed to have little impact on thermohydrologic processes at the potential repository horizon. Perched water is confined to the lower units of the TSw and the upper layer of the CHn, which lie 100 to 150 m (330 to 490 ft) below the repository horizon (CRWMS M&O 2000i, Section 5.3, p. 25). Because the dominant mechanism of heat transfer at these locations is heat conduction, the effect of perched water on mountain-scale thermohydrologic processes was ignored. Finally, because of predominantly vertical percolation in the unsaturated zone, it was deemed unnecessary to use the entire unsaturated zone flow and transport model domain for the thermohydrologic model (CRWMS M&O 2000i, Section 6.2.1, p. 31). Thus, only the repository submodel domain (Figure 8.10-32) was used for the thermohydrologic simulations.

In the thermohydrologic model grid (same as in the unsaturated zone flow and transport model flow-field grid), the potential repository horizon is represented by a 5-m-thick (16-ft-thick) grid layer (Figures 8.10-33 and 8.10-34), which is bounded immediately above and below by 5-m-thick (16-ft-thick) layers (CRWMS M&O 2000i, Section 6.2, p. 29). The lateral spacing over the potential repository area in the thermohydrologic submodel grid and the NS#1 cross-section grid is equal to the spacing between the drifts (81 m [270 ft]) and about 270 m (890 ft) along the drifts. Although this grid is sufficient to resolve mountain-scale unsaturated zone flux, it would not provide enough resolution for detailed studies of flow around and between drifts. Because liquid flux in the unsaturated zone at Yucca Mountain is predominantly vertical and drifts are widely spaced, there is potential for flow between the drifts. In addition, there also may be significant differences in temperature and saturation laterally between a heated drift and the middle portion of the rock between the drifts, particularly during earlier times of thermal loading. Such processes cannot be simulated using the unsaturated zone flow and transport model flow-field grid or any submodel extracted from it because there are no numerical grid nodes between the drifts. Therefore, the numerical grid for the thermohydrologic model was modified in the repository submodel to allow for two-dimensional simulation of individual drifts and the rock between them using the NS#2 cross-section grid (Figure 8.10-34). The NS#2 cross-section grid is a refined north-south grid in which the lateral grid spacing is equal to one-fourth of the drift spacing (CRWMS M&O 2000i, Section 6.2.2, p. 31). These local modifications allowed temperature, saturation, and flux changes to be resolved at and near the repository horizon. Further, local refinement of the grid at the potential repository and lateral refinement over the entire grid allowed the resolution of both ambient infiltration and repository thermohydrologic processes.

#### **8.10.8.2.2 Thermal-Loading Scenario and Effects**

Mountain-scale thermal-loading data developed by YMP were used in the thermohydrologic model (CRWMS M&O 2000i, Section 6.3, p.33). The thermal loading and the resulting temperature field may have a large influence on many thermohydrologic-related processes that can directly impact the performance of the repository. Emplacement of heat-generating high-level radioactive waste will elevate the temperature and cause redistribution of in situ moisture in the repository volume, as well as in the unsaturated zone surrounding the repository. For example, as heat is released from a waste package and transferred to the surrounding host rock, the temperature near the waste packages will approach or exceed the boiling point of water. Boiling of formation water in the host rock will increase vapor pressure and overall gas-phase pressure. This will result in forced convection of the gas phase, with a redistribution of water, accompanied by large latent-heat effects. The phase transformation and gas-phase flow will perturb in situ fluid saturation in both fractures and matrix, thereby setting up capillary-pressure gradients and liquid-phase flow. The impact of heat on the thermohydrologic processes will depend on the thermal load and its distribution at the repository.

The total thermal load for the base-case scenario is  $0.018 \text{ kW/m}^2$  (72.72 kW/acre), based on a repository area of 1,050 acres (CRWMS M&O 2000i, Section 6.3.1, p. 33). This thermal load was used in all the base-case thermal-load simulations and was input as a function of time in accordance with plans for emplacing wastes in the potential repository and rates of radionuclide decay. The effective mountain-scale thermal load under ventilation also was simulated in the thermohydrologic model (CRWMS M&O 2000i, Section 6.3.2, p. 33). Ventilation was assumed

to remove 70 percent of the heat generated by the radioactive waste during the first 50 yr.; after that, the thermal load reverts to the no-ventilation rate.

In all simulations, each repository drift was represented by a single element (with both matrix and fracture continua for a dual-permeability formulation) and was simulated with the properties of the unsaturated zone flow and transport model layer in which the element was located (CRWMS M&O 2000i, Section 6.3.3, p. 33). Thermal load was applied directly only to the matrix continuum of the repository node. The distribution of heat source depends on the discrete representation of the drifts within the repository nodes and the grid spacing.

If the grid spacing within the repository was equal to the drift spacing, then the entire repository node was used to represent the drift (CRWMS M&O 2000i, Section 6.3.3.1, p. 34). This resulted in a continuous and smeared heat source across the repository laterally. This approach cannot provide detailed resolution for studies of thermohydrologic processes in terms of temperature, saturation, and flux for the intervening space between the drifts. While not allowing these phenomena to be modeled near the drifts, this coarse-grid model did allow for simple and rapid estimation of the long-term, average response to thermal loading after 500 yr. Beyond this time, heat distribution is sufficiently diffused at the repository such that the model provides a good approximation of the heat source distribution. This modeling approach was used only in the repository submodel and the NS#1 cross-section model. The major advantage of this approach is that it allowed direct comparison of fluid, temperature, and flux distribution between the ambient flow-field models and the thermohydrologic model over the repository domain. The impact of thermal hydrology on flow and transport could then be directly estimated using flow fields extracted from the thermohydrologic model.

Although the repository thermal load was computed based on the total acreage of the repository, the heat-generating radioactive waste will be stored in the drifts within the repository at a discrete spacing (CRWMS M&O 2000i, Section 6.3.3.2, p.34). The current repository design has 5.5-m (18-ft)-diameter drifts spaced 81 m (270 ft) apart and trending in a west-northwest/east-southeast direction (Figure 8.10-32). Because of the large spaces between the drifts and the variability in net infiltration across the model, a potential for large differences or gradients in temperature, saturation, and flux exists between the heated drifts. The discrete (drift-by-drift) model provided a refined-grid model that accounted for such phenomena to investigate their importance and effects on the mountain-scale thermohydrologic processes. Therefore, the drift-by-drift distribution of the heat source was simulated in the thermohydrologic model by making the grid spacing finer than the drift spacing. Although this locally refined grid allowed for flow between drifts, the refinement was limited to the repository horizon such that surface infiltration still was applied based on the original coarser grid spacing. However, in the refined north-south NS#2 cross-sectional grid (Figure 8.10-34), the grid refinement extended vertically through the entire model so that surface infiltration could be discretely resolved between the drifts.

#### **8.10.8.2.3 Boundary and Initial Conditions**

For the thermohydrologic model, the steady-state, ambient mountain-scale temperature and saturation conditions served as initial conditions for the various thermal-load and infiltration scenarios (CRWMS M&O 2000i, Section 6.4, p.37). Liquid saturation, water potential, and

pneumatic pressure data were used to calibrate the flow and transport properties (Sections 8.10.6.3 and 8.10.6.4), while temperature data, which were not used directly in parameter calibration for flow and transport properties, were required to simulate geothermal conditions in the unsaturated zone. A steady-state ambient moisture, pressure, and temperature distribution in the unsaturated zone was obtained using the TOUGH2 version 1.4 simulation under fixed upper-boundary and lower-boundary temperature, pressure, and saturation conditions. The upper-boundary temperature for the thermohydrologic model was defined in the same manner as described in Section 8.10.6.5 for the unsaturated zone flow and transport model. For thermohydrologic simulations in which temperature changes at the water table due to the repository thermal loading were deemed insignificant, the lower temperature boundary was defined in the same manner as described in Section 8.10.6.5 for the unsaturated zone flow and transport model. This temperature distribution indicated that over the repository domain, average temperature at the water table (elevation of 730 m [2,400 ft]) is between 30° and 33° C.

For thermohydrologic simulations in which changes in temperature at the water table arising from thermal loading seemed possible, the lower temperature boundary was extended to 1,000 m (3,300 ft) below the water table (CRWMS M&O 2000i, Section 6.4.2, p. 38). For the extended lower boundary, thermal conductivity at the water table was set to zero to avoid conductive heat flow into the extended domain of the model. The temperature at the extended boundary was fixed at 65°C based on an average geothermal gradient of 35°C/km at the water table. The permeability of the extended model domain was set to zero so that all fluid-mass exchange was limited to the water-table boundary and only heat conduction was simulated below the water table. Steady-state simulations using extended-temperature boundary conditions showed that the temperature distribution at the water table was within  $\pm 2^\circ\text{C}$  of the calibrated temperature distribution. This result effectively verified the hypothesis that ambient infiltration and geothermal gradients are the primary controls on temperature distribution in the unsaturated zone.

#### **8.10.8.2.4 Thermal Properties**

The thermal properties (grain density, wet and dry thermal conductivity, and heat capacity) assigned to the matrix blocks of the various layers in the thermohydrologic model were obtained from Francis (1997) and Ho and Francis (1997) and are listed in CRWMS M&O (2000i, Table 4). The thermal properties initially assigned to the lower boundary elements also were applied to the extended model domain below the water table. The thermal conductivity to the fluid boundary elements were set to zero to prevent heat conduction into this boundary. Very low thermal conductivity values (10,000 times lower than matrix thermal conductivity) were assigned to the fracture continuum to minimize fracture-to-fracture thermal conduction. This is because the large fracture-to-fracture interface areas specified in the dual-permeability grids are for fluid flow and do not apply to heat conduction. In addition, heat conduction in global fracture-to-fracture connections was much smaller than matrix-to-matrix connections or advection through fractures in the same domain because of the small areas of fracture-to-fracture connections in the unsaturated zone.

### 8.10.8.2.5 Infiltration

Distributions of net infiltration flux input to the upper layer of the thermohydrologic model were derived from the distributions calculated by the infiltration model (Section 8.2.10) and then interpolated onto the thermohydrologic model numerical grid (CRWMS M&O 2000i, Section 6.6, p. 42). The accuracy with which the infiltration data was mapped onto the numerical grid depended on the grid resolution at the upper boundary. The higher grid resolution used in the NS#2 cross-section grid not only better resolved the infiltration patterns, but also provided vertical flow paths for percolation between drifts. Evaluation of the extent of this bypass flow is important for TSPA because the fluid displaced by heat at the drifts will condense and drain between the drifts. A coarse grid with a continuous heat source cannot simulate such phenomena.

The following infiltration scenarios were used in the thermohydrologic model (CRWMS M&O 2000i, Section 6.7, p. 43):

- Mean present-day infiltration was used for the base case with no ventilation and for 0 to 600 yr. in ventilated and nonventilated climate-change scenarios.
- Mean monsoon infiltration was used for 600 to 2,000 yr. in ventilated and nonventilated climate-change scenarios.
- Mean glacial-transition infiltration was used for more than 2 k.y. in ventilated and nonventilated climate-change scenarios.

In the thermohydrologic model, infiltration flux was applied as a constant-mass injection of water to the fracture continuum at the upper boundary of the model (CRWMS M&O 2000i, Section 6.6, p. 42). For the nonisothermal simulations, a constant enthalpy of 75.6 kJ/kg, corresponding to pure water at 15°C was assigned. Because of the proximity of the infiltration nodes to the upper boundary of the thermohydrologic model, at which temperature was held constant, the temperature in the infiltration nodes was controlled by the boundary temperature and not by temperature of the infiltration fluid.

### 8.10.8.3 Simulations Performed with the Mountain-Scale Coupled Thermohydrologic Model and Associated Submodels

Six numerical simulations were performed to investigate mountain-scale thermohydrologic processes in the unsaturated zone under thermal loading (CRWMS M&O 2000i, Section 6.7, p. 4, Table 5). Two three-dimensional simulations were performed using the repository area submodel (Figure 8.10-32) under mean present-day infiltration, the 0.018-kW/m<sup>2</sup> (72.7-kW/a.) thermal load, no discrete drifts, and no ventilation. The only difference between the two three-dimensional simulations was that in one the lower temperature boundary was placed 1,000 m (3,300 ft) below the water table and in the other it was placed at the water table. Four additional two-dimensional simulations were performed, two along each of the two north-south cross sections shown in Figure 8.10-32. The two simulations performed along cross section NS#1 included mean present-day infiltration, the 0.018-kW/m<sup>2</sup> (72.7-kW/a.) thermal load, no ventilation, and the lower temperature boundary at 1,000 m (3,300 ft) below the water table. The difference between the two NS#1 cross-section simulations was that one did not include discrete

drifts, whereas the other used the locally refined numerical grid that allowed simulation of discrete drifts and individual heat sources. Both of the NS#2 cross-section simulations included discrete drifts, sequencing of infiltration scenarios as described in Section 8.10.8.2.5, the  $0.018\text{-kW/m}^2$  ( $72.7\text{-kW/a.}$ ) thermal load, and the deep temperature boundary. The difference between the two NS#2 cross-section simulations was that one did not include ventilation and one did. These simulations of the nonisothermal fluid and heat flow were conducted for a total thermal-loading period of 100 k.y. (CRWMS M&O 2000i, Section 6.8.1, p. 44). This sequence of three-dimensional and two-dimensional simulations allowed investigation of the effect of important thermohydrologic factors (lower temperature boundary, type of heat source, infiltration scenario, and ventilation) by way of similar but progressively complex simulations.

### 8.10.8.3.1 Results of Three-Dimensional Thermohydrologic Simulations

Figure 8.10-35 shows the distribution of temperature resulting from the three-dimensional repository area submodel simulation along cross section NS#1 after 500 yr. This simulation included mean present-day infiltration, the  $0.018\text{-kW/m}^2$  ( $72.7\text{-kW/a.}$ ) thermal load, no discrete drifts, no ventilation, and the lower temperature boundary at 1,000 m (3,300 ft) below the water table (CRWMS M&O 2000i, Section 6.8.1, p.44). The plot indicates that extensive boiling was predicted only in the area at and immediately above the potential repository horizon (CRWMS M&O 2000i, Section 6.8.2.1, p.44). The three-dimensional model predicted that temperatures at the repository horizon rise to boiling conditions ( $97^\circ\text{C}$ ) in about 10 yr. The boiling may take place in localized horizons, with heat-pipe conditions developing and being maintained for more than 100 yr. Beyond 100 yr., the temperatures at the repository were predicted to decline. For example, at reference location #1 (Figure 8.10-32), simulation results indicate that the temperature declines from  $97^\circ$  to  $77^\circ\text{C}$  after 2 k.y. and that in areas 100 m (330 ft) or more outside the potential repository, no boiling was predicted. Furthermore, the predicted maximum temperature was  $37^\circ\text{C}$  at 100 m (330 ft) outside the northern boundary, and is about  $40^\circ\text{C}$  at 100 m (330 ft) outside the eastern boundary. This response confirms convection-dominated processes both within and outside the repository area, controlled by boiling and high fracture permeability inside the repository area and by high fracture permeability and ambient infiltration flux outside of the repository boundaries. Also, the predicted maximum temperature on top of the CHn unit was  $70^\circ\text{C}$ , resulting in little potential for temperature-induced mineralogical changes within that unit.

Because of the coarse grid blocks and no explicit representation of the drifts in the three-dimensional thermohydrologic simulations, the simulation results indicated very little change in matrix saturation under this thermal-load scenario (CRWMS M&O 2000i, Section 6.8.2.1, p. 45). Therefore, no large local mobilization of liquid or vapor existed even in those grid blocks with heat generated from the emplaced waste, except in a few columns where local ambient infiltration was low (less than  $1.0\text{ mm/yr.}$ ). Consequently, the three-dimensional model did not predict extensive dryout zones or zero matrix saturation at any location within the model domain.

Nevertheless, as the repository temperature reaches boiling conditions, rapid vaporization and strong gas flow occurred within the fracture network at the repository, which reduced liquid saturation (CRWMS M&O 2000i, Section 6.8.2.1, p. 50). The lower saturation in the fractures at the repository created a sufficient capillary gradient that promoted liquid back flow into the

repository and, therefore, increased percolation fluxes in those areas. This phenomenon is demonstrated clearly by simulated changes in fracture liquid flux over time at the potential repository horizon along cross section NS#1 (Figure 8.10-36). Figure 8.10-36 shows that fracture liquid percolation flux increased significantly at the repository horizon because of changes in fracture saturation from boiling and condensation. At the center of the repository, the simulation predicts a maximum flux of 75 mm/yr. (20 times higher than the ambient flux) at 50 yr. However, the flux reduced to less than 10 mm/yr. at 500 yr. and to near-ambient conditions at 1 k.y. Simulation results indicate no significant changes in the percolation flux outside the repository.

Results of the second three-dimensional thermohydrologic simulation, in which the lower temperature boundary was placed at the water table, indicated that distributions of saturation and flux were very similar to those for the three-dimensional simulation with the lower temperature boundary 1,000 m (3,300 ft) below the water table (CRWMS M&O 2000i, Section 6.8.2.2, p. 54). Thus, it was apparent that placement of the lower temperature boundary had little effect on saturation and flux because the boiling zones generated at the repository are small and far away from the lower temperature boundary. Although simulated temperatures above the repository were nearly the same as in the first simulation, below the repository temperatures were strongly influenced by the fixed temperature boundary at the water table. Consequently, all subsequent thermohydrologic simulations were performed with the lower temperature boundary placed 1,000 m (3,300 ft) below the water table.

#### **8.10.8.3.2 Results of Two-Dimensional Thermohydrologic Simulations**

Although four two-dimensional cross-section thermohydrologic simulations were performed, only two of them are described here for simplicity. More detailed information about the other two simulations can be found in CRWMS M&O (2000i, Sections 6.10, 6.11, pp. 59 to 88).

The second two-dimensional simulation, oriented along cross section NS#1, simulates the same conditions as the first three-dimensional simulation (mean present-day infiltration,  $0.018\text{-kW/m}^2$  (72.7-kW/a.) thermal load, no ventilation, and the deeper temperature boundary) except that it used a locally refined 5-m (16-ft) drift element within the repository area. The denser grid in the repository area provided better resolution of temperature, saturation, and flux because it has two elements between each of the drift elements (CRWMS M&O 2000i, Section 6.10.2, p. 64). Figure 8.10-37 shows simulated temperatures along cross section NS#1 after 500 yr. of thermal load. The figure shows that boiling conditions occurred mainly above the repository, which is at an elevation of about 1,100 m (3,600 ft). This simulation shows more temperature spikes laterally across the repository area than the three-dimensional simulation (Figure 8.10-35) because of greater resolution of spatial variations in infiltration. Simulated temperatures at reference location #1 (Figure 8.10-32) in the center of the repository exceeded  $103^\circ\text{C}$  after 50 yr., compared to  $97^\circ\text{C}$  for the simulation without explicit representation of the drifts. At the repository, the simulation resulted in local peak temperatures exceeding  $150^\circ\text{C}$  after 100 yr. in completely dried-out zones (Figure 8.10-38). Beyond 500 yr., temperatures began to decline and were down to  $90^\circ\text{C}$  after 2 k.y., while temperatures outside the repository quickly dropped to near-ambient conditions. However, because the two-dimensional simulation cannot account for heat conduction in the third dimension (perpendicular to the line of the cross section), it probably overestimated thermal buildup compared to the three-dimensional simulation, which indicated a

temperature of 77°C at the repository after 2 k.y. yr. At the water table, the predicted maximum temperature was about 70°C.

Results of the second two-dimensional simulation indicated significant changes in matrix liquid saturation only near the repository after 500 and 1,000 yr. of thermal loading (CRWMS M&O 2000i, Section 6.10.2). The simulation resulted in significant decreases in matrix liquid saturation in the vicinity of the repository drifts, but only a few drift elements became completely dry between 10 and 50 yr. However, all fractures within the repository volume were completely dry within the first few years of thermal loading.

Percolation fluxes calculated by the second two-dimensional simulation along the repository horizon were much higher in the vicinity of the drifts than predicted by the three-dimensional simulations because of high capillary suction created at dry zones (CRWMS M&O 2000i, Section 6.10.2). In the middle of the repository at location #1 (Figure 8.10-32), maximum flux exceeded 200 mm/yr. after 5 yr. and declined to less than 30 mm/yr. after 100 yr. Liquid flux from fractures into drifts quickly rose to more than 1,000 mm/yr. after 10 yr., but dropped to zero as the fractures became completely dry (Figure 8.10-39). The matrix flux at the repository for the same period rose to a maximum of about 200 mm/yr. at the drifts, but stayed at ambient conditions in the regions between the drifts.

The last two two-dimensional simulations were conducted along cross section NS#2 and included all three infiltration scenarios, as described in Section 8.10.8.2.5. One of these simulations included mechanical ventilation of the potential repository for the first 50 yr., with an efficiency of 70 percent, and the other did not. Figure 8.10-40 shows the temperature along cross section NS#2 after 500 yr. of thermal load and ventilation. Even with ventilation, simulation results indicate that a two-phase heat-pipe region has developed at the repository horizon, but it has been limited to within a few meters above the potential repository (CRWMS M&O 2000i, Section 6.11.2). However, the simulation indicated much lower elevated temperatures with ventilation than without ventilation. The thermal load from the wastes in the potential repository raised temperatures in the unsaturated zone only immediately above and below the repository. Zones at about 100 m (330 ft) from the northern and southern ends of the repository area had a maximum temperature rise of only 10° to 15°C during the thermal-loading period. Areas more than 200 m (660 ft) from the edges of the repository remained at near-ambient thermal conditions throughout the thermal-loading period. After the 50 yr. of ventilation, average temperatures within the central part of the repository area rose to the boiling point, although in a few locations temperatures were above 110°C (Figure 8.10-41). Simulation results indicate that although local temperature within the drift would rise to the boiling point, temperatures in the rock mass between the drifts would rise to only 90°C and no boiling was predicted.

With ventilation, simulation results indicated that significant drying, as evidenced by matrix liquid saturation, occurred only at or near the repository (CRWMS M&O 2000i, Section 6.11.2). Results indicated that completely dry conditions were created in few drift elements that were under areas of low surface infiltration. The saturation in several drifts with high ambient infiltration remained above 90 percent, probably due in part to onset of the monsoon climate conditions. After 5 k.y., matrix liquid saturation recovered to the ambient conditions of the glacial transition infiltration climate that was in place by that time.

Simulation results indicated that percolation fluxes were much lower with ventilation than without ventilation (CRWMS M&O 2000i, Section 6.11.2). Results indicated that at location #1 (Figure 8.10-32) near the potential repository, the percolation flux reached a maximum of about 58 mm/yr. after 10 yr. (CRWMS M&O 2000i, Figure 67). Within the potential repository, maximum fracture fluxes were 270 to 300 mm/yr. after 10 yr. and decreased to less than 10 mm/yr. after 100 yr. (Figure 8.10-42). The flux then increased to more than 150 mm/yr. at 500 yr. as a result of increased heating after ventilation ceased. After 1 k.y., the fracture flux decreased to values equivalent to surface infiltration. The fracture flux between the drifts remained above ambient conditions throughout the thermal-loading period, rising to 15 to 20 mm/yr. (about two to three times the ambient flux) at 500 yr. due to condensate drainage. After 500 yr., the fracture flux between the drifts rose due to the high ambient infiltration during the monsoon and glacial transition climates.

### 8.10.8.3.3 Summary of Thermohydrologic Simulations

In both three-dimensional and two-dimensional simulations, when the thermal load was applied as a continuous, smeared heat source over the repository block (without ventilation), the simulated distributions of temperature were very similar (CRWMS M&O 2000i, Section 7). Significant differences in the simulated temperature profiles between the two types of simulations occur only at the center of the repository horizon. The three-dimensional simulation simulated more rapid cooling at the end of the boiling period than the two-dimensional simulation because of lateral heat conduction into the third dimension. After 2 k.y., the simulated temperature at the repository was 77°C in the three-dimensional simulation compared to 92°C in the two-dimensional simulation. The simulated maximum temperature at the water table was 70°C in both types of simulations for the scenario of current thermal-loading, mean present-day infiltration, and no ventilation.

In the two-dimensional simulations without ventilation, heat-pipe conditions developed in a region above the repository during 10 to 100 yr. (CRWMS M&O 2000i, Section 7). Complete dryout conditions were predicted near the drifts, mainly within fracture elements, with drift temperatures exceeding 100°C for hundreds of years. In the rock mass between the drifts, temperatures may rise to boiling conditions and saturation may be reduced slightly. No complete dryout conditions were predicted between the drifts except in zones under low surface infiltration. The flux into the drifts may exceed 1,200 mm/yr., particularly in the low infiltration areas due to drier conditions and consequentially high capillary-pressure gradients. However, the high percolation fluxes were predicted to occur only at early times (less than 100 yr.). The two-dimensional simulations indicated that although vertical flux between the drifts will continue at a rate close to the ambient percolation fluxes for most of the thermal-loading period, this flux may be enhanced by condensate drainage for the first 1 k.y. of thermal load.

According to the model results, thermal loading at the repository will result in significant changes in the temperature conditions and moisture distribution at the repository, as well as the zone directly above and below the repository (CRWMS M&O 2000i, Section 7). Without ventilation, strong liquid and gas flow fields will develop in the fracture network. Two-phase heat-pipe conditions will occur only above the repository, in a region extending up to 200 m (660 ft) to the base of the PTn stratigraphic unit. These conditions will occur between 500 and 1,000 yr. Complete dryout of both the fracture and matrix continua at the repository will develop

over the first 100 yr. Recovery to the ambient saturation was predicted to occur during 500 to 5,000 yr.

Model results indicated that localized dryout of the matrix at the repository and in areas with low infiltration rates will occur even with ventilation (CRWMS M&O 2000i, Section 7). Temperatures may be elevated to approximately 250°C within the completely dry drifts when no ventilation is implemented, and most of the repository will remain at boiling temperature (about 97°C) for nearly 1 k.y. When ventilation is employed, only localized boiling at the drifts was predicted.

Without ventilation and with present-day mean infiltration for the entire thermal-loading period, simulations indicated 30° to 35°C increases in temperature at the water table to an average of 70°C (CRWMS M&O 2000i, Section 7). With ventilation and the change to monsoon and glacial transition climate conditions, the predicted maximum temperature at the water table was about 65°C. At the top of the CHn stratigraphic unit, the predicted maximum temperature was 75° to 80°C for a period of between 2 and 7 k.y.

Even with ventilation, the models predicted a zone with substantial changes in matrix liquid saturation that extends about 50 m below and above the potential repository horizon (CRWMS M&O 2000i, Section 7). In the two-dimensional simulations, surface infiltration rates resulting from monsoon and glacial transition climates have little impact on the duration and extent of boiling zones at the repository. However, beyond 2 k.y., the higher percolation rates resulting from the two wetter climates were predicted to accelerate the processes of cooling and resaturation and elevate the ambient percolation flux.

#### **8.10.9 Drift-Scale Coupled Thermohydrologic-Chemical Seepage Models**

Drift-scale models of the near-field environment of the potential repository in the unsaturated zone at Yucca Mountain were developed to evaluate the potential effects of coupled thermohydrologic-chemical processes on unsaturated zone flow and transport (CRWMS M&O 2000j, p. 13; Section 1). These models include the Drift Scale Test thermohydrologic-chemical model and the thermohydrologic-chemical seepage model. These models provide the framework to evaluate thermohydrologic-chemical coupled processes at the drift scale, predict flow and transport behavior for specified thermal-loading conditions, and predict the chemistry of waters and gases entering potential emplacement drifts. The Drift Scale Test thermohydrologic-chemical model was used to predict thermohydrologic-chemical processes prior to and during the Drift Scale Test. Measured data from the Drift Scale Test were used to evaluate the conceptual and numerical models. The iterative approach of evaluating, refining, and comparing the Drift Scale Test numerical model against measured data was performed throughout the Drift Scale Test study. The thermohydrologic-chemical seepage model provides an analysis of the effects of thermohydrologic-chemical processes in the near-field host rock surrounding the potential emplacement drifts on the seepage water chemistry and gas-phase composition. The thermohydrologic-chemical analysis included a detailed investigation of pertinent mineral-water processes in the host rock and their effects on the near-field environment. The model was used to evaluate the effects of mineral dissolution and precipitation, the effects of CO<sub>2</sub> exsolution and transport in the region surrounding the drift, the potential for forming calcite, silica, or other

mineral assemblage precipitation caps, and the resulting changes in porosity, permeability, and seepage.

The thermohydrologic-chemical seepage model was developed with data for a specific hydrogeologic unit, the Topopah Spring crystal-poor, middle nonlithophysal unit (Tptpmn), in which part of the potential repository would be sited (CRWMS M&O 2000j, p. 13, Section 1). Although many aspects of the model are applicable to other host rock units of the potential repository, differences in the mineralogy, geochemistry, and thermohydrologic properties must be considered before the results are directly applied elsewhere in the potential repository. The model used a dual permeability continuum approach with limited initial heterogeneity and was meant to represent the overall changes in space and time. Therefore, it cannot be applied with certainty at a specific location.

#### **8.10.9.1 Data Sources and Software for the Drift-Scale Coupled Thermohydrologic-Chemical Seepage Models**

Data sources for development and application of the drift-scale thermohydrologic-chemical models are documented in CRWMS M&O (2000j, Section 4.1, pp. 19 to 26, Table 2). Primary input data used for the thermohydrologic-chemical models include the following:

- Hydrologic and thermal rock properties
- Mineralogical data
- Water and gas chemistry data
- Repository drift design and thermal-load data
- Seepage model grid data.

Hydrologic and thermal rock properties included the calibrated properties sets for matrix and fractures (Section 8.10.5); uncalibrated properties, such as porosity, heat capacity, and thermal conductivity; and infiltration rates from the infiltration model (Section 8.2.10). Mineralogical data were specific to the geologic units encountered in borehole USW SD-9 (the borehole closest to the drift-scale thermal test) and in host rocks of ESF Alcove 5 where the test was located (CRWMS M&O 2000j, Section 4.1.2, p. 19). Mineralogical data were input as volume fractions of a given mineral per total solid volume, and as reactive surface areas. Other mineralogical data included mineral stoichiometries, mass densities, grain size, and fracture-matrix surface area. Initial water-chemistry data were derived from two pore-water samples obtained from the Tptpmn in Alcove 5 near the Drift Scale Test (CRWMS M&O 2000j, Section 4.1.3, p. 21). The initial CO<sub>2</sub> partial pressure in fractures and matrix was calculated as the partial pressure in chemical equilibrium with the initial pore-water at 25°C, assuming ideal gas behavior. Thermodynamic data included dissociation constants for aqueous species, minerals, and CO<sub>2</sub> gas as a function of temperature taken primarily from the EQ3/6 version 7.2b database (CRWMS M&O 2000j, Section 4.1.4, p. 22). Other thermodynamic data included molecular weights, molar volumes, and parameters used for calculation of activity coefficients for aqueous species. Kinetic data included reaction-rate constants, activation energies, and related data required to describe the rates of dissolution and precipitation of minerals at different temperatures and fluid chemistries (CRWMS M&O 2000j, Section 4.1.5, p. 22). Transport parameters considered in the thermohydrologic-chemical models include diffusion coefficients for aqueous and gaseous species and tortuosities of the fracture, matrix, and engineered system

components (CRWMS M&O 2000j, Section 4.1.6). Diffusion coefficients for all aqueous species were assumed to be equal to the tracer diffusion coefficient of chlorine at infinite dilution.

Development of the two-dimensional numerical meshes for the thermohydrologic-chemical models was dependent on the drift, including drift diameter, concrete invert, bulkhead, and insulation and location of wing heaters (CRWMS M&O 2000j, Section 4.1.7.1, p. 25). Two time periods were considered in the drift design and related data input into the model (CRWMS M&O 2000j, Section 4.1.7.2, p. 25):

- A 50-yr. preclosure period during which 70 percent of the heat released by the waste packages is removed by ventilation
- A postclosure period immediately following the initial 50-yr. preclosure period and extending to 100 k.y., during which a drip shield and backfill are above the waste packages and no heat is removed by ventilation.

The thermohydrologic-chemical seepage model also required an array of data relative to drift geometry and thermal-physical properties of design elements, such as waste packages and backfill (CRWMS M&O 2000j, Table 5). The initial heat transfer from the waste package used in the thermohydrologic-chemical seepage model was 1.54 kW/m of drift and decays with time to 0.187 kW/m at 50 yr., and less than 0.003 kW/m after 1 k.y. For the simulated first 50 yr., only 30 percent of this heat was input into the model to account for 70 percent heat removal by ventilation.

Computer software items used in the development of the thermohydrologic-chemical model are described in CRWMS M&O (2000j, pp. 17 and 18, Section 3, Table 1). TOUGHREACT, version 2.2, was the primary code used in the Drift Scale Test thermohydrologic-chemical and thermohydrologic-chemical seepage models. The codes SOLVEQ/CHILLER, version 1.0, were used to perform supporting computations for the models. SUPCRT92, version 1.0, was used to generate thermodynamic databases for use by SOLVEQ/CHILLER and TOUGHREACT. The code TOUGH2, version 1.4, was used to generate hydrologic and pneumatic boundary conditions. The code AMESH, version 1.0, was used to generate grids for TOUGH2 and TOUGHREACT.

#### **8.10.9.2 Drift-Scale Thermohydrologic-Chemical Conceptual Model**

The Drift Scale Test thermohydrologic-chemical and thermohydrologic-chemical seepage numerical models considered a number of physical and chemical processes. These include liquid and vapor flow, heat transport and thermal effects due to boiling and condensation, transport of aqueous and gaseous species, mineralogical characteristics and changes, and aqueous and gaseous chemistry (CRWMS M&O 2000j, Section 6.1, p. 33). In addition, the models also considered reaction-transport processes in the fractured welded tuffs of the potential repository host rock and the different rates of transport in very permeable fractures, compared to the much less permeable rock matrix. Transport rates greater than the rate of diffusion can lead to chemical disequilibrium between waters in fractures and matrix (CRWMS M&O 2000j, Section 6.1.1). This can lead to differences in the stable mineral assemblage and in reaction rates.

Because the repository system is unsaturated and undergoes boiling, the transport of gaseous species also was an important consideration in the model. Therefore, the thermohydrologic-chemical models must capture the differences between initial mineralogy in fractures and matrix and their evolution. To account for these separate yet interacting processes in fractures and matrix, the dual permeability formulation was used for developing the thermohydrologic-chemical models. In this method, each grid block is separated into a matrix and fracture continuum, each of which is characterized by its own pressure, temperature, liquid saturation, water and gas chemistry, and mineralogy.

The geochemical module incorporated in TOUGHREACT, version 2.2, solves simultaneously a set of chemical mass-action, kinetic rate expressions for mineral dissolution-precipitation, and mass-balance equations (CRWMS M&O 2000j, Section 6.1.3, p. 35). This provides the extent of reaction and mass transfer between a set of given aqueous species, minerals, and gases at each grid block of the flow model. Equations for heat, liquid and gas flow, aqueous and gaseous species transport, chemical reactions, and permeability-porosity changes are solved sequentially. Additional provisions are made for mineral dissolution and precipitation under kinetic constraints and a volume-dependent formulation for gas equilibrium. The chemical system is described in terms of primary aqueous species (the independent variables). Minerals, gases, and secondary aqueous species are defined in terms of reactions involving only the primary species. It has been shown that if the diffusivities of all aqueous species are equal, only the transport of primary species (in terms of total dissolved concentrations) needs to be considered to solve the entire reactive flow-transport problem.

In consideration of fracture surface areas for mineral reaction using the dual-permeability method, the porosity of the fracture medium could be taken as 1.0 (CRWMS M&O 2000j, Section 6.1.5.1, p. 38). However, in using this value for modeling of mineral dissolution and precipitation, there would be no rock to be dissolved by percolating water. Because the dissolution rates of many minerals are quite small at temperatures below 100°C, only a small volume of rock adjoining the open space of a fracture needs to be considered as the starting rock fraction. Therefore, the porosity of the fracture medium was set to 0.99, making 1 percent of the total fracture volume available for reaction, but producing a minimal effect on flow and transport in the fracture continuum. Reactive surface areas of minerals on fracture walls were calculated from the fracture-matrix interface area-volume ratio, the fracture porosity, and the derived mineral volume fractions. The fracture-matrix interface areas and fracture porosities for each unit were taken from the calibrated properties set (Section 8.10.5). These areas were based on the fracture densities, fracture porosities, and mean fracture diameter. The wall of the fracture was treated as a surface covered by mineral grains halving the form of uniform hemispheres. At a very low liquid saturation, the surface area of the rock contacted by water likely is much smaller than the total area. Two methods were implemented to address this phenomenon. The first method considers that the surface area contacted by water diminishes proportionately to the saturation. The second method employs the active-fracture-model concept (Section 8.10.3.6) with a modification for the consideration of water-rock reactions taking place below the residual saturation.

Mineral surface areas in the rock matrix were calculated using the geometric area of a cubic array of truncated spheres that make up the framework of the rock (CRWMS M&O 2000j, p. 40, Section 6.1.5.2). Clay minerals were considered as coatings of plate-like grains. The mineral

surface areas of framework grains (truncated spheres) in contact with the open pore space were calculated using an initial grain diameter, followed by successive truncation of the grains in the vertical direction until the porosity of this system is close to the measured porosity of the rock. In the welded tuff, crystals are often tightly intergrown with little or no pore space within the aggregate. Thus, a check was made so that the resultant, mean pore-throat size and spacing yields a permeability that is relatively close to the measured saturated permeability. The grains forming the framework of this rock were considered to be the primary high-temperature phases of the tuff (quartz, cristobalite, tridymite, and feldspars). The abundance of secondary phases that formed as alteration products or low temperature coatings on the primary assemblage, such as clay minerals, were used to reduce the free surface area of the framework grains. The surface areas of the secondary phases were calculated assuming a tabular morphology.

The thermohydrologic-chemical conceptual model also considered the effects of mineral precipitation and dissolution on hydrologic properties because changes in porosity and permeability from mineral dissolution and precipitation have the potential to modify percolation fluxes and seepage fluxes at the drift wall (CRWMS M&O 2000j, p. 40, Section 6.1.6.1). In this model, porosity changes in matrix and fractures are directly tied to the volume changes due to mineral precipitation and dissolution. Because the molar volumes of minerals created by hydrolysis reactions (anhydrous phases, such as feldspars, reacting with aqueous fluids to form hydrous minerals, such as zeolites or clays) often are larger than those of the primary reactant minerals, dissolution-precipitation reactions often lead to porosity reductions. These changes were taken into account in the model. Fracture permeability changes were approximated using the porosity change and an assumption of plane parallel fractures of uniform aperture (cubic law). Matrix permeability changes were calculated from changes in porosity using ratios of permeabilities. Changing permeability and porosity also implies changes in the unsaturated flow properties of the rock, which is treated by modifying the calculated capillary pressure using an appropriate scaling relation.

Finally, consistent with the conceptual model, two sets of chemical components and mineral assemblages were used for the simulations for the Drift Scale Test and the thermohydrologic-chemical seepage model (CRWMS M&O 2000j, p. 41, Section 6.1.7, Tables 7 and 8). The first set represents a relatively full set of minerals and aqueous species needed to fully describe the chemistry of the near-field environment. The second set consists of fewer species and minerals, but captures many basic aspects of the Drift Scale Test water and gas chemistry, such as the pH and gas-phase CO<sub>2</sub> concentrations. This more basic set of chemical components also includes the common aqueous ions and common minerals such as calcite, tridymite,  $\alpha$ -cristobalite, quartz, amorphous silica, glass, and gypsum. This second set of chemical components also is called the calcite-silica-gypsum geochemical system.

### **8.10.9.3 Drift Scale Test Thermohydrologic-Chemical Model**

The Drift Scale Test was the second underground thermal test being conducted in the ESF at Yucca Mountain (CRWMS M&O 2000j, p. 43, Section 6.2). The purpose of the test was to evaluate the coupled thermal, hydrological, chemical, and mechanical processes that take place in unsaturated fractured tuff over a range of temperatures from approximately 25° to 200°C. The Drift Scale Test thermohydrologic-chemical model provides an important validation test for the extension of the thermohydrologic-chemical conceptual model to the thermohydrologic-chemical

seepage model. The overall goal of the Drift Scale Test thermohydrologic-chemical model was to gain a better understanding of coupled processes so that thermohydrologic-chemical models can be applied to long-term predictions of near-field thermohydrologic-chemical processes. The Drift Scale Test began with the heating of drift walls in December 1997 with a planned 4-yr. period of heating followed by 4 yr. of cooling (CRWMS M&O 2000j, Section 6.2.1, p. 43). The objectives of the modeling were to make predictions of the coupled thermal, hydrological, and chemical processes brought about by the Drift Scale Test, refine the model as appropriate based on field observations, and then compare model results to measured data. Much of the measured data consisted of hydrochemical analyses of water and gas samples collected from boreholes throughout 1998 and 1999.

#### **8.10.9.3.1 Description of the Drift Scale Test Thermohydrologic-Chemical Model**

The two-dimensional, dual-permeability numerical grid for the Drift Scale Test thermohydrologic-chemical model (Figure 8.10-43) consisted of 4,485 grid blocks, including fracture and matrix (CRWMS M&O 2000j, Section 6.2.2). The grid is oriented on a vertical, planar cross section through the test drift at a distance approximately 30 m (98 ft) from the bulkhead. The grid was designed so that heat could be applied directly to the grid elements representing the drift wall rather than attempting to calculate the heat transfer across the air mass inside the drift.

The most recent calibrated heater-power measurements were used in the model to ensure accurate representation of the actual heating (CRWMS M&O 2000j, p. 45, Section 6.2.3). The Drift Scale Test thermohydrologic-chemical model simulated a 9-mo. period of preheat ventilation at ambient temperature followed by 21 mo. of heating at full power, together representing actual heating history to early September 1999. The remainder of the heating scenario consisted of a 10 percent power reduction for each of the next 4 mo., continuous heating at 60 percent of full power until 4 yr. after initiation of heating, and 4 yr. of cooling. Only the model results up to September 1999 were used for validating the thermohydrologic-chemical conceptual model because this was the period for which hydrochemical data had been collected.

The upper boundary of the Drift Scale Test thermohydrologic-chemical model was approximately 99 m (330 ft) above the drift center, with the lower boundary at approximately 157 m (515 ft) below the drift center (CRWMS M&O 2000j, p. 45, Section 6.2.4). The upper and lower boundaries were set to constant temperature, pressure, and liquid saturation based on steady-state values obtained from simulations of a one-dimensional column extending from the land surface to the water table. These values were obtained using the calibrated drift-scale hydrologic parameter set for the present-day mean infiltration of approximately 1.05 mm/yr., at the location of the drift. The side boundaries of the model were considered as no-flux boundaries and were 81.5 m (267 ft) away from the drift center on each side. The air pressure and temperature in the observation drift were set to constant values and, therefore, did not reflect temporal fluctuations in barometric pressure or tunnel air temperatures. The heater drift wall was open to advection and conduction of heat and mass and vapor diffusion.

The upper and lower boundaries were set as constant-concentration boundaries that are subject to aqueous and gaseous species transport but no mineral reactions (CRWMS M&O 2000j, p. 45, Section 6.2.5). Their volumes were set to extremely large values so that they act essentially as

constant concentration boundaries. Initial concentrations for all aqueous and gaseous species were uniformly set except for the heater drift, alcove, and observation drift whose CO<sub>2</sub> concentrations were set to approximately that of the atmosphere. In the model, CO<sub>2</sub> concentrations in the alcove and observation drift were kept essentially constant, but the heater drift was allowed to exchange CO<sub>2</sub> between the rock and the observation drift. The side boundaries were treated as no-flux to advection and diffusion.

Two main sources of data were used for comparison to simulation results: (1) aqueous species concentrations and pH for water samples collected from hydrology boreholes, and (2) gas-phase CO<sub>2</sub> concentrations and stable isotopic ratios from gas samples collected from the same boreholes (CRWMS M&O 2000j, p. 46, Section 6.2.6). For the gas-phase compositions, direct comparisons of model results were made only to CO<sub>2</sub> concentrations. The observation drift and the hydrology boreholes from which hydrochemical samples were collected are shown in Figure 8.10-43.

### 8.10.9.3.2 Drift Scale Test Thermohydrologic-Chemical Model Results and Validation

**Thermohydrology Evolution**—The thermal and hydrologic evolution of the Drift Scale Test is illustrated by the results of the Drift Scale Test thermohydrologic-chemical model after 20 mo. of heating (Figure 8.10-44). The strong thermal load applied to the system resulted in changes in temperature, liquid saturation, and gas-phase compositions, which in turn caused changes in the chemistry of the system (CRWMS M&O 2000j, p. 46, Section 6.2.7.1). Simulated distributions of temperature and liquid saturation (Figures 8.10-44a to 8.10-44d) show that the zone of dryout increased between 12 and 20 mo., and a wider separation between the 90° and 100°C isotherms at 20 mo. indicates the presence of a boiling-condensation zone, especially above the wing heaters at the sides of the test drift. Large predicted drainage zones are apparent in the fractures below the heaters after 20 mo. (Figures 8.10-44d). The simulated buildup of water above the heaters was fairly localized, but moved up into the region of the upper hydrology boreholes after 20 mo. of heating. The temperature and liquid-saturation trends simulated here agree well with those calculated with the three dimensional thermohydrologic model of the Drift Scale Test (CRWMS M&O 2000r, Section 6.1.2), which themselves have been shown to agree with observed data (CRWMS M&O 2000r, Sections 6.22 and 6.4.2). As noted in Section 8.10.8.3.3, temperatures predicted by the two-dimensional model tend to be somewhat higher than for a three-dimensional model of the real system because there is no heat loss in the third dimension. Therefore, this model is most applicable to areas near the center of the test, away from bulkhead, or end of the heater drift.

**Gas-Phase CO<sub>2</sub> Evolution**—To evaluate gas-phase CO<sub>2</sub> evolution during the Drift Scale Test, CO<sub>2</sub> concentrations measured in gas samples taken from the hydrology boreholes (Figure 8.10-43) were compared to simulation results from the Drift Scale Test thermohydrologic-chemical model (CRWMS M&O 2000j, p. 48, Section 6.2.7.2). Changes in gas-phase CO<sub>2</sub> concentrations under the thermal regime of the Drift Scale Test are very important because they are sensitive to temperature and strongly influence the pH of condensate waters. Furthermore, CO<sub>2</sub> transport is sensitive to fracture hydrologic properties and affects bicarbonate concentrations in fracture waters, which are important for the in-drift geochemical environment. Simulated distributions of CO<sub>2</sub> concentrations and temperature in the fractures and matrix for the calcite-silica-gypsum geochemical system after 15 and 20 mo. of heating are

shown in Figure 8.10-45. The simulation showed that as early as 6 mo. into the heating phase of the test, a halo (dark blue, oval-shaped band) of increased CO<sub>2</sub> concentrations focused in both the fractures and the matrix centered approximately at the 60°C isotherm. The model predicted that between 6 and 20 months of the heating phase, the halo increased considerably in extent and magnitude of concentration. Maximum CO<sub>2</sub> concentrations were located above and below the wing heaters and below the heater drift itself. In a region between approximately the 90° and 100°C isotherms modeled fracture CO<sub>2</sub> concentrations decreased to approximately 1,000 ppmv but matrix concentrations are still elevated. This region encompasses an isothermal, boiling zone, as evidenced by the wider space between the simulated 90° and 100°C isotherms compared to adjacent lower and higher temperature contours. More rapid boiling in the matrix led to higher partial pressures of CO<sub>2</sub> relative to the dry or nearly dry fractures. Within the dryout zone close to the drift and wing heaters, simulated CO<sub>2</sub> concentrations decreased markedly in both fractures and matrix.

To evaluate the predictions of the Drift Scale Test thermohydrologic-chemical model, measured CO<sub>2</sub> concentrations from borehole intervals that were repeatedly sampled from February 1998 to August 1999 were compared to model results for the same times (CRWMS M&O 2000j, Section 6.2.7.2). Because the concentrations were measured from borehole intervals that are several meters long, the model results used for comparison were selected from the grid block that was closest to the center of the interval. If there was no grid block centered on the borehole, a node closest to the center was chosen on the outer (cooler) side of the borehole. Model results for nodes on the cooler side are more comparable to the measured data because the two-dimensional model, not allowing for heat loss in the rock perpendicular to the drift, predicted temperatures that were somewhat higher than the measured temperatures at a given time. Figure 8.10-46 shows the time evolution of CO<sub>2</sub> concentrations in borehole intervals 74-3, 75-3, 76-3, and 78-3. Locations of boreholes are shown in Figure 8.10-43. (Note: In Figure 8.10-43, boreholes are numbered 74 through 78. Solid circles along boreholes show locations of temperature sensors near the end of packed-off borehole intervals. Borehole intervals are numbered sequentially away from the wall of the observation drift). For borehole interval 74-3, the model contained only grid nodes above (cooler side) and below (hotter side) the interval and, therefore, results from both nodes were plotted to see if they bracketed the measured compositions. For borehole interval 78-3, two grid nodes (center and end) were chosen for comparison because of the strong thermal gradient across this region.

Overall, simulated CO<sub>2</sub> concentrations generally follow the trends in measured CO<sub>2</sub> concentrations (until about 12 mo.) (CRWMS M&O 2000j, p. 54, Section 6.2.7.2). One exception was when a heater power loss occurred at about 19 mo., as evidenced by the change in slope of the trend in measured CO<sub>2</sub> concentrations in borehole intervals 74-3 and 75-3 at 20 mo.. A second exception was when gas samples were at boiling temperatures and were nearly all water vapor instead of air and had much of the water condensed out during sampling, as evidenced by the largest peaks for borehole intervals 76-3 and 78-3. In the latter case, the modeling results should diverge from the measured data because they reflect the CO<sub>2</sub> concentration of the full water vapor-air mixture (CRWMS M&O 2000j, p. 57, Section 6.2.7.2).

**Water-Chemistry Evolution**—To evaluate the evolution of water chemistry during the Drift Scale Test, fracture water samples were collected from selected hydrology boreholes in the zone below the wing heaters at about 12 and 13 mo. into the heating cycle (CRWMS M&O 2000j,

p. 60, Section 6.2.7.3.1, Table 9). The fracture water generally was more dilute (lower chloride and sulfate) and lower in pH than the initial pore water. Aqueous silica concentrations were similar to or much higher than in the pore water, indicating that these waters were not simple mixtures of pore water and pure condensate water. Trends in chemistry of the condensate over time included increases in pH and silica concentration and decreases in calcium concentration. Processes that could account for these changes in water chemistry include mixing of condensate water with fracture water, equilibration of condensate with matrix pore water by molecular diffusion, reaction of condensate with fracture-lining minerals, and mineral precipitation due to reaction, boiling, temperature changes, or pH changes. Higher silica concentrations in fracture water over time indicated dissolution of a silicate phase rather than increased concentration by boiling. However, concentrations of potassium, magnesium, and sodium in fracture water were higher than would be expected by dilution of original pore water, as evidenced by the low chloride concentrations. Therefore, the silicate phases that dissolved must have been some combination of cristobalite, opal, feldspar, clays, or zeolites, rather than just a silica phase. The decreases in calcium concentrations over time were consistent with calcite precipitation, which would be expected as the condensate waters were heated further and underwent CO<sub>2</sub> degassing, resulting in an increase in pH.

Although the Drift Scale Test thermohydrologic-chemical model simulated the evolution of numerous aqueous species during the heating cycle (CRWMS M&O 2000j, Section 6.2.7.3.2), changes in pH were indicative of the major hydrochemical trends. Simulated distributions of pH and temperature after 12 and 20 mo. of the heating cycle for the calcite-silica-gypsum geochemical system (Figure 8.10-47) shows a reduction to values of about 6.5 in the condensate region, corresponding directly to the halo of increased CO<sub>2</sub> concentrations in the gaseous system (Figure 8.10-45). As with CO<sub>2</sub> concentrations, the zone of low pH increased in size and moved outward with time. Within the dryout zone, the simulated pH of the last residual water in the fractures reached a maximum of nearly 9.5, although the liquid saturation associated with these values was usually well below residual liquid saturation. The simulated pH of condensate water in fractures compares favorably with that of water collected from the hydrology boreholes.

Simulated variations in chloride were indicative of the effects of dilution through condensation of pure water vapor, of increases in concentration due to boiling, and of the effects of fracture-matrix interaction (CRWMS M&O 2000j, p. 64, Section 6.2.7.3.2). Accordingly, simulated chloride concentrations showed marked decreases in the condensation zone. Differences in simulated chloride concentrations between 12 and 20 mo. indicated slow imbibition of dilute condensate water into the matrix. The simulation showed that at 12 mo., there was a relatively large region of diluted chloride in fractures due to condensation and drainage well below the wing heaters and the heater drift; in the matrix, however, there was little change, except in the dryout zone where the residual waters reached high concentrations at very low liquid saturations. Model results also showed that at 20 mo., the matrix began to show signs of imbibition of fracture waters in the drainage zone and significant dilution effects in the condensate zone as well.

**Mineralogical Changes**—Although mineralogical changes occurred over the course of the Drift Scale Test and strongly influenced water and gas chemistry, the total amount of minerals precipitated or dissolved was very small compared to the available fracture or matrix porosity (CRWMS M&O 2000j, p. 65, Section 6.2.7.4). Over the short duration of the test, model results

indicated that calcite was the most important mineral in terms of its effect on the chemistry of the system and its abundance in the precipitated mineral assemblage. After 20 mo. of heating, the simulation showed that there was a well-defined region of calcite precipitation in the fractures above and to the margins of the heater drift and wing heaters; within the matrix, there was a fairly uniform region of calcite precipitation in the dryout zone. Modeling also indicated that precipitation in the matrix was driven mainly by increasing temperature, whereas in the fractures, there was continuous boiling of condensate water that subsequently drained back to the heat source from cooler regions above. It was predicted that this water would pick up calcium through interaction with calcite and from mixing of ambient fracture water. The continuous process of condensate formation and drainage leads to a well-defined zone of calcite precipitation in the fractures. These results were consistent with the decrease in calcium observed in the condensate water sampled over time.

**Porosity and Permeability Changes**—Results of the Drift Scale Test thermohydrologic-chemical model indicated that changes in porosity and permeability due to mineral dissolution and precipitation were negligible over 20 mo. of heating (CRWMS M&O 2000j, p. 67, Section 6.2.7.5). Total changes in either fracture or matrix porosity were less than 0.1 percent. The greatest change in porosity took place above the heater drift and wing heaters and was due to calcite precipitation.

#### **8.10.9.4 Thermohydrologic-Chemical Seepage Model**

After testing of the Drift Scale Test thermohydrologic-chemical model against actual hydrologic and chemical measurements during the first 21 mo. of the Drift Scale Test, the thermohydrologic-chemical seepage model was developed (CRWMS M&O 2000j, p. 67, Section 6.3). The thermohydrologic-chemical seepage model applied the same methods of simulating coupled thermohydrologic-chemical processes to predict, at a drift scale, the performance of the potential repository during 1 k.y. Thermohydrologic-chemical seepage model simulations were performed in two dimensions along a laterally continuous, vertical geologic section with stratigraphy similar to that in borehole USW SD-9, which is one of the deep boreholes within the footprint of the potential repository (Figure 8.10-2). The simulations consider a potential repository drift located in the Topopah Spring Tuff middle nonlithophysal geologic unit (Ttpmn) corresponding to unsaturated zone flow and transport model layer tsw34 (Table 8.10-1). Only part of the potential repository is planned to be located in the Ttpmn, and therefore the model may not be representative of the entire potential repository. However, most hydrogeologic data available for the potential repository are from the Ttpmn unit, including data from the Single Heater Test, the Drift Scale Test, and many other data collected in the ESF. The use of these data characterizing the Ttpmn was necessary to satisfy model-validation requirements.

##### **8.10.9.4.1 Description of the Thermohydrologic-Chemical Seepage Model**

Simulations were performed on a vertical two-dimensional mesh using a drift spacing of 81 m (270 ft) (center to center) and a drift diameter of 2.75 m (9.02 ft) (CRWMS M&O 2000j, p. 68, Section 6.3.1). With rock properties laterally homogeneous between drifts, this configuration is equivalent to a series of symmetrical, identical, half-drift models with vertical no-flow boundaries between them. Accordingly, the numerical mesh was reduced to a half-drift model

with a width of 40.5 m (133 ft), corresponding to the midpoint between drifts, with the mesh coordinate system referenced to the center of the drift (Figure 8.10-48). The mesh has a total of 2,510 grid blocks, including those representing matrix, fracture, and in-drift design elements. Geologic data from borehole USW SD-9, as implemented in the unsaturated zone flow and transport model calibration grid (Figure 8.10-3), were used as a basis to map geologic contacts into the two-dimensional mesh. The grid block size was kept fine enough to provide sufficient resolution at key model locations, such as the drift wall and geologic contacts, but as coarse as possible elsewhere to provide the computing efficiency needed for reasonable simulation times. The area extending approximately 50 m (160 ft) above the drift was more finely gridded than other areas to capture thermohydrologic-chemical effects potentially affecting seepage into the drift. Outside the drift, the smallest grid spacing was specified at the drift wall 0.20 m (0.66 ft), and increased outward. The drift itself was discretized (338 grid blocks) to include pertinent design elements and dimensions, and the grid-block size inside the drift was chosen to be small enough to provide a realistic drift model. Two drift configurations were considered in the thermohydrologic-chemical seepage model:

- Preclosure configuration: waste package, invert, and one open space between the waste package and the drift wall during the first 50 yr.
- Postclosure configuration: waste package, invert, drip shield, backfill, and two open zones (the inner zone between the waste package and the drip shield and the outer zone between the backfill and drift wall).

Boundary conditions imposed on the thermohydrologic-chemical seepage model were similar to those used in the Drift Scale Test model (Section 8.10.9.3.1) (CRWMS M&O 2000j, p. 72, Section 6.3.2, Table 11) and can be summarized as follows:

- Upper boundary: stepwise changing infiltration rate (Table 8.10-9), temperature, pressure, and gas saturation (representing open atmosphere); constant CO<sub>2</sub> partial pressure and composition of infiltrating water
- Lower boundary: constant temperature, pressure, and liquid saturation (representing the water table); constant, equilibrium water composition and CO<sub>2</sub> partial pressure
- Side boundaries: no heat, fluid, and chemical fluxes
- Waste package: variable heat load with time, including the effects of the 70 percent reduction in waste package heat by ventilation during the 50-yr. preclosure period (Section 8.10.9.1).

Table 8.10-9 indicates the infiltration rates and corresponding rock properties sets used in the thermohydrologic-chemical seepage model simulations (CRWMS M&O 2000j, Section 6.3.2, p. 72, Table 12). The first infiltration case used the ambient, present-day mean infiltration rate at the location of borehole USW SD-9, as estimated by the numerical infiltration model (Section 8.2.10). The other three cases did not use infiltration rates from the infiltration-model results. Instead, the infiltration rates were derived from results of column models of drift-scale thermohydrologic processes generally described in Section 11 and documented in CRWMS M&O (2000b, Table 5-3). Although these infiltration rates used in the thermohydrologic-

chemical seepage simulations follow the same general, climatic trends as the spatially averaged infiltration rates listed in Table 8.2-19 for the potential repository area, the rates are significantly different.

#### **8.10.9.4.2 Thermohydrologic-Chemical Seepage Model Results**

The thermohydrologic-chemical seepage model was run using the same two sets of chemical components and mineral assemblages as used for the Drift Scale Test model simulations (Section 8.10.9.1), the full geochemical system and the calcite-silica-gypsum geochemical system (CRWMS M&O 2000j, p. 74, Section 6.3.4). Simulations were made for both geochemical systems, thermal loading, and the three climate-change infiltration cases listed in Table 8.10-9. For comparison, a pair of simulations also were made for the two geochemical systems using the ambient, present-day, mean infiltration at borehole USW SD-9 with no thermal load. Model simulated temperatures, liquid saturations, water compositions, CO<sub>2</sub> concentrations, and liquid-gas fluxes were examined as a function of time at three locations around the simulated drift (CRWMS M&O 2000j, Section 6.3.5, p. 75). These locations were the crown, the side (approximately 0.20 m [0.66 ft] above the springline), and the base, at points in the rock mass 0.10 m (0.33 ft) outside the drift wall.

**Thermohydrology Evolution**—For comparison to the fully coupled thermohydrologic-chemical simulations, the thermohydrologic-chemical seepage model was run with thermal loading but without reactive transport, thus considering only thermal and hydrological effects (CRWMS M&O 2000j, Section 6.3.5.1, p. 75). This simulation was run using the mean infiltration rates and corresponding rock properties set (Table 8.10-9) and served as a basis for interpreting the effects of water-gas-rock chemical interaction on the thermal and hydrological behavior of the system. Simulation results indicated that temperatures rose quickly above the boiling point (about 97°C at Yucca Mountain) early in the postclosure period, and were higher at the base of the drift where the waste package was closest to the drift wall. The simulated return to ambient temperatures after heating would take 50 to 100 k.y. The modeled maximum temperature in the waste package (about 270°C) occurred at about 55 yr., shortly after closure, whereas the maximum temperature at the drift base was about 190°C (CRWMS M&O 2000j, Figure 20). Around the drift, the rock matrix and most of the fractures were predicted to rewet after 1 to 2 k.y., whereas rewetting of fractures at the drift base did not occur until about 3 k.y. Matrix saturations at a simulated time of 600 yr. (near maximum dryout) indicated that the dryout zone (represented by zero matrix saturations) extended about 10 m (33 ft) above, 17 m (56 ft) to the side, and 22 (72 ft) m below the drift (CRWMS M&O 2000j, Section 6.3.5.1, p. 75, Figure 21). Air mass fractions at the drift wall were predicted to be essentially identical in matrix and fractures and to drop to near-zero values during dryout, meaning that the gas phase was almost entirely water vapor.

The results of the thermohydrologic-chemical seepage model simulation without reactive transport (thermohydrologic simulation) were compared to fully coupled simulations with mean infiltration rates for both the full geochemical system and the calcite-silica-gypsum geochemical system (thermohydrologic-chemical simulations). Temperatures, liquid saturations, and air mass fractions calculated with the thermohydrologic and thermohydrologic-chemical simulations were essentially identical, indicating that the thermal and hydrologic behavior of the system is not

significantly affected by water-gas-rock chemical interactions (CRWMS M&O 2000j, Section 6.3.5.2, pp. 78 and 79).

Simulations of the three climate-change infiltration cases and the full geochemical system indicated that temperatures around the drift did not differ by more than about 15°C among the different infiltration cases (CRWMS M&O 2000j, Section 6.3.5.2, p. 79). The simulations also indicated that the return to ambient temperatures would take about 100 k.y. for all infiltration cases. At the drift crown, rewetting of fractures was predicted to occur at about the same time (1 to 2 k.y.) for all infiltration cases. Matrix rewetting at the drift crown would occur around the same time period as fractures, except for the high infiltration case where the matrix would rewet approximately 200 yr. earlier. Figure 8.10-49 shows simulated temperatures and liquid saturations in the rock matrix for the three infiltration cases after 600 yr., which was the approximate time of maximum dryout. The size of the dryout zone (represented by zero matrix saturations) was smallest for the upper-bound infiltration case and extended about 6 m (20 ft) above, 12 m (39 ft) to the side, and 16 m (52 ft) below the drift. The smaller dryout zone in the lower-bound infiltration case compared to the mean infiltration case apparently was the result of the differing property sets, rather than the infiltration rate. Simulated air mass fractions were little affected by the different infiltration rates.

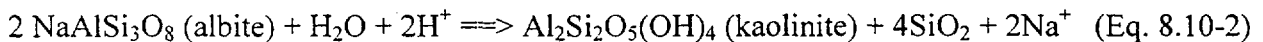
**Gas-Phase CO<sub>2</sub> Evolution**—Simulated CO<sub>2</sub> concentrations in the gas phase of fractures at equilibrium with the fracture water around the drift are shown in Figure 8.10-50 for the full geochemical system. The simulation results indicate that CO<sub>2</sub> concentrations in fractures would drop significantly during the dryout period (about 50 to 2,000 yr.) and then increase again during rewetting (CRWMS M&O 2000j, Section 6.3.5.2). The simulated increase in CO<sub>2</sub> concentration during rewetting probably was caused by heating of the water as it approached the drift wall. For the full geochemical system, the largest CO<sub>2</sub> concentration after rewetting (to about 33,000 ppmv) was predicted to occur in the lower-bound infiltration case. Similar results were obtained from the simulation of the calcite-silica-gypsum geochemical system, except that the largest CO<sub>2</sub> concentration after rewetting (about 12,000 ppmv) was predicted to occur in the upper-bound infiltration case.

**Water-Chemistry Evolution**—The evolution of water chemistry in response to repository heating was evaluated by examining simulated changes in several major aqueous constituents and properties: chloride, fluoride, pH, carbonate, calcium, and sodium (CRWMS M&O 2000j, Section 6.3.5.2). Several of these, along with CO<sub>2</sub>, are important to the dissolution and/or precipitation of minerals such as calcite, feldspar, and calcium-zeolite. Simulated chloride concentrations in fracture water for the full and the calcite-silica-gypsum geochemical systems were essentially identical, due to the conservative behavior of chloride, which is not affected by pH or the reaction rates of mineralogical processes in the simulation. Simulated chloride concentrations generally increased prior to the dryout period (at about 75 yr.), particularly at the drift base (CRWMS M&O 2000j, Figures 38 and 39). Upon rewetting (at about 2 to 3 k.y.), modeled chloride concentrations decreased quickly to below 400 mg/L for all infiltration cases and trended toward ambient values near 110 mg/L. These results indicate that water seeping back into repository drifts after the dryout period will not be significantly more concentrated with chloride than the ambient pore water. Fluoride, which was included only in the full geochemical system simulations, showed similar behavior as chloride. Upon rewetting,

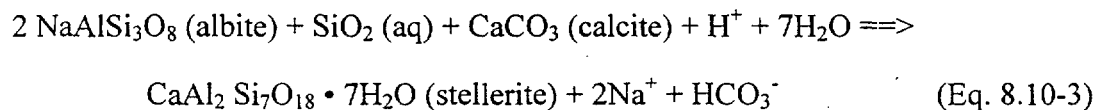
simulated fluoride concentrations in fracture water quickly decreased below 2 mg/L toward ambient values of less than 1 mg/L (CRWMS M&O 2000j, Figure 40).

Simulated pH and total aqueous carbonate concentrations (as bicarbonate) in fracture water showed that the calculated pH generally was higher for the full geochemical system (8.5 to 10) (CRWMS M&O 2000j, Section 6.3.5.2, Figures 30 and 32) than for the calcite-silica-gypsum system, which ranged from 7 to 8.5 (Figures 8.10-51 and 8.10-52). The simulated composition of water reaching the drift wall during rewetting was roughly neutral in pH (7.2 to 8.3) for the calcite-silica-gypsum system and about 8.6 to 9.0 for the full geochemical system. Total aqueous carbonate concentrations predicted were larger for the full geochemical system, reaching a maximum after rewetting of nearly 10,000 mg/L for the lower-bound infiltration case, whereas for the calcite-silica-gypsum system, the simulated maximum concentrations were near ambient values of 200 mg/L after rewetting.

**Mineralogical Changes**—Simulation of the evolution of pH, carbonate, and CO<sub>2</sub> with the thermohydrologic-chemical seepage model was found to be highly dependent on the mineral assembled whether the full and the calcite-silica-gypsum geochemical systems were considered (CRWMS M&O 2000j, Section 6.3.5.2, p. 93). This resulted from competing effects, depending on the relative rates of infiltration, calcite dissolution-precipitation, feldspar dissolution, and calcium-zeolite precipitation. The full geochemical system simulations were quite sensitive to the effective reaction rates of aluminum silicate minerals, particularly calcium zeolites. The dissolution of feldspars to form zeolites and clays directly affected the simulated pH. For example, the dissolution of albite (sodium feldspar) to form kaolinite (clay) resulted in an increase in pH because H<sup>+</sup> was consumed, as follows:



It was found in the simulation that feldspar dissolution also indirectly caused an increase in pH when calcium-rich zeolites precipitated, depleting calcium from solution and destabilizing calcite, as in the following reaction:



As a result, simulations of the full geochemical system, which considered aluminosilicate reactions, generally yielded higher pH and total aqueous carbonate concentrations and lower CO<sub>2</sub> partial pressures than the calcite-silica-gypsum system simulations. Calcium depletion and increased sodium concentrations were further indicators of feldspar (albite) dissolution and calcium-zeolite precipitation in the full geochemical system simulations. These trends were not observed in the calcite-silica-gypsum system simulations. Evidence that the full geochemical system simulations overestimated feldspar dissolution and zeolite precipitation rates also was indicated by the calcium depletion and increasing sodium concentrations calculated under ambient conditions. In addition, the simulations under ambient conditions (no thermal loading) using the full mineral assemblage revealed a chemical system that was less steady than for the calcite-silica-gypsum system simulations. This reflects the model uncertainty with respect to reaction rates and the difficulty in reproducing an initially balanced hydrogeochemical system,

which depends on infiltration rates and rock properties as well as reaction rates. The calibration of the Drift Scale Test model (Section 8.10.9.3.2), indicated that the calcite-silica-gypsum system mineral assemblage provided better estimates of pH and CO<sub>2</sub> concentrations than the full geochemical system assemblage for the first 20 months of heating. However, it also is possible that over longer and more stable periods of boiling and reflux, the system may trend toward the chemistry of the more complex system.

**Porosity and Permeability Changes**—Thermohydrologic-chemical seepage model results indicated that fracture porosity in the vicinity of the drift after 10 k.y. for the three infiltration cases considered would mostly decrease, but by less than 0.5 percent (CRWMS M&O 2000j, Section 6.3.5.2, p. 101, Figures 41, 42). The changes in fracture porosity for the calcite-silica-gypsum geochemical system simulation (Figure 8.10-53) shows that the maximum porosity reduction would occur with the upper-bound infiltration case and was predominantly above the drift, adjacent to the tsw33 and tsw34 hydrogeologic unit contact. The porosity decrease was due primarily to zeolite precipitation in the full geochemical system simulation and calcite precipitation in the calcite-silica-gypsum simulation. Because the simulated porosity changes were very small, permeability changes also were negligible, and thermohydrological processes were not significantly affected by mineral precipitation or dissolution. Thus, based on the results of the thermohydrologic-chemical seepage model using the calcite-silica-gypsum geochemical system, the formation of a mineral cap in the fractures above repository drifts that could effectively divert downward percolation seems unlikely. This conclusion needs to be verified by modeling with the full geochemical system.

**Overall Thermohydrologic-Chemical Seepage Model Results**—Comparison of the results of a purely thermohydrologic simulation to that including coupled thermohydrologic-chemical processes showed virtually no differences in the water and gas fluxes, liquid saturations, porosity, and permeability around the drift (CRWMS M&O 2000j, Section 7, p. 106). Mineral precipitation and dissolution did result in early, localized heterogeneities in the hydrologic properties around the drift, which increased over time. With both geochemical systems, a zone of enhanced mineral precipitation formed at the contact of the Topopah Spring nonwelded and upper lithophysal zones, about 15 to 18 m (49 to 59 ft) above the drift center. With both geochemical cases, silica precipitation was subordinate to calcite or zeolites, therefore confirming the necessity of considering a comprehensive geochemical system to capture the relevant coupled thermohydrologic-chemical processes in the near-field environment. Although the full geochemical system containing aluminosilicates may overestimate the effect of mineral-water reactions on the geochemistry of waters and gases, it may provide a better upper limit on the extent of changes in hydrological properties than the calcite-silica-gypsum geochemical system.

#### **8.10.10 Radionuclide Transport Models under Ambient Conditions**

The unsaturated zone radionuclide transport model of Yucca Mountain and its submodels were developed to evaluate radioactive solute and colloid transport under ambient conditions from the potential repository horizon to the water table (CRWMS M&O 2000l, Section 1, p. 13). The unsaturated zone radionuclide transport models considered:

- Transport of radionuclides through fractured tuffs

- Effects of differences in intensity and configuration of fracturing among the principal hydrogeologic units
- Colloid transport
- Physical and retardation processes
- Effects of perched water.

The unsaturated zone radionuclide transport model has the capabilities to simulate saturated and/or unsaturated flow and transport in porous and/or fractured media.

Simulations of transport of radioactive solutes and colloids from the repository horizon to the water table were performed to support performance assessment studies of the potential repository (CRWMS M&O 20001, Section 1, p. 13). The results of the simulations were used to evaluate the transport of radioactive solutes and colloids, and to determine the processes, mechanisms, and geologic features that have a significant effect on transport. The contributions of daughter products of radioactive decay to transport were evaluated from the bottom of the potential repository to the water table. The effects of the various conceptual models of perched water on transport also were evaluated. Simulation results must be used with care because many transport parameters input to the models were based on sparse site data. For some input parameters, best estimates from the scientific literature were used because no specific data were available for Yucca Mountain. In addition, the unsaturated zone radionuclide transport model was based on the conceptual models and numerical approaches used for developing spatial distributions of net infiltration and flow fields at various depths within the unsaturated zone and, thus, the unsaturated zone radionuclide transport model shares the same limitations as those models.

The overall approach used in the unsaturated zone transport modeling was to simulate radionuclide transport in individual two-dimensional vertical slices of the unsaturated zone and in the larger three-dimensional system using the flow fields calculated by the unsaturated zone flow and transport model (Section 8.10.6.8) for use in TSPA (CRWMS M&O 20001, Section 6, p. 31). The primary objectives of the unsaturated zone radionuclide transport model are:

- Using the comprehensive, calibrated, three-dimensional model of unsaturated zone flow to integrate the available data for the development of a comprehensive model of radionuclide transport through the unsaturated zone at Yucca Mountain under a range of current and future climate conditions
- Identify the controlling transport processes and phenomena, and evaluate the effectiveness of matrix diffusion and sorption as retardation processes
- Identify the geologic features that are important to radionuclide transport
- Obtain an estimate of the migration of important radionuclide solutes and their daughter products from the potential repository toward the water table (saturated zone)
- Evaluate the effects of various climatic conditions on radionuclide transport

- Evaluate the effect of perched-water conditions on radionuclide transport
- Obtain an estimate of the migration of radioactive colloids from the potential repository toward the regional water table (saturated zone) and determine the sensitivity of colloid transport to the kinetic coefficients of colloid filtration
- Evaluate the effect of fracture spacing, intensity, and configuration on radionuclide transport and retardation through important hydrogeologic units.

#### **8.10.10.1 Data Sources and Software for Radionuclide Transport Models**

Data sources for development and application of unsaturated zone radionuclide transport models are documented by in CRWMS M&O (2000I, Section 4, p. 18, Table 4.1). Primary categories of input data used for the unsaturated zone radionuclide transport models include the following:

- Transport properties
- Calibrated fracture and matrix properties
- Base-case flow fields
- Geochemical data
- Numerical grids.

Computer software items used in the development of unsaturated zone radionuclide transport models are described and identified in CRWMS M&O (2000I, Section 3, p. 17, Table 3.1). The primary software code used for the radionuclide transport models was TOUGH2 version 1.11 Module EOS9nT version 1.0, which simulates saturated and/or unsaturated flow and transport of a multiple number of radioactive solutes and/or colloids in complex subsurface systems involving porous and/or fractured media. The transport mechanism simulated includes advection, molecular diffusion, hydrodynamic dispersion, kinetic or equilibrium physical and chemical sorption (linear, Langmuir, Freundlich, or combined), first-order linear chemical reaction, colloid filtration, and colloid-assisted solute transport.

#### **8.10.10.2 Technical Assumptions Regarding Radionuclide Transport Models**

A series of technical assumptions were made in order to develop radionuclide transport models for the unsaturated zone at Yucca Mountain (CRWMS M&O 2000I, Section 5, pp. 23 to 30). The assumptions fall into five categories:

- Assumptions underlying the three-dimensional flow component of the transport model
- Assumptions about three-dimensional transport processes
- Assumptions involving the treatment and mathematical representation of the fractured rocks using the three-dimensional, dual-continuum approach
- Assumptions related to the initial and boundary conditions of the three-dimensional model domain

- Assumptions involved in the semianalytical transport solution used for two-dimensional transport submodels.

The basic flow assumptions for the unsaturated zone radionuclide transport model were consistent with those of the unsaturated zone flow and transport model (Section 8.10.6) because they share identical conceptual models (CRWMS M&O 2000l, Section 5.1, p. 23). These assumptions include:

- The macroscopic-continuum approach is a valid concept for the description of the flow and transport processes in the fractured rocks of the unsaturated zone.
- Darcy's law is a valid model to describe the flow of gas and water in the matrix and fractures of the unsaturated zone.
- Richards' equation is a valid model of unsaturated zone water flow in both the matrix and the fractures of the unsaturated zone.
- Relative permeabilities and capillary pressures were assumed to follow the van Genuchten-Mualem model and are continuous functions of the effective liquid and gas saturations.
- Water flow is isothermal. This assumption is a reasonable approximation except in the immediate vicinity of the waste package because of the heat generated by the radioactive-decay process.
- Water flow through the unsaturated zone in numerical simulations of radionuclide transport was assumed to be at steady state.

Assumptions involved in the transport processes (CRWMS M&O 2000l, Section 5.2 p. 25) include the following:

- The individual and combined effects of diffusion (molecular and/or colloidal), surface diffusion, and hydrodynamic dispersion follow a Fickian model.
- Transport was assumed to occur isothermally at 25°C.
- The concentration of the radioactive solutes or colloids is at a tracer level, that is, too low to have any measurable effect on the flow regime.
- There would be no phase change, meaning that no water evaporation and condensation would occur during radionuclide transport.
- Filtration of colloids was limited to deep filtration, (i.e., filtration would not affect the medium porosity and permeability).

The treatment of fracture-matrix interactions was a critical issue in the simulation of flow and transport under the two-phase flow conditions of the fractured rocks in the unsaturated zone (CRWMS M&O 2000l, Section 5.3, p. 27). In the development of the unsaturated zone

radionuclide transport model, the dual-permeability model was used a valid to approximate flow and transport in the fractured rocks of the unsaturated zone.

Assumptions involving initial and boundary conditions for the unsaturated zone radionuclide transport model (CRWMS M&O 2000l, Section 5.4, p. 28) include:

- The upper boundary was maintained at spatially variable but temporally constant gas pressure and saturation, temperature, and temporally constant infiltration rates (to represent steady state flow conditions).
- The lower boundary was chosen to coincide with the water table, which was maintained at spatially variable but temporally constant water pressure, water saturation, and temperature.
- The side boundaries were made such that no lateral flow and/or transport would occur.
- The potential repository was assumed to be located in the TSw hydrogeologic unit.
- In transport studies of radionuclide releases from the wastes emplaced in the potential repository, the initial tracer (solute or colloidal species) concentrations were assumed to be constant in the grid blocks representing the potential repository and zero elsewhere.

The two-dimensional, semi-analytical model of transport through layered, fractured media was based on some of the same assumptions stated above, including isothermal steady-state flow and the validity of the dual-permeability model (CRWMS M&O 2000l, Section 5.5, p. 29). Additional assumptions made in the semi-analytical mode include:

- Advection would occur only in the fractures so that the only mechanism of radionuclide transport from the fractures to the matrix would be molecular diffusion (matrix diffusion).
- The upper-bound radionuclide transport predictions could be made by assuming that transport between the nonaligned fractures in adjacent layers is continuous (i.e., by neglecting transport along the layer interface between the offset fractures).

### **8.10.10.3 Physical and Flow Processes Important to Radionuclide Transport**

Radionuclide transport is highly affected by the same processes that control water flow through the unsaturated zone. Transport of radioactive solutes and/or colloids involves advective flow processes, hydrodynamic dispersion, sorption (solutes) or filtration (colloids), matrix diffusion, and radioactive decay (CRWMS M&O 2000l, Section 6.1.2, pp. 35-50).

#### **8.10.10.3.1 Advection**

Advection is the movement of dissolved or colloidal species resulting from the bulk flow of fluid (CRWMS M&O 2000l, Section 6.1.2.1). In advective transport, the flowing water carries contaminants, and transport pathways coincide with flow pathways determined by the characteristics of the faults, hydrogeologic units, and perched water. Because flow in the

unsaturated zone at Yucca Mountain is predominantly downward due to gravity, so is advective transport. The presence of perched water bodies may result in lateral flow and subsequent transport of the radionuclides. Laterally diverted flow ultimately finds a pathway to the water table through other, more permeable zones such as faults.

Advection is probably the most important mechanism for fast radionuclide transport through the unsaturated zone to the water table (CRWMS M&O 2000l, Section 6.1.2.1). Advection through fractures is expected to dominate transport behavior in welded units because water flows largely through fracture networks. Dominant fracture flow in the zeolitic components of CHn also provides relatively short travel times for the transport to the water table, whereas the dominant matrix flow in the CHn vitric components leads to much longer travel times.

#### **8.10.10.3.2 Hydrodynamic Dispersion**

Hydrodynamic dispersion includes mechanical dispersion that arises from local velocity variations and molecular diffusion that is driven by concentration gradients (CRWMS M&O 2000l, Section 6.1.2.2). Dispersion of the radionuclides occurs both along (longitudinal) and transverse to the average flow direction. Hydrodynamic dispersion dilutes and smears sharp concentration gradients and reduces the breakthrough time of radionuclides to the water table. The dispersion coefficient is a function of dispersivity and flow velocity.

Values of dispersivity are difficult to determine without site-specific measurements (CRWMS M&O 2000l, Section 6.1.2.2). Dispersivity has been shown to increase as a function of observation scale, attributed mainly to mixing, as more heterogeneities are sampled at larger scales. Furthermore, reported field measurements of transverse dispersivity show it to be significantly less than longitudinal dispersivity.

Dispersion is not expected to play an important role in unsaturated zone transport (CRWMS M&O 2000l, Section 6.1.2.2). First, dispersion effects are implicitly accounted for by the fracture-matrix dual-continuum approach, which explicitly simulates local velocity variations (CRWMS M&O 2000m, Section 6.2.5). Second, the potential repository emplacement area is very broad (relative to the distance to the water table), which tends to suppress dispersion effects.

#### **8.10.10.3.3 Sorption**

Sorption is a general term to describe the binding of a solute (radionuclide) onto the sorbent, which is either the immobile rock matrix or colloids (CRWMS M&O 2000l, Section 6.1.2.3). As a result of sorption, the advancing rate of sorbing radionuclides is retarded. On the other hand, the attachment of sorbing radionuclides onto colloids can potentially facilitate their transport.

In Yucca Mountain studies, the effective sorption distribution coefficient ( $K_d$ ) approach is employed to quantify the extent of radionuclide-sorbent interactions (CRWMS M&O 2000l, Section 6.1.2.3). This approach does not require identifying the specific underlying interactions of sorption, such as surface adsorption, precipitation, and ion exchange. While the use of  $K_d$  to describe the complex radionuclide-sorbent interactions in a flowing fluid of variable chemistry is a simplification, the results from numerous laboratory batch and column experiments (CRWMS M&O 2000n, Sections 6.4 to 6.6) have not produced recommendations to abandon the  $K_d$  approach for modeling radionuclide retardation in the YMP.

Experimentally determined  $K_d$  values have been predominantly derived from batch experiments using crushed tuff (with the sample size of 75 to 500  $\mu\text{m}$ ) under water-saturated conditions for a variety of rock types and radionuclides (CRWMS M&O 2000l, Section 6.1.2.3). There are concerns that this experimental approach may overestimate the  $K_d$  values in unsaturated zone transport.

Sorption onto fracture surfaces will retard radionuclide migration. The minerals coating the fracture surfaces generally differ from the host-rock mineralogy as a result of different exposure to precipitation of hydrothermal or meteoric waters, or alteration of the preexisting minerals (CRWMS M&O 2000n, Section 6.5.3). Laboratory sorption experiments showed that trace minerals might be quite effective at retarding  $^{237}\text{Np}$  transport when they are concentrated on fracture surfaces (CRWMS M&O 2000n, Section 6.5.3). Numerical simulations also showed that the limited sorption on the fracture walls is sufficiently important to retard transport of strongly sorbing radionuclides such as  $^{239}\text{Pu}$  (CRWMS M&O 2000l, Section 6.17.1). However, sorption in the fractures is not considered in the TSPA transport evaluations because of the limited data and conservative nature of this assumption regarding the radionuclide transport to the water table.

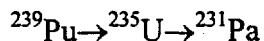
#### **8.10.10.3.4 Matrix Diffusion**

Matrix diffusion can play an important role in radionuclide exchange between the fractures and the rock matrix (CRWMS M&O 2000l, Section 6.1.2.4). Radionuclide diffusion into the rock matrix and away from the fracture surface is driven by the concentration gradient and will slow the advance of radionuclides by removing them from the fast flow paths. The significance of matrix diffusion depends mainly on factors such as effective contact area between fracture and matrix, the diffusion coefficient of the species, and characteristics of fracture networks (CRWMS M&O 2000m, Section 6.2.2). The presence of inactive and relatively dry fractures could serve as barriers for matrix diffusion.

The effective diffusion coefficient, which is the product of the molecular diffusion coefficient, tortuosity, porosity, and water saturation, is used to account for rock geometry and saturation effects on matrix diffusion (CRWMS M&O 2000l, Section 6.1.2.4). Laboratory measured tortuosity on geologic materials ranges from 0.5 to 0.01 (Fetter 1993, p. 44). Because very limited experimental data exist on the tortuosity distribution in the various Yucca Mountain hydrogeologic units, porosity values have been used to approximate tortuosity. Tortuosity measurements on devitrified tuffs showed good agreements with this approximation, thereby validating the approach.

#### **8.10.10.3.5 Radioactive Decay and Daughter Products**

The production of daughter products from chain-decay adds complexity because transport simulations must compute the total radioactivity distribution, that is, the sum of the concentrations of all the members of the radioactive decay chain (CRWMS M&O 2000l, Section 6.1.2.8). This is especially significant if the daughters have long half-lives. Daughter products with short half-lives relative to the simulation periods may not need to be considered. The daughter products may have significantly different transport behavior than the parent radionuclide, as in the  $^{239}\text{Pu}$  decay chain:



(Eq. 8.10-4)

This equation includes only the most important radioactive chain members and omits daughter products with short half-lives. The daughter product  $^{235}\text{U}$  has significantly smaller  $K_d$  values compared to its parent  $^{239}\text{Pu}$ .

### 8.10.10.3.6 Colloidal Transport

Colloids are very fine particles, such as clay minerals, metal oxides, viruses, bacteria, and organic macromolecules, that range in size from 1 to 10,000 nm and have high specific surface areas (CRWMS M&O 2000l, Section 6.1.3.3). Generation and mobilization of colloids has become an important issue in the facilitated transport of radionuclides as intrinsic colloids, such as colloidal plutonium (IV) and colloidal plutonium (V), or as radionuclide-bearing pseudocolloids for  $^{239}\text{Pu}$  and  $^{243}\text{Am}$  (CRWMS M&O 2000l, Section 6.1.2.6). Colloidal transport differs from solute transport because of colloidal particle interactions (flocculation), pore exclusion, and surface reactions, such as deposition or attachment (CRWMS M&O 2000l, Section 6.1.3.3).

There is some field evidence of colloid-facilitated transport of radionuclides. In one case, the rapid migration of plutonium and americium, attributed to colloidal transport, was found more than 30 m (98 ft) downward through unsaturated tuff over the course of approximately 30 yr. from a low-level waste site at Los Alamos National Laboratory. At the Nevada Test Site,  $^{240}\text{Pu}/^{239}\text{Pu}$  isotope ratio "fingerprints" of the source of plutonium in the saturated zone showed that it had been transported more than 1.3 km over a 30-yr. period in colloidal form. This colloidal transport occurred even though in soluble form plutonium is strongly sorbed at the Nevada Test Site and was assumed to be immobile (CRWMS M&O 2000l, Section 6.1.3.3).

Few published data exist on colloid concentrations in the unsaturated zone or the saturated zone. Preliminary results of a Nevada Test Site survey have shown that saturated-zone water in the Pahute Mesa drainage, both on and off the Nevada Test Site, has colloidal-particle (more than 3 nm in diameter) loadings of 0.8 to 6.9 mg/L (CRWMS M&O 2000l, Section 6.1.3.5). Furthermore, analysis and modeling have indicated that waste-form colloids will play a more significant role than natural colloids because the actinides are already incorporated into the structure and do not have to compete with matrix and fracture minerals for the actinides. For the waste-form colloids, the most significant mechanism is size exclusion of colloids from the matrix, which leads to fracture-dominated transport of these colloids. Although this effect occurs for natural colloids, the reaction of actinides with the colloids is not restricted to the fracture, and transport of the colloids without actinides do not affect repository performance (CRWMS M&O 2000o, Section 7).

In addition to natural colloids, anthropogenic colloids may be produced from the waste itself or from potential repository construction and sealing materials (CRWMS M&O 2000l, Section 6.1.3.5). This was demonstrated in a 50-mo. experiment of simulated weathering of a high-level nuclear-waste glass, in which spallation and nucleation were identified as the main mechanisms of inorganic colloid genesis. The same study determined that plutonium and americium released from waste were predominantly in the colloidal, rather than in the dissolved, form.

Both hydrophilic and hydrophobic colloids may be irreversibly sorbed at the gas-water interface, with the degree of sorption increasing with the increase of colloid surface hydrophobicity (CRWMS M&O 2000l, Section 6.1.3.4.2). Hence, colloidal transport may be reduced because of sorption onto stationary gas bubbles or gas-water interfaces or enhanced if gas bubbles are able to migrate in the unsaturated zone with colloids attached.

#### **8.10.10.4 Transport Properties Important to Radionuclide Transport**

Several transport properties were critical inputs to the unsaturated zone radionuclide transport model. These include dispersivities, sorption coefficients, matrix diffusion coefficients, fracture aperture and spacing, and parameters for colloid-facilitated radionuclide transport.

##### **8.10.10.4.1 Dispersivities**

No data were available to determine dispersivity in the unsaturated zone over the travel distance between the potential repository and the water table. Longitudinal dispersion in a transport simulation results in earlier arrivals, but generally lower concentrations. Given this behavior, no simple conservative bound could be identified for the longitudinal dispersion. However, a selected dispersivity value of 20 m (66 ft) over the approximately 300-m (980-ft) unsaturated zone travel distance (used in TSPA calculations) is consistent with the dispersivity versus scale correlation of Neuman (1990, pp. 1749 to 1758). Furthermore, longitudinal dispersivity (primarily in the vertical direction) was not expected to have a large effect on radionuclide transport processes in the unsaturated zone. This is because of the strong dispersive effects of fracture-matrix interactions that are explicitly captured in the Finite-Element Heat and Mass Transfer particle-tracking calculation. Transverse dispersion acts only to reduce concentrations, with generally little effect on breakthrough time. Therefore, a conservative value of zero for transverse dispersivity was used in the unsaturated zone radionuclide transport models. The base-case distribution for longitudinal dispersivity was selected to be normal, with a mean of 20 m (66 ft) and a standard deviation of 5 m (16 ft), which captured a range of 7.5 to 32.5 m (25 to 107 ft) within the 99 percent probability limits. This dispersivity distribution was used for transport simulations of all model units for both the fracture and matrix continua, but values for fracture and matrix were sampled independently for the unsaturated zone radionuclide transport analyses.

##### **8.10.10.4.2 Sorption Coefficients**

The main experimental program for sorption was carried out using batch sorption experiments (CRWMS M&O 2000n, Section 6.4, p. 36). Table 8.10-10 lists the sorption distribution coefficients recommended for the unsaturated zone radionuclide transport model (CRWMS M&O 2000n, Section 6.4.2, p. 38). For some radionuclides, specific sorption measurements using rock and water samples from Yucca Mountain had not been performed. For these radionuclides, sorption behavior was evaluated on a theoretical basis.

Three assumptions were made to develop values of  $K_d$  for use in performance assessment (CRWMS M&O 2000n, Section 5, p. 31). First, the water compositions from wells UE-25 J-13 and UE-25 p#1 were assumed to provide an adequate range of compositions to capture the influence of water compositional variability on sorption in the unsaturated zone. Second, the

effects of mineral variations on sorption in the unsaturated zone were approximated using three rock types: devitrified tuff, vitric tuff, and zeolitic tuff. Finally, the effects of temperature were assumed to be bounded by measurements of sorption at ambient temperature. However, the effects of mineral alteration because of thermal history were not included in the evaluation of this assumption.

The use of a linear, infinite-capacity sorption model is important both for describing sorption and for modeling the transport of sorbing radionuclides. Sorption of uranium shows nonlinear sorption behavior, in which the sorbed concentration is reduced from that of a linear model at higher concentrations (CRWMS M&O 2000n, Section 6.4.4.1.4.4, pp. 64 and 65). A linear model is justified for the lower concentration levels that will constitute the earliest releases. In addition, any nonlinear effects will only act to self-sharpen the solute fronts, indicating a decrease in longitudinal dispersion. Therefore, the linear sorption model was considered valid for conservatively predicting radionuclide movements and breakthrough times for the unsaturated zone.

#### **8.10.10.4.3 Matrix Diffusion Coefficients**

The matrix diffusion values for radionuclides were based on measured diffusion coefficients of tritium and technetium (CRWMS M&O 2000n, Section 6.6.1, pp. 109 to 111). The measurements (in water-saturated rock) showed that tritium diffused at a rate between  $1 \times 10^{-10}$  m<sup>2</sup>/s and  $3.5 \times 10^{-10}$  m<sup>2</sup>/s in several samples of devitrified tuff. For technetium, the matrix diffusion coefficient varied between  $1 \times 10^{-11}$  m<sup>2</sup>/s and  $4.9 \times 10^{-11}$  m<sup>2</sup>/s, which is lower than that of tritium (CRWMS M&O 2000n, Table 16). The lower diffusion rate of technetium was believed to be caused by exclusion of the pertechnetate anion (TcO<sub>4</sub><sup>-</sup>), the predominant aqueous species of technetium from some matrix pores caused by its large ion size and negative charge.

A distribution for technetium diffusion coefficients was assigned to account for variations in rock type and water content. (The measured technetium diffusion coefficients show the diffusion coefficient for different rock types, a factor of 10.) This range was roughly captured by the distribution shown in Table 8.10-11 for anionic and cationic radionuclides.

Transport predictions for cationic radionuclides using the diffusion coefficient for tritium and measured batch sorption coefficients were found to be conservative (slower) relative to measured radionuclide concentrations (CRWMS M&O 2000n, Section 6.6.1.3, p. 111). The more rapid measured uptake of sorbing radionuclides was believed to be a result of deviations from the linear  $K_d$  model for sorption. These results showed that the diffusion coefficients for sorbing radionuclides were conservatively assigned values representative of tritium.

#### **8.10.10.4.4 Fracture Aperture and Spacing**

Fracture aperture and spacing affect flow and transport between fractures and matrix. For a continuous, parallel fracture pattern, the inverse of the fracture aperture is the area of contact between the fracture and matrix continua per unit volume of fracture pore space. Therefore, the larger the aperture, the less the diffusion (in a saturated system). For an unsaturated fracture, the relevant volume (per unit matrix area) is not the fracture pore volume itself but the volume of water. In either case (saturated or unsaturated), specification of the aperture is necessary for

transport model. Fracture spacing also affects the diffusion process because it sets the boundary for the depth of penetration for matrix diffusion.

The fracture apertures for the unsaturated zone radionuclide transport model were derived from the fracture porosity and fracture-matrix connection area (CRWMS M&O 2000p, Section 6.2.1). Aperture distributions were described using a log-normal distribution of apertures for all the model layers beneath the potential repository. Apertures were sampled stochastically in the radionuclide transport calculations. The sensitivity of transport to fracture spacing was found low, so a constant value for each layer was used (CRWMS M&O 2000q, Section 3.11.3.4).

#### **8.10.10.4.5 Parameters for Colloid-Facilitated Radionuclide Transport**

In the unsaturated zone radionuclide transport model, the association of radionuclides with colloids was modeled using two end-member representations: reversible equilibrium exchange with the aqueous phase and irreversible attachment. Radionuclides associated with colloids in either condition (reversible or irreversible) may be subject to size exclusion for fracture-matrix exchange. Colloids are excluded from moving from a fracture into matrix pores smaller than the colloid diameter. This tends to keep colloids (and the associated radionuclides) in the fractures, which leads to more rapid transport of the radionuclide. The chance of exclusion of a colloid from the matrix during fracture-matrix exchange is computed using a probabilistic method that considers the colloid size distribution and pore size distribution (CRWMS M&O 2000o, Section 6.4, p. 33).

The description of reversible, colloid-facilitated radionuclide transport for the particle-tracking transport model used in performance assessment was quantified through two parameters (CRWMS M&O 2000p, p. 17). One parameter,  $K_c$ , defines the equilibrium partitioning of radionuclides between the aqueous phase and colloids. The other parameter,  $R_c$ , is a retardation factor that captures the details of an equilibrium balance between colloid deposition and resuspension. The retardation factor in the colloid model abstraction applies to the transport through fractures. The distribution of retardation factors used was derived from C-Wells data for saturated zone colloid transport (CRWMS M&O 2000p, p. 17).

#### **8.10.10.5 Two-Dimensional Radionuclide Transport Simulations**

Two-dimensional radionuclide transport from the potential repository to the water table at Yucca Mountain was investigated using representative hydrogeologic profiles embedded in the unsaturated zone radionuclide transport model (CRWMS M&O 2000l, Section 6.5, pp. 76 to 82). These profiles are two-dimensional cross sections in the sense that concentrations were computed in both the vertical and horizontal directions in the fractures and the matrix blocks of each layer in the hydrogeologic units in the cross sections. However, these cross sections span only a very short distance in the horizontal direction, which is the minimum necessary to simulate the matrix-fracture system in the representative hydrogeologic profile at the given location. The purpose of the transport simulations was to evaluate the integrated transport through the complete hydrogeologic system beneath the potential repository as well as the individual hydrogeologic units. The hydrogeologic units considered are the same as those defined for the site-scale unsaturated zone flow and transport model (Table 8.10-1) and include the subunits of the TSw, the vitric and zeolitic portions of the Calico Hills Formation, and

subunits of the Prow Pass Tuff. The simulations accounted for fracture aperture, fracture frequency, active-fracture spacing, and saturation distribution (in the fractures and the matrix) across hydrogeologic unit interfaces. Two of these vertical cross sections, representative of the hydrologic and mineralogical variability below the potential repository horizon, were located in the vicinity of borehole USW SD-6 in the southern part of the potential repository area and borehole USW UZ-14 in the northern part (Figure 8.10-2). Figure 8.10-54 shows hydrogeologic profiles of these two cross sections and indicates the model layers involved in radionuclide transport and their elevation and thickness. Of importance to the radionuclide-transport simulations is the fact that perched water occurs beneath the repository horizon at borehole USW UZ-14, whereas perched water does not occur at borehole USW SD-6 (Section 8.10.6.4) (Figures 8.10-13 and 8.10-14).

#### **8.10.10.5.1 Simulation Approach**

The two-dimensional, semi-analytical code FRACL version 1.0, which can analyze transport of reactive solutes and true colloids through layers of fractured and porous media, was used to perform the radionuclide transport simulations (CRWMS M&O 2000l, Section 6.3.2, p. 64). The transport equations in the matrix accounted for molecular and surface diffusion, mass transfer between the mobile and immobile water fractions, and physical, chemical, or combined sorption following a linear-equilibrium, kinetic, or irreversible isotherm. Radioactive decay, first order chemical reactions, and tracking of up to five products of radioactive decay or chemical reactions were also included in the solution. The transport equations in the fractures accounted for the same processes, in addition to advection and hydrodynamic dispersion. FRACL version 1.0 can accommodate layers of fractured rocks or a combination of fractured rock and nonfractured strata and can account for the effects of different fracture spacing and misalignment of fractures. However, in these two-dimensional simulations, misalignment of fractures was not accounted for (CRWMS M&O 2000l, Section 6.5.4, p. 78). Thus, the results represent the worst-case scenario, yield the shortest possible breakthrough times, and provide the upper limit of radionuclide transport.

Three representative radionuclides were considered in the two-dimensional simulations:  $^{99}\text{Tc}$  (nonsorbing),  $^{237}\text{Np}$  (moderately sorbing), and  $^{239}\text{Pu}$  (strongly sorbing) (CRWMS M&O 2000l, Section 6.5.2, p. 76). In the simulations, radionuclides were released continuously at the top of the domain, which coincides with the potential repository or the individual unit of interest, and the calculated contaminant distributions (as relative concentrations) were monitored over time. When occurring, sorption was assumed to follow a linear-equilibrium isotherm. It was assumed that advection occurs only in fractures with the longitudinal dispersivity of 1 m (CRWMS M&O 2000l, Section 6.6, Table 6.7). The only mechanism of radionuclide transport from the fracture to the matrix was by matrix diffusion. The simulated percolation rate was 6 mm/yr., which is close to the mean present-day rate (CRWMS M&O 2000l, Section 6.5.1, p. 76). Simulations also were made using a higher infiltration rate (33.5 mm/yr.) to represent glacial climatic conditions (CRWMS M&O 2000l, Section 6.9.3, p. 76).

#### **8.10.10.5.2 Simulation Results**

**Transport in Individual Hydrogeologic Unit**—The model results indicate that the TSw unit does not effectively retard radionuclide transport because of the dominance of fracture flow that

consequently reduces matrix diffusion and sorption (CRWMS M&O 2000l, Section 6.6.1.2, p. 83). The breakthrough times for the radionuclides was in the order of  $^{99}\text{Tc}$  less than  $^{237}\text{Np}$  less than  $^{239}\text{Pu}$ , which corresponds to their difference in sorptive strength  $K_d$ . At borehole USW SD-6, for example, transport of the nonsorbing  $^{99}\text{Tc}$  reached the lower boundary of the TSw unit in about 1 yr. Breakthrough of the moderately sorbing  $^{237}\text{Np}$  was estimated to take about 35 yr., while  $^{239}\text{Pu}$  occurs at about 300 yr.

Flow in the vitric portion of the Calico Hills Formation (CHv) is primarily matrix flow, and the model predicted that the unit behaves similarly to a nonfractured porous medium (CRWMS M&O 2000l, Section 6.7, p. 89). The reduced flow velocity and increased contact time for matrix diffusion and sorption made the CHv unit an effective transport barrier. At borehole USW SD-6, the Calico Hills Formation was represented in the model by five vitric layers (ch1v, ch2v, ch3v, ch4v, and ch5v) and one zeolitic layer (ch6z) at the bottom (Figure 8.10-54a). In the simulation, the  $^{99}\text{Tc}$  front reached the bottom of the CHv unit in a few hundred years, while the  $^{237}\text{Np}$  took several thousand years. Advancement of  $^{239}\text{Pu}$  was limited to the uppermost ch1v layer because of its strong sorptive tendency.

Flow in the zeolitic portion of the Calico Hills Formation (CHz) is dominantly in the fractures, and radionuclide transport through the unit was expected to be rapid, similar to that in the TSw unit (CRWMS M&O 2000l, Section 6.7, p. 89). At borehole USW UZ-14, the Calico Hills Formation was represented in the model by six zeolitic layers: ch1z, ch2z, ch3z, ch4z, ch5z, and ch6z (Figure 8.10-54b). As expected, the simulation results showed that both  $^{99}\text{Tc}$  and  $^{237}\text{Np}$  would reach the bottom boundary in less than 10 yr. It should be noted that the value of  $K_d$  used for  $^{237}\text{Np}$  was 4 mL/g in the zeolitic tuffs, compared to 1 mL/g in the vitrified tuffs. The larger  $K_d$  value did not lead to more retardation in the CHz unit than in the CHv unit because the contact time for  $^{237}\text{Np}$  with the tuffs was much shorter in the CHz unit where fracture flow is dominant. The results also show that strongly sorbing  $^{239}\text{Pu}$  needs several thousand years to cover this distance.

Within the Prow Pass Tuff, simulation results indicated that fracture flow may be dominant in pp4 and pp1 layers, while pp3 and pp2 layers behave like nonfractured porous media (CRWMS M&O 2000l, Section 6.8). At borehole USW SD-6, the simulation indicated that radionuclides would penetrate the uppermost pp4 layer quickly and then radionuclide transport would be controlled by pp3 and pp2 layers. The modeling shows these layers are quite efficient in retarding transport even for the nonsorbing  $^{99}\text{Tc}$ , which took more than 1 k.y. to pass through them. In the simulation, it takes several thousand years for  $^{237}\text{Np}$  to reach the pp1 layer. The simulated  $^{239}\text{Pu}$  front did not reach the pp3 boundary even after 100 k.y.

**Transport Simulations below the Potential Repository**—Simulated migration of radionuclides at borehole USW SD-6 was slow because of the presence of the CHv unit, through which matrix flow is dominant (CRWMS M&O 2000l, Section 6.9.2, p. 95). The simulated  $^{99}\text{Tc}$  front reaches the water table in several thousand years (more than 1 k.y. but less than 10 k.y.) as indicated in Figure 8.10-55. In Figure 8.10-55, the 10-k.y. and 100-k.y. concentration lines both plot along the upper horizontal axis of the figure, indicating that by these times the relative concentration of  $^{99}\text{Tc}$  has reached 1.0 at the water table. The simulated  $^{237}\text{Np}$  breakthrough takes longer than 10 k.y. but less than 100 k.y. to reach the water table because of the moderate sorption (Figure 8.10-

56). In the simulation, the strongly sorbing  $^{239}\text{Pu}$  does not advance past the ch1v layer, less than 60 m (200 ft) from the point of release, even after 100 k.y. (Figure 8.10-57).

Because perched water was detected in the vicinity of borehole USW UZ-14, near the interface of the TSw and CHn units, the effect of perched water on radionuclide transport was investigated by approximating perched-water conditions in the FRACL simulations (CRWMS M&O 2000I, Section 6.9.8, pp. 99 to 101). In the simulations, fracture and matrix water saturations were set to 1.0 in the model layers tsw38 and tsw39 layers, which are the layers immediately above the TSw-CHn interface (CRWMS M&O 2000I, Section 6.9.8.1, p. 99). Additionally, the fractures in the ch1z (the uppermost zeolitic layer of CHn at this location) were assumed to be filled and to have the same saturation and transport properties as the matrix in the same layer. Thus, the ch1z layer was acting as a porous, rather than a fractured, medium. This perched-water condition was similar to the bypassing perched-water conceptual model described in Section 8.10.6.4.

The perched-water body in the vicinity of borehole USW UZ-14 (in the northern part of the potential repository area) and the geological conditions that lead to perched water resulted in some significant differences in simulated radionuclide transport behavior from that at borehole USW SD-6 (in the southern part of the potential repository area). The modeling results (Figure 8.10-58) indicate that despite the presence of perched-water, nonsorbing  $^{99}\text{Tc}$  would move about 65 m (210 ft) deeper into the subsurface at borehole USW UZ-14 after 10 to 100 years than at borehole USW SD-6 (Figure 8.10-55). Furthermore, in the borehole USW UZ-14 simulation, a significant concentration of  $^{99}\text{Tc}$  reached the water table after 1 k.y. Similarly, moderately sorbing  $^{237}\text{Np}$  was predicted to move about 200 m (660 ft) deeper into the subsurface after 1 k.y. at borehole USW UZ-14 (Figure 8.10-59) than at USW SD-6 (Figure 8.10-56). The borehole USW UZ-14 simulation results also indicate that after 10 k.y., the concentration of  $^{237}\text{Np}$  at the water table would be relatively large (Figure 8.10-59), whereas in the borehole USW SD-6 simulation,  $^{237}\text{Np}$  had not yet reached the water table after 10 k.y. (Figure 8.10-56). The simulations show that even strongly sorbing  $^{239}\text{Pu}$  would move about 200 m (660 ft) deeper into the subsurface after 100 k.y. at borehole USW UZ-14 (Figure 8.10-60) than at USW SD-6 (Figure 8.10-57). Nevertheless, the simulations for borehole USW UZ-14 did indicate that the CHz is effective in attenuating strongly sorbing radionuclides.

The overall results of the two-dimensional radionuclide transport simulations seem counterintuitive in that simulated radionuclide transport was more rapid at the location of borehole USW UZ-14, where perched water occurs, than at the location of borehole USW SD-6, where perched water does not occur. This probably is because the two-dimensional transport model constructed using FRACL was too simplified to simulate actual perched-water conditions, as was achieved with the site-scale, unsaturated zone flow model (Section 8.10.6.4). Apparently, setting the fracture properties of only the ch1z layer equivalent to the matrix properties was insufficient to simulate perched-water conditions with the FRACL model and the simulated system still was dominated by the fracture properties of the other five CHz layers. The overall result was a two-dimensional simulation that either did not actually represent perched-water conditions at all, or, at best, represented the flow-through perched-water conceptual model described in Section 8.10.6.4.1. In either case, it appears that the relatively faster radionuclide transport simulated at borehole USW UZ-14 was a consequence of fracture-dominated flow through the zeolitic CHn. In contrast, the relatively slower transport simulated at borehole USW SD-6 was a consequence of matrix-dominated flow in the vitric CHn. In this context, it is

important to note that the fracture permeability of the CHz in the calibrated-properties model generally is greater than the matrix permeability of the CHv (Table 8.10-2).

#### **8.10.10.6 Three-Dimensional, Site-Scale Radionuclide Transport Simulations**

The three-dimensional, site-scale simulations of radionuclide transport with the unsaturated zone radionuclide transport model used the same horizontal numerical grid (Figure 8.10-4) and vertical layering scheme (Figure 8.10-5 and Table 8.10-1) as were used to calculate flow fields for input to TSPA (CRWMS M&O 2000l, Section 6.11.2, pp. 108 and 109). The transport simulations were run under the same three climate-oriented infiltration regimes (present-day, monsoon, and glacial-transition) as were simulated by the site-scale flow model for input to TSPA (Section 8.10.6.8), each with lower-bound, mean, and upper-bound estimates (CRWMS M&O 2000l, Section 6.11.1, p. 108). The values of percolation flux resulting from the infiltration regimes and used in the three-dimensional, site-scale, radionuclide-transport simulations are indicated in Table 8.10-12. These values differ only slightly from the net infiltration rates determined for the 38.7-km<sup>2</sup> (14.9-mi.<sup>2</sup>) unsaturated zone flow and transport model area in Section 8.2.10 (Tables 8.2-11, 8.2-14, 8.2-17). The differences are due to a small component of lateral flow as infiltration percolates to the repository horizon (Section 8.10.6.8.1) and interpolation of values onto the horizontal numerical grid used for site-scale simulations. Although the radionuclide-transport simulations used all three infiltration regimes, only simulations for present-day infiltration are discussed here. The simulations implemented the flow-through perched-water conceptual model, as described in Section 8.10.6.4.1 (CRWMS M&O 2000l, Section 6.12.1, p. 112).

The release rates of radionuclides at the potential repository were considered constant over time (CRWMS M&O 2000l, Section 6.11.2, p. 109). Radionuclides considered in the simulations were <sup>99</sup>Tc (nonsorbing), <sup>237</sup>Np (moderately sorbing), and <sup>239</sup>Pu (strongly sorbing). Important members of the decay chains of <sup>237</sup>Np and <sup>239</sup>Pu also were considered. These include <sup>233</sup>U, <sup>229</sup>Th, <sup>235</sup>U, and <sup>231</sup>Pa. The longitudinal dispersivity used in the three-dimensional transport simulations was 1 m (3.3 ft) in the fractures and 0.1 m (0.33 ft) in the matrix (CRWMS M&O 2000l, Table 6.14).

##### **8.10.10.6.1 The EOS9nT Code**

EOS9nT version 1.0 is a TOUGH2 (version 1.11) module for the simulation of an arbitrary number of solutes and/or colloids in the subsurface (Moridis et al. 1999). The code can simulate the following transport mechanisms: advection, hydrodynamic dispersion, molecular diffusion, mass transfer between the mobile and immobile water fractions, sorption, radioactive decay, filtration (for colloids only), first-order chemical reactions, and colloid-facilitated transport. EOS9nT version 1.0 considers equilibrium (linear, Freundlich, or Langmuir) sorption and kinetic sorption (linear, Freundlich, or Langmuir). Daughter products of radioactive decay can also be tracked (Moridis et al. 1999).

EOS9nT version 1.0 offers the option of a Laplace space formulation of the transport equations (in addition to conventional time-stepping) after the flow field reaches steady state (CRWMS M&O 2000l, Section 6.3.1, p. 64, Attachment I). The Laplace transform formulation eliminates the need for time discretization, and an unlimited time-step size is thus possible without loss of

accuracy or stability. It also completely linearizes all the kinetic transport equations and, thus, does not increase the order of the matrix to be solved. Additionally, the Laplace transform alleviates accuracy problems that may arise from the inaccurate weighting of the radioactive decay. All the three-dimensional transport simulations were conducted by using the De Hoog implementation of the Laplace transform formulation of EOS9nT version 1.0 (CRWMS M&O 2000l, Section 6.11.5, p. 111).

#### **8.10.10.6.2 Transport Simulations of Technetium-99 under Present-Day Infiltration**

Radionuclide breakthrough was described by the normalized release rate  $R$ , which is the radionuclide mass release rate at the water table divided by the release rate at the potential repository (CRWMS M&O 2000l, Section 6.12.2.1, p.112). For  $^{99}\text{Tc}$  transport, the normalized release rate in Figure 8.10-61 shows a very strong dependence on the infiltration regime. As the infiltration rate increased from low to mean present-day level, the  $t_{10}$  time (defined as the time at which  $R = 0.1$ ) decreased from about 1 k.y. to about 300 yr. and the  $t_{50}$  (the time at which  $R = 0.5$ ) decreases from about 45 k.y. to about 4 k.y. Higher infiltration rate would further reduce breakthrough time (Table 8.10-13). Figure 8.10-61 also shows that the maximum attainable  $R$  decreases with the infiltration rate, because lower infiltration results in lower velocities and longer travel times, thus higher radioactive decay.

#### **8.10.10.6.3 Transport Simulations of Neptunium-237 and Its Daughter Products under Present-Day Infiltration**

Figure 8.10-61 indicates that the sorption of  $^{237}\text{Np}$  retards its transport through the unsaturated zone system, as compared to  $^{99}\text{Tc}$  (CRWMS M&O 2000l, Section 6.13.1.1, p. 144). From the simulated values of  $t_{10}$  and  $t_{50}$ , the moderate sorption of  $^{237}\text{Np}$  would be sufficient to delay the time to reach the water table by a factor of about 40 (Table 8.10-13). Because of significant retardation, the maximum attainable  $R$  would vary over a large value range and was not achieved within the simulation period. At 1 m.y.,  $R$  is 0.98, 0.86, and 0.42 for the three high, mean, and low infiltration rates, respectively (Figure 8.10-61).

Important members in the  $^{237}\text{Np}$  decay chain are  $^{233}\text{U}$  and  $^{229}\text{Th}$  (CRWMS M&O 2000l, Section 6.11.3, p. 109). The simulated relative flux fraction,  $M_R$ , of each member of the chain, defined as the fraction of each radionuclide in the sum of the mass fluxes at the water table, shows that the daughter contribution would only reach a maximum of 2 percent at 1 m.y. (CRWMS M&O 2000l, Section 6.13.1.2, p. 14). As such, daughter contributions to the  $^{237}\text{Np}$  transport are rather insignificant and could be safely ignored.

#### **8.10.10.6.4 Transport Simulations of Plutonium-239 and Its Daughter Products under Present-Day Infiltration**

The simulated value of  $R$  for  $^{239}\text{Pu}$  never reached the 0.1 level even after 1 m.y. of continuous release because of the strong sorption (Figure 8.10-61) (CRWMS M&O 2000l, Section 6.14.1.1, p. 152). The picture changed dramatically, however, when the daughter contributions to the release rate at the water table were accounted for in the computations (Figure 8.10-61). Given the long half-lives of  $^{239}\text{Pu}$  and  $^{235}\text{U}$ , the daughter contributions can become significant under the high-infiltration regime (Table 8.10-13).

The simulated relative flux fractions of the daughter products (Figure 8.10-61) show that the  $^{234}\text{Pu}$  contribution to the release rate would decline rapidly after 1 k.y., and  $^{235}\text{U}$  would be by far the dominant species after 20 k.y. (CRWMS M&O 2000l, Section 6.14.1.2). Earlier emergence of  $^{235}\text{U}$  would be associated with the lower infiltration rates because less  $^{239}\text{Pu}$  would reach the water table owing to strong sorption. Thus, after 1 k.y., the release at the water table would consist mostly (more than 95 percent) of  $^{235}\text{U}$  under low present-day infiltration conditions. The  $^{231}\text{Pa}$  contribution would be negligible because of the very long half-life of  $^{235}\text{U}$ .

#### 8.10.10.6.5 Features Affecting Radionuclide Transport

The simulation results reveal that radionuclide transport from the repository to the water table is affected significantly by the faults, especially at the early times (CRWMS M&O 2000l, Section 6.12.2.2, pp. 115 to 133). Splay G of the Solitario Canyon fault (Figure 8.10-2) is the primary transport-facilitating feature. This is indicated by the distribution of the fracture mass fraction of  $^{99}\text{Tc}$  (with respect to that at the point of release in the potential repository) at the bottom of the TSw at  $t = 100$  yr. (Figure 8.10-62). Once contaminants reach the TSw-CHn interface, they move in an easterly direction, with the water that drains along the downward-sloping, low-permeability interface.

The Ghost Dance fault splay is the next most important transport-facilitating feature, as indicated by Figure 8.10-62 (CRWMS M&O 2000l, Section 6.12.2.2, p. 116). The simulation showed that although it facilitates downward migration, this fault appears to act as a barrier to the lateral migration of radionuclides, as evidenced by simulated mass fraction distributions both at the bottom of the TSw and at the water table. The Sundance fault and the Drill Hole Wash fault are also important. The Drill Hole Wash fault appears to act as a barrier to migration while providing pathways for relatively fast transport to the water table (Figure 8.10-62). The main Ghost Dance fault does not play an important role in transport at the bottom of the TSw, because  $^{99}\text{Tc}$  does not reach the fault at this level even after 100 k.y. The Ghost Dance fault, apparently, is more important at the water table, where it acts as a barrier to transport while facilitating downward migration into the saturated zone.

As time progresses, contributions of fractures and matrix become important (CRWMS M&O 2000l, Section 7.2, pp. 181 to 187). Fractures act as the important pathways of transport, whereas diffusion from the fractures into the matrix is the main retardation process in radionuclide transport. By sorbing onto the matrix into which they diffuse, the migration of radionuclides is retarded.

The emerging transport pattern from the simulation indicates that radionuclide transport to the water table is faster in the southern part of the potential repository block, where it is also areally concentrated (CRWMS M&O 2000l, Section 6.12.2.3, p. 113). This result is contrary to the results of the two-dimensional simulations (Section 8.10.10.5.2). This is because the simplistic two-dimensional model cannot account for the three-dimensional processes (such as perched water, flow diversion, focusing, and advective transport from outside its narrow two-dimensional domain (CRWMS M&O 2000l, Section 6.12.2.5). There are three major reasons for this transport pattern resulting from the three-dimensional simulations. First, the water flow pattern dictates the advective transport pattern, and the maximum downward water flow within the footprint of the potential repository is in the southern part under the flow-through perched-water

conceptual model. The maximum downward water flow in the southern part of the potential repository area can be seen in Figure 8.10-9 (mean present-day infiltration of this land surface), Figure 8.10-21 (percolation flux at the repository horizon), and Figure 8.10-24 (percolation flux at the water table). Second, the presence of the highly conductive faults, such as Splay G of the Solitario Canyon fault and the Ghost Dance fault splay, act as conduits for fast transport, despite the fact that the vitric CHn unit underneath the TSw behaves as a porous medium (with relatively lower water velocities). This may be facilitated by flow focusing in the vitric unit, whose vertical distribution shows a funnel-type structure in the south. Third, the low-permeability zones at the TSw-CHn interface in the northern part of the potential repository act as barriers to water drainage, and lead to low water velocities and the presence of perched-water bodies. Radionuclides move slowly through the perched water before reaching the underlying conductive zeolitic CHn, hence the delay in transport.

#### **8.10.10.7 Three-Dimensional Site-Scale Transport of Plutonium True Colloids**

As a submodel of the unsaturated zone radionuclide transport model, the EOS9nT version 1.0 module of TOUGH2 was used to simulate three-dimensional transport of plutonium colloids (CRWMS M&O 2000l, Section 6.16, p. 166). The colloid simulations used the same horizontal numerical grid (Figure 8.10-4) and vertical layering scheme (Figure 8.10-5, Table 8.10-1) as were used to calculate flow fields for input to TSPA (Section 8.10.6.8) under the mean present-day infiltration regime.

##### **8.10.10.7.1 Colloidal Forms, Properties, and Filtration Model**

True colloids are assumed to have the properties of PuO<sub>2</sub> (plutonium oxide) and are subject to radioactive decay (CRWMS M&O 2000l, Section 6.16, p. 166). Four colloids of different sizes (450 nm, 200 nm, 100 nm, and 6 nm) were considered, with their accessibility factors into the geological units taken from CRWMS M&O (2000o, Table 1). The linear kinetic model of colloid filtration was used, with the clogging kinetic coefficient  $\kappa^+$  directly computed (CRWMS M&O 2000l, Section 6.16.2, p. 167). There was no information on the kinetic declogging (reverse) coefficient  $\kappa^-$ , which was entered as a fraction of  $\kappa^+$  to examine the sensitivity of this parameter on colloidal transport.

##### **8.10.10.7.2 Colloid Transport Simulations**

For a given  $\kappa^+$ , the simulations showed that the transport of radioactive true colloids is strongly influenced by the  $\kappa^-$  so that when no declogging was allowed, no colloids would reach the water table (CRWMS M&O 2000l, Sections 6.16.3 to 6.16.7, pp. 169 to 176). For a given  $\kappa^+$ , the colloid size has a significant effect on transport, as indicated in Figure 8.10-63 (CRWMS M&O 2000l, Sections 6.16.3 to 6.16.7, pp. 169 to 176). Small values of  $\kappa^-$  (slow declogging) were shown to lead to significant retardation of colloids and long travel times to the water table. In the case, of  $\kappa^- = 10\% \kappa^+$   $t_{10}$  was more than 10 k.y., and  $t_{50}$  could not be reached because the maximum attainable  $R$  at the water table never exceeds 0.3 (Figure 8.10-63). Large values of  $\kappa^-$  (fast declogging) would result in very fast travel rates for the radioactive colloids to the water table. In the case of  $\kappa^- = 100\kappa^+$ ,  $t_{10}$  can be as low as 15 yr. (Figure 8.10-63). The extreme sensitivity of colloid filtration on  $\kappa^-$  and the dearth of representative information on this value for

the various geologic units in the unsaturated zone point to the need for additional study in this area.

Given the fact that fractures are the primary transport conduit at Yucca Mountain, the inability of larger colloids to diffuse into the matrix because of smaller diffusion coefficient values and size exclusion results in fast transport to the water table. Smaller colloidal particles can diffuse easier into the matrix and, thus, their transport is more retarded. Size exclusion at the interfaces of different geologic units leads to colloid concentrations that can be significantly higher than those in the water released from the potential repository. This phenomenon is more pronounced for larger colloids.

#### **8.10.10.8 Alternative Model of Radionuclide Transport**

As discussed in Sections 8.10.10.6 and 8.10.10.7, the primary mechanism for radionuclide retardation in the unsaturated zone is diffusion from fractures into the matrix. This process transfers radionuclides from the fast pathways to the matrix, where their transport is retarded because of the much slower water velocities and matrix sorption for sorbing radionuclides. An alternative conceptual model that does not allow diffusion into the matrix also was investigated (CRWMS M&O 2000l, Section 6.17, pp. 177 to 180), as described below.

##### **8.10.10.8.1 Radionuclide Transport Simulations without Matrix Diffusion**

For mean present-day infiltration, the alternative model showed that the nonsorbing  $^{99}\text{Tc}$  and the moderately sorbing  $^{237}\text{Np}$  would move unhindered in the fractures with their  $t_{10}$  and  $t_{50}$  values being about 5 and 30 yr., respectively (CRWMS M&O 2000l, Section 6.17.1 p. 177). A characteristic plateau at 50 yr. marks their arrival at the water table from fracture flow (Figure 8.10-64). The effects of the matrix flow become evident for  $t > 100$  yr. when matrix flow and radionuclides begin to arrive at the water table. The nonsorbing  $^{99}\text{Tc}$  arrives at the water table earlier than the moderately sorbing  $^{237}\text{Np}$ . The phase of constant  $^{237}\text{Np}$  release from fracture flow lasts from 50 to about 2,000 yr., after which time the matrix flow (and the  $^{237}\text{Np}$  it transports) arrives at the water table.

The model also showed that the limited sorption on the fracture walls is, however, sufficiently important to retard transport of strongly sorbing  $^{239}\text{Pu}$  in the fractures (CRWMS M&O 2000l, Section 6.17.1, pp. 178 and 179). When only  $^{239}\text{Pu}$  was considered, the simulated fracture release rate reached a plateau at about 300 yr., which is a very short time considering its half-life. The simulation showed that there was no matrix flow contribution to the release of  $^{239}\text{Pu}$  in the first 1 m.y. Accounting for the daughter products led to matrix contributions to the water table after 10 k.y., consisting almost exclusively of the  $^{235}\text{U}$  daughter, which sorbs less strongly than  $^{239}\text{Pu}$  (Figure 8.10-64).

##### **8.10.10.8.2 Colloidal Transport Simulation without Matrix Diffusion**

Analysis of the alternative model indicates that diffusion is less significant in colloid transport than in radionuclide transport (CRWMS M&O 2000l, Section 6.17.2, p. 179). This is because colloid diffusion is smaller than radionuclide molecular diffusion because of the larger colloid size, and size-exclusion effects at the interfaces of different geologic units further limit entry of

colloids into the matrix by diffusion, especially larger colloids. However, the effect of matrix diffusion becomes increasingly important for decreasing colloid size (Figure 8.10-64).

The colloid breakthrough curves (Figure 8.10-64) do not exhibit the plateaus in the 100-yr. to 10-k.y. time range, denoting pure fracture transport with no matrix contribution, that the radionuclide curves do (CRWMS M&O 2000l, Section 6.17.2, p. 179). The more continuous slope of the colloid curves through this time period indicates slower transport in the fractures (as a result of filtration at the geologic unit interfaces) and evolution of concentrations larger than those in the water released from the potential repository. Hence, within the 100-yr. to 10-k.y. time range, the colloid concentration gradients keep increasing over time and do not reach steady state as those for the radionuclides do.

#### **8.10.10.9 Model Validation Using Data from the Busted Butte Test Facility**

The conceptual and numerical models of radionuclide transport of the unsaturated zone radionuclide transport model were validated, to the extent possible, using data from the Busted Butte test facility. The Busted Butte test facility was chosen based on the presence of a readily accessible exposure of the TSw and the CHn hydrogeologic units and the similarity of these units at this location to their occurrence beneath the potential repository horizon (CRWMS M&O 2000l, Section 6.10, p. 102). A detailed description of the Busted Butte Test Facility studies is provided in Section 10.7.2.

##### **8.10.10.9.1 Laboratory Radionuclide-Sorption Measurements**

Table 8.10-14 presents the radionuclide-sorption ( $K_d$ ) test results obtained on rock samples collected from the TSw and CHn hydrogeologic units at Busted Butte (CRWMS M&O 2000n, Section 6.8.5.1.2.2, pp. 170 and 171). Although values of  $K_d$  for americium in Table 8.10-14 are similar to those in Table 8.10-10, the sorption values for plutonium and neptunium from the Busted Butte data are significantly larger. The fines from sample crushing were not removed during the Busted Butte sorption study, while removal of fines was a routine step used in the standard batch-sorption procedures of the YMP. If this is the cause of the difference in sorption, it shows that the standard procedure and the  $K_d$  values used for TSPA (Table 8.10-10) are conservative.  $K_d$  values could be related to the sample sizes used for sorption measurement, and using small-sized samples could generate larger  $K_d$  values.]

The effect of a large  $K_d$  on the transport of  $^{237}\text{Np}$  in the vitric tuff of the unsaturated zone was evaluated by conducting three-dimensional, site-scale numerical modeling. Figure 8.10-65 shows the concentration profiles for  $^{237}\text{Np}$  using the  $K_d$  value of 1 mL/g (Table 8.10-10) and the  $K_d$  value of 20 mL/g (Table 8.10-14) in the vitric CHn unit. Concentration profiles for  $^{99}\text{Tc}$  and  $^{239}\text{Pu}$  (Figure 8.10-61) also are shown in Figure 8.10-65. The large  $K_d$  for  $^{237}\text{Np}$  delays the  $t_{10}$  (arrival of the 0.1 relative concentration at the water table) from 10 to 13 k.y., and delays the  $t_{50}$  from 120 to 290 k.y.

##### **8.10.10.9.2 Field Tracer Tests**

The Busted Butte unsaturated zone transport test is a phased long-term experiment being conducted at Yucca Mountain. The field work for the first phase has been completed, but the analysis of the experimental results is currently underway. A complete description of the Busted

Butte field transport studies, including objectives, is provided in Section 10.7.2. A summary of the numerical results of the Phase 1A and Phase 1B tests is provided below. Numerical simulations of two components of the first phase of the tracer test (Phases 1A and 1B) were conducted (CRWMS M&O 2000l, Section 6.10).

**Phase 1A Test**—The Phase 1A Busted Butte tracer test was conducted in the vitric CHn unit, corresponding to specifically layers ch1v and ch2v of the unsaturated zone radionuclide transport model (CRWMS M&O 2000l, Figure VI.1). The test involved injection rates of 10 mL/hr into boreholes 1 and 3, with borehole 3 located about 20 m (66 ft) above the ch1v-ch2v interface in the ch1v and borehole 1 farther away from the interface in the ch1v (CRWMS M&O 2000l, Section 6.10.1, p. 103). Injections were conducted continuously for 285 days, starting from April 2, 1998. At the end of the test, digital photographs were taken to evaluate tracer distribution, and rock samples were collected for moisture and tracer analysis. A three-dimensional modeling study, using data from calibrated-properties model (Section 8.10.5) and hydraulic-property measurements from field samples, was conducted to predict the concentration of a nonreactive tracer (bromine) and water saturation distributions.

The simulated bromine distribution in borehole 1 exhibits symmetric, near-circular patterns, and indicated the dominance of capillary over gravitational forces in the vitric CHn unit (CRWMS M&O 2000l, Section 6.10.1, p. 104). This was consistent with the experimental results and the expected flow and transport behavior in the CHv unit. Simulations of borehole 3 using only data from the calibrated-properties model showed that the flattening of tracer distribution occurs as the tracer moves preferentially laterally along the ch1v–ch2v interface. Experimental results from the tracer test also showed the flattening behavior for borehole 3. When the hydraulic-property measurements from field samples were used in the simulation, the bromine distribution followed a more uniform pattern, which exhibits little flattening. These results suggest that the hydraulic properties from the calibrated-properties model are more representative of the in situ conditions than the limited number of core measurements from the test location.

**Phase 1B Test**—In the Phase 1B field test, three tracers were injected into the lower portion of the TSw basal vitrophyre, which is a relatively low-permeability fractured rock (CRWMS M&O 2000l, Section 6.10.2, p.105). The three tracers were Br<sup>-</sup> (nonsorbing), 2,6-difluorobenzoate (2,6-DFBA, nonsorbing, used to evaluate possible molecular size effects on transport) and Li<sup>+</sup> sorbing). The tracer solution was injected into borehole 5 at a rate of 10 mL/hr at a depth of 1.30 m (4.3 ft) from the rock surface. Injections took place between on May 12, 1998 and November 9, 1998. Liquid samples were collected regularly from borehole 6 and analyzed for the three tracers. Boreholes 5 and 6 are horizontal, parallel to one another, and 0.28 m (0.92 ft) apart (see CRWMS M&O 2000l, Figure VI.6). For the three-dimensional numerical simulations, the domain of the test was treated as a homogeneous, unfractured rock matrix. Although this geologic layer was known to have fractures, the representation of unfractured rock matrix in the simulation was justified by the system behavior during the injections, which did not show evidence of fracture flow. Experimental breakthrough data for both the nonsorbing and sorbing tracers can be found in CRWMS M&O (2000n, Section 6.8.5.3.2, pp. 174 to 178). Peak concentrations were observed directly beneath the injection point of borehole 5. The measured concentrations indicate transport consistent with flow in the matrix (rather than in the fractures), which appeared to quickly imbibe the injected solution.

Visual inspection of the predicted breakthrough curves for nonsorbing tracer at several sampling locations indicated that the model predictions were in good agreement with the measured data (CRWMS M&O 2000l, Section 6.10.2, p. 107). The breakthrough curves of sorbing tracer  $\text{Li}^+$  (lithium) follow a distinctively different pattern. Sorption of  $\text{Li}^+$  resulted in maximum relative concentrations significantly lower than the ones observed in the nonsorbing tracers. Model predictions based on the laboratory-derived  $K_d$  (1 mL/g for  $\text{Li}^+$ ) were higher than the measured concentrations in CRWMS M&O (2000n, Section 6.8.5.3.2). The  $K_d$  measurements of  $\text{Li}^+$  were preliminary and more detailed sorption measurements are in progress (CRWMS M&O 2000n, Section 6.8.5.1.1, pp. 169 and 170). When  $K_d$  was increased to 2 mL/g, model predictions were consistent with the measured  $\text{Li}^+$  concentrations (CRWMS M&O 2000l, Section 6.10.2, p. 107).

INTENTIONALLY LEFT BLANK

## **8.11 EVIDENCE OF PAST PERCOLATION THROUGH THE UNSATURATED ZONE**

Deposits of secondary minerals (mainly low-temperature calcite and opal) in fractures and cavities mark pathways of past percolation of water through the unsaturated zone (Paces, Marshall et al. 1997, p. 1). These mineral coatings preserve a history of deposition that can be deciphered by isotopic dating. Morphologic relations, as well as chemical and isotopic compositions of these secondary minerals, provide an interpretable record of paleohydrologic conditions within Yucca Mountain. An understanding of the origins of calcite and opal in these settings provides a set of observational data that may provide constraints on fracture flow through the mountain and on the unsaturated zone hydrologic models used to represent this flow (Paces et al. 1998, p. 36).

### **8.11.1 Data Sources**

The principal sources of data, analyses, and interpretations for the investigation of past percolation through the unsaturated zone are Paces, Marshall et al. (1997); Neymark et al. (1998); and Paces, Neymark et al. (1996). Data include U/Pb and Th isotope ratios, <sup>14</sup>C analyses, C and O stable isotope ratios, and strontium and rubidium isotope data for secondary minerals in the Exploratory Studies Facility (ESF) and selected surface-based boreholes.

### **8.11.2 Hydrologic Implications of Deposits of Secondary Minerals in the Unsaturated Zone at Yucca Mountain**

Detailed studies of secondary minerals within the ESF (Paces, Marshall et al. 1997, pp. 1 to 3) have shown multiple episodes of mineral deposition. Most of the secondary mineralization within the unsaturated zone occurs as coatings on the footwalls of fractures or as accumulations on the floors of lithophysal cavities. Within the bedded tuffs, however, calcite occurs locally as a pore-filling cement. The preferred localization of secondary minerals demonstrates precipitation under water-unsaturated conditions, and results of dating of the minerals (Neymark et al. 1998, pp. 85 to 87) show that the undersaturated conditions, at least at the level of the ESF, have persisted for several million years.

Textural evidence further supports deposition of secondary minerals from aqueous solutions within the unsaturated zone (Paces, Neymark et al. 1996, p. 1). Calcite typically forms equant, blocky prisms on high-angle fracture surfaces, and unusual delicately bladed crystals in lithophysal cavities and in low-angle fractures. Opal typically forms water-clear solid-hemispherical bubbles, botryoidal bubbly masses, or thin sheets coating calcite substrates. Opal commonly occurs at the tops of calcite blades. Both opal and calcite are finely layered (micron to submicron) and commonly are intimately intergrown. Outermost surfaces of both minerals show little evidence of dissolution, although scattered patches of basal porous zones may be related to dissolution of early-formed calcite blades. Textural evidence indicates that the deposition of low-temperature minerals occurred under unsaturated hydrologic conditions, with no indication of zones of water ponding even locally. Open space appears to be required for mineral deposition, and the occurrence of secondary mineral coatings on fracture footwalls and cavity floors indicates the strong influence of gravity on water percolating through the unsaturated zone. Bladed calcite textures, along with the occurrence of opal at the topographically highest sites, indicate mineral growth preferentially on tips and edges rather than

on faces. Mineral textures require solutions to transport ions to crystal tips where conditions of mineral saturation or supersaturation are attained. A depositional scenario consistent with observed textures involves water moving down fracture surfaces as sheets or films that drip into cavities where interactions between the liquid and an independently migrating gas phase result in the slow-growing secondary mineral deposits.

Ages of the low-temperature minerals have been investigated using radiocarbon (calcite),  $^{230}\text{Th}/\text{U}$  (calcite and opal), and  $\text{U}/\text{Pb}$  (opal) methods (Paces, Neymark et al. 1996; Paces, Marshall et al. 1997; Neymark et al. 1998). Sampling for the first two techniques emphasized the outermost growth surfaces in order to determine ages of the youngest depositional events. Most  $^{14}\text{C}$  measurements indicate at least small amounts of modern carbon resulting in a range of ages from 44 to 16 k.y. (Figure 8.11-1) with the greatest number of ages distributed between 38 and 28 k.y. (Paces, Neymark et al. 1996, p. 2). Multiple subsamples of outermost calcite layers from the same occurrence typically show discordant  $^{14}\text{C}$  ages well outside of analytical error. Calcite and opal dating show similarly wide ranges of ages for subsamples from the same surface; however, in the case of  $^{230}\text{Th}/\text{U}$ , calculated ages range from 28 k.y. to greater than 500 k.y., with most analyses between 50 and 400 k.y. (Figure 8.11-1). Like radiocarbon results, calcite and opal ages for outermost materials are not in secular equilibrium, implying that growth surfaces contain components that are less than 500 k.y. No systematic age differences are observed between calcite and opal regardless of occurrence, indicating that lithophysal cavities are as likely to receive percolating water as are fracture pathways. Like radiocarbon ages,  $^{230}\text{Th}/\text{U}$  ages from secondary minerals near or within the discrete zones of elevated  $^{36}\text{Cl}/\text{Cl}$  showed similar distributions relative to those in zones with background levels of  $^{36}\text{Cl}/\text{Cl}$  (Figure 8.11-2a). To date, no anomalously young mineral deposits dated by radiocarbon or  $^{230}\text{Th}/\text{U}$  have been identified in the zones with elevated (bomb-pulse)  $^{36}\text{Cl}/\text{Cl}$  (Paces, Neymark et al. 1996, Section 3.2.2, p. 18). Therefore, if the elevated  $^{36}\text{Cl}/\text{Cl}$  values are proved to be the result of bomb-pulse water moving down fast pathways, then that water seems not to be responsible for mineral deposition in these zones.

Calculated initial  $^{234}\text{U}/^{238}\text{U}$  ratios representing the isotopic composition of percolating waters at the time of mineral deposition range from 4 to 9.5 (Figure 8.11-2b) for samples younger than 100 k.y. (Paces, Neymark et al. 1996, p. 2). Like the ages, these wide ranges of initial  $^{234}\text{U}/^{238}\text{U}$  are observed from subsamples from the same occurrence, indicating that minerals were deposited from solutions that were highly variable on a small spatial scale. The highest initial ratios, the youngest ages, and the thickest ESF mineral coatings are observed within the potential repository horizon. In addition, the data show a distinct negative covariance between age and calculated initial  $^{234}\text{U}/^{238}\text{U}$  that is not readily explained by conventional episodic/instantaneous depositional models. As with the  $^{230}\text{Th}/\text{U}$  ages, there seems to be no correlation between  $^{234}\text{U}/^{238}\text{U}$  values and zones of elevated  $^{36}\text{Cl}/\text{Cl}$  (Paces, Neymark et al. 1996, Section 3.2.3, p. 19).

Initial  $^{234}\text{U}/^{238}\text{U}$  ratios show modifications from compositions typical of surface waters and pedogenic sources as a consequence of percolation (Paces, Neymark et al. 1996, p. 3). Initial  $^{234}\text{U}/^{238}\text{U}$  in the ESF materials increase with depth to values as high as 8 to 9.5 at the repository horizon (Figure 8.11-2b). Wholesale dissolution or leaching of U would not result in elevated  $^{234}\text{U}/^{238}\text{U}$ . Rather, the increases in excess  $^{234}\text{U}$  fit a model of preferential dissolution of U isotopes during downward percolation of solutions because  $^{234}\text{U}$  is located in more readily accessible sites than  $^{238}\text{U}$  because of alpha-recoil decay processes. Perched and shallow

saturated-zone waters beneath Yucca Mountain are consistent with the large  $^{234}\text{U}/^{238}\text{U}$  ratios found in secondary mineral deposits. The high  $^{234}\text{U}/^{238}\text{U}$  ratios observed in ESF minerals indicate that rates of water percolation are low enough to allow selective dissolution of  $^{234}\text{U}$  and to allow replacement of  $^{234}\text{U}$  to percolation-accessible sites by further decay of U so that high ratios are maintained with time.

The available data on mineral deposits are consistent with a depositional model in which very thin layers are added, more or less continuously, at a scale much finer than sampling techniques can resolve (Paces, Neymark et al. 1996, p. 2). This hypothetical model is formulated on the assumptions that deposition proceeds at very slow but uniform rates so that all samples of finite size will integrate multiple, infinitely thin layers with continuously varying ages. Resulting isotopic measurements will represent mixtures of materials intermediate between the oldest and the youngest layers. Calculated  $^{230}\text{Th}/\text{U}$  ages and initial  $^{234}\text{U}/^{238}\text{U}$  for hypothetical samples follow trends that approximate the observations. In addition, the model predicts:

- Age discordance will exist between isotopic systems, with the amount and direction of discordance dependent on the respective half-lives of the isotopic systems.
- Samples will always have ages less than the theoretical maximum limit of the isotopic system, if even the thinnest layers of modern materials are present on the exterior of the sample.
- The youngest ages will be from the thinnest samples of the outermost mineral coatings.

An important condition of this model is that deposition must occur very slowly and over very long periods of time (Paces, Neymark et al. 1996, p. 2). Observed rates of deposition are in accord with this condition. Rates of deposition (1 to 10 mm of mineral per 1 m.y.) inferred from outermost materials are similar to those calculated, assuming that the total thickness of mineral coatings accumulated since the time of tuff emplacement. Ages determined by  $^{230}\text{Th}/\text{U}$  are more representative of true average ages than are radiocarbon ages because of the longer half-life of  $^{230}\text{Th}$ , but young radiocarbon ages document the addition of calcite younger than about 15 to 20 k.y. on outermost surfaces. Interpretation of geochronological data in this scenario also implies that deposition of a finite amount of material occurred over a longer period of time than represented by the numerical age alone, and, as a result, lower fluxes can account for the same thickness of deposits.

Stable and radiogenic isotopes incorporated into calcite and opal at the time of formation reflect the isotopic compositions of percolating fluids, which, in turn, relate to sources and climate conditions prevalent at the time of infiltration (Paces, Neymark et al. 1996, pp. 2 to 3). Infiltrating solutions acquire C and Sr isotopic signatures through interactions with soils and remain largely unmodified during percolation. Values for  $\delta^{18}\text{O}$ ,  $\delta^{13}\text{C}$ , and  $^{87}\text{Sr}/^{86}\text{Sr}$  for outermost calcites vary over limited ranges, reflecting the compositions of modern calcite-rich soils and fractionation because of present geothermal gradients. In contrast, early-stage calcite shows distinct differences in all three isotope systems, including lighter values for  $\delta^{18}\text{O}$ , heavier values for  $\delta^{13}\text{C}$ , and less radiogenic values for  $^{87}\text{Sr}/^{86}\text{Sr}$ . The three systems show covariance, indicating that common mechanisms controlled the variations in isotopic compositions of early infiltrating solutions. Data for the earliest calcite indicate that geothermal gradients may have been steeper,

methane may have been an important carbon species controlling carbon fractionation in the subsurface, and Sr was derived from a source that was less radiogenic than the current soil reservoir. Thus, the unsaturated zone may have changed substantially over 12 m.y., with the present-day soil-subsurface system having been established only within the last several million years. These isotopic variations support the concept that the secondary mineral records date back to the early history of flux through the mountain. At the scale sampled, the isotopic data show no evidence of a cyclic pattern within the younger parts of the deposits that could be related to climate variation over the last 500 k.y.

The mineral record can be used to estimate past water flux through the unsaturated zone, if the distribution of secondary minerals is known in space and time, and if the volumes of water required to account for the mineral deposits can be estimated (Paces, Neymark et al. 1996, p. 3). Preliminary estimates of the abundance of secondary minerals have been made from ESF observations. Hydrochemical compositions of surface runoff are nearly saturated with respect to calcite and opal and are assumed to represent shallow, infiltrating solutions. Assuming all  $\text{Ca}^{+2}$  is extracted from these waters en route to the saturated zone, a minimum value of flux of about 2 mm/yr. is obtained as an average over the last 12.7 m.y.. Although similar values have recently been determined for current flux from other data sets, this value is considered to be provisional.

Calculation of percolation flux based on the abundance of secondary minerals was refined by Paces, Marshall et al. (1997, Appendix F) (Section 8.7.5). These results suggest that the percolation flux is about 1.4 mm/yr., based on the deposition of calcite, and about 2.5 mm/yr., based on the deposition of opal. More recent analysis by Marshall et al. (1998, p. 129, Figure 1) has shown that percolation flux values from secondary mineral deposition correlate quite well with estimates from the infiltration model (Section 8.2) in the Tiva Canyon welded unit above the Paintbrush nonwelded (PTn) unit. However, there was no correlation between the two methods for the Topopah Spring welded unit below the PTn. These results suggest that percolation is diverted laterally or substantially redistributed by the PTn. Further, the secondary mineral abundances below the PTn suggest that percolation fluxes are as much as 10 times lower than estimates from the infiltration model.

Surface records from the Yucca Mountain area indicate that the regional climate over the last 1 m.y. was characterized by wetter and cooler conditions, relative to the present, for as much as 80 percent of the time (Paces, Neymark et al. 1996, p. 3). However, there is no indication in the subsurface that deposition rates of calcite and opal varied greatly during this interval, even though higher water tables throughout the region reflect greater recharge during pluvial periods. Evidence for nondeposition or substantial dissolution of youngest calcite or opal surfaces that might be expected if infiltrating waters were significantly more dilute is also lacking. Instead, observed  $^{230}\text{Th}/\text{U}$  ages are more or less evenly distributed throughout the last 400 k.y., with the possibility that depositional hiatuses may have occurred during interglacials about 100 and 200 k.y.. The isotopic age distributions are consistent with a model in which the rock mass remained transmissive in areas represented by secondary mineral deposits over much of the last several hundred thousand years. These observations suggest that percolation (and mineral deposition) through most of the Topopah Spring Tuff may have been buffered from variations in effective moisture except in the zones of highest flux (highly transmissive pathways associated with through-going structures).

Further evidence of the stability of hydrologic conditions in the deep unsaturated zone is provided by the results of U/Pb age dating of secondary minerals (Neymark et al. 1998, pp. 85 to 87). These results indicate that average long-term rates of deposition of calcite and opal in the Topopah Spring welded unit have not varied substantially during the last 8 m.y., despite probable major climatic shifts toward conditions of increasing aridity and greater seasonality. Further, the difference between rates of deposition for shallow and deep secondary minerals suggest that the PTn acts as a significant diversionary or buffering unit for the unsaturated zone hydrologic system.

INTENTIONALLY LEFT BLANK

## 8.12 SUMMARY OF UNSATURATED ZONE HYDROLOGY

The Yucca Mountain site occupies an intermediate position between areas of recharge and discharge of the regional groundwater flow system (Section 8.1). The aridity and small average rate of recharge produce a correspondingly small groundwater flux, which is readily transmitted through the extensively fractured rocks that compose most of the region. As a result of these conditions, the water table commonly is deep beneath the land surface, particularly beneath prominent ridges such as Yucca Mountain. The combination of aridity, large topographic relief, and transmissive rocks results in a thick unsaturated zone, which is a principal hydrologic attribute of the site and is proposed as the host environment for the repository. At the crest of Yucca Mountain, the water table is about 750 m (2,500 ft) below land surface and about 360 m (1,200 ft) below the potential repository horizon.

The rock units that comprise the unsaturated zone include Quaternary surface deposits (alluvium and colluvium, soil) and the Tertiary volcanic tuffs (Section 8.1). The six principal hydrogeologic units defined in the unsaturated zone at the site are unconsolidated alluvium, Tiva Canyon welded (TCw), Paintbrush nonwelded (PTn), Topopah Spring welded (TSw), Calico Hills nonwelded (CHn), and Crater Flat undifferentiated (CFu). These hydrogeologic units, together with natural hydrologic processes, control water and gas movement in the unsaturated zone, including net infiltration, percolation, fracture-matrix interaction, accumulation of perched water, lateral flow, and deep percolation to the water table. These processes determine the amount of water that may seep into repository drifts and possibly come in contact with waste packages, thus enabling the dissolution and transport of radionuclides away from the repository. The occurrence of these processes, especially percolation, is greatly affected by the vertical stratification and specific sequencing of hydrogeologic units, as well as transitions between them.

### 8.12.1 Site Infiltration

Data and interpretations from field studies at Yucca Mountain, combined with insights about hydrologic processes documented in the scientific literature, have led to a detailed understanding of the physical processes and properties that control net infiltration (Section 8.2). These processes include precipitation, surface runoff and run-on, infiltration, evapotranspiration, and the redistribution of moisture in the shallow subsurface. Precipitation, which is the dominant hydrologic process at the site, depends mostly on meteorological factors, but also is affected by geographic location, elevation, and physiography. Evapotranspiration is the second most dominant hydrologic process and depends on vegetation, the distribution of moisture stored in the shallow subsurface, soil thickness, and the heat energy balance between the shallow subsurface and the atmosphere. Redistribution of moisture in the shallow subsurface, which is dynamically integrated with evapotranspiration, occurs in response to gravity and matrix potentials of the rock and depends strongly on soil and bedrock properties. Because all these physical processes are involved, net infiltration is both temporally and spatially variable.

Because the topography of Yucca Mountain significantly affects hydrologic processes, the spatial distribution of infiltration can be defined in terms of generalized topographic positions that represent zones of infiltration: ridgetops, sideslopes, terraces, and channels (Section 8.2.2.3). The ridgetops generally are flat to gently sloping, have little or no soil cover,

and are relatively stable morphologically. The bedrock underlying ridgetops tends to be moderately to densely welded and moderately to highly fractured. The higher elevations of the ridgetops and upper slopes have significant potential for sustaining a thin snow cover for up to several weeks during the winter. Sideslopes are distinguished from the terraces and channels by depth of soils and slope. Soil cover on sideslopes is thin to nonexistent, and in most locations, bedrock is densely welded and highly fractured. The sideslopes are approximately north or south facing in the southern part of the site and, therefore, have different seasonal solar radiation loads. In the northern washes, although the sideslopes face more southwestward and northeastward, the steepness of the slopes accentuates seasonal radiation differences. Terraces and channels are located at lower elevations of primary washes and have thin soil cover in the upper washes and thick soils farther down. Very little bedrock is exposed in the washes. The surface of terraces and washes is relatively flat and dissected by old soil channels and active channels. Channels differ from terraces in that the periodic runoff that occurs in the channels in response to extreme precipitation conditions can rework the channel materials. Although channels occupy a very small surface area of the wash, they can contribute significantly to net infiltration during runoff events. Over the area of the site-scale unsaturated zone flow model, ridgetops encompass about 7 percent of the model area, sideslopes about 47 percent, terraces about 44 percent, and active channels about 2 percent.

A numerical, water-balance, net infiltration model was developed for the Yucca Mountain area, including the area of the three-dimensional, site-scale unsaturated zone flow model (Section 8.2.5). The net infiltration model uses a wide range of detailed physiographic and hydrologic information, including location identification, latitude, longitude, elevation, slope, aspect, soil type, soil depth, underlying geologic formation, geomorphic position, and the location of the surrounding topography that blocks the site for diffuse or direct-beam solar radiation. Using these data and a daily precipitation record as input, the model calculates daily values of net infiltration using a water-balance approach, first by calculating the amount of water available for net infiltration and then calculating actual net infiltration based on the effective hydraulic conductivity of the bedrock. The initial net infiltration model was calibrated by comparison of evapotranspiration calculated by the Priestley-Taylor equation to water loss from the water content profiles of the 99 neutron boreholes (Section 8.2.5.5). The total water content change in the soil profile through time was compared to model results for the same period using the estimated or measured record of daily precipitation for each borehole site.

Simulation results from the model, using a scaled 100-yr. stochastic precipitation record, indicated that average annual precipitation for the Yucca Mountain site was 150 mm/yr. and average net infiltration was 3.2 mm/yr. (Section 8.2.6.1). Maximum net infiltration of 63 mm/yr. was simulated at relatively high elevations north of the potential repository site where high-permeability, nonwelded tuffs are exposed at the surface. Minimum values of 0.0 mm/yr. net infiltration were simulated at all locations with soil 6 m (20 ft) thick or greater, which tend to be the terraces and channels in washes.

The initial net infiltration model (1996) was modified substantially in order to more accurately simulate net infiltration in the vicinity of Yucca Mountain (Section 8.2.7). The most important modifications involved reformulation of model boundaries into 10 small watershed domains; formulation of a surface-flow, runoff-routing module; and improved modeling of surface evaporation and root-zone transpiration. The revised net infiltration model (1999) was calibrated

by comparison of model-simulated streamflow to discharge measures at five stream-gauging sites on Yucca Mountain during 1994 to 1995 (Section 8.2.9).

The numerical infiltration model was used to simulate lower-bound, mean, and upper-bound infiltration associated with three climate scenarios determined to be pertinent to performance of the potential repository: modern (present-day), monsoon, and glacial-transition (Section 8.2.10). The modern, or present-day, climate conditions are expected to prevail for about the next 600 yr. Monsoon climate conditions, with wetter summers than the modern climate, are expected to prevail for the following 1,400 yr. Glacial-transition climate conditions, with cooler air temperatures and higher annual precipitation than the modern climate, are expected to begin in about 2 k.y. and continue for about 10 k.y.

For the area of the potential repository (4.7 km<sup>2</sup> [1.8 mi.<sup>2</sup>]), simulation of the mean modern climate scenario resulted in average precipitation of 196.9 mm/yr. and average net infiltration of 4.7 mm/yr. (Section 8.2.10.4). For the lower-bound modern climate, precipitation was 191.6 mm/yr. and net infiltration was 0.4 mm/yr. For the upper-bound modern climate, precipitation was 277.5 mm/yr. and net infiltration was 11.6 mm/yr. Simulation of the mean monsoon climate scenario resulted in average precipitation of 309.3 mm/yr. and average net infiltration of 12.5 mm/yr. Simulation of the mean glacial-transition climate scenario resulted in average precipitation of 323.1 mm/yr. and average net infiltration of 19.8 mm/yr.

## **8.12.2 Properties of Hydrogeologic Units**

### **8.12.2.1 Matrix Hydrologic Properties**

Properties of hydrogeologic units in the unsaturated zone at Yucca Mountain were measured directly by use of two distinctly different methods: matrix properties analysis of rock cores and field-scale air-injection testing (Section 8.3). To define a physical and hydrologic properties database adequate for three-dimensional modeling of fluid flow in the unsaturated zone, an intensive study of matrix properties was performed using core samples from 31 boreholes. Nearly 5,000 core samples were analyzed in the laboratory to measure important hydraulic properties, including porosity, bulk density, particle density, water content, water potential, saturated and unsaturated hydraulic conductivity, and moisture retention characteristics. Unsaturated zone air-injection testing measured the bulk (or total) pneumatic permeability and porosity of the rock mass. When combined with other information, these data were used to analyze the flow of both water and gas through the unsaturated zone. Air-injection tests were performed to determine field-scale bulk permeability, porosity, and anisotropy (spatial variability) of the major rock units above, below, and within the potential repository horizon.

To support three-dimensional flow modeling of the unsaturated zone, intensive analysis of matrix hydrologic properties was performed and resulted in the delineation of 30 detailed hydrogeologic units (Section 8.3.2.2). The distributions of physical properties and hydrologic parameters at the Yucca Mountain site are complex because of the depositional, cooling, and alteration history of the rocks. This history has resulted in differences in porosity, connectivity and tortuosity of flow paths, water retention character, vertical heterogeneities, and scales of features that all influence the resulting hydrology of the unsaturated zone. Because water is stored in and flows through the interconnected pores of the rock matrix, porosity has proved to

be very useful for characterizing the hydrologic character of the various rock types (Section 8.3.2.2.1). In general, porosity can be related primarily to the depositional features and amount of welding of a rock, with the lowest porosities occurring in the most densely welded rocks and the highest porosities occurring in the nonwelded and bedded rocks. Field data indicate that distinct vertical changes in porosity, particle density, and saturation correspond with various lithostratigraphic boundaries. Consequently, the relations between porosity and saturation were used to subdivide the major hydrogeologic units into detailed hydrogeologic units. The TCw was divided into five detailed units, the PTn into six, the TSw into eight, the CHn into five, and the CFu into six.

Mineral alteration has a significant influence on the hydrologic properties such as porosity, because clays, zeolites, opal, and calcite form in situ or are deposited in pore spaces, causing a reduction in porosity (Section 8.3.2.2.1). However, the occurrence of clay or zeolite zones reduces the measured porosity only slightly because water is stored in clay and zeolite mineral structures rather than in pore spaces. Rocks containing clay or zeolites typically contain a relatively large volume of water, but because the water is held tightly within clay structures and very small pores, the permeability is reduced. The effects of alteration minerals on the hydrologic properties of the unsaturated rocks were evaluated further by comparing the relative-humidity porosity with the measured saturated hydraulic conductivity for 593 samples collectively representing all lithostratigraphic units (Section 8.3.2.2.2). Mineral alteration is particularly significant in the zeolitic rocks of the Calico Hills Formation in that these rocks have relatively high porosity (greater than 0.2) but very low saturated conductivity (generally less than  $1 \times 10^{-10}$  m/s). The presence of low-permeability, zeolitic rocks in the CHn apparently is a major factor in the formation of perched water below the potential repository horizon in the northern part of the site area.

To facilitate the use of matrix hydrologic properties data in numerical flow models, mean values and standard deviations for all measured properties were calculated for each of the 30 detailed hydrogeologic units using regression analyses (Section 8.3.2.2.3). These properties included bulk density, particle density, porosity, volumetric water content, saturation, water potential, and saturated conductivity. Moisture-retention van Genuchten curve-fit parameters ( $\alpha$ ,  $n$ , and  $m$ ) for each detailed hydrogeologic unit also were calculated (Section 8.3.2.2.4). Subsequently, moisture-retention curve-fit parameters were used to estimate unsaturated hydraulic conductivity based on values of saturated conductivity. These estimates then were compared with direct measurements of unsaturated hydraulic conductivity made using a steady-state ultra-centrifuge and were found to be in good agreement.

#### **8.12.2.2 Air-Injection Testing**

Air-injection testing was conducted in surface-based boreholes UE-25 UZ#16, USW SD-12, USW NRG-6, and USW NRG-7a (Section 8.3.3.1). Bulk air-injection permeability (fractures and matrix) values were determined from 194 single-hole air-injection tests conducted in the Tiva Canyon Tuff, Yucca Mountain Tuff, Pah Canyon Tuff, Topopah Spring Tuff, Calico Hills Formation, and three bedded tuffs within the PTn. Air-injection permeability values were compared to permeability values derived from laboratory tests and pneumatic monitoring. Because the air permeability of rock changes with water content, a given permeability also has

an associated capillary pressure. Consequently, the relationship between air-injection permeability and capillary pressure also was evaluated.

The mean air-injection permeability for the Tiva Canyon Tuff from the surface-based boreholes was  $12.0 \times 10^{-12} \text{ m}^2$  (Section 8.3.3.1.2). For the PTn, the mean air-injection permeability was  $0.54 \times 10^{-12} \text{ m}^2$ . Test results also indicated that the Yucca Mountain and Pah Canyon tuffs of the PTn exhibit decreasing permeability with increased depth, corresponding with decreasing welding with depth. For the Topopah Spring Tuff, the mean permeability values for individual boreholes ranged from  $0.4 \times 10^{-12} \text{ m}^2$  to  $4.7 \times 10^{-12} \text{ m}^2$ . Only one air-injection test was conducted in the Calico Hills Formation and it yielded a permeability value of  $1.7 \times 10^{-14} \text{ m}^2$  (Section 8.3.3.1.1). These data indicate that the Tiva Canyon and the Topopah Spring tuffs have similar permeabilities, although the Topopah Spring Tuff may be less permeable in the northern part of the site area. In general, however, the Tiva Canyon and the Topopah Spring tuffs are about 10 times more permeable than the PTn. The PTn, in turn, is about 30 times more permeable than the Calico Hills Formation.

Similar results were obtained from air-injection testing conducted in the first three alcoves of the Exploratory Studies Facility (ESF), although the ESF tests were at a different scale, consisted of a larger number of individual tests, and generally focused on specific subunits within the Tiva Canyon Tuff and the PTn (Section 8.3.3.2.1). The testing included air-permeability and gaseous-tracer testing of the Bow Ridge fault.

### 8.12.3 Gaseous-Phase Flow

Several deep boreholes at Yucca Mountain have been instrumented in the unsaturated zone and continuously monitored to record changes in pneumatic pressure with depth in response to changes in barometric pressure of the atmosphere (Section 8.4.2). Computed phase lags and residual amplitudes of the in situ pressure data indicate that individual lithostratigraphic units can be grouped into four distinct pneumatic systems that correspond to the major hydrogeologic units: TCw, PTn, TSw, and CHn (Section 8.4.2.1). Changes in atmospheric pressure are transmitted very rapidly throughout the TCw and, at many locations, the atmospheric signal is indistinguishable from the downhole pressure signal (8.4.2.1.1). In contrast, the PTn significantly attenuates the atmospheric-pressure signal because of higher porosity and water content and much lower fracture density and bulk permeability than the TCw (Section 8.4.2.1.2). Pneumatic attenuation by the PTn is greater in the northern part of the site area than the southern part because of differences in thickness, porosity, water content, and fracture density among the individual units that make up the PTn. In general, attenuation of the atmospheric pressure signal across the TSw is negligible (Section 8.4.2.1.3). Pressure signals seem to be transmitted nearly instantaneously throughout most of the entire vertical section of the TSw. Nearly all the pressure data from the TSw indicate that the fractures within the TSw apparently are very permeable and highly interconnected within both the lithophysal and nonlithophysal units. In situ pressure records indicate that essentially all of the remaining barometric signal is attenuated by the CHn, primarily due to low permeability and the presence of perched-water zones.

The magnitudes of the amplitude reductions and phase lags in pneumatic pressure are a reflection of the pneumatic diffusivities of the layers through which the pneumatic pressure signal has passed (Section 8.4.2.2). Therefore, the time-varying pneumatic pressures were used to estimate

the pneumatic diffusivities, and, ultimately, the effective gas permeabilities of single and combined stratigraphic layers bounded by monitoring stations.

Pneumatic pressure interference effects associated with excavation of the ESF by the tunnel-boring machine have been observed in all monitored boreholes (Section 8.4.2.3). The effects of ESF excavation on in situ pneumatic pressure were carefully monitored because such effects offer some insight on how the overall gaseous-phase system in the unsaturated zone has been effected by the direct exposure of deeply buried rock units to atmospheric pressure by way of the ESF tunnel. Further, monitoring of such effects also presented an opportunity to use the pneumatic stress caused by ESF excavation to determine large-scale pneumatic properties of the rock units and to identify pneumatic fast pathways within the subsurface. The most significant ESF-excavation-related events that produced pneumatic pressure interference effects were the penetration of the PTn and crossing of major faults, particularly the Drill Hole Wash fault. Pneumatic monitoring data indicate that some faults transmit pneumatic pressure signals over distances of several hundred meters nearly instantaneously. The pneumatic pressure interference effects observed in several boreholes were used in the formulation of a numerical model to estimate the permeability to air of the PTn and TSw (Section 8.4.2.4). Particular emphasis was placed on estimating horizontal permeability and the ratio of horizontal to vertical permeability of the TSw. The simulations confirmed that the ratio of vertical to horizontal permeability in the TSw is at least 2:1 (Section 8.4.2.4.3).

#### **8.12.4 Water Potential and Perched Water**

In situ water potential has been monitored at multiple depths in the unsaturated zone in seven deep, instrumented boreholes at Yucca Mountain (Section 8.5.1). Overall, the in situ water-potential profiles of these boreholes indicate that water potentials are generally high, greater than about 300 kPa (-3 bars), and are nearly depth-invariant across the entire TSw (Section 8.5.1.2). Although water potentials in the overlying PTn are slightly lower than in the TSw, the measured values in these two hydrogeologic units are considerably greater than would result if water potentials in the unsaturated zone were in a state of static equilibrium with the water table. This implies that the downward percolation flux is non-zero. The relatively large water potentials also indicate that the rock matrix of the TSw is sufficiently wet, at least near fractures, that should water flow through the fractures, it would undergo little imbibition by the rock matrix, due to small matrix permeability and small water-potential gradients across the fracture-matrix interface. Across the TCw, water potentials are progressively lower with decreasing depth, indicating greater imbibition capacity associated with the TCw and upward matrix flow across this unit. However, these observations do not exclude the possibility of episodic, downward fracture flow across this unit.

Water-potential data, together with pneumatic pressure characteristics prior to ESF excavation, indicate that the pneumatic characteristics of the TSw in the Ghost Dance fault zone are much different than elsewhere at Yucca Mountain (Section 8.5.1.2). Specifically, within the Ghost Dance fault zone, the TSw is much less isolated from the atmosphere than elsewhere, probably due to higher fracture densities in the PTn. This enhanced connection to the atmosphere and the effects of more deeply penetrating barometric pumping result in a moisture regime that has the potential to be more dynamic than elsewhere because it may be subject to both rapid, focused percolation of liquid water and the drying effects of barometric pumping.

Water-potential data from at least two boreholes indicate drying of the rock mass near the boreholes due to excavation and ventilation of the ESF (Section 8.5.1.3). In one case, the drying of the rock mass has been sufficient to cause increases in drained porosity and decreases in pneumatic diffusivity of the rock, resulting in changes in the pneumatic characteristics of the affected units. In another case, the drying of the rock mass was sufficient to reverse a slow but steady wetting trend that had begun when the borehole was instrumented. The drying in the vicinity of this borehole was accompanied by a slight warming of the rock surrounding the borehole interval nearest in elevation to the ESF.

Perched water has been identified below the potential repository horizon in seven boreholes in the Yucca Mountain site area (Section 8.5.2). In all cases, accumulation of perched water seems to be caused by either the basal vitrophyre of the Topopah Spring Tuff or the vitric-zeolitic boundary in the Calico Hills Formation acting in concert with a lateral structural barrier. Site-scale, numerical model simulations of the unsaturated zone flow system indicate that perched water probably is more extensive beneath the site area than might be suggested by the occurrences in the seven boreholes. Two water bodies were detected in a borehole north of the potential repository in the area of the large hydraulic gradient (Section 8.5.2.7). The first water body was identified as perched water based on drilling data. The elevation of the fully recovered water level in the second water body was in the range of the large hydraulic gradient in the saturated zone.

#### **8.12.5 Temperature and Heat Flow**

Temperature measurements were made in numerous boreholes within the central block of Yucca Mountain and in the surrounding area in the 1980s as part of a regional heat-flow study (Section 8.5.3). More recently, in situ temperature measurements were made as part of the instrumented borehole monitoring program at Yucca Mountain. The measured temperature profiles provided a means for calibrating field-scale values of thermal conductivity and for calculating heat fluxes, from which estimates of percolation flux were made. Temperature measurements made in instrumented boreholes since 1994 confirm the general findings and conclusions of earlier studies: (1) heat flow in the unsaturated zone primarily is conductive, and (2) temperature gradients in the unsaturated zone vary, but generally consist of multiple linear segments (Section 8.5.3.2). The temperature profiles also indicate that the depth of downward propagation of seasonal surface temperature changes is approximately 15.2 m (50 ft). Below this depth, the temperature gradient is very small (if not nearly isothermal) across the TCw. Temperature data are too limited to adequately define the gradient across the TCw. However, a small temperature gradient can be inferred from temperature measurements made immediately below the TCw. A larger temperature gradient across the PTn is required to conserve conductive heat flux across the PTn and this, in turn, implies a lower temperature gradient across the TCw.

Temperature profiles in boreholes generally indicate that temperature gradients in the TSw exhibit nearly linear character through thick intervals of the unit (Section 8.5.3.2). The gradients vary significantly from one location to another within the study area, and range from 1.59°C per 100 m (330 ft) to 2.55°C per 100 m (330 ft). In general, smaller gradients in the TSw appear to be associated with active channels or valley floors of major drainages. Larger gradients are present beneath channel margins and hillslopes immediately adjacent to these channels, reaching a maximum beneath ridges or in hydrologically inactive areas. Small temperature gradients in

the TSw beneath alluvium-filled channels and large gradients along hillslopes and ridges indicate higher heat flow in the TSw where the unsaturated zone section is thickest.

Temperature gradients within the PTn are larger than those in the underlying TSw because of lower thermal conductivity (Section 8.5.3.2). Gradients across the composite PTn section vary from less than 2°C per 100 m (330 ft) to greater than 4° to 5°C per 100 m (330 ft). Temperature gradients within the PTn tend to show more geographic variability than gradients within the TSw. Temperature gradients within the TCw tend to be small and are strongly affected by seasonal surface temperature changes.

Comparison of calculated and estimated heat flow through the major hydrogeologic units indicates a large heat flow deficit across the TSw-PTn contact (Section 8.5.3.4). The heat flow estimated for the Pah Canyon Tuff in Pagany Wash of approximately 15.5 mJ/s/m<sup>2</sup> is substantially less than the conductive heat flow of 32 to 40 mJ/s/m<sup>2</sup> estimated as typical for the TSw in the northern part of the site area. The reduction in heat flow from 32 to 40 mJ/s/m<sup>2</sup> in the TSw to approximately 15.5 mJ/s/m<sup>2</sup> within the Pah Canyon Tuff indicates the presence of heat-consuming processes, such as the downward movement of water from cooler to warmer thermal regimes. Sensible-heat losses alone would require a downward, liquid infiltration rate of 52 to 96 mm/yr. at the boreholes studied if liquid flow were the only nonconductive heat-transfer mechanism. Heat losses due to a downward infiltration in the range of 52 to 96 mm/yr. are extremely unlikely unless substantial lateral flow occurs within the PTn. Water-potential profiles across the TCw indicate drier conditions with decreasing depth and an upward matrix flux component. These two conditions suggest limited downward matrix flux within the Tiva Canyon hydrogeologic unit but do not preclude the possibility of episodic fracture flow.

#### 8.12.6 Hydrochemistry

Aqueous-phase hydrochemical data have been interpreted to determine possible flow mechanisms and residence times for pore water in the unsaturated zone (Section 8.6.2). In spite of large distances separating boreholes, chemical compositions of pore waters generally are similar within a given stratigraphic unit and markedly dissimilar between different host lithologies (Section 8.6.2.1). The total concentration of major ions in pore waters is highly variable and in many samples is greater near contacts than in the middle of stratigraphic units. Chloride concentrations in perched water are fairly small, ranging from about 4 to 15 mg/L, and are much lower than the chloride concentrations of pore water from the PTn and the TSw. The low chloride concentrations result from very little interaction with the matrix of the overlying rocks and indicate that perched water probably was derived from fracture flow.

High tritium values in pore water sampled fairly deep in the unsaturated zone are strong evidence of fracture and lateral flow (Section 8.6.2.3). Fast transport through the TCw also is indicated by bomb-pulse <sup>36</sup>Cl in several boreholes that intersect the PTn. Other evidence of fast pathways that persist into the TSw includes bomb-pulse chlorine-36 at locations in the northern part of the ESF.

Carbon-14 values of perched waters range from 66.9 to 27.2 percent modern, corresponding to apparent residence times of about 3.5 to 11 k.y. (Section 8.6.2.4). The corrected ages could be younger if the dissolved inorganic carbonate has been diluted by dead carbon through isotopic

exchange with old calcite along its flow path. The carbon-14 content of pore waters from both the PTn and CHn suggest an apparent age of less than 10 k.y.

Stable-isotope values for both unsaturated zone pore water and perched water generally are heavier than values for saturated zone water, which has uncorrected carbon-14 ages between 9 and 18 k.y. (Section 8.6.2.5). Therefore, pore water in the TSw probably has a post-glacial origin and an age on the order of 2 to 10 k.y.

Carbon-14 values for gas samples from deep boreholes at Yucca Mountain indicate lower transport velocity within the PTn than in the TSw, probably due to higher porosity and water content in the PTn (Section 8.6.3). Transport velocities through the TSw indicate that gas moves downward through the TSw primarily by diffusion.

**Geochemical Evidence of Past Percolation**—Deposits of calcite and opal in fractures and cavities mark pathways of past percolation of water through the unsaturated zone (Section 8.11). These mineral coatings preserve a history of deposition that can be deciphered by isotopic dating. Morphologic relations, as well as chemical and isotopic compositions of these secondary minerals, provide an interpretable geochemical record of paleohydrologic conditions within Yucca Mountain. An understanding of the origins of calcite and opal in these settings may provide constraints on fracture flow through the mountain and on the unsaturated zone hydrologic models used to represent this flow. Detailed studies of secondary minerals within the ESF have shown multiple episodes of mineral deposition (Section 8.11.2). The preferred localization of secondary minerals demonstrates precipitation under water-unsaturated conditions. Results of dating of the minerals by radiocarbon (calcite),  $^{230}\text{Th}/\text{U}$  (calcite and opal), and  $\text{U}/\text{Pb}$  (opal) methods indicate that the undersaturated conditions, at least at the level of the ESF, have persisted for several million years.

The mineral record can be used to estimate past water flux through the unsaturated zone if the distribution of secondary minerals is known in space and time, and if the volumes of water required to account for the mineral deposits can be estimated (Section 8.11.2). Preliminary estimates of the abundance of secondary minerals have been made from ESF observations. Hydrochemical compositions of surface runoff are nearly saturated with respect to calcite and opal, and are assumed to represent shallow, infiltrating solutions. Assuming all calcium was extracted from these waters en route to the saturated zone, a minimum value of flux of about 2 mm/yr. was obtained as an average over the last 12.7 m.y. A refinement in this initial estimate indicates that the percolation flux is about 1.4 mm/yr. based on the deposition of calcite and about 2.5 mm/yr. based on deposition of opal. More recent analysis has shown that percolation flux values from secondary mineral deposition correlate quite well with estimates from the infiltration model (Section 8.2) in the TCw above the PTn. However, there was no correlation between the two methods for the TSw below the PTn. These results suggest that percolation is diverted laterally or substantially redistributed by the PTn. Further, the secondary mineral abundances below the PTn suggest that percolation fluxes are as much as 10 times lower than estimates from the infiltration model.

Surface records from the Yucca Mountain area indicate that the regional climate over the last 1 m.y. was characterized by wetter and cooler conditions relative to the present for as much as 80 percent of the time (Section 8.11.2). However, there is no indication in the subsurface that

deposition rates of calcite and opal varied greatly during this interval even though higher water tables throughout the region reflect greater recharge during pluvial periods. These observations suggest that percolation and mineral deposition through most of the Topopah Spring Tuff may have been buffered from variations in effective moisture, except in the zones of highest flux associated with throughgoing structures. Further evidence of the stability of hydrologic conditions in the deep unsaturated zone is provided by the results of uranium-lead age dating of secondary minerals. These results indicate that average long-term rates of deposition of calcite and opal in the TSw have not varied substantially during the last 8 m.y. despite probable major climatic shifts toward increasing aridity and greater seasonality. In addition, the difference between rates of deposition for shallow and deep secondary minerals suggest that the PTn acts as a significant diversionary or buffering unit for the unsaturated zone hydrologic system.

### 8.12.7 Estimates of Percolation Flux

The heat flow deficit across the PTn-TSw contact was analyzed to derive percolation flux estimates in the deep unsaturated zone (Section 8.7.2). In Pagany Wash, just north of the potential repository area, analysis of heat flow indicates that the long-term percolation flux within the lower part of the PTn and upper part of the TSw is 10 to 20 mm/yr. (Section 8.7.2.1). Numerical analysis of borehole temperature data also was conducted using the unsaturated zone flow model (Section 8.7.2.2). Results indicate that at the crest of Yucca Mountain, percolation flux rates are about 5 mm/yr., but are as high as 10 to 15 mm/yr. at other locations east and northeast of the crest.

The chloride mass-balance method used the chloride concentration of pore water, perched water, or saturated zone water, the concentration of chloride in precipitation, and the average annual precipitation, to estimate the fraction of precipitation that escapes evapotranspiration and becomes net infiltration (Section 8.7.3). Apparent percolation fluxes average 5.7 mm/yr. and range from 0.8 mm/yr. in the PTn to 25.1 mm/yr. in a perched-water reservoir at the southern end of the potential repository area. However, the average percolation flux computed for perched-water reservoirs is considerably larger (17.8 mm/yr.) than the average of all the other values (3.1 mm/yr.), indicating that water may be moving laterally down-dip along the base in the Topopah Spring Tuff from its outcrop in Solitario Canyon. Further, a significant addition of water to the perched-water reservoirs by lateral flow may cause the downward percolation flux below the perched-water reservoirs to be larger than it otherwise would be.

The hydraulic-conductivity/potential gradient method used measurements or estimates of the effective hydraulic conductivity of the rock at its prevailing state of water potential or saturation, in combination with estimates of the hydraulic head gradient, to directly calculate the percolation flux in accordance with Darcy's law (Section 8.7.4). This method also was the basis for estimates of percolation flux produced from model calibration against existing borehole-saturation and water-potential data sets. A uniform steady-state percolation flux of 0.02 mm/yr. provided the best overall fit to the combined saturation and water potential data from the boreholes studied. The low percolation rate required to match the saturation profiles resulted from the fact that the field saturations were determined for rock core samples and it was assumed that no fracture flow occurs. Improvement of the simulations by incorporating a greater number of geologic layers resulted in estimates of percolation flux of 0.01 to 5.0 mm/yr. If the percolation flux rate at Yucca Mountain was similar to the higher values investigated in the

study, the flux in excess of 1 mm/yr. would probably move as nonsteady pulsed flow through local structural features.

Percolation flux also was estimated directly by multiplying the effective hydraulic conductivity of the rock at a given depth by the hydraulic gradient, which through most of the unsaturated zone is very close to zero, based on water-potential data (Section 8.7.4). Consequently, the hydraulic gradient is approximately equal to the gravitational gradient of unity, and the percolation flux is equal to the effective hydraulic conductivity of the rock. Effective hydraulic conductivity values varied among boreholes within a given hydrogeologic unit because of differences in saturation and the assumed uniformity in the hydraulic properties. Effective hydraulic conductivity values generally indicated a percolation flux through the PTn of 1 to 2 mm/yr. The effective hydraulic conductivity through the TSw at and above the potential repository horizon generally is a few tenths of a millimeter per year or less, whereas the effective hydraulic conductivity values below the potential repository horizon suggest an increase in flux with depth. Effective hydraulic conductivities for the vitric part of the Calico Hills Formation are much greater than 1,000 mm/yr. at locations where perched water occurs on the underlying zeolitic rocks. In contrast, effective hydraulic conductivities are a few tenths of a millimeter per year in the vitric Calico Hills Formation. The zeolitic part of the Calico Hills Formation generally has an effective hydraulic conductivity of a few tenths of a millimeter per year and the pre-Calico Hills bedded tuff has an effective hydraulic conductivity of 1 to 2 mm/yr. The Prow Pass Tuff generally has an effective hydraulic conductivity of 2 mm/yr. or less.

The temporally averaged percolation flux over the last 10 to 12 m.y. was estimated by calculating the mass of secondary minerals (principally calcite) accumulated within fractures along the length of the ESF (Section 8.7.5). Percolation fluxes calculated on the basis of secondary mineral volumes range from 0 to about 9 mm/yr. and generally are much lower than the infiltration rates predicted by the infiltration model. Statistical comparison indicated that although percolation flux values for the two methods correlated quite well for ESF stations in the TCw above the PTn, there was no correlation between the two methods for ESF stations in the TSw below the PTn. These results suggest that percolation is diverted laterally or substantially redistributed by the PTn.

Percolation flux also was estimated based on perched-water volumes and residence times (Section 8.7.6). Results of this analysis indicated that percolation flux ranged from 0.001 to 0.29 mm/yr., considerably lower than values estimated by other methods.

There is only marginal agreement between net infiltration calculated using the infiltration model (Section 8.2.6) and estimates of percolation rates from various methods that rely on subsurface data (Section 8.7.7). Both the net infiltration model and the subsurface methods indicate that net infiltration (or percolation) is a small percentage of the average annual precipitation at Yucca Mountain (about 170 mm/yr.). However, the methods differ significantly on the spatial distribution of percolation. Overall, percolation fluxes estimated from borehole temperature data and chloride mass-balance data compare favorably with net infiltration rates because they differ by less than a factor of 10. However, the temperature fluxes and chloride mass-balance percolation fluxes do not correlate with net infiltration rates on a point-to-point basis. The percolation flux estimates based on matrix saturations, water potentials, and matrix hydraulic conductivity probably are much lower than other estimates because significant fracture flow is

not accounted for. The percolation flux rate estimated on the basis of the perched-water volume and residence time is considerably lower than the rates estimated from other methods, including chloride mass balance.

## **8.12.8 Hydrologic Conditions in the Exploratory Studies Facility**

### **8.12.8.1 Effects of Ventilation**

Ventilation of the ESF has affected the surrounding rocks by creating a dryout zone around tunnels and drifts that extends several meters into the rocks (Section 8.8.2). For conditions in the ESF in 1996, the amount of moisture that could be removed by the ventilation system was estimated to be 285 m<sup>3</sup>/wk., or 75,000 gal./wk. (Section 8.8.2.1). Assuming that all the moisture in the tunnel air is from evaporation, the equivalent evaporation rate from the tunnel walls and inverts is 100 mm/yr. The vapor density differences between different locations, together with a simple approximation of air flow in the tunnel also were used to estimate the moisture removal rate. For this analysis, the equivalent evaporation rate was on the order of 200 mm/yr., for both the TSw units in a 1,400-m (4,600-ft) section centered at the Thermal Test Facility and the PTn unit in a 380-m (1,300-ft) section between Alcove 3 and Alcove 4. The large evaporation rates estimated above could suppress the observations of active seeps and contribute to the apparently dry tunnel conditions.

Drying processes in the rocks of the ESF Main Drift were monitored in three niches where boreholes were instrumented to measure water potential (Section 8.8.2.3). The niches are located on the west side of the ESF Main Drift in the vicinity of the Ghost Dance and Sundance faults. Water-potential data from the niches indicated that:

- There was significant variability in water potential in the niches.
- Ventilation effects may have penetrated the rock, possibly greater than 3 m (9.8 ft).
- Two zones of significantly higher water potential appeared to be associated with the Sundance fault.

### **8.12.8.2 Migration of Construction Water**

The migration of water used for tunnel construction was monitored using a lithium-bromide tracer (Section 8.8.3.1). The apparent penetration depth of the construction water below the floor of the ESF varied considerably with location and ranged from 2 to 30 m (6.6 to 98 ft). Detection of construction water at variable depths and in isolated concentration peaks indicated fracture flow. Water may have migrated considerably deeper through the fracture network than indicated by these data, particularly where the water was applied directly onto the fractured middle nonlithophysal unit of the Topopah Spring Tuff.

Construction water migration also was monitored during excavation of the enhanced characterization of the repository block Cross Drift (Section 8.8.3.2). In the Cross Drift starter tunnel, the advance and retreat of construction water wetting fronts were monitored successfully and the capabilities of detection instruments were quantified. Results of construction water

monitoring at the Main Drift-Cross Drift crossover location indicated the following (Section 8.8.3.3):

- No seepage was observed, nor did any wetting front reach the ESF Main Drift, which is 17.5 m (57.4 ft) below the Cross Drift. Confirmation of no seepage at the crossover location established the lower limit for the drift-to-drift flow and drift seepage processes associated with construction-water usage.
- Because performance confirmation drifts are planned in the potential repository above or below waste-emplacement drifts to monitor the waste-induced impacts, it is important to evaluate the drift-to-drift water migration and drift seepage to assess potential impacts.

### 8.12.8.3 Hydrologic Properties of the Ghost Dance Fault

Geothermal logging, pneumatic monitoring, air and core-water chemistry sampling, air-injection testing, and tracer testing were conducted in the Northern Ghost Dance Fault Alcove (Alcove 6) that was constructed off the ESF (Section 8.8.4). In situ pneumatic pressures monitored in the pre-excavation borehole indicated minimal barometric pressure attenuation (0.5 kPa or less) and small time lags (Section 8.8.4.2). Comparison of the downhole pressure fluctuations to the barometric pressure fluctuation indicated that the permeability of the rock is relatively high. Uncorrected  $^{14}\text{C}$  ages of gas samples ranged from 2.4 to 4.5 k.y., with the ages correlating directly with the amount of pressure attenuation measured during pneumatic monitoring. Nine out of 34 water samples distilled from rock core from various depths of the pre-excavation borehole contained tritium at significant levels, indicating that water has been transported from the ground surface to the depth of the Northern Ghost Dance Fault Alcove during the last approximately 100 yr.

Single-hole air-injection testing conducted in the pre-excavation borehole indicated that the permeability of the hanging wall (west side) of the Ghost Dance fault averaged  $1.1 \times 10^{-12} \text{ m}^2$  (Section 8.8.4.4). The fault zone itself had an average permeability of  $10 \times 10^{-12} \text{ m}^2$ . Permeability of the footwall (east side) of the Ghost Dance fault was very similar to that of the hanging wall. Overall, the permeability of the unaffected rock surrounding the fault was very similar to the permeability of the Tptpmn derived from air-injection testing of surface-based boreholes ( $0.37$  to  $2.7 \times 10^{-12} \text{ m}^2$ ) while the fault-zone permeability was several times larger.

Cross-hole air-injection tests were conducted between the three Northern Ghost Dance Fault Drill Room (NDR) boreholes in the Northern Ghost Dance Fault Alcove (Section 8.8.4.5). The air-injection tests and the test environment were analyzed with an analytical model using type curves, a numerical modeling code, and with a discrete-feature model. Comparison of the cross-hole-test permeability values with the single-hole-test values indicated that the cross-hole-test values were consistently larger (Section 8.8.4.5.1). In the hanging wall, the arithmetic mean permeability from the cross-hole tests ( $5.0 \times 10^{-12} \text{ m}^2$ ) was about five times the mean obtained from the single-hole tests ( $1.1 \times 10^{-12} \text{ m}^2$ ). In the fault zone, the arithmetic mean permeability from the cross-hole tests ( $18.1 \times 10^{-12} \text{ m}^2$ ) was about two times the mean obtained from the single-hole tests ( $10 \times 10^{-12} \text{ m}^2$ ). In the footwall, the difference was even greater with the arithmetic mean permeability from the cross-hole tests ( $8.7 \times 10^{-12} \text{ m}^2$ ) being nearly 10 times the mean obtained from the single-hole tests ( $1.0 \times 10^{-12} \text{ m}^2$ ). The larger permeability values from

the cross-hole tests probably were due to the larger scale of the cross-hole tests as compared to the single-hole tests. Overall, the Northern Ghost Dance Fault Alcove cross-hole permeability values for the Tptpmn were larger than the range of the surface-based permeability values for the Tptpmn ( $0.37$  to  $2.7 \times 10^{-12} \text{ m}^2$ ), probably reflecting the intense fracturing in the Ghost Dance fault zone. The mean porosity values of the fault zone were about three times that of both the hanging wall and the footwall.

Cross-hole convergent-tracer tests were conducted between NDR borehole intervals that had cross-hole pneumatic connections (Section 8.8.4.6). Results of the tracer test Moench type-curve analysis indicated that longitudinal-dispersivity values ranged from  $0.06 \text{ m}$  to  $2.63 \text{ m}$  and transport-porosity values ranged from  $0.001$  to  $0.070$  (Section 8.8.4.6.1). Results of the discrete-feature-network model analysis indicated that the flow paths of the tracked particles were up to six times longer than the straight-line distance (Section 8.8.4.6.2). The long, tortuous flow paths were partially responsible for the high transport-porosity values (up to  $0.070$ ) compared to the true fracture porosity that usually range from  $10^{-2}$  to  $10^{-5}$ . The variability in the length of the flow paths also indicated that a drawn-out arrival-time tail might not result from matrix diffusion but could result from a complex, variable, nonlinear tracer transport pathway.

#### **8.12.8.4 Estimation of Seepage into Drifts**

An evaluation of seepage into mined underground openings or drifts was part of a larger ambient field-testing program being conducted in the ESF at Yucca Mountain (Section 8.8.5). This program was designed to investigate in situ flow and transport processes believed to be critically important to performance of the potential repository. A key issue concerning repository performance is whether infiltration water entering Yucca Mountain, now and under various wetter climate scenarios in the future, will percolate through the deep unsaturated zone to the repository horizon, where the water may seep directly into a waste emplacement drift, or move around the opening.

Air-injection tests and liquid-release tests were conducted prior to excavation of niches off the Main Drift of the ESF to characterize the flow of air and water through relatively undisturbed fractures (Section 8.8.5.1). Similar tests were conducted after excavation to quantify the effect of excavation on air-permeability measurements and to quantify water seeping into an underground opening from a small-scale percolation event of known duration and intensity. Comparison of the pre-excavation and post-excavation mean air-permeability values for a given niche indicated that the post-excavation air-permeability values were 10 to 40 times larger than pre-excavation values (Section 8.8.5.1.1). Results from multiple liquid-release tests conducted in one niche indicated that the seepage percentage ranged from 0 to 56.2 percent (Section 8.8.5.1.2). In the early stages of testing, the seepage percentages resulting from two tests were significantly different even though the tests were conducted at nearly the same liquid-release rate. The large difference in seepage percentage was attributed to the effect of wetting history.

The seepage threshold flux, defined as the liquid-release flux at and below which water will no longer seep into the drift, was determined for a given test interval by performing multiple seepage tests at different liquid-release fluxes (Section 8.8.5.2). Forty liquid-release tests were

performed on 16 test intervals positioned above the niche. In one of these tests, seepage threshold fluxes ranged from  $6.35 \times 10^{-9}$  to  $4.31 \times 10^{-6}$  m/s (200 to 136,000 mm/yr.).

To analyze and extend the results of the liquid-release tests, a numerical seepage calibration model was constructed to facilitate the subsequent development of process models that calculate drift seepage for a variety of geologic units, hydrologic property sets, and waste emplacement configurations (Section 8.8.5.3). The seepage calibration model was a template fracture-continuum model that was developed based on air-permeability and liquid-release test data from the ESF niche experiments. The seepage calibration model was calibrated using seepage data from the niche liquid-release tests, which provided model-related, effective parameters relevant to the processes involved in drift seepage (Section 8.8.5.3.3). A key aspect of the modeling approach was that seepage-relevant parameters were determined using flow data from a seepage experiment rather than determining parameters from geometric information such as fracture density and aperture. Steady-state simulations were performed with the seepage calibration model to calculate seepage for a large range of percolation fluxes in order to estimate the seepage threshold for the drift geometry and rock type for the potential repository (Section 8.8.5.3.5). Results from three-dimensional heterogeneous simulations of a range of percolation fluxes yielded a seepage threshold of approximately 250 mm/yr. Although there was significant uncertainty in the seepage percentage predictions, there seems to be a low seepage probability for percolation fluxes less than 100 mm/yr.

#### **8.12.9 Conceptual Models of Flow and Transport**

The conceptual model of fluid flow in the unsaturated zone at Yucca Mountain consists of several important flow processes and issues (Section 8.9.1). Infiltration is spatially and temporally variable because of the nature of the storm events that supply precipitation and variation in soil cover and topography (Section 8.9.1.1). As a result of the relatively high density of interconnected fractures and low matrix permeabilities in the TCw, infiltration pulses move rapidly through the fracture system with little attenuation relative to travel times in the matrix (Section 8.9.1.2). Once liquid water leaves the TCw and percolates downward into the PTn, totally different flow processes are evident. Because of relatively high matrix permeability and porosity and low fracture densities of the PTn, predominantly fracture flow in the TCw becomes dominantly matrix flow in the PTn. Lateral flow of liquid water seems to be insignificant within the PTn unit. Unsaturated flow of liquid water in the TSw is primarily through the fractures. Assuming a unit gradient, the matrix percolation rate will be the same as the matrix hydraulic conductivity and is a small fraction of the average infiltration.

The occurrence of perched water near the TSw-CHn contact indicates that the TSw basal vitrophyre and the CHn serve as barriers to vertical flow and cause lateral flow (Section 8.9.1.2). Below the potential repository, both the CHn and CFu units have vitric and zeolitic components that differ by the degree of hydrothermal alteration. Because the zeolitic rocks of the CHn and the CFu have low matrix permeability and some fracture permeability, a relatively small amount of water may flow through the zeolitic units. However, most of the water that percolates to the zeolitic horizon is diverted laterally in the perched-water bodies and then vertically down faults. Conversely, but similar to the PTn unit, the vitric rocks of the CHn and the CFu have relatively high matrix porosity and permeability and, therefore, mostly porous-medium flow predominates in these rocks. Fracture flow is believed to be limited in these units.

Fracture-matrix interaction is likely limited within the welded units in the unsaturated zone, as evidenced by perched water derived mainly from fracture flow and by bomb-pulse  $^{36}\text{Cl}$  at the repository level in the ESF (Section 8.9.1.3).

Faults can act as transient fast-flow conduits for vertical liquid-water flow through the PTn, particularly as a result of temporally variable infiltration (Section 8.9.1.5). However, this transient flow along the major faults is expected to carry only a small amount of water and may not be a major liquid-flow mechanism above the potential repository horizon. Fault zones also can act as barriers to lateral liquid-water flow because highly fractured rocks and coarse openings can create a capillary barrier. Faults also can act as barriers to lateral flow when fault displacement results in a low-permeability unit being adjacent to a relatively high-permeability unit within a fault zone.

In general, flow in the unsaturated zone at Yucca Mountain is time dependent, or transient, because of temporal variations in infiltration flux at the surface (Section 8.9.1.6). Because of matrix flow and relatively low matrix saturation, the PTn greatly attenuates short-term episodic infiltration pulses such that liquid-water flow below the PTn is approximately in steady state. Longer-term climate change, however, has a more pronounced influence on flow pattern within the unsaturated zone and ultimately impacts the entire flow field. In total system performance assessment (TSPA) simulations of radionuclide transport, however, the transient period during which the system responds to a climate change has been found to be less significant because the change in flow in the fractures responds relatively quickly to a change in infiltration. Therefore, a quasi-steady flow model was used to estimate the effects of climate change on radionuclide transport.

Focusing flow, leading to fast pathways across the PTn, may occur, as evidenced by bomb-pulse chlorine-36 being found associated with localized fault structures in the lower PTn (Section 8.9.1.7). However, it is expected that these fast flow paths probably carry only a very small amount of water. A variety of observations indicate that the fracture water flow paths in the TSw are many and widely dispersed.

Gas flow in the unsaturated zone at Yucca Mountain mainly depends on the characteristics of fracture networks (Section 8.9.1.8). In the welded units, the fractures generally are much more permeable than the matrix, whereas in the nonwelded PTn, the permeability of the fracture continuum and the matrix continuum are about the same. The ambient gas flow processes occurring at Yucca Mountain include barometric pumping, wind, and density-driven flow. Barometric pumping is the response of subsurface pneumatic pressure to changes in atmospheric pressure. Because this is a transient process, both the permeability and storage of the media affect the subsurface response. In the welded units, this translates into little change in the pneumatic pressure signal with depth. In the PTn, however, the bulk permeability and the high gas-filled porosity serve to attenuate and lag the response to barometric pumping between the top and the bottom of the unit.

The conceptual model of radionuclide transport in the unsaturated zone encompasses all aspects of the conceptual model for flow (Section 8.9.2). In addition, the conceptual model of radionuclide transport takes into account physical and chemical processes unique to transport.

These processes include the following:

- Advection, which is the movement of dissolved or colloidal materials because of the bulk flow of fluid
- Matrix diffusion, which is solute transport from fracture networks to surrounding matrix blocks resulting from molecular diffusion
- Fracture and matrix sorption, which is a combination of chemical interactions between dissolved solutes and the solid phases (immobile rock matrix or colloids)
- Colloid-facilitated transport
- Radioactive decay
- Dispersion is a transport mechanism caused by localized variations in flow velocity.

Advective transport pathways are consistent with flow pathways (Section 8.9.2.6). Matrix diffusion is a major mechanism for mass transfer between fractures and the matrix and contributes to the retardation of the radionuclide transport when fracture flow is dominant. Sorption can act to retard the movement of radionuclides in the unsaturated zone. However, sorptive interactions may enhance radionuclide transport if the aqueous species sorbs to colloids. Dispersion is not expected to be a major transport mechanism in the unsaturated zone at Yucca Mountain.

If a geologic repository is constructed at Yucca Mountain, the emplaced radioactive wastes will emit a significant amount of heat from the radioactive decay (Section 8.9.3). This heat will influence hydrologic, mechanical, and chemical conditions in both the near field (drift-scale) and far field (mountain-scale). Consequently, there are several sets of coupled processes that must be taken into account in order to determine the overall performance of the repository in the unsaturated zone. These coupled processes include thermohydrologic, thermomechanical, and thermochemical processes. Mountain-scale thermohydrologic effects are summarized in Section 8.10.8 and drift-scale thermohydrologic chemical effects are summarized in Section 8.10.9.

#### **8.12.10 Modeling of Fluid Flow and Transport**

Over the past 15 yr., the unsaturated zone model of Yucca Mountain has evolved from simple one-dimensional and two-dimensional models that included little geological or hydrological detail, to a fully coupled, three-dimensional model that incorporates much of the known geologic, hydrologic, chemical, and thermal complexity of Yucca Mountain (Section 8.10.2). The most recent improvements and advances in the site-scale unsaturated zone flow and transport model are described in a series of analysis and modeling reports. These reports encompass the complete range of technical topics necessary to document the current status of the unsaturated zone model. Technical topics include numerical methods, numerical grids, calibrated properties model, the primary unsaturated zone models and submodels, seepage model for performance assessment, mountain-scale coupled thermohydrologic models, drift-scale coupled thermohydrologic chemical seepage models, and the radionuclide transport model.

### 8.12.10.1 Numerical Methods

A variety of numerical approaches have been proposed in the literature to deal with flow and transport processes in fractured media at the field scale (Section 8.10.3). In continuum approaches, fractures are considered to be sufficiently ubiquitous and distributed in such a manner that they can be described statistically in a meaningful way (Section 8.10.3.1). The role of individual fractures in fractured media is considered to be similar to that of individual pores in porous media. In continuum approaches, connected fractures and rock matrix are viewed as two or more overlapping, interacting continua. Depending on the number of continua and methodologies used to treat fracture-matrix interaction, continuum approaches can be further classified as effective continuum, dual-continua, and multiple interacting continua approaches.

Discrete fracture network approaches are based on an assumption that flow and transport behavior can be predicted from knowledge of the fracture geometry and data on hydraulic properties of individual fractures (Section 8.10.3.2). These approaches involve computational generation of synthetic fracture networks and subsequent modeling of flow and transport in each individual fracture.

Continuum approaches have been considered to be appropriate for use in the unsaturated zone flow and transport model (Section 8.10.3.3). As a compromise between accuracy and feasibility, the dual-permeability method has become the primary modeling approach currently used in the unsaturated zone model and submodels to simulate water flow, heat transfer, and chemical transport.

In general, there are two kinds of numerical algorithms for modeling chemical transport in the subsurface, the conventional algorithm based on finite difference and/or finite element methods and the particle-tracking algorithm (Section 8.10.3.5). Because particle-tracking algorithms can be used only for chemical transport with simple chemical reactions, conventional algorithms are appropriate for transport with complex reactions. Because radionuclide transport is a transient process, the dual-continua approach may underestimate the chemical concentration gradient at the fracture-matrix interface and, therefore, may underestimate chemical transfer from fractures to matrix under certain conditions. Because matrix transport processes correspond to relatively long travel times to the water table compared with those in fractures, the dual-continua approach is expected to give conservative predictions of radionuclide transport in the unsaturated zone.

In a dual-continua approach, the treatment of fracture-matrix interaction is important for accurate modeling flow and transport and the active-fracture model accounts for this interaction in a realistic manner (Section 8.10.3.6). Fingering flow at a fracture network scale is considered to be a key mechanism for limiting fracture-matrix interaction. For unsaturated fractured rock, the water flow pattern is expected to exhibit significant preferential (fingering) flow at a fracture network scale because of the large nonlinearity involved in an unsaturated system and heterogeneities of fracture structure at different scales. The active-fracture concept is based on the reasoning that as a result of fingering flow, only a portion of fractures in a connected, unsaturated fracture network contribute to liquid-water flow, while others are simply bypassed. Because the number of active fractures in the unsaturated zone at Yucca Mountain is small compared to the total number of connected fractures, active fractures, rather than total connected fractures, must be used in numerical models. In addition, because the number of active fractures

within a grid block is large, a continuum approach is still valid for describing fracture flow. These hypotheses are consistent with the consideration that flowing fractures in the unsaturated zone are many and highly dispersed.

#### 8.12.10.2 Numerical Grids

Numerical grid generation was an integral part of the development of the complex, three-dimensional, unsaturated zone flow and transport model of Yucca Mountain (Section 8.10.4). The development of numerical grids required consideration of the form and abundance of all geologic, hydrologic, and mineralogical data available for the study area. Numerical grid generation is an iterative process that must achieve a proper balance between desired numerical accuracy in terms of grid block size and computational time controlled by the total number of grid blocks. The products of grid development include:

- A set of one-dimensional vertical columns of grid blocks for hydrogeologic property set inversions
- Two-dimensional unsaturated zone flow and transport model vertical cross-sectional grid for fault hydrogeologic property calibrations
- Three-dimensional unsaturated zone flow and transport model grid for additional model calibrations
- Three-dimensional unsaturated zone flow and transport model grid for generating flow fields for performance assessment.

Geologic data extracted from the geologic framework model (GFM) Version 3.1, and the integrated site model (ISM) Version 3.0, formed the basis for numerical grid development (Section 8.10.4.3). With these data, an initial two-dimensional (plan view) grid was developed defining borehole, fault, ESF, enhanced characterization of the repository block, and repository column locations. Using the two-dimensional grid as the basis for column locations, a three-dimensional (effective continuum) grid was constructed using layer horizon and thickness data from the GFM, Version 3.1. Initial grid generation was followed by an iterative process of grid evaluation and modification to achieve appropriate spatial resolution and representation of important features and to ensure proper connections between the various elements of the grid. Next, the three-dimensional (effective continuum) grid was modified to allow for dual-continua processes (matrix and fracture flow) using a dual-permeability (dual-k) mesh-maker, which incorporated information from fracture data analyses (fracture porosity, spacing, aperture, and fracture-matrix interaction area) into the grids.

The areal domain of the unsaturated zone flow and transport model encompasses approximately 40 km<sup>2</sup> (15 mi.<sup>2</sup>) of the Yucca Mountain area (Section 8.10.4.4). Yucca Wash marks the northern model boundary, while the approximate latitude of borehole USW G-3 defines the southern boundary. The eastern model boundary coincides with the Exile Hill, "Toe," and Bow Ridge faults, and the western boundary lies approximately 1 km west of the Solitario Canyon fault. The model grid was designed to accurately represent the repository boundary, the paths of the ESF and enhanced characterization of the repository block Cross Drift, ESF alcoves and niches, major faults defined in the GFM, Version 3.1, and selected boreholes. The upper

boundary of the unsaturated zone flow and transport model is the bedrock surface and the lower boundary is the water table.

Layering within the unsaturated zone flow and transport model grid was configured to correspond as closely as possible to detailed hydrogeologic units in order to facilitate usage of rock properties data (Section 8.10.4.5). The unsaturated zone flow and transport model calibration grid contains 32 layers: 3 for the TCw, 6 for the PTn, 9 for the TSw, 10 for the CHn, and 4<sup>+</sup> for the CFu. The maximum thickness of any cell within the unsaturated zone grids was 60 m (200 ft) (Section 8.10.4.8). For some applications, a finer mesh grid was developed to increase vertical resolution within and below the potential repository horizon. The potential repository volume encompasses five grid layers, each 5 m (16 ft) thick. The average slopes of all faults included within the domain of the unsaturated zone flow and transport model were evaluated to determine which could be approximated by vertical columns of grid blocks in unsaturated zone flow and transport model grids (Section 8.10.4.5). The following faults were represented by vertical columns of grid blocks in the unsaturated zone flow and transport model grids: Solitario Canyon (west), "Soljfat," Sundance, "Toe," Sever Wash, Pagany Wash, Drill Hole Wash, Ghost Dance, Ghost Dance (west), Imbricate, and Exile Hill faults. The remaining faults, Solitario Canyon, Splay "S," Dune Wash, Dune Wash "X," and Dune Wash (west1), were represented by nonvertical columns of grid blocks in the three-dimensional model grids.

The unsaturated zone flow and transport model calibration grid contains 1,434 vertical columns, and when the grid is projected vertically downward through the model layers, it encompasses 53,512 grid blocks in the effective continuum formulation for the site-scale model (Section 8.10.4.7). The number of grid blocks nearly doubles for the dual-permeability formulation. The grid, designed for flow-field calculations and used mainly for performance assessment studies, contains nodes only for fault traces and borehole locations, but has a denser grid mesh within the potential repository area.

### **8.12.10.3 Calibrated Properties Model**

The calibrated properties model provides calibrated parameter sets (interpreted input data) for unsaturated zone flow and transport process models for the Yucca Mountain Site Characterization Project (Section 8.10.5). These calibrated property sets include matrix and fracture hydrologic property values for the unsaturated zone flow and transport model, drift seepage models, drift-scale and mountain-scale coupled process models, and TSPA models. These process models provide the necessary framework to test conceptual hypotheses of flow and transport at different scales and predict flow and transport behavior under a variety of possible climatic and thermal loading conditions for the potential repository at Yucca Mountain. The properties calibration process involved a series of inverse modeling simulations (inversions) using the computer code ITOUGH2. Property sets were generated corresponding to lower-bound, mean, and upper-bound present-day net infiltration.

Calibration of the unsaturated zone flow and transport model was necessary in order to refine the property estimates derived from laboratory and field data so that they were suitable for use in the unsaturated zone flow and transport model and so that the unsaturated zone flow and transport model accurately depicts hydrologic conditions in the mountain (Section 8.10.5). Because the unsaturated zone flow and transport model considers hydrologic processes on a mountain scale

and properties are scale-dependent, upscaling is an inherent part of the calibration process. The calibration process also reduces property estimate uncertainty and bias. Because property estimates from laboratory and field data collected at Yucca Mountain have uncertainty associated with them, data inversion was used to calibrate some of the numerical model parameters (properties). Inversion is an iterative process where predictions from a numerical model are compared to data and the numerical model parameters are adjusted (calibrated) in order to improve the match between the model prediction and the data. The data for the unsaturated zone flow and transport model that were inverted to provide the calibrated properties include saturation in the rock matrix, water potential in the rock matrix, and pneumatic pressure in the fractures. Hydrologic property estimates from laboratory and field measurements, which provide initial guesses for model parameters, also were included as data in the inversions. Model parameters that were estimated through the inversion process were fracture and matrix permeability, van Genuchten parameters for the fractures and matrix, and the fracture activity parameter. These parameters were estimated for 31 model layers, although in some cases a common parameter value was estimated for groups of layers, and for 3 of the 4 layers in fault zones.

Calibration of properties for the unsaturated zone flow and transport model through inversion was carried out in a series of steps (Section 8.10.5). One-dimensional vertical column submodels were used for the calibration of the nonfaulted formation rock parameters for the mountain-scale and drift-scale conceptual models. The one-dimensional submodels correspond to 11 surface-based boreholes in which saturation, water potential, and pneumatic pressure have been measured. Water flow (and gas flow in the pneumatic simulations) was simulated simultaneously in all columns. An effective average value of each parameter was estimated for each geologic layer in all 11 columns. A two-dimensional model, consisting of an east-west, vertical cross section through the Ghost Dance fault zone was used to calibrate parameters for the faults. Because data on faults are so limited (one borehole that only partially penetrates the unsaturated zone), the data were separated into four layers (TCw, PTn, TSw, and CHn/CFu) to reduce the number of parameters used to characterize the fault zones. Data for inversion were available for only the first three layers, so only the parameters of these layers were calibrated.

#### **8.12.10.4 Site-Scale Unsaturated Zone Flow Model and Submodels**

The primary purpose of the unsaturated zone flow and transport model was to generate flow fields in the unsaturated zone for direct use by the TSPA model (Section 8.10.6). These flow fields also were used by other performance assessment activities including abstractions, particle-tracking transport simulations, and the unsaturated zone radionuclide transport model. After incorporating the hydrologic parameter sets from the calibrated properties model and other site data, the unsaturated zone flow and transport model was used to generate flow fields for spatially varying lower-bound, mean, and upper-bound net infiltration for the current climate, a postulated future monsoon climate, and a postulated future glacial-transition climate. Each net infiltration case scenario was evaluated using two different perched-water models (flow-through and bypassing), resulting in a total of 18 flow fields. Additional three-dimensional flow fields were generated to evaluate the uncertainty and sensitivity of the unsaturated zone flow and transport model relative to fracture-matrix parameters and infiltration rates over the mountain by using three sets of model parameters and the nine infiltration scenarios.

The unsaturated zone flow and transport model encompasses several flow process submodels, including temperature, geochemistry, and liquid-water travel and tracer/radionuclide transport (Section 8.10.6). The temperature submodel was used to characterize ambient geothermal conditions with temperature data for use in the unsaturated zone flow and transport model. The geochemical submodel includes two submodels of chloride and strontium. The chloride submodel was constructed to represent the conceptual model for the spatial and temporal variations in chloride chemistry and results were compared with pore-water concentrations measured in samples from boreholes and the ESF. The strontium submodel incorporated the effects of rate-limited dissolution and precipitation on the concentration of a solute in addition to dispersion, radioactive decay, and linear equilibrium sorption.

**Model Calibration**—A critical step in developing the three-dimensional unsaturated zone flow model was the use of field-measured liquid saturation, water-potential, and perched-water data for calibration (Section 8.10.6.4). This additional calibration step was important because it increased confidence in model predictions for site conditions. Although the one-dimensional inversions performed with the calibrated properties model produced a valid and appropriately scaled set of parameters on which to base the three-dimensional unsaturated zone flow and transport model, the one-dimensional models, in general, did not predict perched water in several hydrogeologic units below the repository level. Therefore, the three-dimensional calibration effort focused on reproducing perched water observed in the field by using core-scale matrix liquid saturation data, in situ matrix water-potential data, and perched-water elevations from surface-based boreholes and the enhanced characterization of the repository block Cross Drift. Two perched-water models were investigated in which rock properties were modified locally in several grid layers of the lower basal vitrophyre of the TSw unit and upper zeolites in the CHn unit.

Two numerical representations of perched-water conceptual models were developed for the unsaturated zone flow and transport model (Section 8.10.6.4.1). The first representation was of a permeability barrier conceptual model, called the flow-through model, developed for the perched-water bodies in the vicinity of the ESF North Ramp. In this area, perched water occurs above the base of the TSw and is underlain by a zone of low-permeability, zeolitized rock. Although these perched-water bodies in the northern part of the potential repository area may be interconnected, the perched-water zones farther south are considered to be local, isolated bodies. In this conceptual model, both vertical and lateral water movement in the vicinity of the perched zones is controlled mainly by the fracture-permeability and matrix-permeability distributions. The second perched-water conceptual model, called the bypassing model, considers the zeolitic rocks of the CHn to be unfractured. In the numerical representation of this model, it is presumed (similar to the permeability barrier model) that the occurrence of perched water at Yucca Mountain results mainly from the lack of globally connected fractures within zeolitic rocks of the CHn. This model is a special case of the permeability barrier model in which only the low-permeability zeolitic matrix controls water perching because, presumably, fractures are not present in the perching layers. To calibrate the three-dimensional unsaturated zone flow model against observed perched-water conditions at Yucca Mountain, some local modification of rock properties was necessary. In general, permeability was adjusted only within the model layers associated with the perched-water occurrences.

A series of simulations of the perched-water conceptual models were used to analyze percolation fluxes at the potential repository horizon and flow beneath the potential repository (Section 8.10.6.4.2). Percolation fluxes at the repository horizon were calculated for both the flow-through and bypassing perched-water conceptual models under all three present-day infiltration scenarios. In each case, the distribution of percolation flux at the repository horizon was nearly the same as the distribution of net infiltration used as the upper boundary condition, regardless of which perched-water conceptual model was simulated. This is because the perched-water conceptual models differed only in the rock properties used in the bottom layers of the TSw and zeolitic units of the CHn, which had little effect on flow at and above the potential repository horizon. The simulated distribution of percolation flux shows only a small amount of lateral diversion of flow between the land surface and the repository horizon.

The simulations of perched-water conceptual models also were analyzed to determine the fracture and matrix components of percolation flux at the potential repository horizon and at the water table beneath the potential repository. The simulation results indicate that fracture flow is dominant both at the potential repository horizon and at the water table for both conceptual models. At the repository horizon, fracture flow is more than 80 percent of the total percolation flux with virtually no difference between the two conceptual models. Fracture flow at the water table ranges from 70 to 90 percent of the total flow, with the bypassing model consistently predicting lower fracture-flow components at the water table than the flow-through model. For present-day, mean infiltration, the flow-through model predicts that about 87 percent of the flow at the water table is fracture flow, whereas the bypassing model predicts about 73 percent fracture flow.

**Simulation of Temperature**—The unsaturated zone flow and transport model was used to simulate the three-dimensional distribution of temperature in the unsaturated zone as input to thermohydrologic studies of the effects of repository thermal loading under the various infiltration scenarios (Section 8.10.6.5). This simulated temperature distribution was calibrated against temperature data from several boreholes in the site area. The calibrated temperature distribution indicates that mean temperatures at the water table (elevation 730 m [2,400 ft]) range from 28° to 32°C over the model domain.

**Geochemical Modeling**—Geochemical data from the unsaturated zone at Yucca Mountain were analyzed and modeled to evaluate the hydrologic system and assess the magnitude and spatial distribution of surface net infiltration over time (Section 8.10.6.6). Geochemical data provide additional information to analyze the unsaturated zone system. Pore-water chemical concentration data were used to calibrate the unsaturated zone flow and transport model and to bound the infiltration flux, flow pathways, and transport time. Distribution of chemical constituents in both liquid and solid phases of the unsaturated zone depends on many factors, such as hydrologic and geochemical processes of surface precipitation, evapotranspiration, the fracture-matrix interactions of flow and transport, large-scale mixing during lateral transport, and history of climate changes and recharge. A dual-permeability, transient model was necessary to investigate fluid flow and chemical transport phenomena and represent the large spatial and temporal chemical variations. Chemical concentration data were analyzed and modeled by three-dimensional chemical transport simulations and analytical methods, and a distribution of net infiltration based on pore-water chloride concentrations was developed. The chloride-based infiltration rates in different regions of the model domain were compared to the water-balance

model infiltration rates. These data indicate that the chloride-based infiltration analysis has effectively smoothed out the very low and very high values of infiltration from the water-balance model that would have resulted in chloride concentrations much higher or lower than observed. However, the data also indicate that within each of the regions and for the entire domain of the unsaturated zone flow and transport model, average infiltration rates and volumes for the water-balance model and the chloride-based model are very similar.

**Simulation of Calcite Deposition**—Calcite deposition in the rocks of the unsaturated zone was investigated using geochemical, reaction-transport modeling that accounted for the complex interplay of fluid flow, chemical transport, and reaction processes that lead to calcite deposition (Section 8.10.6.7). Overall, simulation results indicate that calcite precipitation values for the TCw unit obtained using simple mineralogy and average TSw water are closer to the measured data than those obtained using complex mineralogy and the measured TSw water (Section 8.10.6.7.2). The simple mineralogy simulations also reproduced the calcite deposition in the PTn satisfactorily. Simulation results for the TSw unit from both mineralogy conditions generally fall in the wide range of measured calcite data. However, the simple mineralogy simulations better represent the field observation that calcite coatings are frequently found on fractures and lithophysal cavities in the TCw and TSw tuffs. This is especially true for the TCw unit close to the land surface, in which reactants of calcite deposition come primarily from percolation water and calcite precipitation occurs mostly in the preferential water flow path in the fractures. The results of simulated calcite deposition were sensitive to percolation flux in that calcite deposition values obtained from the highest percolation rate (20 mm/yr.) were close to the high bound of the measurements. Results from the base-case (5.92 mm/yr.) and lower percolation rate (2 mm/yr.) fall in the middle of the range of measured data for the TSw. This may imply that 20 mm/yr. is an upper bound for percolation, whereas the base-case percolation (5.92 mm/yr.) may be a median value.

**Simulation of Flow Fields for TSPA**—Flow fields needed as input to TSPA modeling were calculated in a series of 18 simulations using the calibrated, three-dimensional, unsaturated zone flow model (Section 8.10.6.8). The 18 simulations encompassed all 9 infiltration scenarios (lower-bound, mean, and upper-bound for present-day, monsoon, and glacial-transition climates) for each of the two perched-water conceptual models: flow-through and bypassing. The flow fields depict the simulated distribution of percolation flux at the potential repository horizon and at the water table for the entire area of the unsaturated zone flow and transport model domain. All simulations were performed using the dual-permeability formulation of the unsaturated zone flow and transport model, the more detailed numerical grid of the potential repository area, and the calibrated parameter sets derived from the hydrologic property and perched-water calibration exercises.

Model-simulated percolation flux at the repository horizon equals or exceeds 15 mm/yr. in relatively small areas in the northern part of the unsaturated zone flow and transport model domain (Section 8.10.6.8.1). In addition, percolation flux equals or exceeds 15 mm/yr. in a small area along the Solitario Canyon fault just west of the potential repository area and in a small area of the southwestern quadrant of the repository area. However, percolation flux is less than about 10 mm/yr. over most of the repository area. For the mean monsoon infiltration scenario, the highest percolation fluxes occur in about the same places as for the present-day scenario, but the highest percolation flux equals or exceeds 40 mm/yr. Over most of the repository area,

percolation flux is less than 15 mm/yr., but in small parts of the repository area percolation flux equals or exceeds about 40 mm/yr. For the mean glacial-transition infiltration scenario, the areas where percolation flux equals or exceeds 40 mm/yr. are significantly larger than for the monsoon scenario. Percolation flux equals or exceeds 40 mm/yr. over much of the northern one-third of the unsaturated zone flow and transport model area and over about one-third of the potential repository area.

Model-simulated percolation flux at the water table differs significantly between the flow-through and the bypassing perched-water conceptual models (Section 8.10.6.8.2). With the flow-through simulation, percolation fluxes at the water table under the northern part of the potential repository area are less than about 1.5 mm/yr., but are between about 1.5 and 6.0 mm/yr. under the southern part. With the bypassing simulation, percolation fluxes at the water table still are less than about 1.5 mm/yr. under the northern part of the repository area. Under the southern part, fluxes generally are less than 3 mm/yr., except near the Ghost Dance (west) fault where they exceed 15 mm/yr. Although the flow-through model predicts large lateral diversion under the northern part of the potential repository, overall, there is much greater vertical flow and much less lateral flow than predicted by the bypassing model. Furthermore, the bypassing model predicts greater bypassing of the perching layers and the zeolitic rocks of the CHn. The lateral flow simulated by both perched-water conceptual models results in concentrations of high percolation flux in the major faults, but this effect is more pronounced with the bypassing model than with the flow-through model.

Patterns of percolation flux at the water table similar to the present-day scenario resulted from simulations of the mean monsoon infiltration scenario and the two perched-water conceptual models, but the fluxes are higher. For the mean monsoon scenario and the flow-through model, percolation fluxes are less than about 4 mm/yr. under the northern part of the potential repository area and between 4 and 35 mm/yr. under the southern part. For the bypassing model, fluxes generally are less than 4 mm/yr. under most of the repository area but are close to 40 mm/yr. near the Ghost Dance (west) fault. For the mean glacial-transition infiltration scenario and the flow through model, percolation fluxes at the water table still are less than 4 mm/yr. under the northern part of the potential repository. However, the areas where fluxes equal or exceed 35 mm/yr. are larger under the southern part of the repository than they were with the monsoon scenario. For the mean glacial-transition infiltration scenario and the bypassing model, percolation fluxes at the water table remain less than 4 mm/yr. under most of the repository area, but are close to 40 mm/yr. near the Ghost Dance (west) Fault. The fact that the simulated distributions of percolation flux at the water table do not change very much as the climate gets wetter is further evidence of the strong lateral flow that occurs above the perching layers under the bypassing model.

**Liquid-Water Travel Time**—Liquid-water travel and tracer transport times for both conservative (nonsorbing) and reactive (sorbing) constituents were estimated using the TSPA flow fields (Section 8.10.6.9.1). Liquid-water travel times from the potential repository to the water table were analyzed as cumulative or fractional breakthroughs. The simulations yielded a wide range of liquid-water travel or tracer transport times for different infiltration rates, tracers, and perched-water conceptual models. The predominant factors affecting liquid-water travel times or tracer transport were net infiltration rates and sorption effects, depending upon whether the tracer was conservative or reactive. To a certain extent, perched water conceptual models also affected

liquid-water travel/transport times, but their effect was secondary compared to the effects of infiltration and sorption. Several conclusions about liquid-water travel times from the potential repository to the water table can be drawn from these simulations:

- Nonsorbing tracers migrate about 100 times faster than adsorbing tracers.
- For both nonsorbing and sorbing tracers, the differences in travel times between the two perched-water conceptual models are relatively small, with the bypassing model producing shorter travel times in most cases.
- Liquid-water travel or tracer transport times are inversely proportional to average net infiltration rate over the model domain. As average net infiltration increases from 5 to 35 mm/yr., average liquid-water travel times for the 50 percent breakthrough decrease by a factor of 100 to 1,000.

#### **8.12.10.5 Seepage Model for Performance Assessment**

Two critical models were developed that provide quantitative descriptions of potential water seepage into drifts of the potential repository at Yucca Mountain: the seepage model for performance assessment and the disturbed drift seepage submodel (Section 8.10.7). The results from these models will be used by performance assessment to develop the probability distributions of water seepage into waste emplacement drifts in the potential repository. These models were used to perform numerical simulations of drift seepage with stochastic representations of hydrological properties and to evaluate the effects of a partially collapsed drift on drift seepage.

Seepage percentage was defined as the model-simulated liquid that seeped into the drift divided by the total liquid arriving on a cross-sectional area corresponding to the footprint of the drift (Section 8.10.7.3). Model results indicate that seepage percentage decreases with increasing van Genuchten  $1/\alpha$ , or fracture continuum permeability. At a percolation flux of 5 mm/yr., the seepage percentage was zero or very near zero for most simulations, with the highest seepage percentages ranging from 33 to 38 percent. At a percolation flux of 14.6 mm/yr., the highest seepage percentages range from 58 to 68 percent. At a percolation flux of 73.2 mm/yr., the highest seepage percentages ranged from 70 to 80 percent. Simulation results indicated that drift degradation had little effect on seepage for the degradation conditions simulated (Section 8.10.7.4).

#### **8.12.10.6 Mountain-Scale Coupled Thermohydrologic Models**

The mountain-scale thermohydrologic model was developed to evaluate the effects of coupled thermohydrologic processes on mountain-scale conditions in the unsaturated zone at Yucca Mountain (Section 8.10.8). The mountain-scale thermohydrologic model and associated submodels provide the necessary framework to test conceptual hypotheses of flow and predict flow behavior under thermal loading conditions. The thermohydrologic model was used to determine the effect of thermal loading in the potential repository on mountain-scale liquid and gas flux and temperature and moisture distribution in the unsaturated zone. Of particular interest is the impact of thermal loading imposed by waste emplacement on percolation at and near the

repository host rock and the potential flow-barrier effects in the basal vitrophyre underlying the repository horizon. The mountain-scale thermohydrologic flow fields were developed using the unsaturated zone flow and transport model with input parameters based on the calibrated properties set. The flow fields were simulated with the spatially varying mean infiltration rates for the three climate states that are likely to occur during the thermal loading period. The simulations were performed using the average thermal load of  $0.018 \text{ kw/m}^2$  ( $72.7 \text{ kW/a.}$ ) and a ventilation efficiency of 70 percent for 50 yr. In all simulations, each repository drift was represented by a single element (with both matrix and fracture continua for a dual-permeability formulation) and was simulated with the properties of the unsaturated zone flow and transport model layer in which the element was located (Section 8.10.8.2.2).

Several numerical simulations were performed to investigate mountain-scale thermohydrologic processes in the unsaturated zone under thermal loading (Section 8.10.8.3). Two three-dimensional simulations were performed using the repository area submodel under mean, present-day infiltration, the  $72.7 \text{ kW/a.}$  thermal load, no discrete drifts, and no ventilation. Four two-dimensional simulations were performed, two along each of two north-south cross sections. Variable conditions simulated in the two-dimensional simulations included the presence or absence of ventilation during the first 50 yr., the position of the lower temperature boundary, the presence or absence of discrete drifts, and the sequencing of infiltration scenarios. These simulations of the nonisothermal fluid and heat flow were conducted for a total thermal loading period of 100 k.y. This sequence of three-dimensional and two-dimensional simulations allowed investigation of the effect of important thermohydrologic factors (lower-temperature boundary, type of heat source, infiltration scenario, and ventilation) by way of similar but progressively complex simulations.

In both three-dimensional and two-dimensional simulations, when the thermal load was applied as a continuous, smeared heat source over the repository block (without ventilation), the simulated distributions of temperature were very similar (Section 8.10.8.3.3). Significant differences in the simulated temperature profiles between the two types of simulations occur only at the center of the repository horizon. The three-dimensional simulation simulated more rapid cooling at the end of the boiling period than the two-dimensional simulation because of lateral heat conduction into the third dimension. After 2 k.y., the simulated temperature at the repository was  $77^\circ\text{C}$  in the three-dimensional simulation compared to  $92^\circ\text{C}$  in the two-dimensional simulation. The simulated maximum temperature at the water table was  $70^\circ\text{C}$  in both types of simulations for the current thermal loading scenario, mean present-day infiltration, and no ventilation.

In the two-dimensional simulations without ventilation, heat-pipe conditions develop in a region above the repository during 10 to 100 yr. Complete dryout conditions were predicted near the drifts, mainly within fracture elements, with drift temperatures exceeding  $100^\circ\text{C}$  for hundreds of years. In the rock mass between the drifts, temperatures may rise to boiling conditions and saturation may be reduced slightly. No complete dryout conditions were predicted between the drifts except in zones under low surface infiltration. The flux into the drifts may exceed  $1,200 \text{ mm/yr.}$ , particularly in the low infiltration areas due to drier conditions and consequentially high capillary-pressure gradients. However, the high percolation fluxes occur only at early times (less than 100 yr.). The two-dimensional simulations indicate that although vertical flux between the drifts will continue at a rate close to the ambient percolation fluxes for

most of the thermal loading period, this flux may be enhanced by condensate drainage for the first 1 k.y. of thermal load.

According to model results, thermal loading at the repository will result in significant changes in the temperature conditions and moisture distribution at the repository as well as the zone directly above and below the repository. Without ventilation, strong liquid and gas flow fields will develop in the fracture network. Two-phase heat-pipe conditions will occur only in a region extending up to 200 m (660 ft) above the repository to the base of the PTn stratigraphic unit. These conditions will occur between 500 and 1,000 yr. Complete dryout of both the fracture and matrix continua at the repository will develop over the first 100 yr. Recovery to the ambient saturation occurs during 500 to 5,000 yr. Model results indicate that localized dryout of the matrix at the repository and in areas with low infiltration rates will occur even with ventilation. Temperatures may be elevated to approximately 250°C within the completely dry drifts when no ventilation is implemented, and most of the repository remains at boiling temperature (about 97°C) for nearly 1 k.y. When ventilation is used, only localized boiling at the drifts is predicted.

Without ventilation and with present-day mean infiltration for the entire thermal loading period, simulations indicate 30 to 35°C increases in temperature at the water table to an average of 70°C. With ventilation and the change to monsoon and glacial-transition climate conditions, the predicted maximum temperature at the water table is about 65°C. At the top of the CHn stratigraphic unit, the predicted maximum temperature is 75° to 80°C for a period of between 2 and 7 k.y.

Even with ventilation, the models predict a zone with substantial changes in matrix liquid saturation that extends about 50 m (160 ft) below and above the potential repository horizon. In the two-dimensional simulations, surface infiltration rates resulting from monsoon and glacial-transition climates have little impact on the duration and extent of boiling zones at the repository. However, beyond 2 k.y., the higher percolation rates resulting from the two wetter climates accelerate the processes of cooling and resaturation and elevate the ambient percolation flux.

#### **8.12.10.7 Drift-Scale Coupled Thermohydrologic Chemical Seepage Models**

Drift-scale models of the near field environment of the potential repository in the unsaturated zone at Yucca Mountain were developed to evaluate the potential effects of coupled thermohydrologic chemical processes on unsaturated zone flow and transport (Section 8.10.9). These models include the Drift Scale Test thermohydrologic chemical model and the thermohydrologic chemical seepage model. These models provide the framework to evaluate thermohydrologic chemical coupled processes at the drift scale, predict flow and transport behavior for specified thermal loading conditions, and predict the chemistry of waters and gases entering potential emplacement drifts. The Drift Scale Test thermohydrologic chemical model, constructed for the Drift Scale Test, was used to predict thermohydrologic chemical processes prior to and during the Drift Scale Test. Measured data from the Drift Scale Test were used to evaluate the conceptual and numerical models. The iterative approach of evaluating, refining, and comparing the Drift Scale Test numerical model against data was performed throughout the Drift Scale Test study. The thermohydrologic chemical seepage model provides an analysis of the effects of thermohydrologic chemical processes in the near-field host rock surrounding the potential emplacement drifts on the seepage water chemistry and gas-phase composition. The

thermohydrologic chemical analysis included complete investigation of pertinent mineral-water processes in the host rock and their effect on the near-field environment. The model was used to evaluate the effects of mineral dissolution and precipitation; the effects of CO<sub>2</sub> exsolution and transport in the region surrounding the drift; the potential for forming calcite, silica, or other mineral assemblage precipitation caps; and the resulting changes to porosity, permeability, and seepage. The thermohydrologic chemical seepage model was developed with data for the Topopah Spring crystal-poor, middle nonlithophysal unit, in which part of the potential repository would be sited.

The Drift Scale Test thermohydrologic chemical model and thermohydrologic chemical seepage numerical model involve a number of physical and chemical processes, including liquid and vapor flow, heat transport and thermal effects due to boiling and condensation, transport of aqueous and gaseous species, mineralogical characteristics and changes, and aqueous and gaseous chemistry (Section 8.10.9.2). In addition to these processes, the thermohydrologic chemical conceptual and numerical models of reaction-transport processes in the fractured welded tuffs of the potential repository host rock must also account for the different rates of transport in very permeable fractures, compared to the much less permeable rock matrix.

Results of the Drift Scale Test thermohydrologic chemical model indicate that the strong thermal load applied to the system results in changes in temperature, liquid saturation, and gas-phase compositions, which in turn cause changes in the chemistry of the system (Section 8.10.9.3.2). Simulated distributions of temperature and liquid saturation after 12 and 20 mo. of the heating phase for both the fractures and the matrix indicate that the zone of dryout increases over time and results in an isothermal boiling/condensation zone. Large drainage zones are apparent in the fractures below the heaters after 20 mo. The buildup of water above the heaters is fairly localized, but moves up into the region of the upper hydrology boreholes after 20 mo. of heating. Simulated distributions of CO<sub>2</sub> concentrations and temperature in the fractures and matrix indicate the development of a halo of increased CO<sub>2</sub> concentrations centered approximately at the 60°C isotherm. Between 6 and 20 mo. of the heating phase, the halo increases considerably in extent and magnitude of concentration. Although the Drift Scale Test thermohydrologic chemical model simulated the evolution of numerous aqueous species during the heating cycle, changes in pH were indicative of the major hydrochemical trends. The most obvious trend in pH is a reduction to values of about 6.5 in the condensate region, corresponding directly to the halo of increased CO<sub>2</sub> concentrations in the gaseous system. As with CO<sub>2</sub> concentrations, the zone of low pH increases in size and moves outward with time. Although mineralogical changes occurred over the course of the Drift Scale Test and strongly influenced water and gas chemistry, the total amount of minerals precipitated or dissolved was very small compared to the available fracture or matrix porosity. Calcite was the most important mineral in terms of system chemistry and its abundance. Changes in porosity and permeability due to mineral dissolution and precipitation were negligible.

The thermohydrologic chemical seepage model applied the same methods of simulating coupled thermohydrologic and chemical processes to predict, at a drift scale, the performance of the potential repository during 100 k.y. (Section 8.10.9.4). Thermohydrologic chemical seepage model simulations were performed in two dimensions along a laterally continuous, vertical geologic section through the footprint of the potential repository. The simulations consider a potential repository drift located in the Topopah Spring Tuff middle nonlithophysal geologic unit

even though only part of the potential repository is planned to be located in this unit. Four infiltration cases were simulated with the thermohydrologic chemical seepage model (Section 8.10.9.4.1). The first infiltration case uses the ambient, present-day mean infiltration rate at a specific location near the edge of the potential repository area. The other three cases use infiltration rates that were selected as representative of the entire potential repository for lower-bound, mean, and upper-bound infiltration. In each of these cases, infiltration rates were increased step-wise in time to correspond to the modern (present-day), monsoon, and glacial-transition climate conditions.

Initially, the thermohydrologic chemical seepage model was run with mean present-day infiltration and thermal loading but without reactive transport, thus considering only thermal and hydrological effects (Section 8.10.9.4.2). Temperatures rose quickly above the boiling point (about 97°C) early in the postclosure period, and were higher at the base of the drift where the waste package is closest to the drift wall. The return to ambient temperatures after heating took 50 to 100 k.y. The maximum temperature in the waste package (about 270°C) occurred after about 55 yr., whereas the maximum temperature at the drift base was about 190°C. Around the drift, the rock matrix and most of the fractures began to rewet after 1 to 2 k.y., whereas rewetting of fractures at the drift base did not occur until about 3 k.y. Matrix saturations at a simulated time of 600 yr. (near maximum dryout) indicated that the dryout zone extends about 10 m (33 ft) above, 17 m (56 ft) to the side, and 22 m (72 ft) below the drift. Comparison of the simulation without reactive transport (thermohydrologic simulation) and simulations of the selected geochemical systems (thermohydrologic chemical simulations) indicated that temperatures, liquid saturations, and air mass fractions were essentially the same, indicating that the thermal and hydrologic behavior of the system was not significantly affected by water-gas-rock chemical interactions.

Simulations of the three climate-change infiltration cases and the full geochemical system indicated that temperatures around the drift did not differ by more than about 15°C among the different infiltration cases. The simulations also indicated that the return to ambient temperatures takes about 100 k.y. for all infiltration cases.

Thermohydrologic chemical seepage model simulations for the full geochemical system indicate that CO<sub>2</sub> concentrations in fractures drop significantly during the dryout period (about 50 to 2,000 yr.) and then increase again during rewetting. The increase in CO<sub>2</sub> concentration during rewetting probably is caused by heating of the water as it approaches the drift wall. The evolution of water chemistry in response to repository heating was evaluated by examining simulated changes in several major aqueous constituents. Results indicate that water seeping back into repository drifts after the dryout period will not be significantly more concentrated with chloride than the ambient pore water. The pH of water reaching the drift wall during rewetting was roughly neutral (7.2 to 8.3) for the calcite-silica-gypsum system and about 8.6 to 9.0 for the full geochemical system. Simulation of the evolution of pH, carbonate, and CO<sub>2</sub> with the thermohydrologic chemical seepage model resulted in very different trends with respect to mineralogy depending on whether the full or the calcite-silica-gypsum geochemical system was considered. Simulations of the full geochemical system, which considered aluminosilicate reactions, generally yielded higher pH and total aqueous carbonate concentrations and lower CO<sub>2</sub> partial pressures than the calcite-silica-gypsum system simulations. Calcium depletion and increased sodium concentrations were further indicators of feldspar (albite) dissolution and

calcium-zeolite precipitation in the full geochemical system simulations. These trends were not observed in the calcite-silica-gypsum system simulations. Evidence that the full geochemical system simulations overestimated feldspar dissolution and zeolite precipitation rates also was indicated by the calcium depletion and increasing sodium concentrations calculated under ambient conditions.

Thermohydrologic chemical seepage model results indicate that the change in fracture porosity in the vicinity of the drift after 10 k.y. for the three infiltration cases considered would be less than 0.5 percent of the initial porosity and mostly negative. For the calcite-silica-gypsum geochemical system simulation, the maximum porosity reduction occurs with the upper-bound infiltration case and is predominantly above the drift. The porosity decrease is due primarily to zeolite precipitation in the full geochemical system simulation and calcite precipitation in the calcite-silica-gypsum simulation. Because the porosity changes were very small, permeability changes also were negligible, and thermohydrological processes were not significantly affected by mineral precipitation or dissolution. Thus, the formation of a mineral cap in the fractures above repository drifts that could effectively divert downward percolation seems unlikely.

#### **8.12.10.8 Radionuclide Transport Model**

The unsaturated zone radionuclide transport model of Yucca Mountain and its submodels were developed to evaluate radioactive solute and colloid transport under ambient conditions from the potential repository horizon to the water table (Section 8.10.10). The unsaturated zone radionuclide transport model considered:

- Transport of radionuclides through fractured tuffs
- Effects of differences in intensity and configuration of fracturing among the principal hydrogeologic units
- Colloid transport
- Physical and retardation processes
- Effects of perched water.

Simulations of transport of radioactive solutes and colloids, incorporating all relevant processes, from the repository horizon to the water table were performed to support model development and performance assessment studies of the potential repository. The results of the simulations were used to evaluate the transport of radioactive solutes and colloids, and to determine the processes, mechanisms, and geologic features that have a significant effect on transport. The contributions of daughter products of radioactive decay to transport were evaluated from the bottom of the potential repository to the water table. The effects of the various conceptual models of perched water on transport also were evaluated.

**Two-Dimensional Radionuclide Transport Simulations**—Two-dimensional radionuclide transport from the potential repository to the water table at Yucca Mountain was investigated using representative hydrogeologic profiles embedded in the unsaturated zone radionuclide transport model (Section 8.10.10.5). These profiles are two-dimensional cross sections in the

sense that concentrations were computed in both the vertical and horizontal directions in the fractures and the matrix blocks of each layer in the hydrogeologic units in the cross sections. However, these cross sections span only a very short distance in the horizontal direction, which is the minimum necessary to simulate the matrix-fracture system in the representative hydrogeologic profile at the given location. The purpose of the two-dimensional transport simulations was to evaluate the integrated transport through the complete hydrogeologic system beneath the potential repository as well as the individual hydrogeologic units. The hydrogeologic units considered are the same as those defined for the site-scale unsaturated zone flow and transport model and include the subunits of the TSw, the vitric and zeolitic portions of the Calico Hills Formation, and subunits of the Prow Pass Tuff. One of these vertical cross sections is located in the southern part of the potential repository area and one is in the northern part.

Three representative radionuclides were considered in the two-dimensional simulations:  $^{99}\text{Tc}$  (nonsorbing),  $^{237}\text{Np}$  (moderately sorbing), and  $^{239}\text{Pu}$  (strongly sorbing) (Section 8.10.10.5.1). In the simulations, radionuclides were released continuously at the top of the domain, which coincides with the potential repository, and the calculated contaminant distributions (as relative concentrations) were monitored over time. For the primary group of simulations, the percolation rate was 6 mm/yr., which is close to the mean present-day rate. Simulations also were made using a higher infiltration rate (33.5 mm/yr.) to represent glacial climatic conditions.

Results of two-dimensional radionuclide-transport simulations for individual hydrogeologic units indicate that the TSw unit does not effectively retard radionuclide transport because of the dominance of fracture flow that consequently reduces matrix diffusion and sorption (Section 8.10.10.5.2). Because flow in the vitric portion of the Calico Hills Formation (CHv) is primarily matrix flow, the resulting reduced flow velocity and increased contact time for matrix diffusion and sorption make the CHv unit an effective transport barrier. Flow in the zeolitic portion of the Calico Hills Formation (CHz) is dominantly in the fractures and radionuclide transport through the unit is expected to be rapid, similar to that in the TSw unit. Within the Prow Pass Tuff, simulation results indicate that fracture flow may be dominant in the uppermost and lowermost layers, but the two middle layers behave like nonfractured porous media. Consequently, these layers are quite efficient in retarding transport even for the nonsorbing  $^{99}\text{Tc}$ , which takes more than 1 k.y. to pass through them.

In the southern part of the repository area, simulated migration of radionuclides from the potential repository to the water table was slow because of the presence of the CHv unit, through which matrix flow is dominant. The simulated  $^{99}\text{Tc}$  front reaches the water table in several thousand years and the  $^{237}\text{Np}$  breakthrough takes between 10 and 100 k.y. to reach the water table because of the moderate sorption. In the simulation, the strongly sorbing  $^{239}\text{Pu}$  does not advance past the chlv layer, less than 60 m from the point of release, even after 100 k.y. In the northern part of the potential repository area, simulations indicated that all three radionuclides moved through the unsaturated zone toward the water table more quickly than in the southern part of the repository area. This probably was due to fracture-dominated flow through the zeolitic CHn.

**Three-Dimensional Radionuclide Transport Simulations**—The three-dimensional, site-scale simulations of radionuclide transport with the unsaturated zone radionuclide transport model

used the same horizontal numerical grid and vertical layering scheme that were used to calculate the TSPA flow fields (Section 8.10.10.6). The transport simulations were run under the same three climate-oriented infiltration regimes (present-day, monsoon, and glacial transition) as were simulated by the site-scale flow model for the TSPA flow fields, each with a lower-bound, mean, and upper-bound estimate. The release rate of radionuclides at the potential repository was considered constant over time. Radionuclides considered in the simulations were  $^{99}\text{Tc}$  (nonsorbing),  $^{237}\text{Np}$  (moderately sorbing), and  $^{239}\text{Pu}$  (strongly sorbing). Important members of the decay chains of  $^{237}\text{Np}$  and  $^{239}\text{Pu}$  also were considered. These include  $^{233}\text{U}$ ,  $^{229}\text{Th}$ ,  $^{235}\text{U}$ , and  $^{231}\text{Pa}$ .

The normalized release rate at the water table for  $^{99}\text{Tc}$  showed a very strong dependence on the infiltration regime. As the infiltration rate increases from low to mean present-day level, the arrival of the 10 percent relative concentration decreases from about 10,000 yr. to about 300 yr. (Section 8.10.10.6.2). The sorption of  $^{237}\text{Np}$  retards its transport through the unsaturated zone system as compared to  $^{99}\text{Tc}$  and is sufficient to increase the time to reach the water table by a factor of about 40 (Section 8.10.10.6.3). The relative concentration of  $^{239}\text{Pu}$  never reaches 10 percent at the water table even after 1 M.y. of continuous release because of the strong sorption of  $^{239}\text{Pu}$  (Section 8.10.10.6.4). However, the daughter products of  $^{239}\text{Pu}$ , such as  $^{235}\text{U}$ , reach the water table much more quickly.

Simulation results reveal that radionuclide transport from the repository to the water table is affected significantly by the faults, especially at the early times (Section 8.10.10.6.5). Splay G of the Solitario Canyon fault is the primary transport-facilitating feature. The Ghost Dance fault splay is the next most important transport-facilitating feature. Although it facilitates downward migration, this fault appears to act as a barrier to the lateral migration of radionuclides, as evidenced both at the bottom of the TSw and at the water table.

Overall, radionuclide transport to the water table is faster in the southern part of the potential repository block, where it is also areally concentrated (Section 8.10.10.6.5). The major reasons for this transport pattern are:

- The water flow pattern dictates the advective transport pattern, and the maximum downward water flow within the footprint of the potential repository is in the southern part under the flow through perched-water conceptual model.
- The presence of the highly conductive faults, such as Splay G of the Solitario Canyon fault and the Ghost Dance fault splay, act as conduits for fast transport, despite the fact that the vitric CHn unit underneath the TSw behaves as a porous medium.
- The low-permeability zones at the TSw-CHn interface in the northern part of the potential repository act as barriers to water drainage, and lead to low water velocities and presence of perched-water bodies that also retard the radionuclides.

**Three-Dimensional Site-Scale Transport of Plutonium True Colloids**—As a submodel of the unsaturated zone radionuclide transport model, three-dimensional transport of Pu colloids also was simulated (Section 8.10.10.7). The colloid simulations used the same horizontal numerical grid and vertical layering scheme as were used to calculate the TSPA flow fields under mean

present-day infiltration. The transport of Pu colloids is strongly sensitive to the declogging parameter (Section 8.10.10.7.2). Small values of the parameter (slow declogging) lead to significant retardation of colloids and long travel times to the water table. In this case, the 10 percent relative concentration takes more than 10 k.y. to reach the water table. Large values of the parameter (fast declogging) lead to dramatically different behavior, with the 10 percent relative concentration reaching the water table in as few as 15 yr. The extreme sensitivity of colloid filtration on the declogging parameter and the dearth of representative information on this value for the various geologic units in the unsaturated zone point to a need for further study.

## 8.13 REFERENCES

### 8.13.1 Documents Cited

Ahlers, C.F.; Bandurraga, T.M.; Bodvarsson, G.S.; Chen, G.; Finsterle, S.; and Wu, Y-S. 1995a. *Performance Analysis of the LBNL/USGS Three-Dimensional Unsaturated Zone Site-Scale Model*. Milestone 3GLM105M. Berkeley, California: Lawrence Berkeley National Laboratory. ACC: MOL.19970116.0146.

Ahlers, C.F.; Bandurraga, T.M.; Bodvarsson, G.S.; Chen, G.; Finsterle, S.; and Wu, Y-S. 1995b. *Summary of Model Calibration and Sensitivity Studies Using the LBNL/USGS Three-Dimensional Unsaturated Zone Site-Scale Model*. Milestone 3GLM107M. Berkeley, California: Lawrence Berkeley National Laboratory. ACC: MOL.19960208.0092.

Ahlers, C.F.; Finsterle, S.; and Bodvarsson, G.S. 1999. "Characterization and Prediction of Subsurface Pneumatic Response at Yucca Mountain, Nevada." *Journal of Contaminant Hydrology*, 38, (1-3), 47-68. New York, [New York]: Elsevier. TIC: 244160.

Anna, L.O. 1998a. *Preliminary Three-Dimensional Discrete Fracture Model of the Topopah Spring Tuff in the Exploratory Studies Facility, Yucca Mountain Area, Nye County, Nevada*. Open-File Report 97-834. Denver, Colorado: U.S. Geological Survey. TIC: 236829.

Anna, L.O. 1998b. *Preliminary Three-Dimensional Discrete Fracture Model, Tiva Canyon Tuff, Yucca Mountain Area, Nye County, Nevada*. Open-File Report 97-833. Denver, Colorado: U.S. Geological Survey. TIC: 236723.

Bandurraga, T.M. and Bodvarsson, G.S. 1999. "Calibrating Hydrogeologic Parameters for the 3-D Site-Scale Unsaturated Zone Model of Yucca Mountain, Nevada." *Journal of Contaminant Hydrology*, 38, (1-3), 25-46. New York, New York: Elsevier. TIC: 244160.

Birkholzer, J.; Li, G.; Tsang, C-F.; and Tsang, Y. 1999. "Modeling Studies and Analysis of Seepage into Drifts at Yucca Mountain." *Journal of Contaminant Hydrology*, 38, (1-3), 349-384. New York, New York: Elsevier. TIC: 244160.

Bodvarsson, G.S. and Bandurraga, T.M., eds. 1996. *Development and Calibration of the Three-Dimensional Site-Scale Unsaturated Zone Model of Yucca Mountain, Nevada*. LBNL-39315. Berkeley, California: Lawrence Berkeley National Laboratory. ACC: MOL.19970701.0692.

Bodvarsson, G.S.; Bandurraga, T.M.; and Wu, Y.S., eds. 1997. *The Site-Scale Unsaturated Zone Model of Yucca Mountain, Nevada, for the Viability Assessment*. LBNL-40376. Berkeley, California: Lawrence Berkeley National Laboratory. ACC: MOL.19971014.0232.

Bodvarsson, G.S.; Boyle, W.; Patterson, R.; and Williams, D. 1999. "Overview of Scientific Investigations at Yucca Mountain—The Potential Repository for High-Level Nuclear Waste." *Journal of Contaminant Hydrology*, 38, (1-3), 3-24. New York, New York: Elsevier. TIC: 244160.

Braester, C. 1973. "Moisture Variation at the Soil Surface and the Advance of the Wetting Front During Infiltration at Constant Flux." *Water Resources Research*, 9, (3), 687-694. Washington, D.C.: American Geophysical Union. TIC: 242383.

Buesch, D.C.; Spengler, R.W.; Moyer, T.C.; and Geslin, J.K. 1996. *Proposed Stratigraphic Nomenclature and Macroscopic Identification of Lithostratigraphic Units of the Paintbrush Group Exposed at Yucca Mountain, Nevada*. Open-File Report 94-469. Denver, Colorado: U.S. Geological Survey. ACC: MOL.19970205.0061.

Christiansen, R.L. and Lipman, P.W. 1965. *Geologic Map of the Topopah Spring NW Quadrangle, Nye County, Nevada*. Geologic Quadrangle Map GQ-444. Washington, D.C.: U.S. Geological Survey. TIC: 212357.

Conca, J.L. and Wright, J. 1998. "The UFA Method for Rapid, Direct Measurements of Unsaturated Soil Transport Properties in Soil, Sediment, and Rock." *Australian Journal of Soil Research*, 36, (2), 291-315. [Melbourne], Australia: CSIRO Publishing. TIC: 248019.

CRWMS M&O 1995. Structural Log, USW SD-12 (5.3'-2166.0'). Las Vegas, Nevada: CRWMS M&O. ACC: DRC.19960926.0176.

CRWMS M&O 1997a. Daily Operations Report: USW WT-24, July 14, 1997 to November 7, 1997. Las Vegas, Nevada: CRWMS M&O. ACC: MOL.19980128.0477.

CRWMS M&O 1997b. *Unsaturated Zone Flow Model Expert Elicitation Project*. Las Vegas, Nevada: CRWMS M&O. ACC: MOL.19971009.0582.

CRWMS M&O 1998a. *Interim Report: Plant and Soil Related Processes Along a Natural Thermal Gradient at Yucca Mountain, Nevada*. B00000000-01717-5705-00098 REV 00. Draft. Las Vegas, Nevada: CRWMS M&O. ACC: MOL.19980727.0263.

CRWMS M&O 2000a. *In Situ Field Testing of Processes*. ANL-NBS-HS-000005 REV 00. Las Vegas, Nevada: CRWMS M&O. ACC: MOL.20000504.0304.

CRWMS M&O 2000b. *Multiscale Thermohydrologic Model*. ANL-EBS-MD-000049 REV 00. Las Vegas, Nevada: CRWMS M&O. ACC: MOL.20000609.0267.

CRWMS M&O 2000c. *Geochemical and Isotopic Constraints on Ground-Water Flow Directions, Mixing, and Recharge at Yucca Mountain, Nevada*. ANL-NBS-HS-000021 REV 00. Las Vegas, Nevada: CRWMS M&O. Submit to RPC URN-0060

CRWMS M&O 2000d. *UZ Flow Models and Submodels*. MDL-NBS-HS-000006 REV 00. Las Vegas, Nevada: CRWMS M&O. ACC: MOL.19990721.0527.

CRWMS M&O 2000e. *Development of Numerical Grids for UZ Flow and Transport Modeling*. ANL-NBS-HS-000015 REV 00. Las Vegas, Nevada: CRWMS M&O. ACC: MOL.19990721.0517.

CRWMS M&O 2000f. *Calibrated Properties Model*. MDL-NBS-HS-000003 REV 00. Las Vegas, Nevada: CRWMS M&O. ACC: MOL.19990721.0520.

CRWMS M&O 2000g. *Analysis of Hydrologic Properties Data*. ANL-NBS-HS-000002 REV 00. Las Vegas, Nevada: CRWMS M&O. ACC: MOL.19990721.0519.

CRWMS M&O 2000h. *Seepage Calibration Model and Seepage Testing Data*. MDL-NBS-HS-000004 REV 00. Las Vegas, Nevada: CRWMS M&O. ACC: MOL.19990721.0521.

CRWMS M&O 2000i. *Mountain-Scale Coupled Processes (TH) Models*. MDL-NBS-HS-000007 REV 00. Las Vegas, Nevada: CRWMS M&O. ACC: MOL.19990721.0528.

CRWMS M&O 2000j. *Drift-Scale Coupled Processes (DST and THC Seepage) Models*. MDL-NBS-HS-000001 REV 00. Las Vegas, Nevada: CRWMS M&O. ACC: MOL.19990721.0523.

CRWMS M&O 2000k. *Analysis of Base-Case Particle Tracking Results of the Base-Case Flow Fields*. ANL-NBS-HS-000024 REV 00. Las Vegas, Nevada: CRWMS M&O. ACC: MOL.20000207.0690.

CRWMS M&O 2000l. *Radionuclide Transport Models Under Ambient Conditions*. MDL-NBS-HS-000008 REV 00. Las Vegas, Nevada: CRWMS M&O. ACC: MOL.19990721.0529.

CRWMS M&O 2000m. *Conceptual and Numerical Models for UZ Flow and Transport*. MDL-NBS-HS-000005 REV 00. Las Vegas, Nevada: CRWMS M&O. ACC: MOL.19990721.0526.

CRWMS M&O 2000n. *Unsaturated Zone and Saturated Zone Transport Properties (U0100)*. ANL-NBS-HS-000019 REV 00. Las Vegas, Nevada: CRWMS M&O. ACC: MOL.20000817.0546.

CRWMS M&O 2000o. *UZ Colloid Transport Model*. ANL-NBS-HS-000028 REV 00. Las Vegas, Nevada: CRWMS M&O. ACC: MOL.20000822.0005.

CRWMS M&O 2000p. *Particle Tracking Model and Abstraction of Transport Processes*. ANL-NBS-HS-000026 REV 00. Las Vegas, Nevada: CRWMS M&O. ACC: MOL.20000502.0237.

CRWMS M&O 2000q. *Unsaturated Zone Flow and Transport Model Process Model Report*. TDR-NBS-HS-000002 REV 00. Las Vegas, Nevada: CRWMS M&O. ACC: MOL.20000320.0400.

CRWMS M&O 2000r. *Thermal Tests Thermal-Hydrological Analyses/Model Report*. ANL-NBS-TH-000001 REV 00. Las Vegas, Nevada: CRWMS M&O. ACC: MOL.20000505.0231.

CRWMS M&O 2000s. *Seepage Model for PA Including Drift Collapse*. MDL-NBS-HS-000002 REV 00. Las Vegas, Nevada: CRWMS M&O. ACC: MOL.19990721.0525.

Day, W.C.; Potter, C.J.; Sweetkind, D.S.; Dickerson, R.P.; and San Juan, C.A. 1998. *Bedrock Geologic Map of the Central Block Area, Yucca Mountain, Nye County, Nevada*. Miscellaneous Investigations Series Map I-2601. [Washington, D.C.]: U.S. Geological Survey. TIC: 237019.

DOE (U.S. Department of Energy) 1998a. *Viability Assessment of a Repository at Yucca Mountain*. DOE/RW-0508. Washington, D.C.: U.S. Department of Energy, Office of Civilian Radioactive Waste Management. ACC: MOL.19981007.0027; MOL.19981007.0028; MOL.19981007.0029; MOL.19981007.0030; MOL.19981007.0031; MOL.19981007.0032.

DOE (U.S. Department of Energy) 1998b. *Total System Performance Assessment*. Volume 3 of *Viability Assessment of a Repository at Yucca Mountain*. DOE/RW-0508. Washington, D.C.: U.S. Department of Energy, Office of Civilian Radioactive Waste Management. ACC: MOL.19981007.0030.

DOE (U.S. Department of Energy) 1999. *Site Characterization Progress Report Yucca Mountain, Nevada*. DOE/RW-0512. Number 19. Washington, D.C.: U.S. Department of Energy, Office of Civilian Radioactive Waste Management. ACC: HQO.19990813.0018.

Doughty, C. 1999. "Investigation of Conceptual and Numerical Approaches for Evaluating Moisture, Gas, Chemical, and Heat Transport in Fractured Unsaturated Rock." *Journal of Contaminant Hydrology*, 38, (1-3), 69-106. New York, New York: Elsevier Science Publishers. TIC: 244160.

Engstrom, D.A. and Rautman, C.A. 1996. *Geology of the USW SD-9 Drill Hole, Yucca Mountain, Nevada*. SAND96-2030. Albuquerque, New Mexico: Sandia National Laboratories. ACC: MOL.19970508.0288.

Fabryka-Martin, J.T.; Turin, H.J.; Wolfsberg, A.V.; Brenner, D.; Dixon, P.R.; and Musgrave, J.A. 1996. *Summary Report of Chlorine-36 Studies*. LA-CST-TIP-96-003. Draft. Los Alamos, New Mexico: Los Alamos National Laboratory. ACC: MOL.19970103.0037.

Fabryka-Martin, J.T.; Wightman, S.J.; Robinson, B.A.; and Vestal, E.W. 1994. *Infiltration Processes at Yucca Mountain Inferred from Chloride and Chlorine-36 Distributions*. LA-CST-TIP-94-019. Draft. Los Alamos, New Mexico: Los Alamos National Laboratory. ACC: MOL.19950630.0316.

Fabryka-Martin, J.T.; Wolfsberg, A.V.; Levy, S.S.; Roach, J.L.; Winters, S.T.; Wolfsberg, L.E.; Elmore, D.; and Sharma, P. 1998. "Distribution of Fast Hydrologic Paths in the Unsaturated Zone at Yucca Mountain." *High-Level Radioactive Waste Management, Proceedings of the Eighth International Conference, Las Vegas, Nevada, May 11-14, 1998*. Pages 93-96. La Grange Park, Illinois: American Nuclear Society. TIC: 237082.

Fetter, C.W. 1993. *Contaminant Hydrogeology*. New York, New York: Macmillan Publishing. TIC: 240691.

Finsterle, S. 1993. *ITOUGH2 User's Guide Version 2.2*. LBL-34581. Berkeley, California: Lawrence Berkeley National Laboratory. TIC: 240901.

Finsterle, S. 1999. *ITOUGH2 User's Guide*. LBNL-40040. Berkeley, California: Lawrence Berkeley National Laboratory. TIC: 243018.

Finsterle, S.; Bandurraga, T.M.; Doughty, C.; and Bodvarsson, G.S. 1996. "Simulation of Coupled Processes in a Two-Dimensional West-East Cross-Section of Yucca Mountain, Nevada." Chapter 12 of *Development and Calibration of the Three-Dimensional Site-Scale Unsaturated Zone Model of Yucca Mountain, Nevada*. Bodvarsson, G.S. and Bandurraga, T.M., eds. Berkeley, California: Lawrence Berkeley National Laboratory. ACC: MOL.19970211.0176.

Flint, A.L. and Childs, S.W. 1991. "Use of the Priestley-Taylor Evaporation Equation for Soil Water Limited Conditions in a Small Forest Clearcut." *Agricultural and Forest Meteorology*, 56, (3-4), 247-260. Amsterdam, The Netherlands: Elsevier. TIC: 241865.

Flint, A.L.; Hevesi, J.A.; and Flint, L.E. 1996. *Conceptual and Numerical Model of Infiltration for the Yucca Mountain Area, Nevada*. Milestone 3GUI623M. Denver, Colorado: U.S. Geological Survey. ACC: MOL.19970409.0087.

Flint, L.E. 1998. *Characterization of Hydrogeologic Units Using Matrix Properties, Yucca Mountain, Nevada*. Water-Resources Investigations Report 97-4243. Denver, Colorado: U.S. Geological Survey. ACC: MOL.19980429.0512.

Flint, L.E. and Flint, A.L. 1995. *Shallow Infiltration Processes at Yucca Mountain, Nevada—Neutron Logging Data 1984-93*. Water-Resources Investigations Report 95-4035. Denver, Colorado: U.S. Geological Survey. ACC: MOL.19960924.0577.

Flint, L.E.; Hudson, D.B.; and Flint, A.L. 1999. "Unsaturated Hydraulic Parameters Determined from Direct and Indirect Methods." *Proceedings of the International Workshop on Characterization and Measurement of the Hydraulic Properties of Unsaturated Porous Media, Part 1, Riverside, California, October 22-24, 1997*. van Genuchten, M.Th.; Leij, F.J.; and Wu, L., eds. Pages 293-302. Riverside, California: University of California. TIC: 247322.

Francis, N.D. 1997. "The Base-Case Thermal Properties for TSPA-VA Modeling." Memorandum from N.D. Francis (SNL) to Distribution, April 16, 1997. ACC: MOL.19980518.0229.

Haukwa, C.B.; Wu, Y-S.; and Bodvarsson, G.S. 1999. "Thermal Loading Studies Using the Yucca Mountain Unsaturated Zone Model." *Journal of Contaminant Hydrology*, 38, (1-3), 217-255. New York, New York: Elsevier Science Publishers. TIC: 244160.

Hevesi, J.A.; Ambos, D.S.; and Flint, A.L. 1994. "A Preliminary Characterization of the Spatial Variability of Precipitation at Yucca Mountain, Nevada." *High Level Radioactive Waste Management, Proceedings of the Fifth Annual International Conference, Las Vegas, Nevada, May 22-26, 1994*. 4, 2520-2529. La Grange Park, Illinois: American Nuclear Society. TIC: 210984.

Hevesi, J.A. and Flint, A.L. 1995. *Geostatistical Model for Estimating Precipitation and Recharge for the Yucca Mountain Region, Nevada-California*. Water-Resources Investigations Report. Draft. Denver, Colorado: U.S. Geological Survey. ACC: MOL.19980223.0573.

Hevesi, J.A.; Flint, A.L.; and Flint, L.E. 1994. "Verification of a 1-Dimensional Model for Predicting Shallow Infiltration at Yucca Mountain." *High Level Radioactive Waste Management, Proceedings of the Fifth Annual International Conference, Las Vegas, Nevada, May 22-26, 1994*. 4, 2323-2332. La Grange Park, Illinois: American Nuclear Society. TIC: 210984.

Ho, C.K. 1997. "Models of Fracture-Matrix Interactions During Multiphase Heat and Mass Flow in Unsaturated Fractured Porous Media." *Proceedings of the ASME Fluids Engineering Division, November 16-21, 1997, Dallas, Texas*. FED-Vol. 244. Pages 401-412. New York, New York: American Society of Mechanical Engineers. TIC: 241082.

Ho, C.K.; Altman, S.J.; and Arnold, B.W. 1995. *Alternative Conceptual Models and Codes for Unsaturated Flow in Fractured Tuff: Preliminary Assessments for GWTT-95*. SAND95-1546. Albuquerque, New Mexico: Sandia National Laboratories. ACC: MOL.19960327.0348.

Ho, C.K. and Francis, N.D. 1997. "Correction to Base-Case Thermal Properties for TSPA-VA Modeling." Memorandum from C.K. Ho and N.D. Francis (SNL) to Distribution, August 7, 1997. ACC: MOL.19980518.0230.

Kneafsey, T.J. and Pruess, K. 1998. "Thermohydrological Laboratory Tests-Insights into Processes and Behavior." *High-Level Radioactive Waste Management, Proceedings of the Eighth International Conference, Las Vegas, Nevada, May 11-14, 1998*. Pages 261-263. La Grange Park, Illinois: American Nuclear Society. TIC: 237082.

Kwicklis, E.M. and Healey, R.W. 1993. "Numerical Investigation of Steady Liquid Water Flow in a Variably Saturated Fracture Network." *Water Resources Research*, 29, (12), 4091-4102. Washington, D.C.: American Geophysical Union. TIC: 226993.

Kwicklis, E.M.; Thamir, F.; Healy, R.W.; and Hampson, D. 1998. *Numerical Simulation of Air- and Water-Flow Experiments in a Block of Variably Saturated, Fractured Tuff from Yucca Mountain, Nevada*. Water-Resources Investigations Report 97-4274. Denver, Colorado: U.S. Geological Survey. ACC: MOL.19981215.0103.

LeCain, G.D. 1997. *Air-Injection Testing in Vertical Boreholes in Welded and Nonwelded Tuff, Yucca Mountain, Nevada*. Water-Resources Investigations Report 96-4262. Denver, Colorado: U.S. Geological Survey. ACC: MOL.19980310.0148.

LeCain, G.D. 1998. *Results from Air-Injection and Tracer Testing in the Upper Tiva Canyon, Bow Ridge Fault, and Upper Paintbrush Contact Alcoves of the Exploratory Studies Facility, August 1994 through July 1996, Yucca Mountain, Nevada*. Water-Resources Investigations Report 98-4058. Denver, Colorado: U.S. Geological Survey. ACC: MOL.19980625.0344.

LeCain, G.D.; Anna, L.O.; and Fahy, M.F. 2000. *Results from Geothermal Logging, Air and Core-Water Chemistry Sampling, Air-Injection Testing and Tracer Testing in the Northern Ghost Dance Fault, Yucca Mountain, Nevada, November 1996 to August 1998*. Water-Resources Investigations Report 99-4210. Denver, Colorado: U.S. Geological Survey. TIC: 247708.

LeCain, G.D.; Patterson, G.L.; and Severson, G.R. 1997. *Results from Pneumatic Monitoring, Hydrochemistry Sampling, Air-Injection, and Tracer Testing in the Upper Tiva Canyon, and Bow Ridge Fault Alcoves, Yucca Mountain, Nevada, November, 1994 to July, 1996*. Milestone 3GUS619M-1996. Denver, Colorado: U.S. Geological Survey. ACC: MOL.19970415.0387.

Lichty, R.W. and McKinley, P.W. 1995. *Estimates of Ground-Water Recharge Rates for Two Small Basins in Central Nevada*. Water-Resources Investigations Report 94-4104. Denver, Colorado: U.S. Geological Survey. ACC: MOL.19960924.0524.

Liu, H.H.; Doughty, C.; and Bodvarsson, G.S. 1998. "An Active Fracture Model for Unsaturated Flow and Transport in Fractured Rocks." *Water Resources Research*, 34, (10), 2633-2646. Washington, D.C.: American Geophysical Union. TIC: 243012.

Loskot, C.L. and Hammermeister, D.P. 1992. *Geohydrologic Data from Test Holes UE-25 UZ #4 and UE-25 UZ #5, Yucca Mountain Area, Nye County, Nevada*. Open-File Report 90-369. Denver, Colorado: U.S. Geological Survey. ACC: NNA.19911219.0001.

Luckey, R.R.; Tucci, P.; Faunt, C.C.; Ervin, E.M.; Steinkampf, W.C.; D'Agnese, F.A.; and Patterson, G.L. 1996. *Status of Understanding of the Saturated-Zone Ground-Water Flow System at Yucca Mountain, Nevada, as of 1995*. Water-Resources Investigations Report 96-4077. Denver, Colorado: U.S. Geological Survey. ACC: MOL.19970513.0209.

Marshall, B.D.; Paces, J.B.; Neymark, L.A.; Whelan, J.F.; and Peterman, Z.E. 1998. "Secondary Minerals Record Past Percolation Flux at Yucca Mountain, Nevada." *High-Level Radioactive Waste Management, Proceedings of the Eighth International Conference, Las Vegas, Nevada, May 11-14, 1998*. Pages 127-129. La Grange Park, Illinois: American Nuclear Society. TIC: 237082.

Maxey, G.B. and Eakin, T.E. 1950. *Ground Water in White River Valley, White Pine, Nye, and Lincoln Counties, Nevada*. Water Resources Bulletin No. 8. Carson City, Nevada: State of Nevada, Office of the State Engineer. TIC: 216819.

Montazer, P. and Wilson, W.E. 1984. *Conceptual Hydrologic Model of Flow in the Unsaturated Zone, Yucca Mountain, Nevada*. Water-Resources Investigations Report 84-4345. Lakewood, Colorado: U.S. Geological Survey. ACC: NNA.19890327.0051.

Moridis, G. and Pruess, K. 1995. *Flow and Transport Simulations Using T2CG1, A Package of Conjugate Gradient Solvers for the TOUGH2 Family of Codes*. LBL-36235. Berkeley, California: Lawrence Berkeley National Laboratory. ACC: MOL.19960321.0035.

Moridis, G.J.; Wu, Y-S.; and Pruess, K. 1999. *EOS9nT: A TOUGH2 Module for the Simulation of Water Flow and Solute/Colloid Transport in the Subsurface*. LBNL-42351. Berkeley, California: Lawrence Berkeley National Laboratory. TIC: 246520.

Moyer, T.C. and Geslin, J.K. 1995. *Lithostratigraphy of the Calico Hills Formation and Prow Pass Tuff (Crater Flat Group) at Yucca Mountain, Nevada*. Open-File Report 94-460. Denver, Colorado: U.S. Geological Survey. ACC: MOL.19941208.0003.

Moyer, T.C.; Geslin, J.K.; and Flint, L.E. 1996. *Stratigraphic Relations and Hydrologic Properties of the Paintbrush Tuff Nonwelded (PTn) Hydrologic Unit, Yucca Mountain, Nevada*. Open-File Report 95-397. Denver, Colorado: U.S. Geological Survey. ACC: MOL.19970204.0216.

Narasimhan, T.N. and Witherspoon, P.A. 1976. "An Integrated Finite-Difference Method for Analyzing Fluid Flow in Porous Media." *Water Resources Research*, 12, 57-64. Washington, D.C.: American Geophysical Union. TIC: 237790.

Neuman, S.P. 1990. "Universal Scaling of Hydraulic Conductivities and Dispersivities in Geologic Media." *Water Resources Research*, 26, (8), 1749-1758. Washington, D.C.: American Geophysical Union. TIC: 237977.

Neymark, L.A.; Amelin, Y.V.; Paces, J.B.; and Peterman, Z.E. 1998. "U-Pb Age Evidence for Long-Term Stability of the Unsaturated Zone at Yucca Mountain." *High-Level Radioactive Waste Management, Proceedings of the Eighth International Conference, Las Vegas, Nevada, May 11-14, 1998*. Pages 85-87. La Grange Park, Illinois: American Nuclear Society. TIC: 237082.

O'Brien, G.M. 1997. *Analysis of Aquifer Tests Conducted in Boreholes USW WT-10, UE-25 WT#12, and USW SD-7, 1995-96, Yucca Mountain, Nevada*. Water-Resources Investigations Report 96-4293. Denver, Colorado: U.S. Geological Survey. ACC: MOL.19980219.0822.

Ortiz, T.S.; Williams, R.L.; Nimick, F.B.; Whittet, B.C.; and South, D.L. 1985. *A Three-Dimensional Model of Reference Thermal/Mechanical and Hydrological Stratigraphy at Yucca Mountain, Southern Nevada*. SAND84-1076. Albuquerque, New Mexico: Sandia National Laboratories. ACC: MOL.19980602.0331.

Paces, J.B.; Marshall, B.D.; Whelan, J.F.; and Neymark, L.A. 1997. "Submission of Milestone: SPC23FM4, Due March 14, 1997." Memorandum from J.B. Paces, B.D. Marshall, J.F. Whelan, and L.A. Neymark (USGS) to R.W. Craig, March 14, 1997, with attachment, "Progress Report on Unsaturated Zone Stable and Radiogenic Isotope Studies." ACC: MOL.19980224.0119.

Paces, J.B.; Neymark, L.A.; Marshall, B.D.; Whelan, J.F.; and Peterman, Z.E. 1996. *Letter Report: Ages and Origins of Subsurface Secondary Minerals in the Exploratory Studies Facility (ESF)*. Milestone 3GQH450M, Results of Sampling and Age Determination. Las Vegas, Nevada: U.S. Geological Survey. ACC: MOL.19970324.0052.

Paces, J.B.; Neymark, L.A.; Marshall, B.D.; Whelan, J.F.; and Peterman, Z.E. 1998. "Inferences for Yucca Mountain Unsaturated-Zone Hydrology from Secondary Minerals." *High-Level Radioactive Waste Management, Proceedings of the Eighth International Conference, Las Vegas, Nevada, May 11-14, 1998*. Pages 36-39. La Grange Park, Illinois: American Nuclear Society. TIC: 237082.

Patterson, G.L.; Peterman, Z.E.; and Paces, J.B. 1998. "Hydrochemical Evidence for the Existence of Perched Water at USW WT-24, Yucca Mountain, Nevada." *High-Level Radioactive Waste Management, Proceedings of the Eighth International Conference, Las Vegas, Nevada, May 11-14, 1998*. Pages 277-278. La Grange Park, Illinois: American Nuclear Society. TIC: 237082.

Patterson, G.L.; Weeks, E.P.; Rousseau, J.P.; and Oliver, T.A. 1996. *Interpretation of Pneumatic and Chemical Data from the Unsaturated Zone Near Yucca Mountain, Nevada*. Milestone 3GGP605M. Denver, Colorado: U.S. Geological Survey. ACC: MOL.19970324.0058.

Philip, J.R.; Knight, J.H.; and Waechter, R.T. 1989. "Unsaturated Seepage and Subterranean Holes: Conspectus, and Exclusion Problem for Circular Cylindrical Cavities." *Water Resources Research*, 25, (1), 16-28. Washington, D.C.: American Geophysical Union. TIC: 239117.

Pruess, K. 1987. *TOUGH User's Guide*. NUREG/CR-4645. Washington, D.C.: U.S. Nuclear Regulatory Commission. TIC: 217275.

Pruess, K. 1991. *TOUGH2-A General-Purpose Numerical Simulator for Multiphase Fluid and Heat Flow*. LBL-29400. Berkeley, California: Lawrence Berkeley Laboratory. ACC: NNA.19940202.0088.

Pruess, K. 1999. "A Mechanistic Model for Water Seepage Through Thick Unsaturated Zones in Fractured Rocks of Low Matrix." *Water Resources Research*, 35, (4), 1039-1051. Washington, D.C.: American Geophysical Union. TIC: 244913.

Pruess, K. and Antunez, E. 1995. "Applications of TOUGH2 to Infiltration of Liquids in Media with Strong Heterogeneity." *Proceedings of the TOUGH Workshop '95, Lawrence Berkeley Laboratory, Berkeley, California, March 20-22, 1995*. Pruess, K., ed. LBL-37200. Pages 69-76. Berkeley, California: Lawrence Berkeley Laboratory. TIC: 216504.

Pruess, K.; Faybishenko, B.; and Bodvarsson, G.S. 1999. "Alternative Concepts and Approaches for Modeling Flow and Transport in Thick Unsaturated Zones of Fractured Rocks." *Journal of Contaminant Hydrology*, 38, (1-3), 281-322. New York, New York: Elsevier. TIC: 244160.

Rautman, C.A. 1995. *Preliminary Geostatistical Modeling of Thermal Conductivity for a Cross Section of Yucca Mountain, Nevada*. SAND94-2283. Albuquerque, New Mexico: Sandia National Laboratories. ACC: MOL.19960320.0109.

Rautman, C.A. and Engstrom, D.A. 1996. *Geology of the USW SD-7 Drill Hole Yucca Mountain, Nevada*. SAND96-1474. Albuquerque, New Mexico: Sandia National Laboratories. ACC: MOL.19971218.0442.

Rautman, C.A.; Flint, L.E.; Flint, A.L.; and Istok, J.D. 1995. *Physical and Hydrologic Properties of Outcrop Samples from a Nonwelded to Welded Tuff Transition, Yucca Mountain, Nevada*. Water-Resources Investigations Report 95-4061. Denver, Colorado: U.S. Geological Survey. ACC: MOL.19971212.0129.

Robinson, B.A.; Wolfsberg, A.V.; Gable, C.W.; and Viswanathan, H.S. 1998. "Radionuclide Transport in the Unsaturated Zone at Yucca Mountain." *High-Level Radioactive Waste Management, Proceedings of the Eighth International Conference, Las Vegas, Nevada, May 11-14, 1998*. Pages 156-158. La Grange Park, Illinois: American Nuclear Society. TIC: 237082.

Rousseau, J.P.; Kwicklis, E.M.; and Gillies, D.C., eds. 1999. *Hydrogeology of the Unsaturated Zone, North Ramp Area of the Exploratory Studies Facility, Yucca Mountain, Nevada*. Water-Resources Investigations Report 98-4050. Denver, Colorado: U.S. Geological Survey. ACC: MOL.19990419.0335.

Rousseau, J.P.; Loskot, C.L.; Thamir, F.; and Lu, N. 1997. *Results of Borehole Monitoring in the Unsaturated Zone Within the Main Drift Area of the Exploratory Studies Facility, Yucca Mountain, Nevada*. Milestone SPH22M3. Denver, Colorado: U.S. Geological Survey. ACC: MOL.19970626.0351.

Rulon, J.; Bodvarsson, G.S.; and Montazer, P. 1986. *Preliminary Numerical Simulations of Groundwater Flow in the Unsaturated Zone, Yucca Mountain, Nevada*. LBL-20553. Berkeley, California: Lawrence Berkeley Laboratory. ACC: NNA.19870908.0027.

Sass, J.H.; Lachenbruch, A.H.; Dudley, W.W., Jr.; Priest, S.S.; and Munroe, R.J. 1988. *Temperature, Thermal Conductivity, and Heat Flow Near Yucca Mountain, Nevada: Some Tectonic and Hydrologic Implications*. Open-File Report 87-649. Denver, Colorado: U.S. Geological Survey. ACC: MOL.19971027.0303.

Sawyer, D.A.; Fleck, R.J.; Lanphere, M.A.; Warren, R.G.; Broxton, D.E.; and Hudson, M.R. 1994. "Episodic Caldera Volcanism in the Miocene Southwestern Nevada Volcanic Field: Revised Stratigraphic Framework,  $^{40}\text{Ar}/^{39}\text{Ar}$  Geochronology, and Implications for Magmatism and Extension." *Geological Society of America Bulletin*, 106, (10), 1304-1318. Boulder, Colorado: Geological Society of America. TIC: 222523.

Scott, R.B. and Bonk, J. 1984. *Preliminary Geologic Map of Yucca Mountain, Nye County, Nevada, with Geologic Sections*. Open-File Report 84-494. Denver, Colorado: U.S. Geological Survey. TIC: 203162.

SNL (Sandia National Laboratories) 1995a. *Yucca Mountain Site Characterization Project Geology and Rock Structure Log, Hole USW NRG-6*. Rev. 1. Albuquerque, New Mexico: Sandia National Laboratories. ACC: MOL.19950327.0091.

- SNL (Sandia National Laboratories) 1995b. *Yucca Mountain Site Characterization Project Geology and Rock Structure Log, USW NRG-7/7a*. Rev. 1. Albuquerque, New Mexico: Sandia National Laboratories. ACC: MOL.19950327.0095.
- Sonnenthal, E.L. and Bodvarsson, G.S. 1999. "Constraints on the Hydrology of the Unsaturated Zone at Yucca Mountain, NV from Three-Dimensional Models of Chloride and Strontium Geochemistry." *Journal of Contaminant Hydrology*, 38, (1-3), 107-156. New York, New York: Elsevier. TIC: 244160.
- Tokunaga, T.K. and Wan, J. 1997. "Water Film Flow Along Fracture Surfaces of Porous Rock." *Water Resources Research*, 33, (6), 1287-1295. Washington, D.C.: American Geophysical Union. TIC: 242739.
- Tsang, Y.W. and Birkholzer, J.T. 1999. "Predictions and Observations of the Thermal-Hydrological Conditions in the Single Heater Test." *Journal of Contaminant Hydrology*, 38, (1-3), 385-425. New York, New York: Elsevier. TIC: 244160.
- Tucci, P. and Burkhardt, D.J. 1995. *Potentiometric-Surface Map, 1993, Yucca Mountain and Vicinity, Nevada*. Water-Resources Investigations Report 95-4149. Denver, Colorado: U.S. Geological Survey. ACC: MOL.19960924.0517.
- USGS (U.S. Geological Survey) 2000a. *Future Climate Analysis*. ANL-NBS-GS-000008 REV 00. Denver, Colorado: U.S. Geological Survey. ACC: MOL.20000629.0907.
- USGS (U.S. Geological Survey) 2000b. *Simulation of Net Infiltration for Modern and Potential Future Climates*. ANL-NBS-HS-000032 REV 00. [Denver, Colorado: U.S. Geological Survey]. ACC: MOL.20000801.0004.
- van Genuchten, M.T. 1980. "A Closed-Form Equation for Predicting the Hydraulic Conductivity of Unsaturated Soils." *Soil Science Society of America Journal*, 44, (5), 892-898. Madison, Wisconsin: Soil Science Society of America. TIC: 217327.
- Wang, J.S.Y. and Elsworth, D. 1999. "Permeability Changes Induced by Excavation in Fractured Tuff." *Rock Mechanics for Industry, Proceedings of the 37th U.S. Rock Mechanics Symposium, Vail, Colorado, June 6-9, 1999*. Amadei, B.; Kranz, R.L.; Scott, G.A.; and Smeallie, P.H., eds. 2, 751-757. Brookfield, Vermont: A.A. Balkema. TIC: 245246.
- Wang, J.S.Y.; Flint, A.L.; Nitao, J.J.; Chesnut, D.A.; Cook, P.; Cook, N.G.W.; Birkholzer, J.; Freifeld, B.; Flint, L.E.; Ellet, K.; Mitchell, A.J.; Homuth, E.F.; Griego, G.J.; Cerny, J.A.; and Johnson, C.L. 1996. *Evaluation of Moisture Evolution in the Exploratory Studies Facility*. Milestone TR31K6M. Berkeley, California: Lawrence Berkeley National Laboratory. ACC: MOL.19961231.0089.
- Wang, J.S.Y. and Narasimhan, T.N. 1993. "Unsaturated Flow in Fractured Porous Media." Chapter 7 of *Flow and Contaminant Transport in Fractured Rocks*. Bear, J.; Tsang, C.F.; and de Marsily, G., eds. San Diego, California: Academic Press. TIC: 235461.

Wang, J.S.Y.; Trautz, R.C.; Cook, P.J.; Finsterle, S.; James, A.L.; and Birkholzer, J. 1999. "Field Tests and Model Analyses of Seepage into Drift." *Journal of Contaminant Hydrology*, 38, (1-3), 323-347. New York, New York: Elsevier. TIC: 244160.

Weeks, E.P. 1978. *Field Determination of Vertical Permeability to Air in the Unsaturated Zone*. Professional Paper 1051. Washington, D.C.: U.S. Geological Survey. TIC: 218986.

Winograd, I.J. 1981. "Radioactive Waste Disposal in Thick Unsaturated Zones." *Science*, 212, (4502), 1457-1464. Washington, D.C.: American Association for the Advancement of Science. TIC: 217258.

Wittwer, C.; Chen, G.; Bodvarsson, G.S.; Chornack, M.; Flint, A.; Flint, L.; Kwicklis, E.; and Spengler, R. 1995. *Preliminary Development of the LBL/USGS Three-Dimensional Site-Scale Model of Yucca Mountain, Nevada*. LBL-37356. Berkeley, California: Lawrence Berkeley Laboratory. ACC: MOL.19960924.0538.

Wu, Y-S.; Haukwa, C.; and Bodvarsson, G.S. 1999b. "A Site-Scale Model for Fluid and Heat Flow in the Unsaturated Zone of Yucca Mountain, Nevada." *Journal of Contaminant Hydrology*, 38, (1-3), 185-215. New York, New York: Elsevier. TIC: 244160.

Wu, Y.S.; Ritcey, A.C.; and Bodvarsson, G.S. 1999a. "A Modeling Study of Perched Water Phenomena in the Unsaturated Zone at Yucca Mountain." *Journal of Contaminant Hydrology*, 38, (1-3), 157-184. New York, New York: Elsevier. TIC: 244160.

Xu, T. and Pruess, K. 1998. *Coupled Modeling of Non-Isothermal Multi-Phase Flow, Solute Transport and Reactive Chemistry in Porous and Fractured Media: 1. Model Development and Validation*. LBNL-42050. Berkeley, California: Lawrence Berkeley National Laboratory. TIC: 243735.

Yang, I.C.; Rattray, G.W.; and Yu, P. 1996. *Interpretation of Chemical and Isotopic Data from Boreholes in the Unsaturated Zone at Yucca Mountain, Nevada*. Water-Resources Investigations Report 96-4058. Denver, Colorado: U.S. Geological Survey. ACC: MOL.19980528.0216.

Yang, I.C.; Yu, P.; Rattray, G.W.; Ferarese, J.S.; and Ryan, J.N. 1998. *Hydrochemical Investigations in Characterizing the Unsaturated Zone at Yucca Mountain, Nevada*. Water-Resources Investigations Report 98-4132. Denver, Colorado: U.S. Geological Survey. ACC: MOL.19981012.0790.

YMP (Yucca Mountain Site Characterization Project) 1997. *Drilling and Testing USW WT-24*. Field Work Package FWP-SB-97-005, Rev. 1. Las Vegas, Nevada: Yucca Mountain Site Characterization Office. ACC: MOL.19980122.0435.

YMP (Yucca Mountain Site Characterization Project) 1998. *Repository Safety Strategy: U.S. Department of Energy's Strategy to Protect Public Health and Safety After Closure of a Yucca Mountain Repository*. YMP/96-01, Rev. 2. Las Vegas, Nevada: Yucca Mountain Site Characterization Office. ACC: MOL.19980727.0001.

### **8.13.2 Source Data, Listed by Data Tracking Number**

GS000200001221.002. Precipitation Data for Nevada Test Site, 1957-1994, from Air Resources Laboratory, from National Oceanographic and Atmospheric Administration (NOAA) Precipitation Data. Submittal date: 02/29/2000.

GS000200001221.003. NAD27 Datum of USGS Digital Elevation Model from Topopah Spring West and Busted Butte 7.5 Minute Quadrangles. Submittal date: 02/18/2000.

GS940708312212.011. Volumetric Water Content from Neutron Moisture Meter Counts for 99 Boreholes from 5/3/89 or from the Time They Were Drilled Until 12/31/93. Submittal date: 07/13/1994.

GS941208312212.017. Subsurface Water Content at Yucca Mountain, Nevada – Neutron Logging Data for 1/1/94 thru FY94. Submittal date: 12/02/1994.

GS950308312231.002. Laboratory Measurements of Core from USW SD-12 and Radial Boreholes. Submittal date: 03/02/1995.

GS950808312212.001. Volumetric Water Content Calculated from Field Calibration Equations Using Neutron Counts from 97 Boreholes at Yucca Mountain from 1 Oct 94 to 31 May 95. Submittal date: 08/01/1995.

GS951108312231.009. Physical Properties, Water Content, and Water Potential for Borehole USW SD-7. Submittal date: 09/26/1995.

GS960108312212.001. Volumetric Water Content Calculated from Field Calibration Equations Using Neutron Counts from 97 Boreholes at Yucca Mountain. Submittal date: 01/31/1996.

GS960808312231.004. Physical Properties, Water Content and Water Potential for Samples from Lower Depths in Boreholes USW SD- 7 and USW SD-12. Submittal date: 08/30/1996.

GS960808312231.005. Water Permeability and Relative Humidity Calculated Porosity for Samples from Boreholes USW SD-7, USW SD-9, USW SD-12 and USW UZ-14. Submittal date: 08/30/1996.

GS960908312211.003. Conceptual and Numerical Model of Infiltration at Yucca Mountain, Nevada. Submittal date: 09/12/1996.

GS960908312231.004. Characterization of Hydrogeologic Units Using Matrix Properties at Yucca Mountain, Nevada. Submittal date: 09/12/1996.

GS970108312231.002. Physical Properties of Surface Samples from the ESF Main Drift (29+00 M to 57+00 M). Submittal date: 01/31/1997.

GS970208312231.003. Physical Properties, Water Content and Water Potential on Samples from Boreholes ESF-NAD-GTB#1 and ESF-NAD-GTB#1A from Alcove 6 in the ESF. Submittal date: 02/05/1997.

GS970708312231.004. Physical Properties of Surface Samples for the ESF Main Drift. Submittal date: 07/18/1997.

GS970908312242.006. Physical Properties of Borehole Samples from the PTN Exposure in the ESF North Ramp (ESF Station 7+28 M to Station 10+71 M). Submittal date: 09/03/1997.

GS971008312231.006. Physical Properties and Saturated Hydraulic Conductivity of Cores from Surface Samples from the ESF Main Drift 29+00 M to 57+00 M. Submittal date: 10/06/1997.

GS980308312242.004. Water Potential Measurements Using the Filter Paper Technique for Borehole Samples from the ESF North Ramp (ESF Station 7+27 M to ESF Station 10+70 M) and the ESF South Ramp (ESF Station 59+65 M to 76+33 M). Submittal date: 03/19/1998.

GS980308312242.005. Physical Properties of Lexan-Sealed Borehole Samples from the PTN Exposure in the ESF North Ramp (ESF Station 7+27 M to ESF Station 10+70 M). Submittal date: 03/11/1998.

GS980308312242.006. Physical Properties of Surface Samples from the PTN Exposure in the ESF North Ramp (ESF Station 7+09 M to ESF Station 10+95 M). Submittal date: 03/13/1998.

GS980408312242.008. Unsaturated Hydraulic Properties of Borehole Samples from the PTN Exposure in the ESF North Ramp (ESF Station 7+27 M to ESF Station 10+70 M) Measured Using a Centrifuge. Submittal date: 04/17/1998.

GS980908312242.032. Physical and Hydrologic Properties of Borehole Core Samples and Water Potential Measurements Using the Filter Paper Technique for Borehole Samples from ESF-LPCA-PTN#1 and ESF-LPCA-PTN#2 in Alcove 4. Submittal date: 09/17/1998.

GS980908312242.033. Physical and Hydrologic Properties of Borehole Core Samples and Water Potential Measurements Using the Filter Paper Technique for Borehole Samples from ESF-UPCA-PTN#1 in Alcove 3 of the ESF. Submittal date: 09/17/1998.

GS980908312242.037. Water Retention Data of Lexan-Sealed Borehole Samples and Surface Samples from ESF North Ramp Moisture Study. Submittal date: 09/23/1998.

GS980908312242.040. Physical Properties and Saturated Hydraulic Conductivity Measurements of Core Plugs from Lexan-Sealed Samples from Boreholes in the ESF North Ramp. Submittal date: 09/24/1998.

GS990308312242.007. Laboratory and Centrifuge Measurements of Physical and Hydraulic Properties of Core Samples from Busted Butte Boreholes UZTT-BB-INJ-1, UZTT-BB-INJ-3, UZTT-BB-INJ-4, UZTT-BB-INJ-6, UZTT-BB-COL-5 and UZTT-BB-COL-8. Submittal date: 03/22/1999.

GS990708312242.008. Physical and Hydraulic Properties of Core Samples from Busted Butte Boreholes. Submittal date: 07/01/1999.

LADV831321AQ97.001. Mineralogic Variation in Drill Holes. Submittal date: 05/28/1997.

MO0004YMP00011.001. Bedrock Geologic Map of the Central Block Area, Yucca Mountain, Nevada. Submittal date: 04/18/2000.

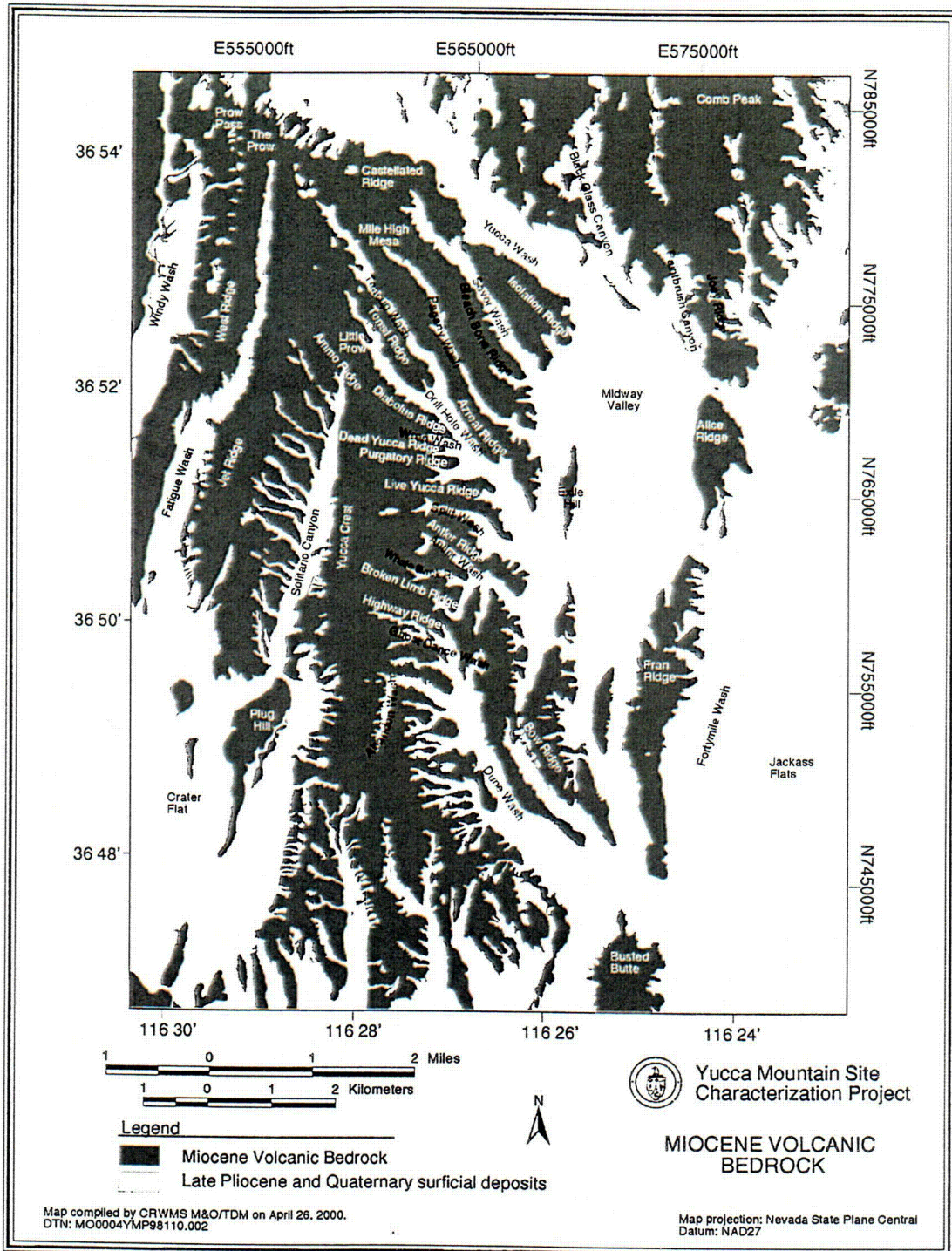
MO0004YMP98110.002. Miocene Volcanic Bedrock. Submittal date: 04/26/2000.

MO0006YMP99068.001. ESF Tunnel and Test Alcoves. Submittal date: 06/07/2000.

MO9912YMP99069.000. Potential Repository Area Boreholes and Exploratory Studies Facility. Submittal date: 12/01/1999.

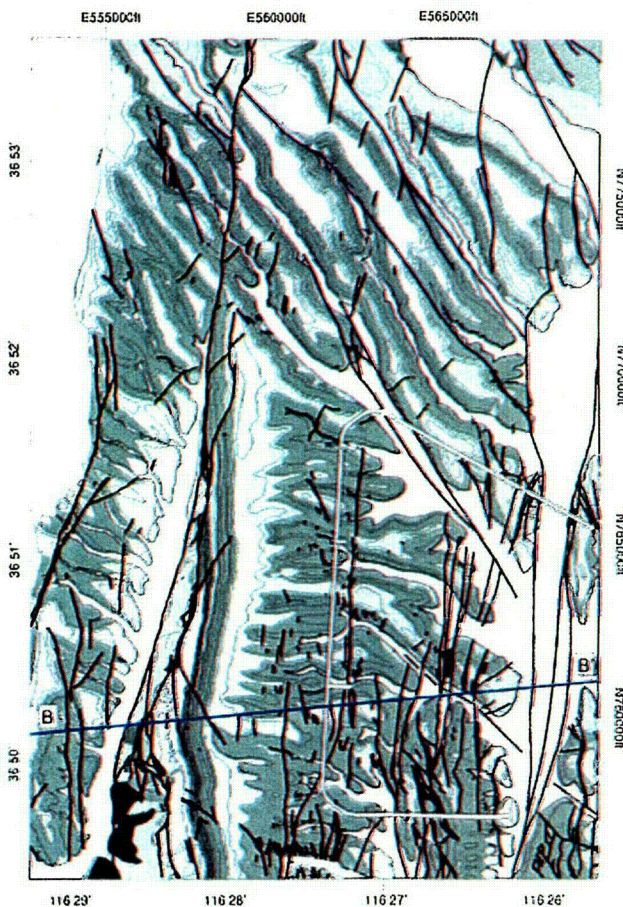
TM00000000UZ16.002. UE-25 UZ#16 Structural Log (30.3-38.9) and Shift Drilling Summaries (0.0-1686.2). Submittal date: 09/14/1995.

INTENTIONALLY LEFT BLANK

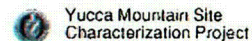


NOTE: Upland areas where bedrock is exposed or very shallow are shaded.

Figure 8.1-1. Index Map Showing the Names of Principal Geographic Features in the Site Area



### BEDROCK GEOLOGIC MAP OF THE CENTRAL BLOCK AREA, YUCCA MOUNTAIN, NEVADA



#### LEGEND

##### Quaternary

Alluvium & Colluvium

##### Tertiary

- Rainier Mesa Tuff
- Comb Peak Rhyolite
- Tiva Canyon Crystal-rich member
- Tiva Canyon Crystal-poor member
- Pah Canyon, Yucca Mountain Tufts-undivided
- Topopah Spring Crystal-rich member
- Topopah Spring Crystal-poor member
- Tiva Canyon & Topopah Spring Tuff (lenses in fault zone)

≡ The ESF Tunnel

∩ Fault

0.5 0 0.5 1 Miles

1 0 1 2 Kilometers



Map compiled by CRWMS M&O/TDM on April 13, 2000.  
DTN MG0004YNP00011 001

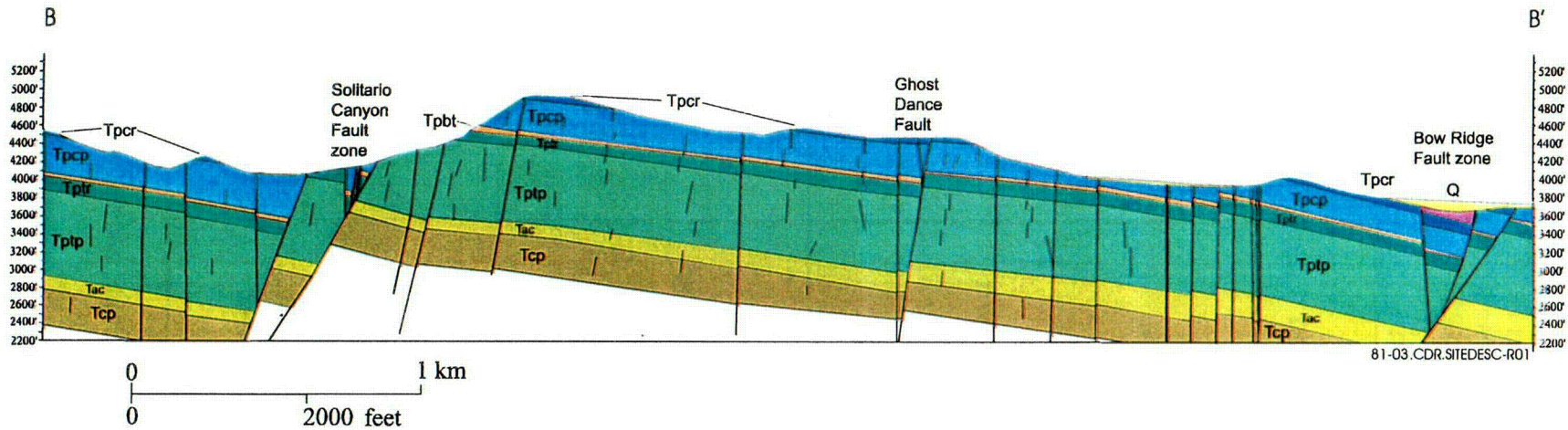
Map projection: Nevada State Plane, Central  
Datum: NAD27

81-02, CRW/TEDS C-101

Source: Day et al. (1998, Sheet 1)

NOTE: Solid black lines are faults, whether exposed or concealed beneath surficial deposits. Line B-B' is the location of the cross section in Figure 8.1-3.

Figure 8.1-2. Simplified Geologic Map of the Central Block



Source: Day et al. (1998, Sheet 2)

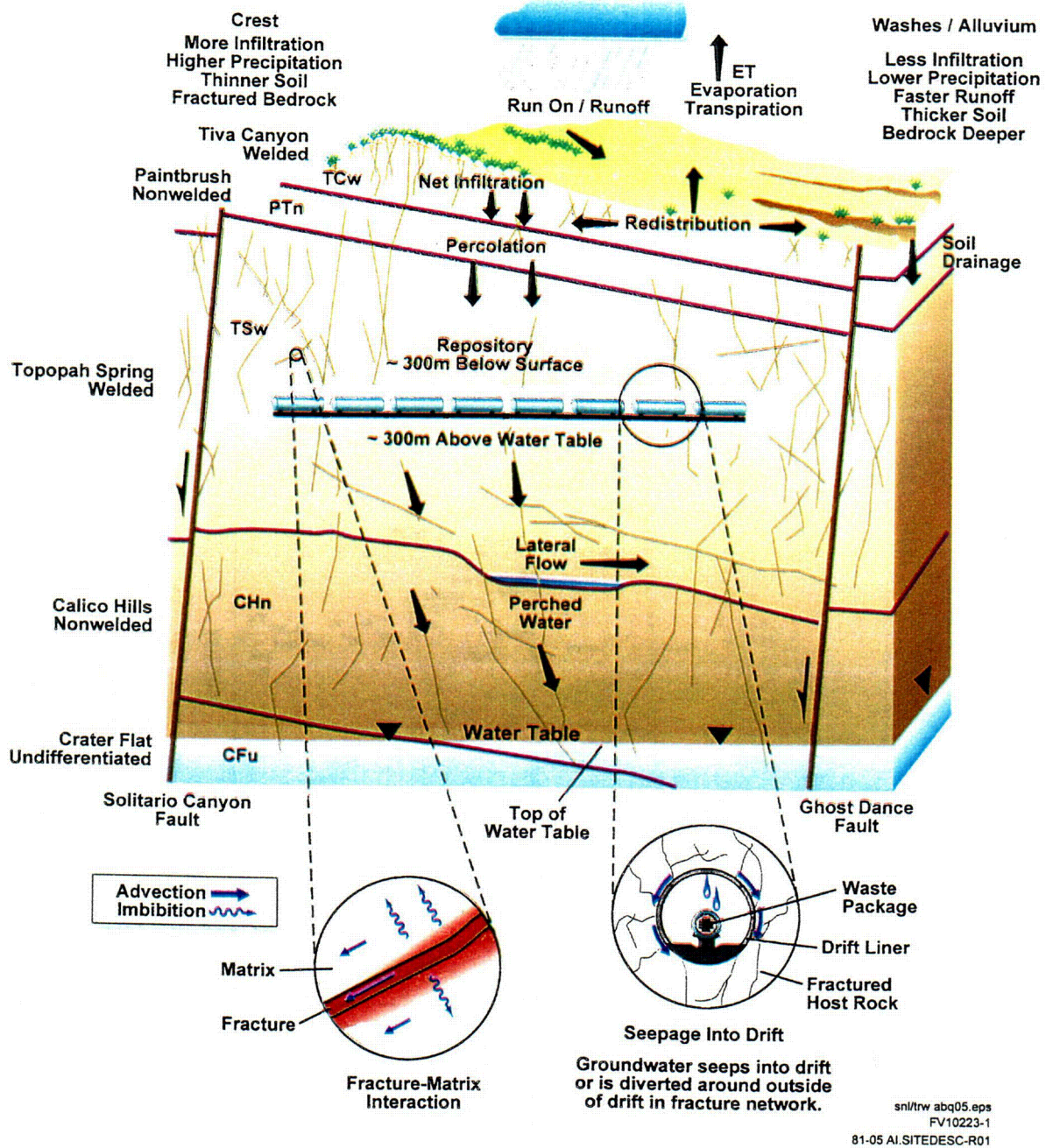
NOTE: The line of section B-B' is from west to east and is shown on Figure 8.1-2. Q, unconsolidated Quaternary deposits; Tpcr and Tpcp, welded members of the Tiva Canyon Tuff; Tpbtt, bedded and on welded tuffs of the Middle Paintbrush Group; Tptr and Tptp, welded members of the Topopah Spring Tuff; Tac, Calico Hills Formation; Tcp, Prow Pass Tuff; unlabeled, deeper units of the Crater Flat Group. The water table is near the bottom of the cross section, at an approximate altitude of 2,400 ft.

Figure 8.1-3. Simplified Geologic Cross Section through the Site Area

Formal Geologic Stratigraphy (after Sawyer et al. 1994)		Hydrogeologic Units (Modified from Montazer and Wilson 1984)	Thermal-Mechanical Units (Ortiz et al. 1985)
Qac		Alluvium	UO
Paintbrush Group	Tiva Canyon Tuff	Tiva Canyon Welded Unit TCw	TCw
	pre-Tiva Canyon bedded tuff	Paintbrush Nonwelded Unit PTn	PTn
	Yucca Mountain Tuff		
	pre-Yucca Mountain bedded tuff		
	Pah Canyon Tuff		
	pre-Pah Canyon bedded tuff		
	Topopah Spring Tuff	Topopah Spring Welded Unit TSw	TSw1
			TSw2
			TSw3
	pre-Topopah Spring bedded tuff	Calico Hills Nonwelded Unit CHn	CHn1v
Calico Hills Formation	CHn1z		
	CHn2z		
Crater Flat Group	Prow Pass Tuff	Crater Flat Unit CFu	CHn3z
	Bullfrog Tuff		PPw
			CFun
	Tram Tuff		BFw
			CFMn
			TRw

81-04.CDR SITEDESC-R01, ICN 01

Figure 8.1-4. Comparison of Lithostratigraphic, Hydrogeologic, and Thermal-Mechanical Units at Yucca Mountain



Source: DOE (1998a, Volume 1, Figure 2-15)

Figure 8.1-5. Conceptual Drawing of Unsaturated Zone Flow Processes

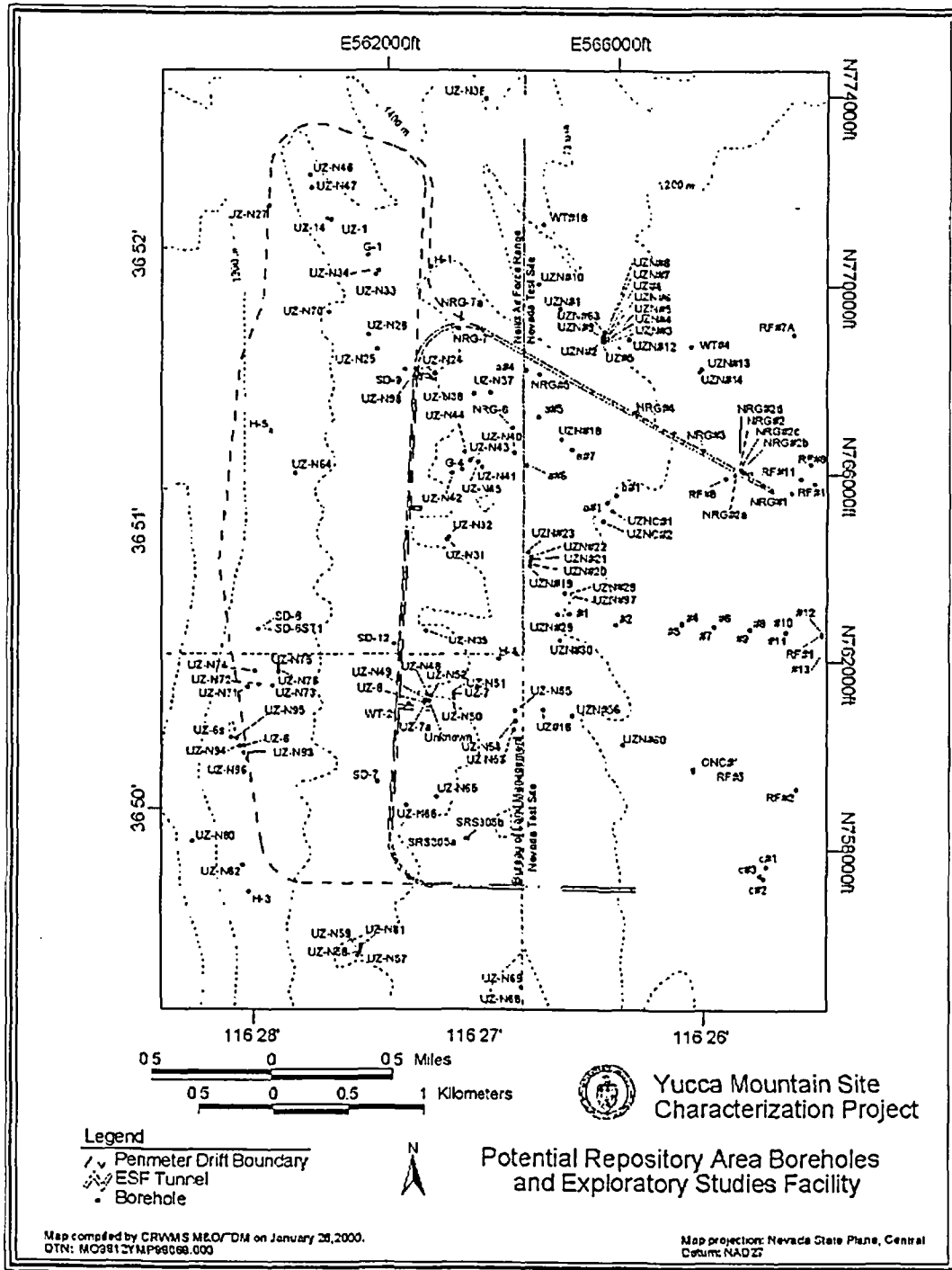
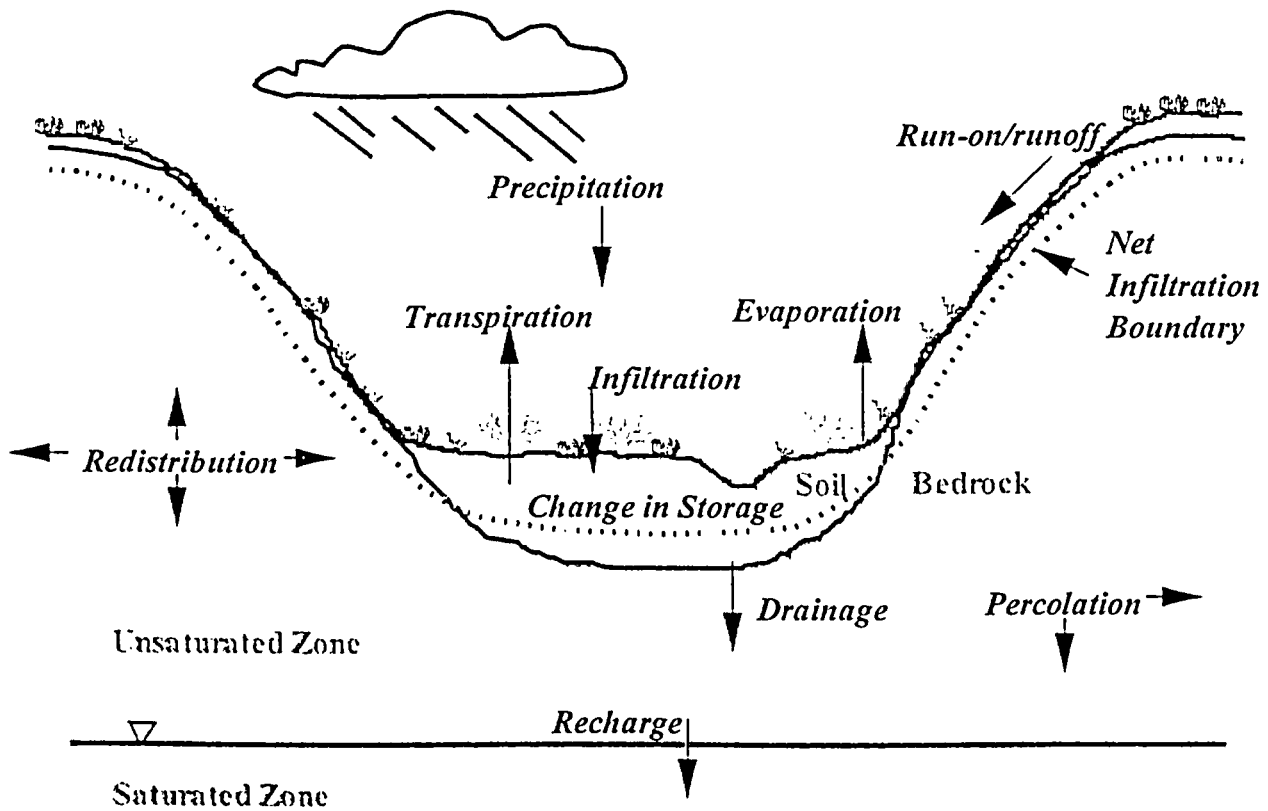


Figure 8.1-6. Map Showing Repository Area Boreholes and the Exploratory Studies Facility

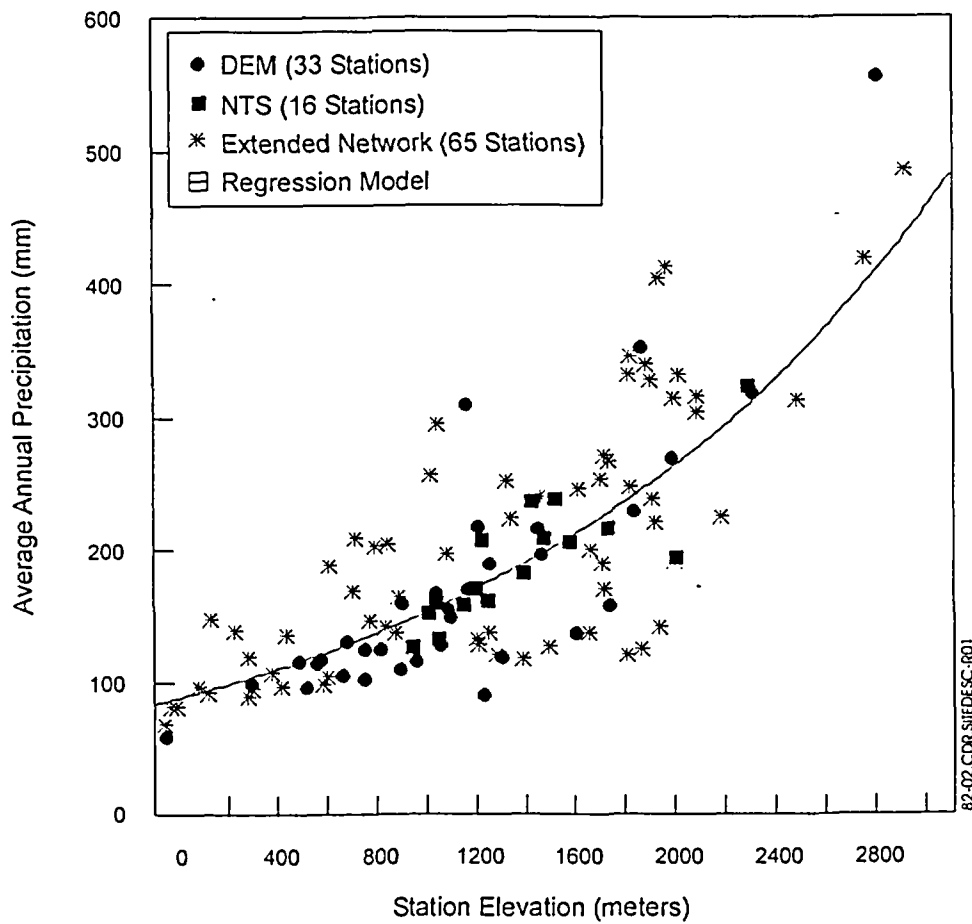


$$\text{Precipitation} + \text{Change in Storage} - \text{Drainage} - \text{ET} - \text{Runoff} = 0$$

82-01.CDR.SITEDESC-R01

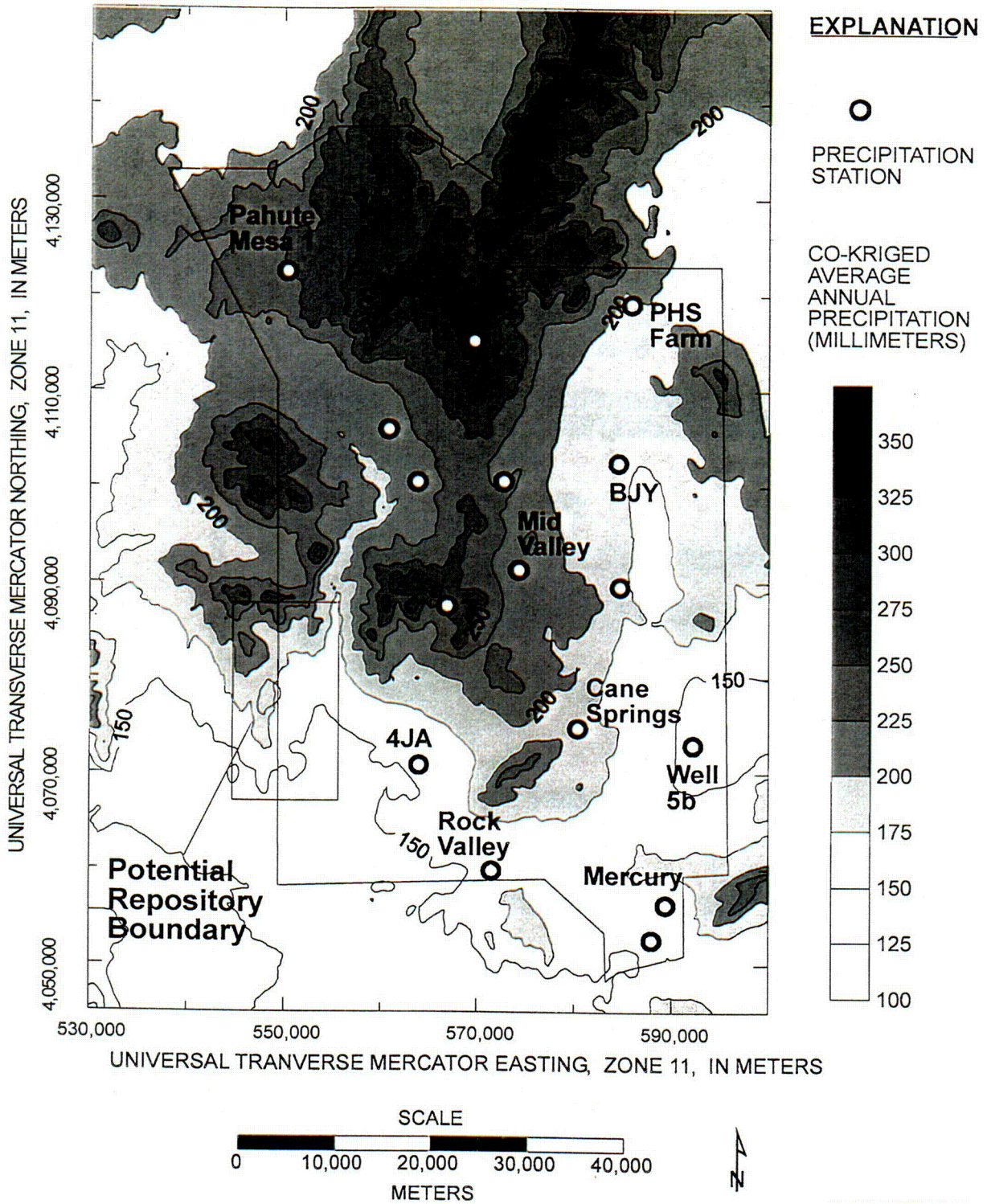
Sources: Flint, A.L. et al. (1996, Figure 3); USGS (2000b, Figure 6-1)

Figure 8.2-1. Schematic of Hydrologic Cycle Illustrating Surficial and Subsurface Processes Affecting Net Infiltration and Recharge



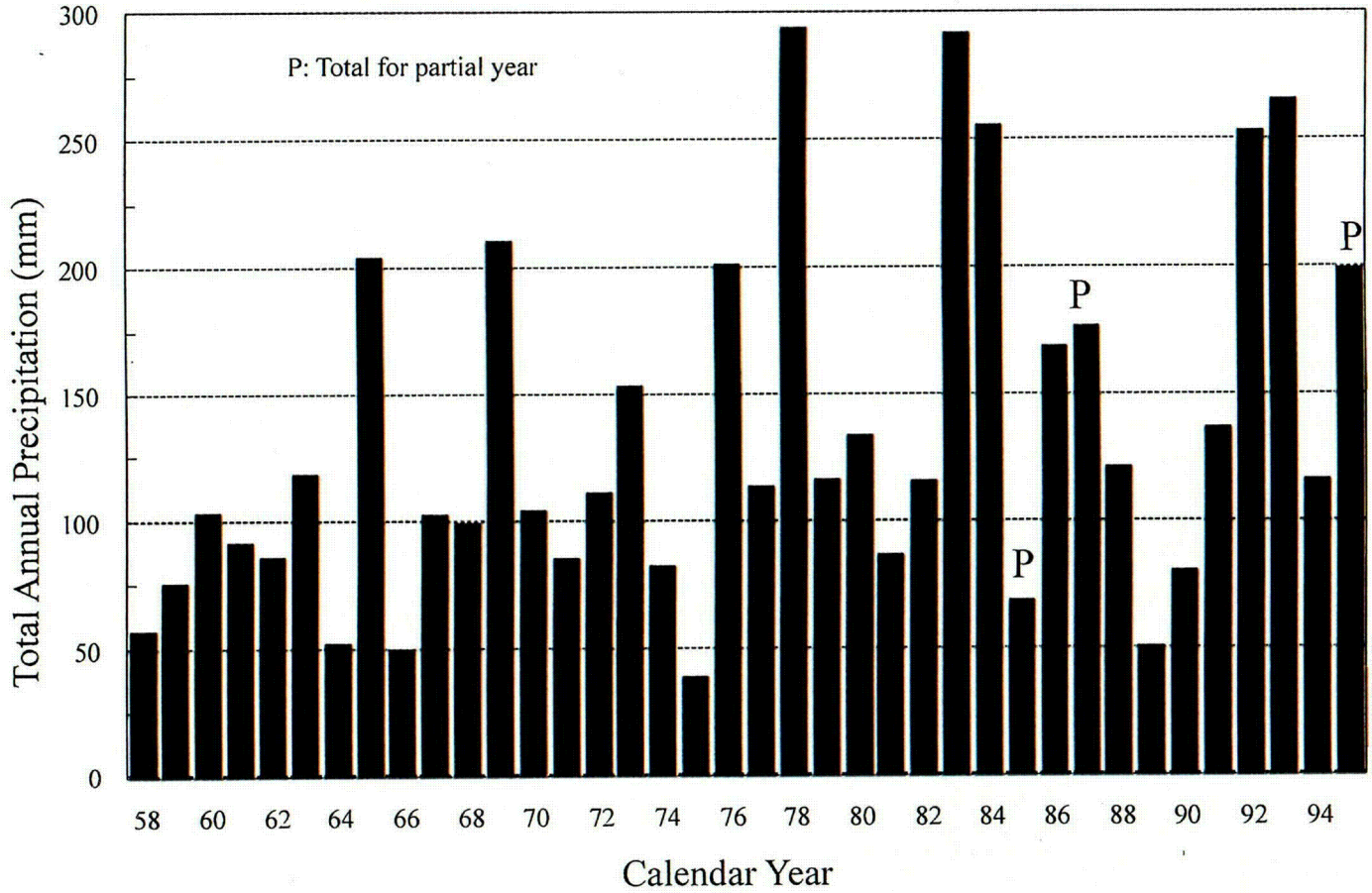
Source: Hevesi and Flint (1995, Figure 9)

Figure 8.2-2. Average Annual Precipitation versus Elevation for 114 Precipitation Stations in the Yucca Mountain Region with a Minimum of Eight Complete Years of Record



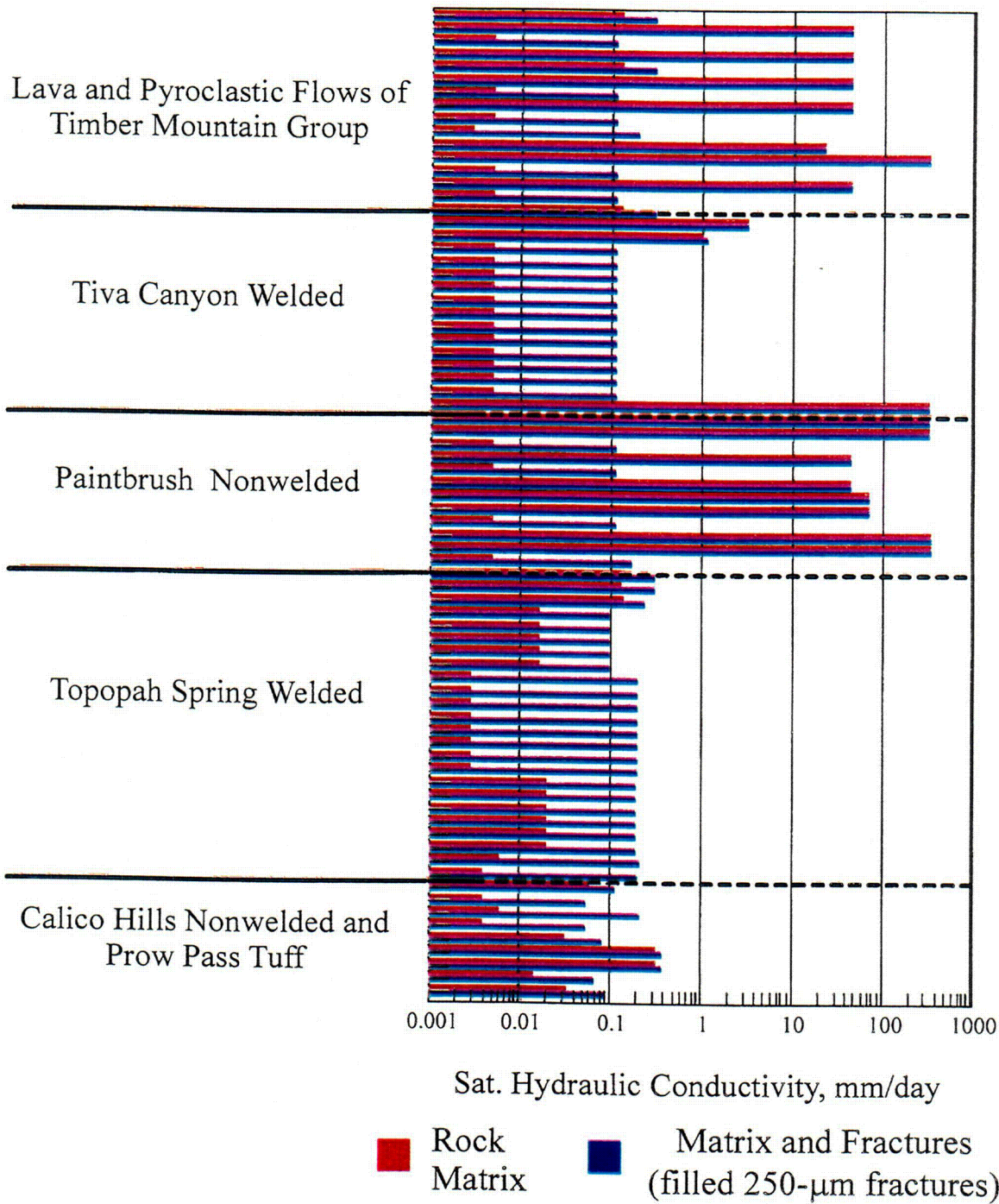
Source: Modified from Hevesi and Flint (1995, Figure 22)

Figure 8.2-3. Estimated Average Annual Precipitation for Yucca Mountain and the Nevada Test Site



Source: GS000200001221.002

Figure 8.2-4. Total Annual Precipitation for Station 4JA from 1958 through 1995

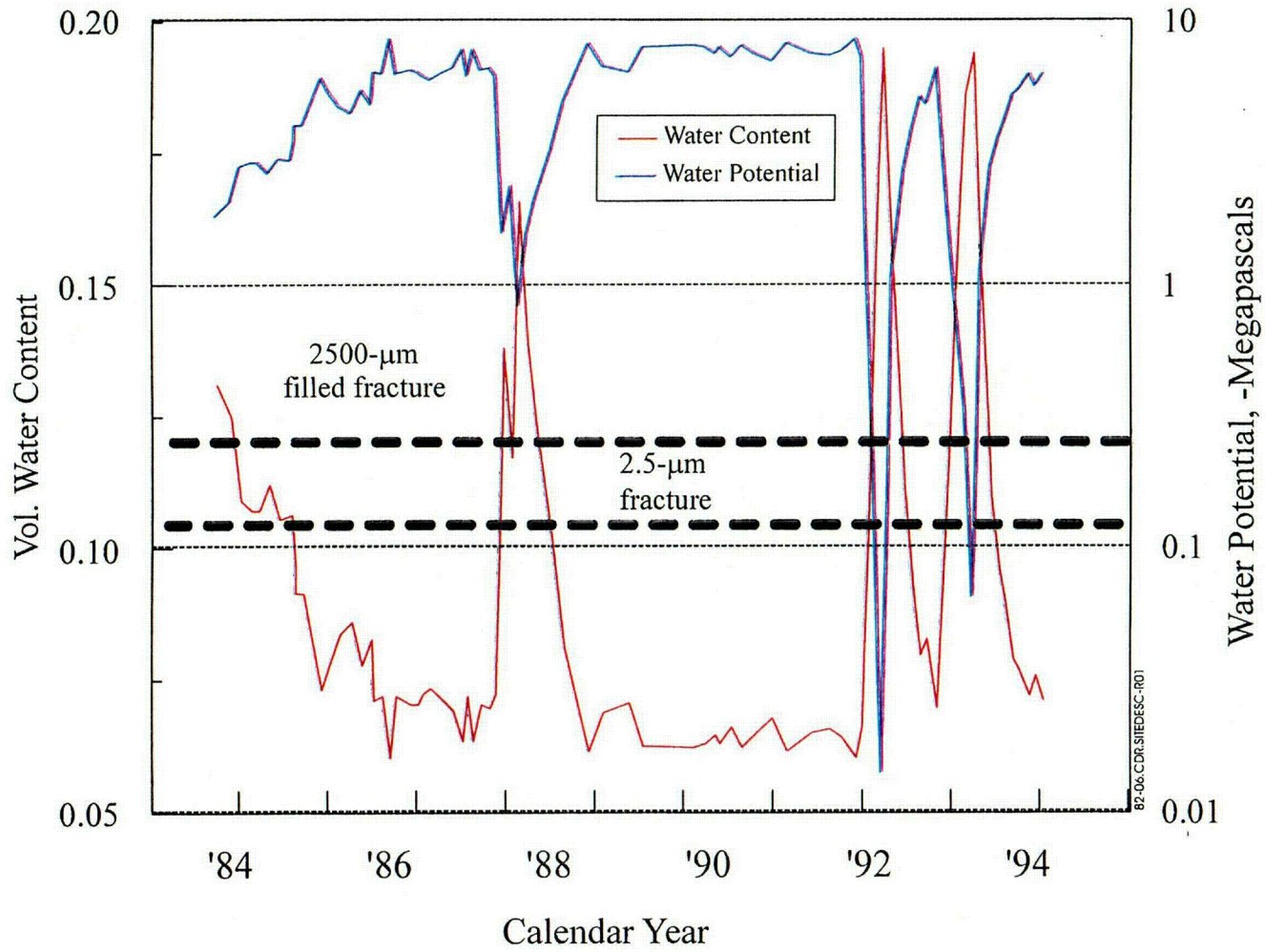


(Individual lithostratigraphic units not labeled)

82-05.CDR.SITEDESC-R01

Source: Data from Flint, A.L. et al. (1996, Table 2)

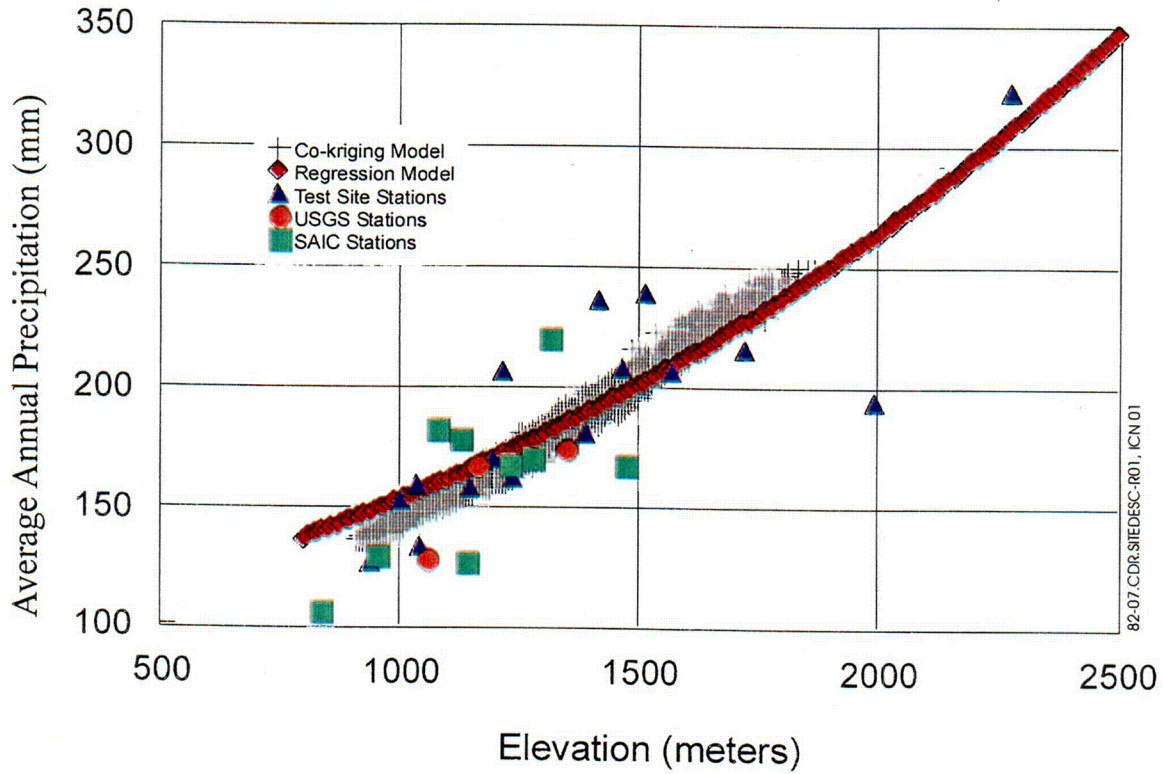
Figure 8.2-5. Saturated Hydraulic Conductivity for Bedrock Matrix and Effective Conductivity for Combined Matrix and Fractures for Filled 250-Micrometer Fractures for Lithostratigraphic Units within Major Hydrogeologic Units



Source: Flint, A.L. et al. (1996, Figure 6)

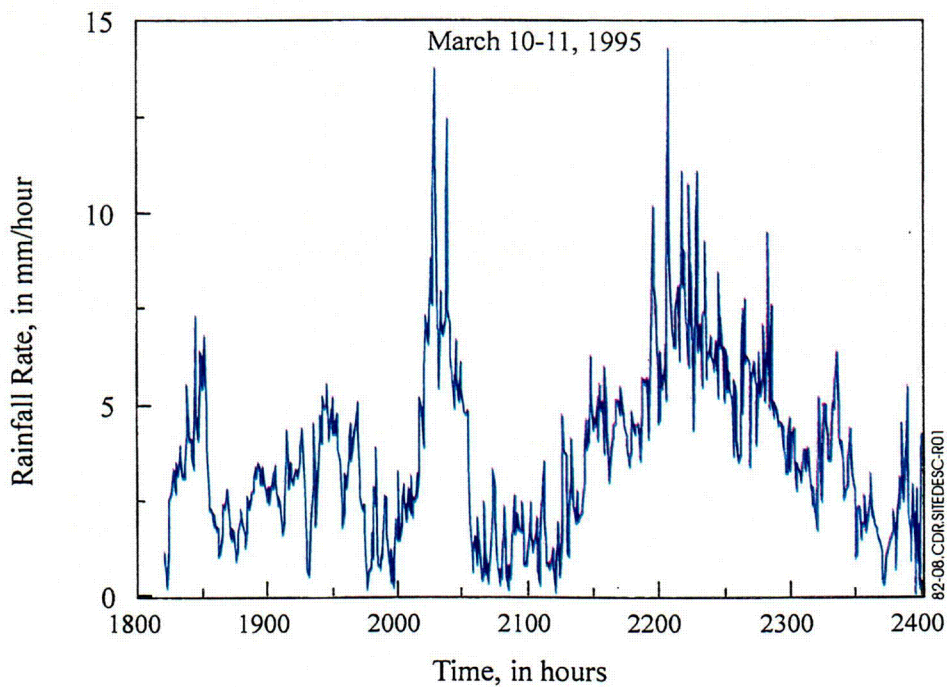
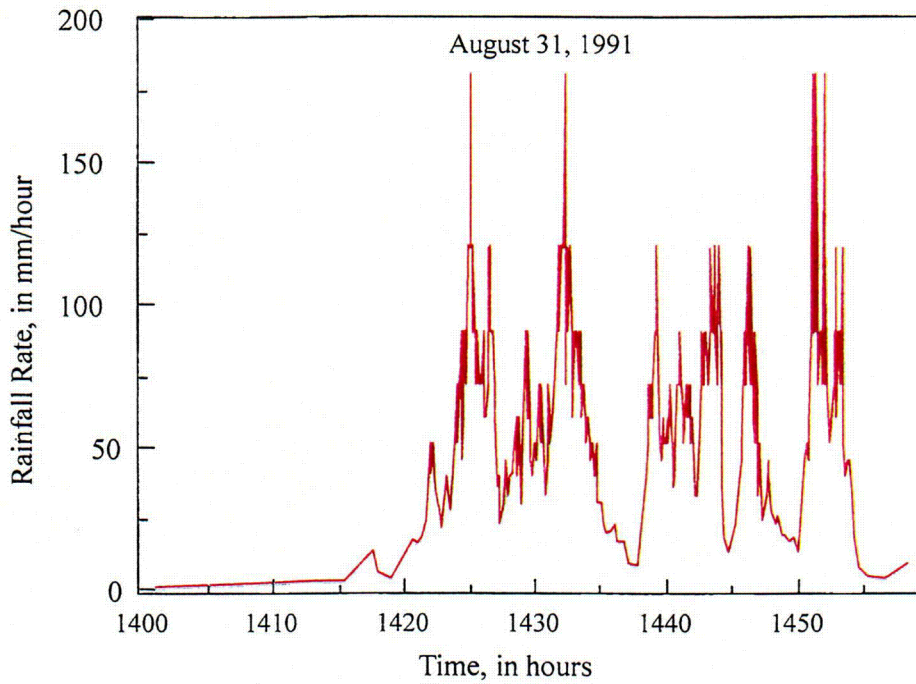
Figure 8.2-6. Water Content and Water Potential at the Soil-Bedrock Interface at a Depth of 2.1 Meters in Borehole USW UZ-N52

BZ-06.CDR.SI/DESC-RO1



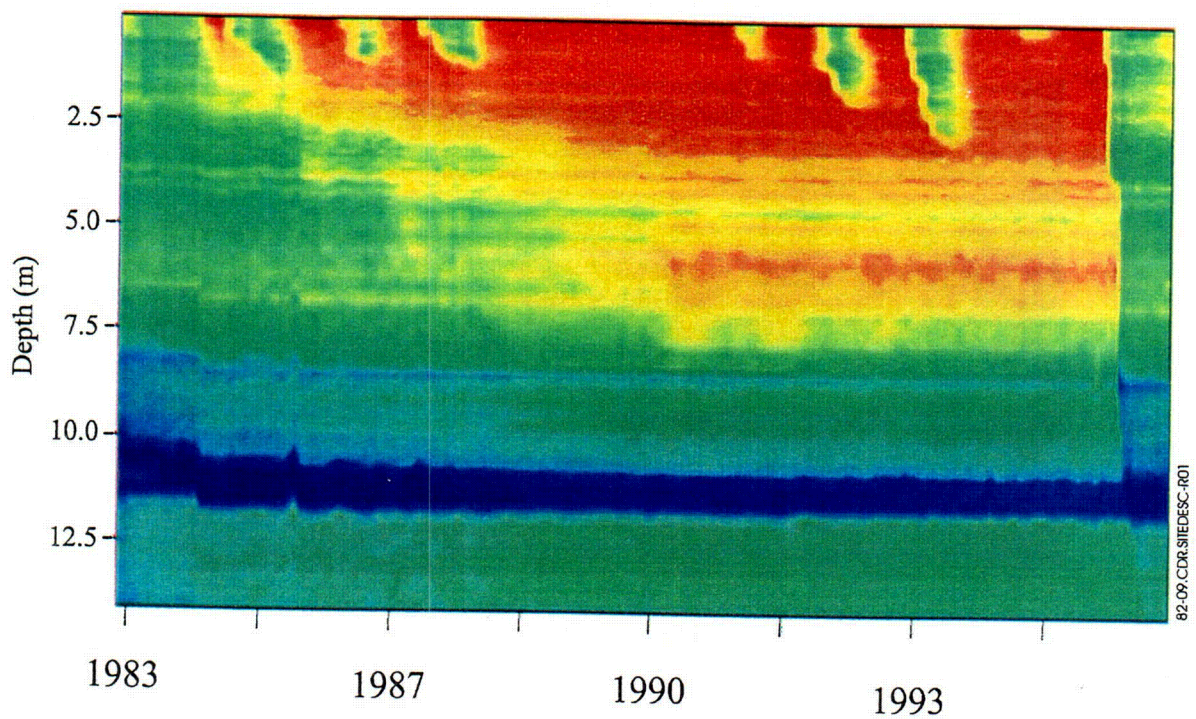
Source: Modified from Hevesi and Flint (1995, Figure 9)

Figure 8.2-7. Comparison of Measured and Modeled Precipitation as a Function of Elevation for Yucca Mountain and the Nevada Test Site



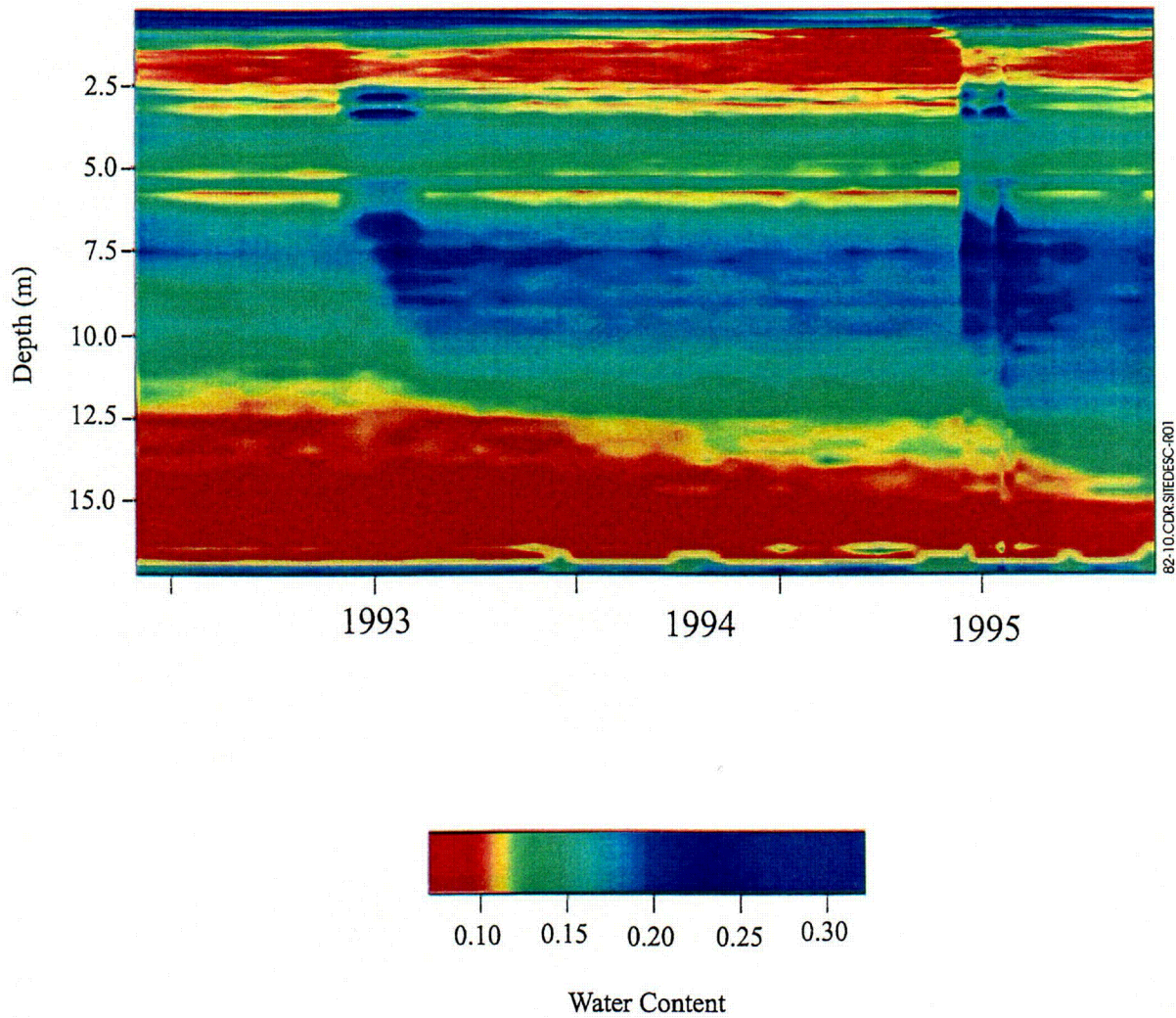
Source: Flint, A.L. et al. (1996, Figure 18)

Figure 8.2-8. Measured Precipitation Rates for the Summer Storm of August 31, 1991, and the Winter Storm of March 10 to 11, 1995



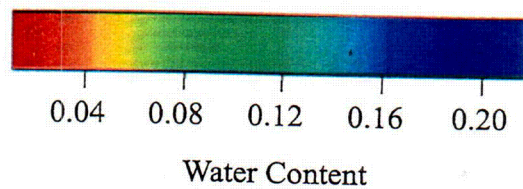
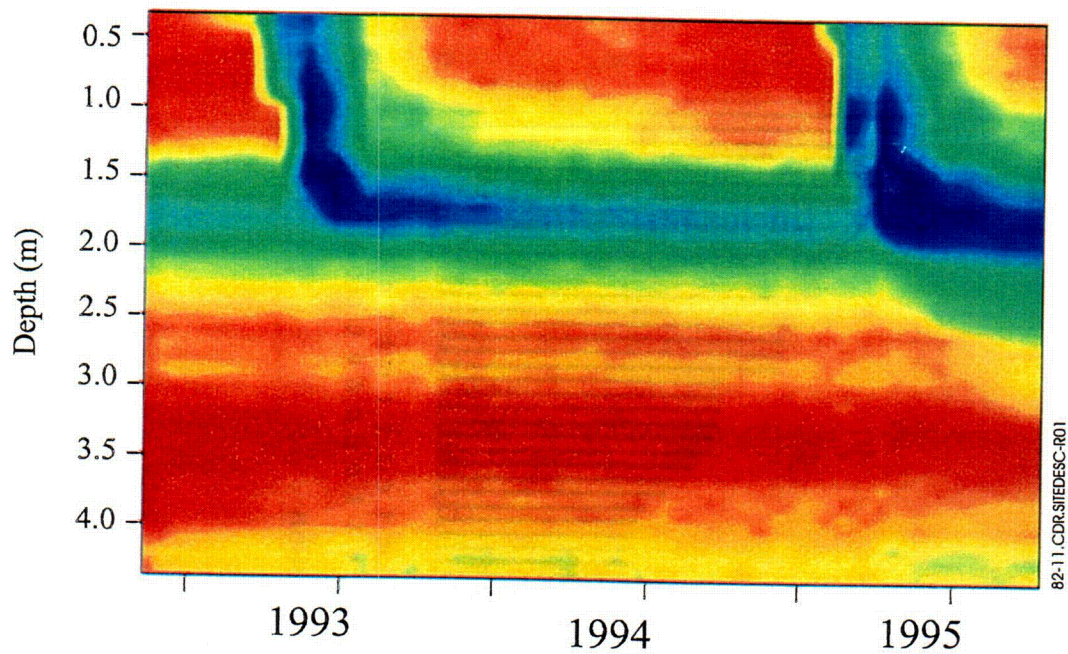
Source: Flint, A.L. et al. (1996, Figure 31)

Figure 8.2-9. Depth versus Time Profile of Measured Water Contents in Borehole N1 for 1984 through 1995



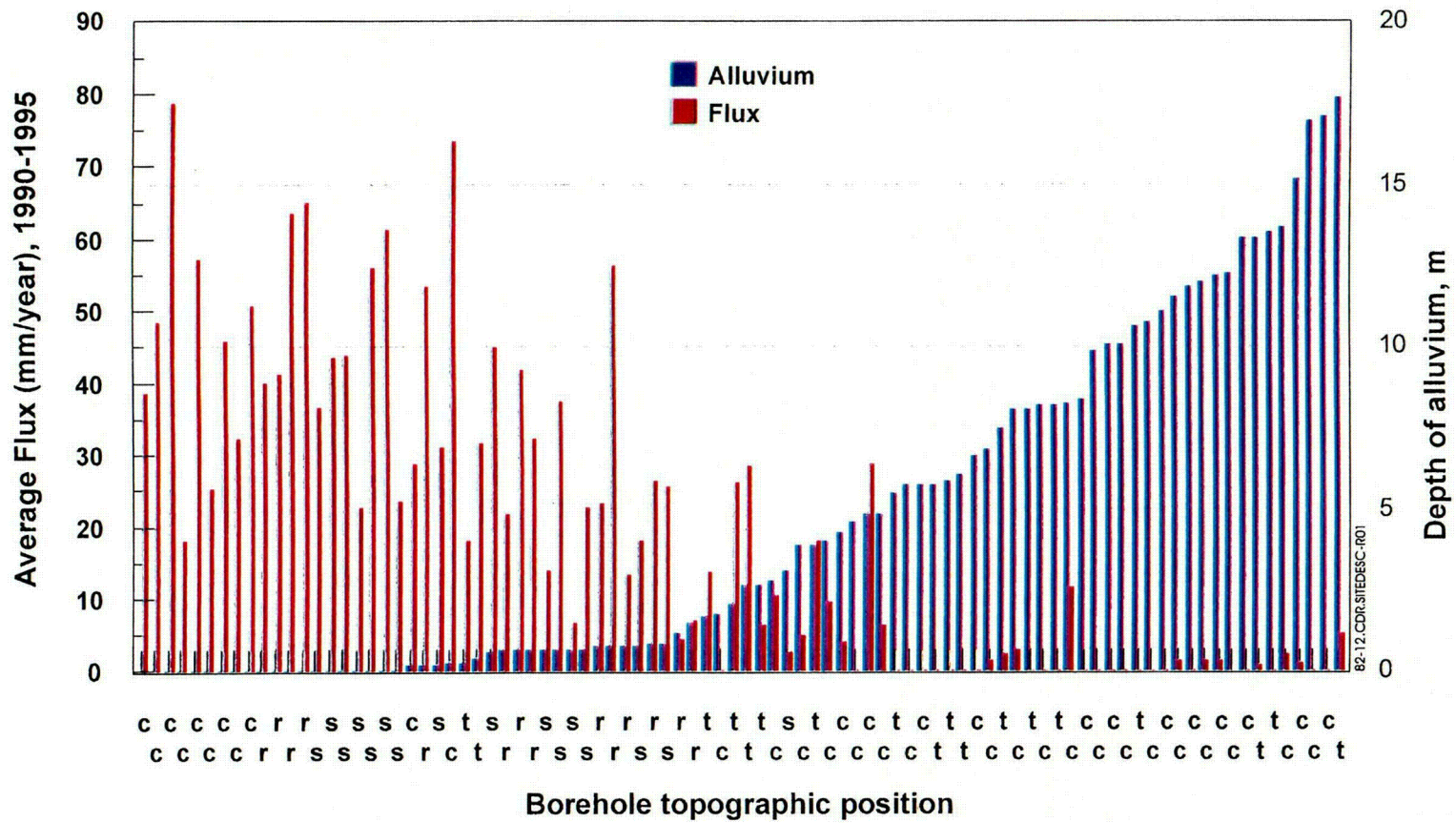
Source: Flint, A.L. et al. (1996, Figure 32)

Figure 8.2-10. Depth versus Time Profile of Measured Water Contents in Borehole N15 for 1993 through 1995



DTNs: GS940708312212.011, GS941208312212.017, GS950808312212.001

Figure 8.2-11. Depth versus Time Profile of Measured Water Contents in Borehole N63 for 1993 through 1995



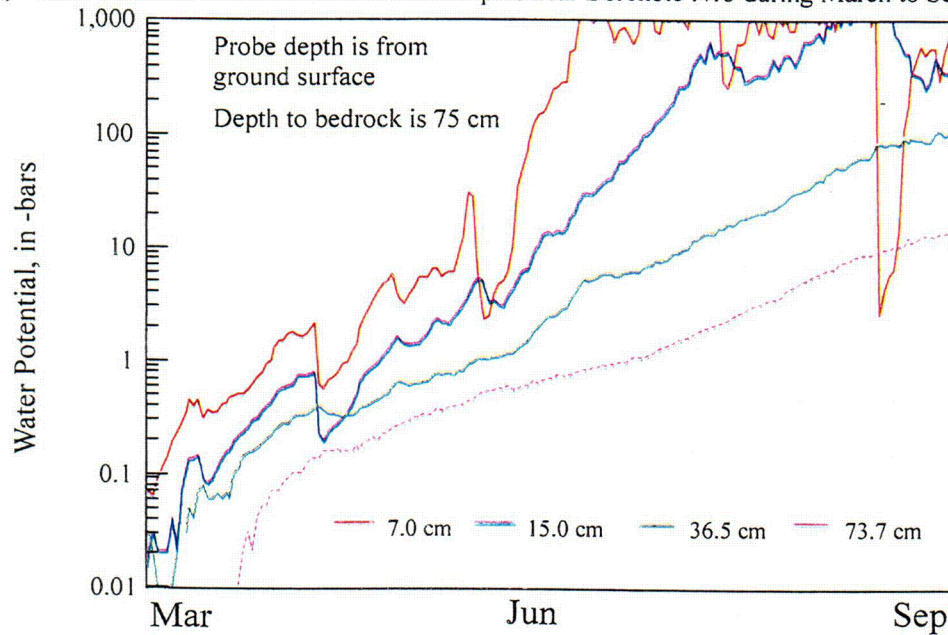
c, Channel, t, Terrace, s, Sideslope, r, Ridgetop

Source: USGS (2000b, Figure 6-5)

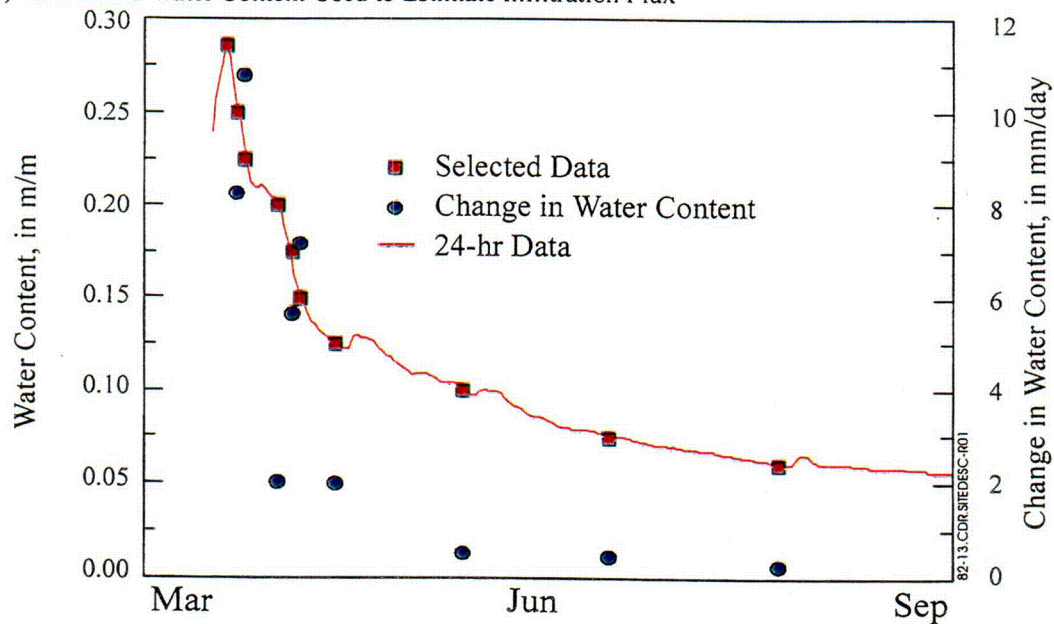
Figure 8.2-12. Average Annual Infiltration through the Top 1 Meter of Bedrock at Neutron Boreholes for 1990 through 1995 Compared to Depth of Alluvium

September 2000  
C 014

(a) Water Potential Measurements at Four Depths near Borehole N15 during March to September 1995

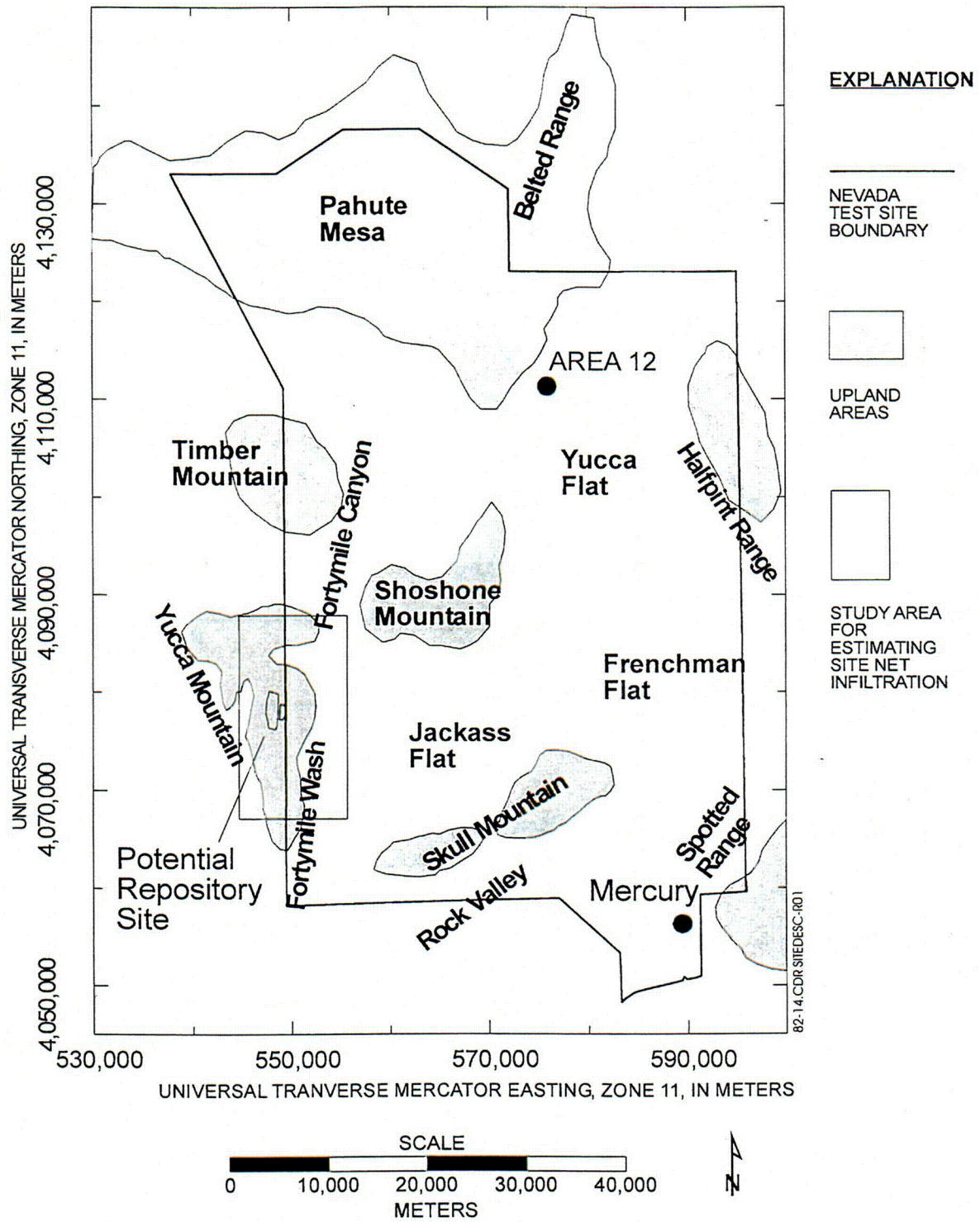


(b) Calculated Water Content Used to Estimate Infiltration Flux



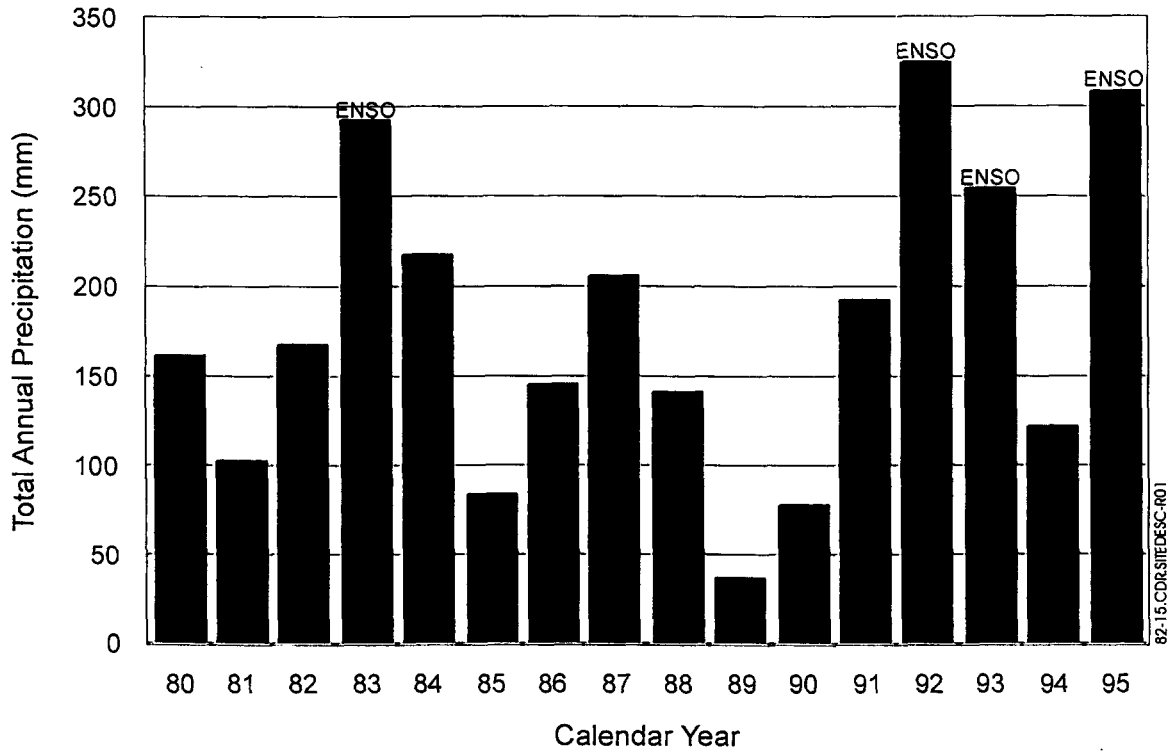
Source: Flint, A.L. et al. (1996, Figure 35)

Figure 8.2-13. Water Potential Measurement Data and Water Content Data Used to Estimate Infiltration Flux



Source: Modified from Hevesi and Flint (1995, Figure 1b)

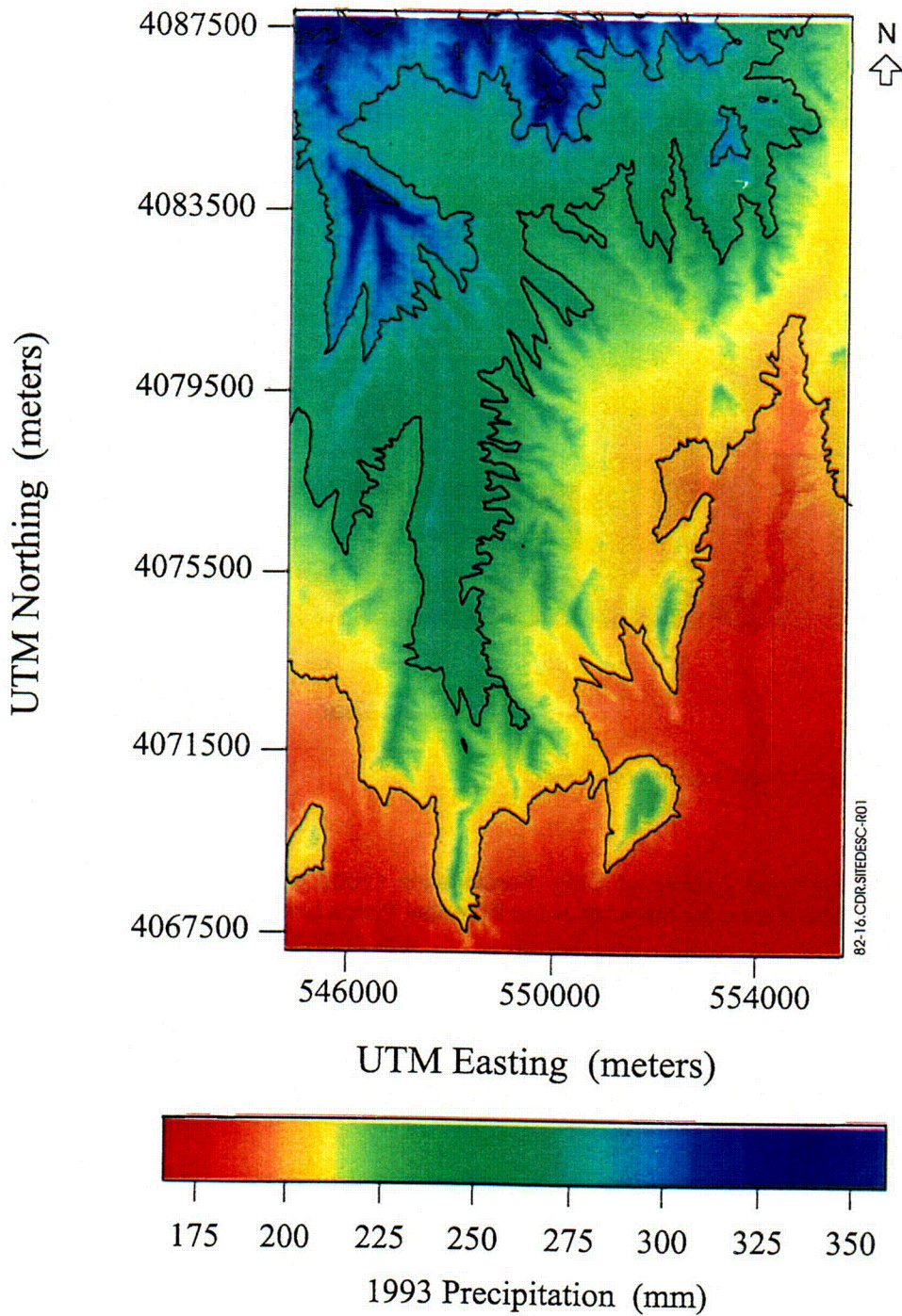
Figure 8.2-14. Location of Study Area for Estimating Site Net Infiltration



ENSO: El Niño Southern Oscillation

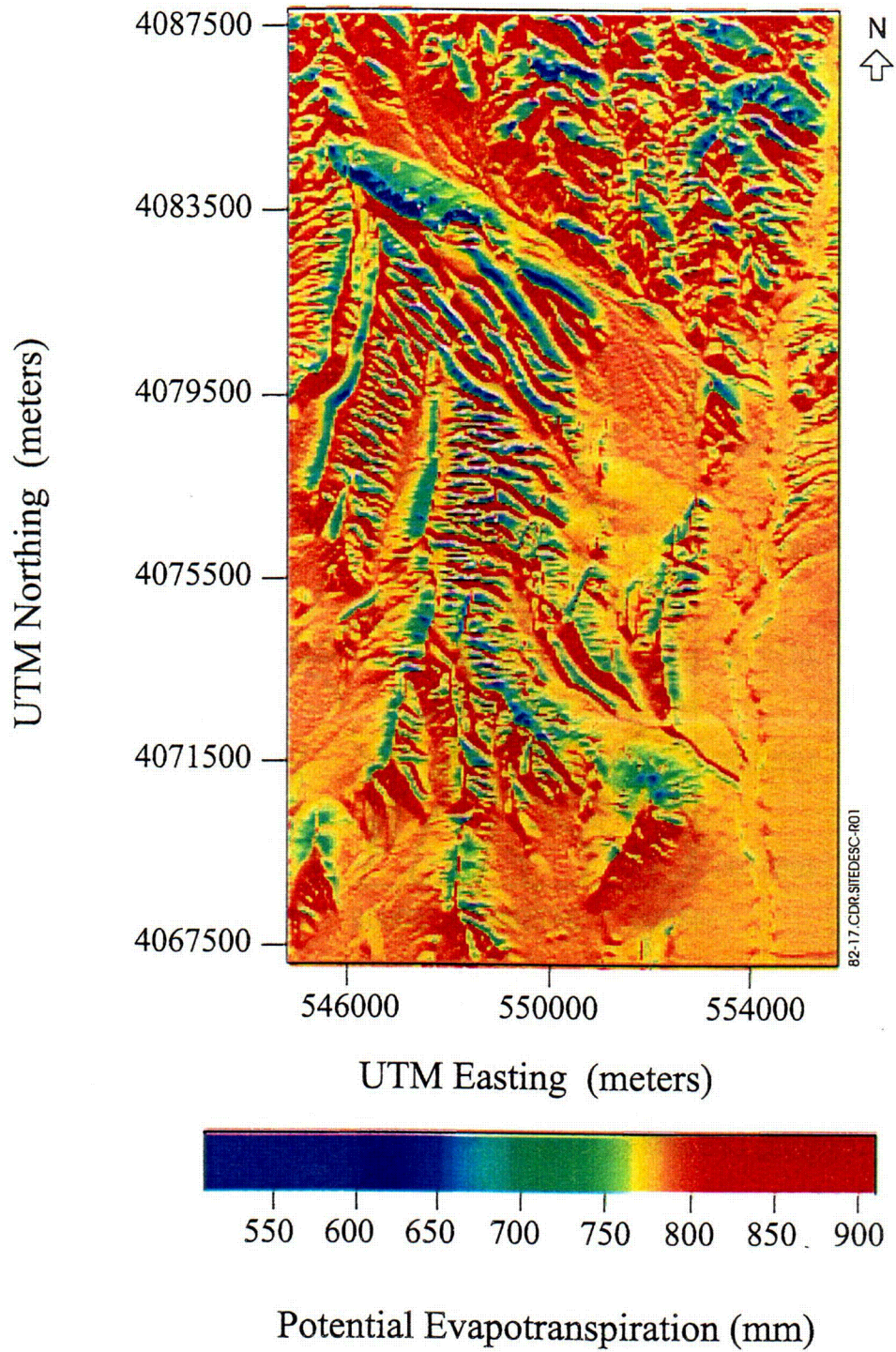
DTN: GS960908312211.003

Figure 8.2-15. Developed Record of Daily Precipitation (1980 to 1995) Adjusted to an Elevation of 1,400 Meters for the Area of the Potential Yucca Mountain Repository



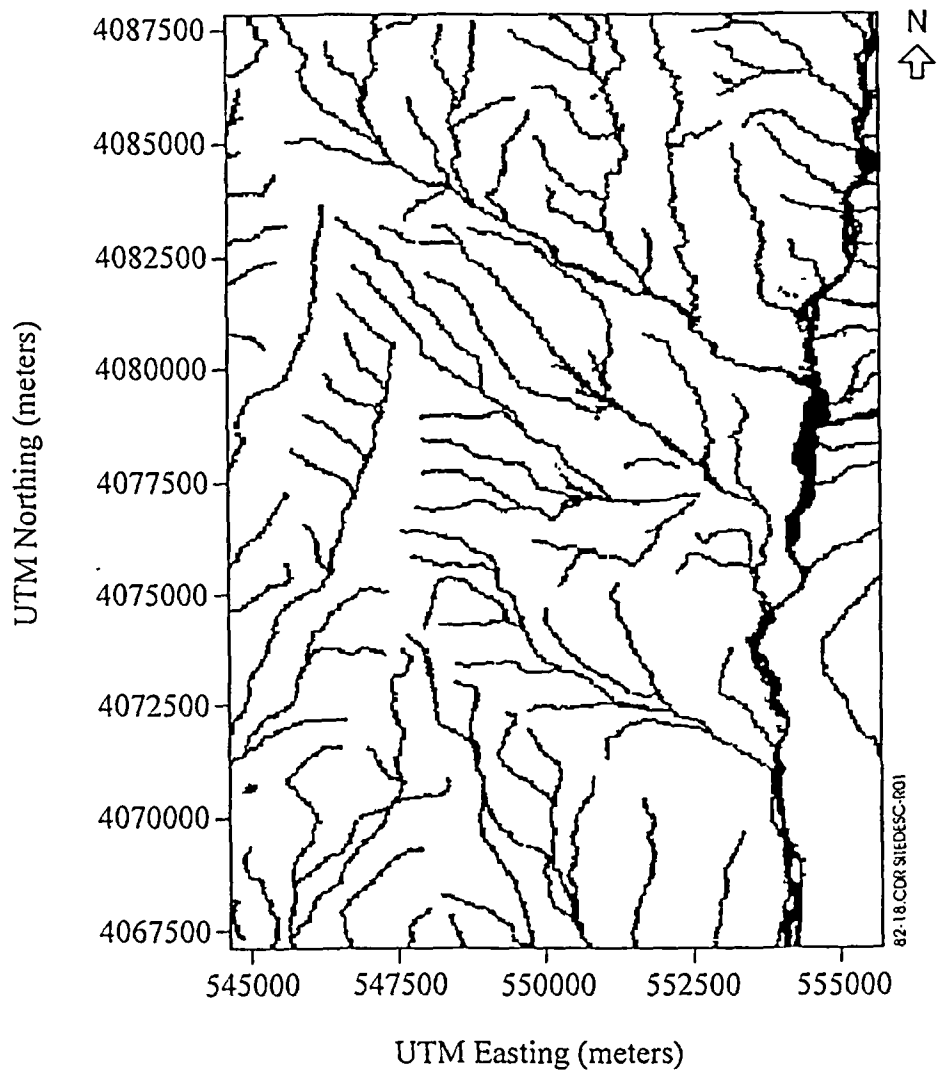
DTN: GS960908312211.003

Figure 8.2-16. Spatially Distributed 1993 Total Annual Precipitation for Yucca Mountain



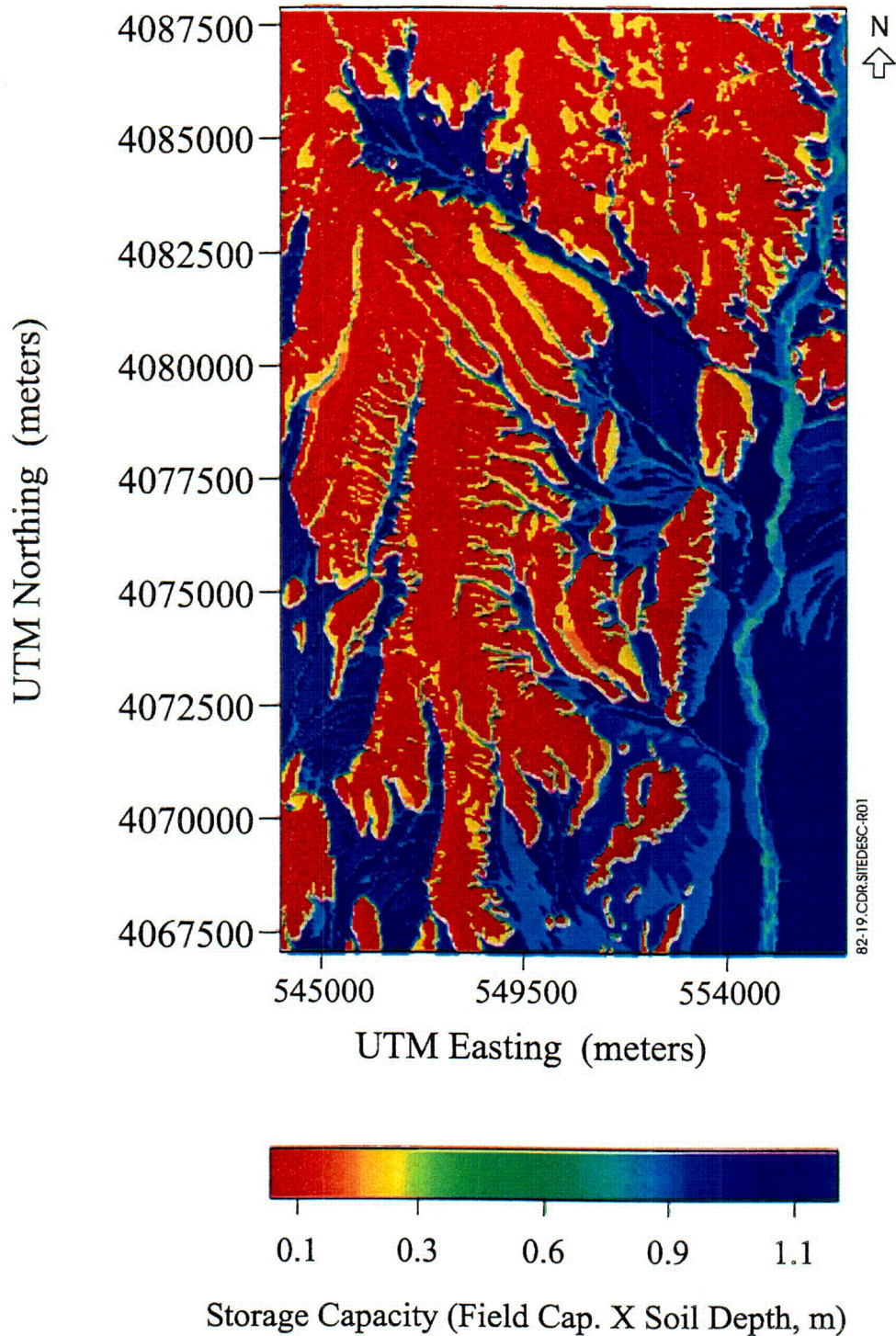
DTN: GS960908312211.003

Figure 8.2-17. Modeled Total Annual Potential Evapotranspiration at Yucca Mountain



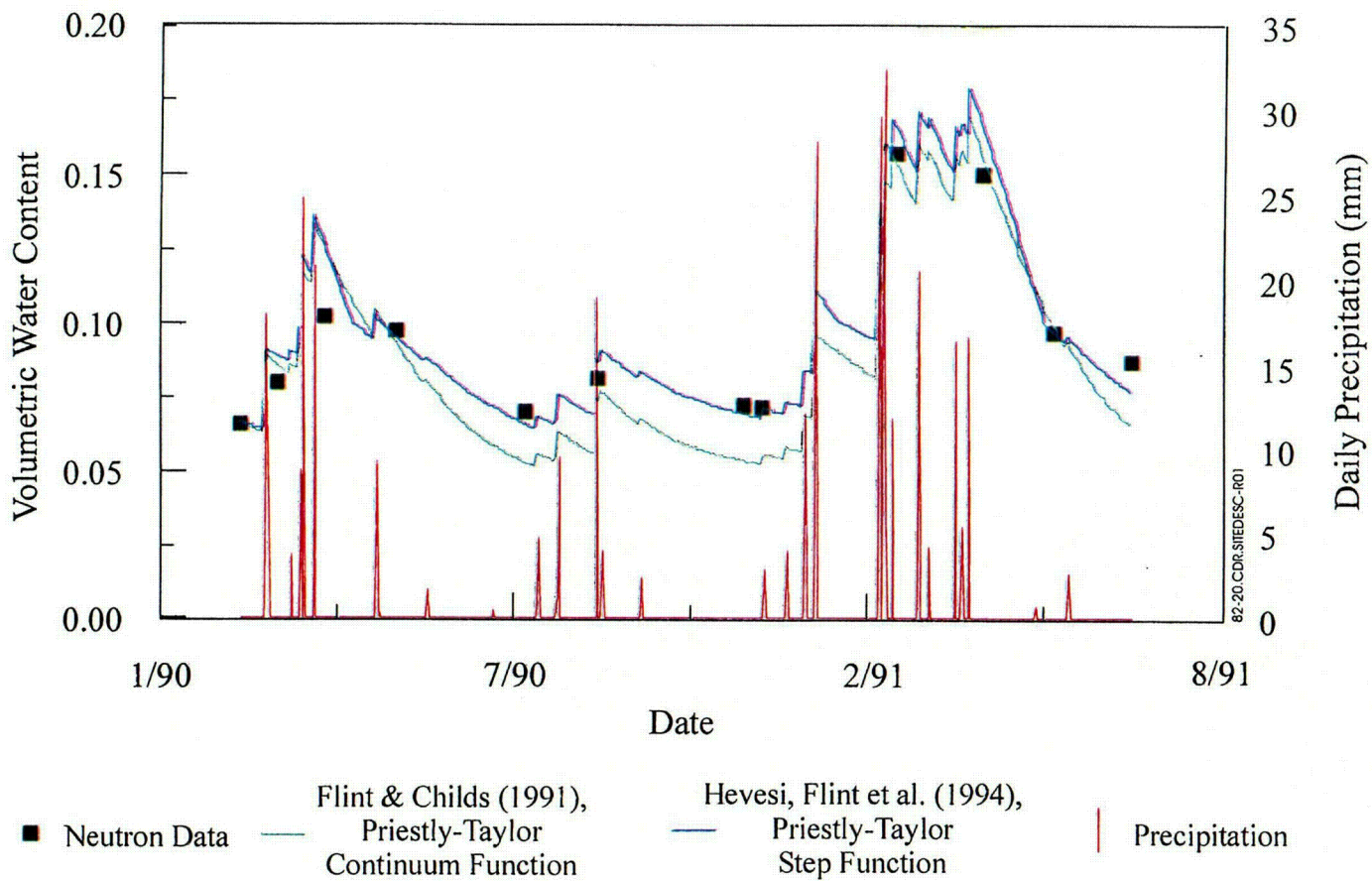
DTN: GS960908312211.003

Figure 8.2-18. Surface Runoff Channel Network for Yucca Mountain Defined by 30-Meter Grid Cells Containing One or More Channel Nodes



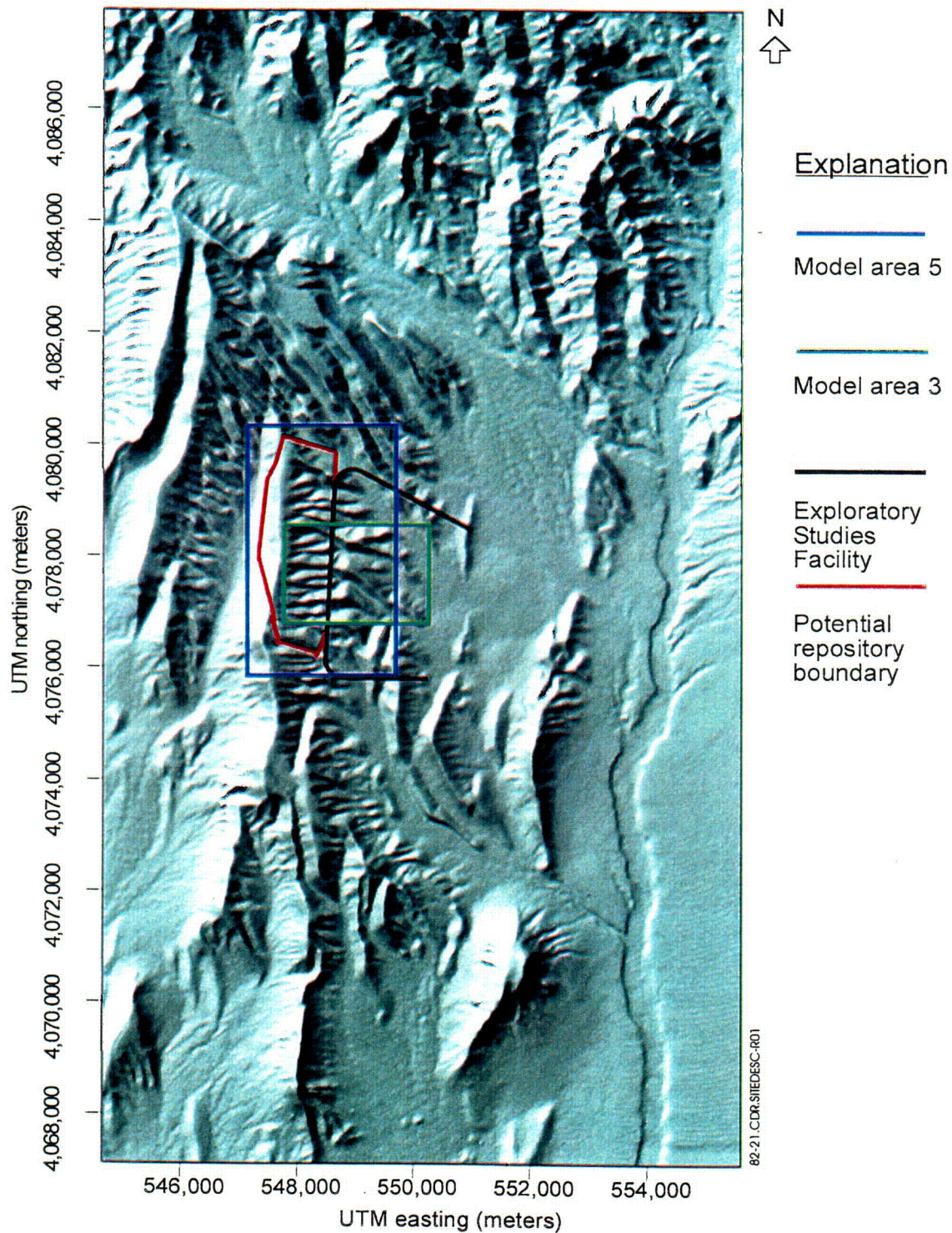
Source: Flint, A.L. et al. (1996, Figure 28)

Figure 8.2-19. Calculated Soil Storage Capacity at Yucca Mountain



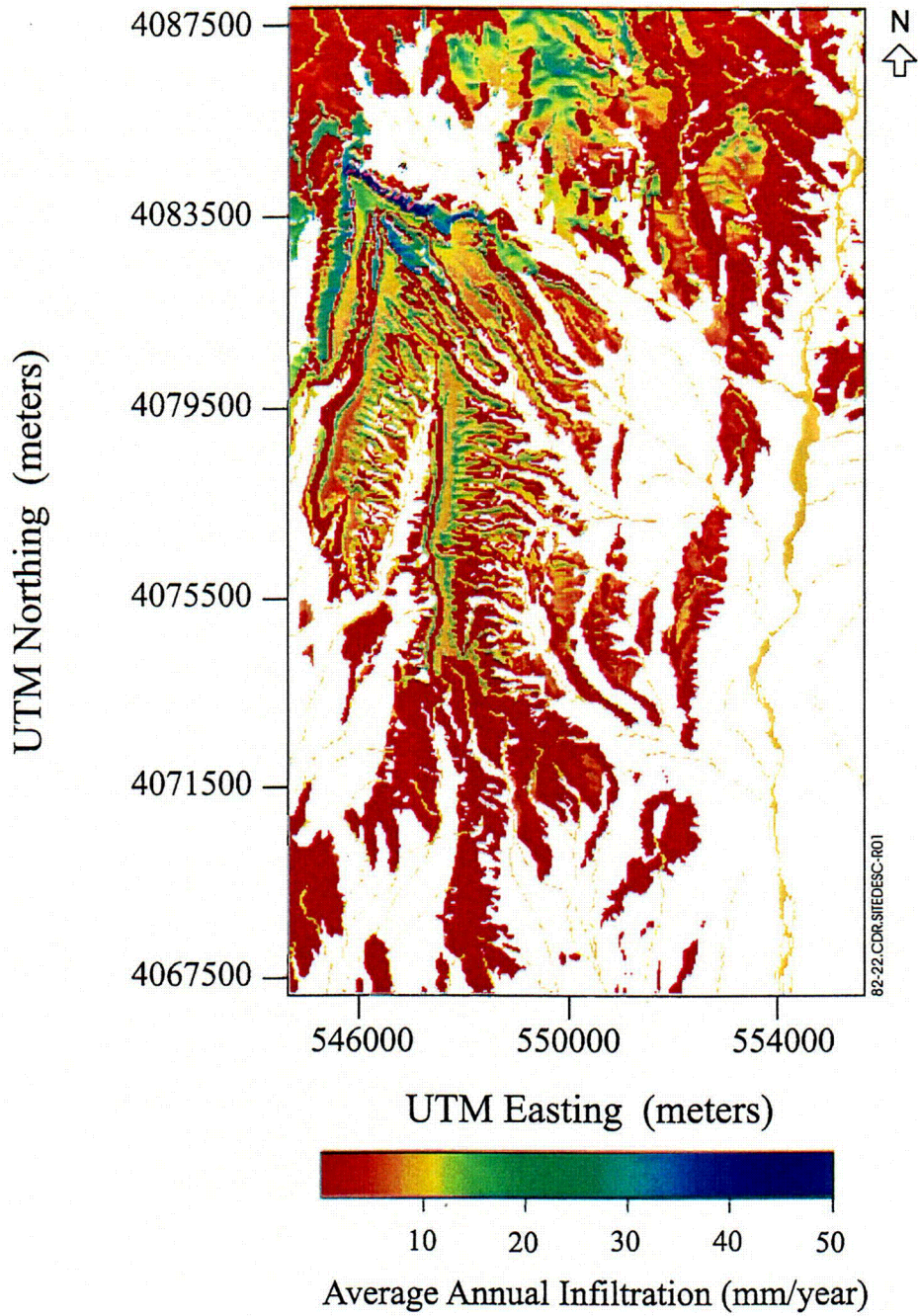
DTN: GS960908312211.003

Figure 8.2-20. Comparison of Modeled and Measured Water Content Changes at Borehole N63 for the Calibrated Net-Infiltration Model



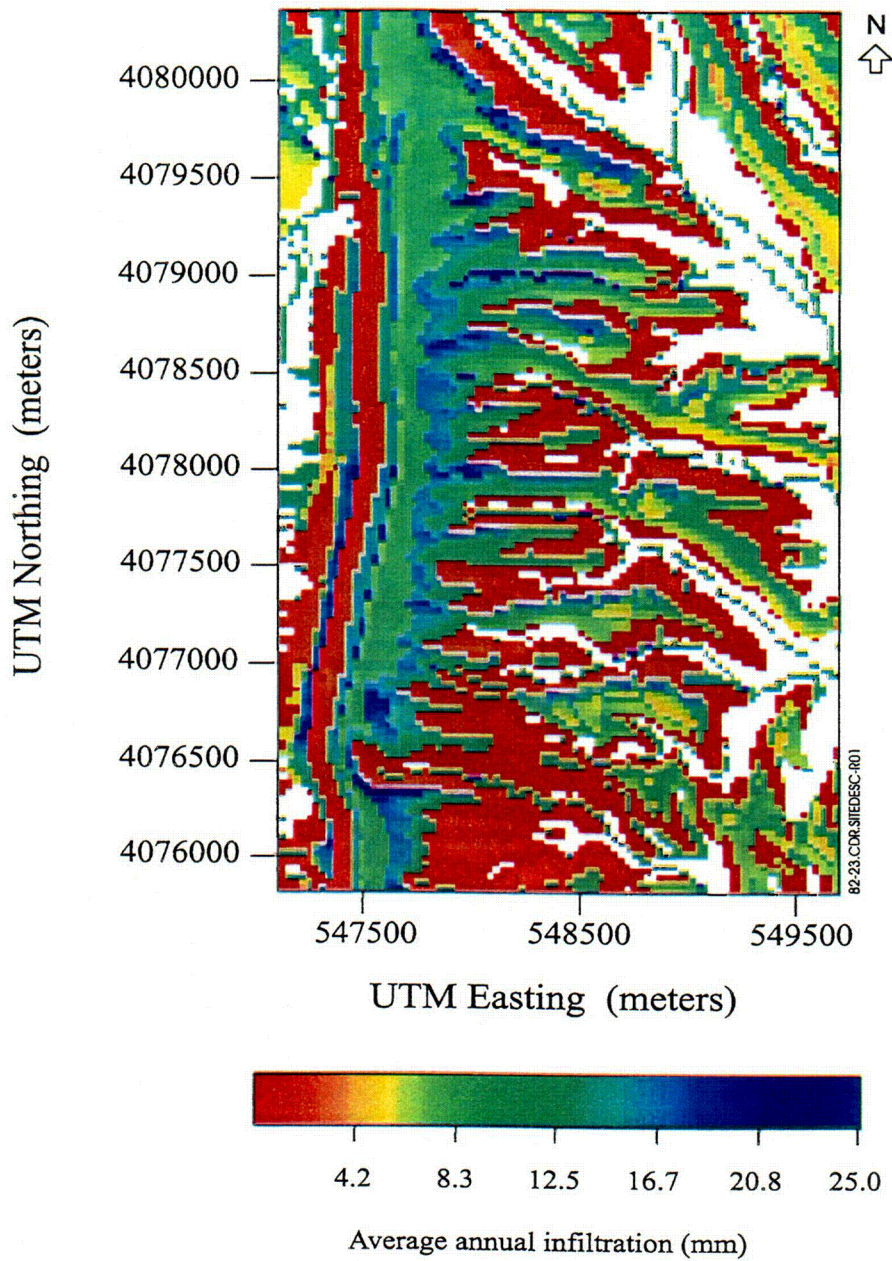
DTNs: GS960908312211.003; GS000200001221.003

Figure 8.2-21. Domains of the 1996 Net-Infiltration Model (Area 1) for the Yucca Mountain Site Area and Submodel Areas in the Vicinity of the Potential Repository Site



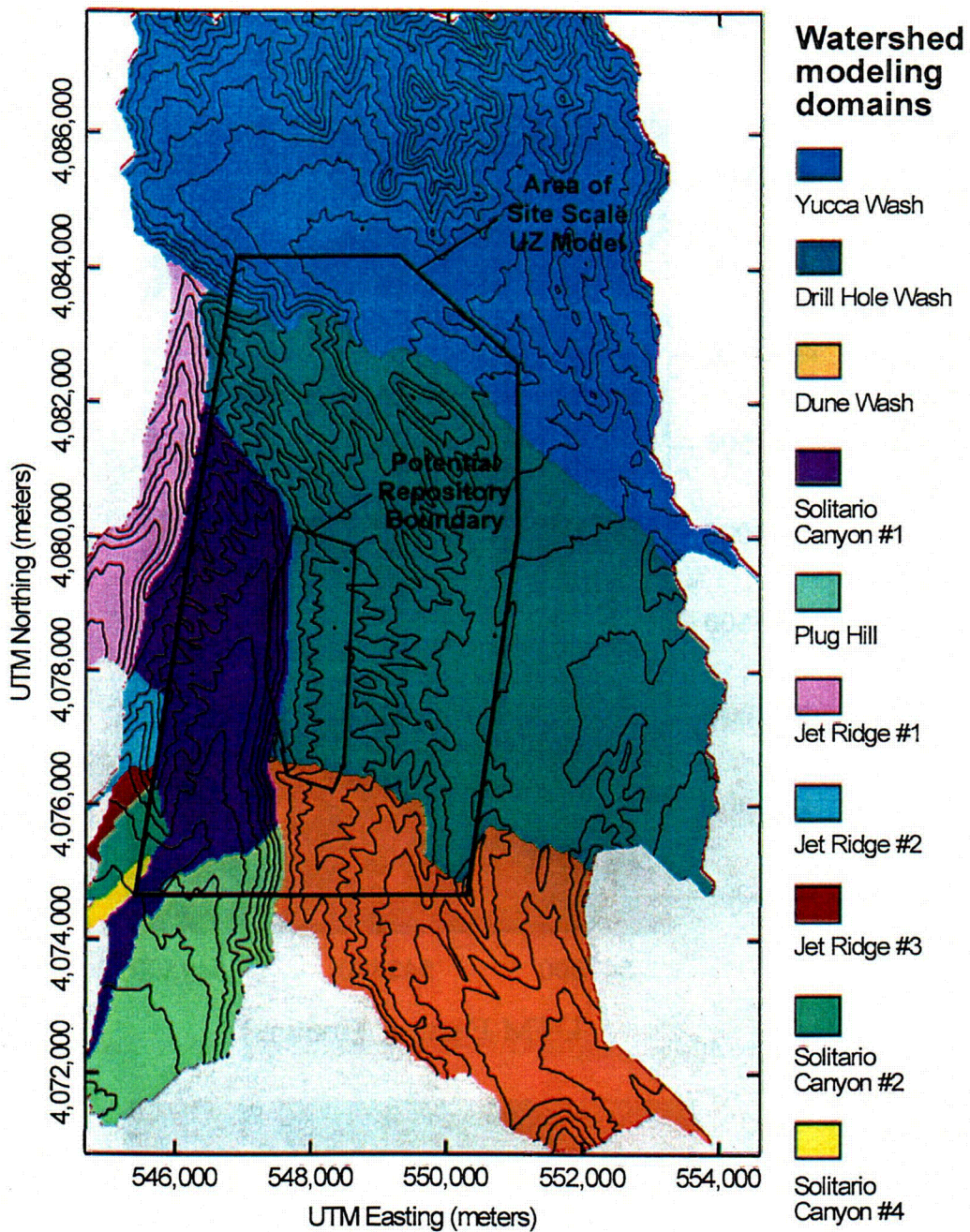
DTN: GS960908312211.003

Figure 8.2-22. Simulated Average Annual Net Infiltration for the Yucca Mountain Site Area Using a Scaled 100-Year Stochastic Simulation of Daily Precipitation for Current Climatic Conditions



DTN: GS960908312211.003

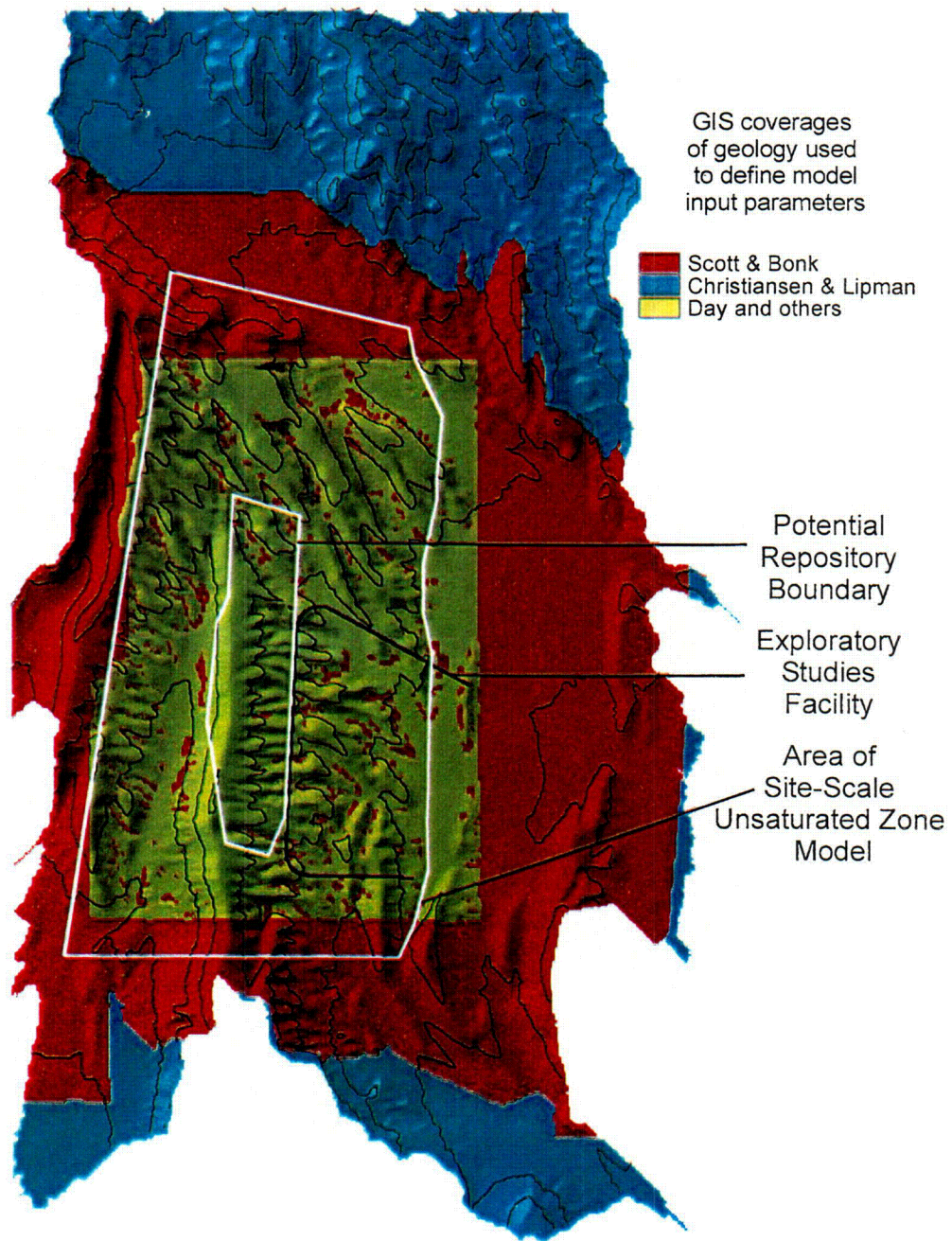
Figure 8.2-23. Simulated Average Annual Net Infiltration for the Area of the Potential Repository (Area 5) Using a Scaled 100-Year Stochastic Simulation of Daily Precipitation for Current Climatic Conditions



82-24.CDR.SITEDESC-R01

Source: USGS (2000b, Figure 6-12)

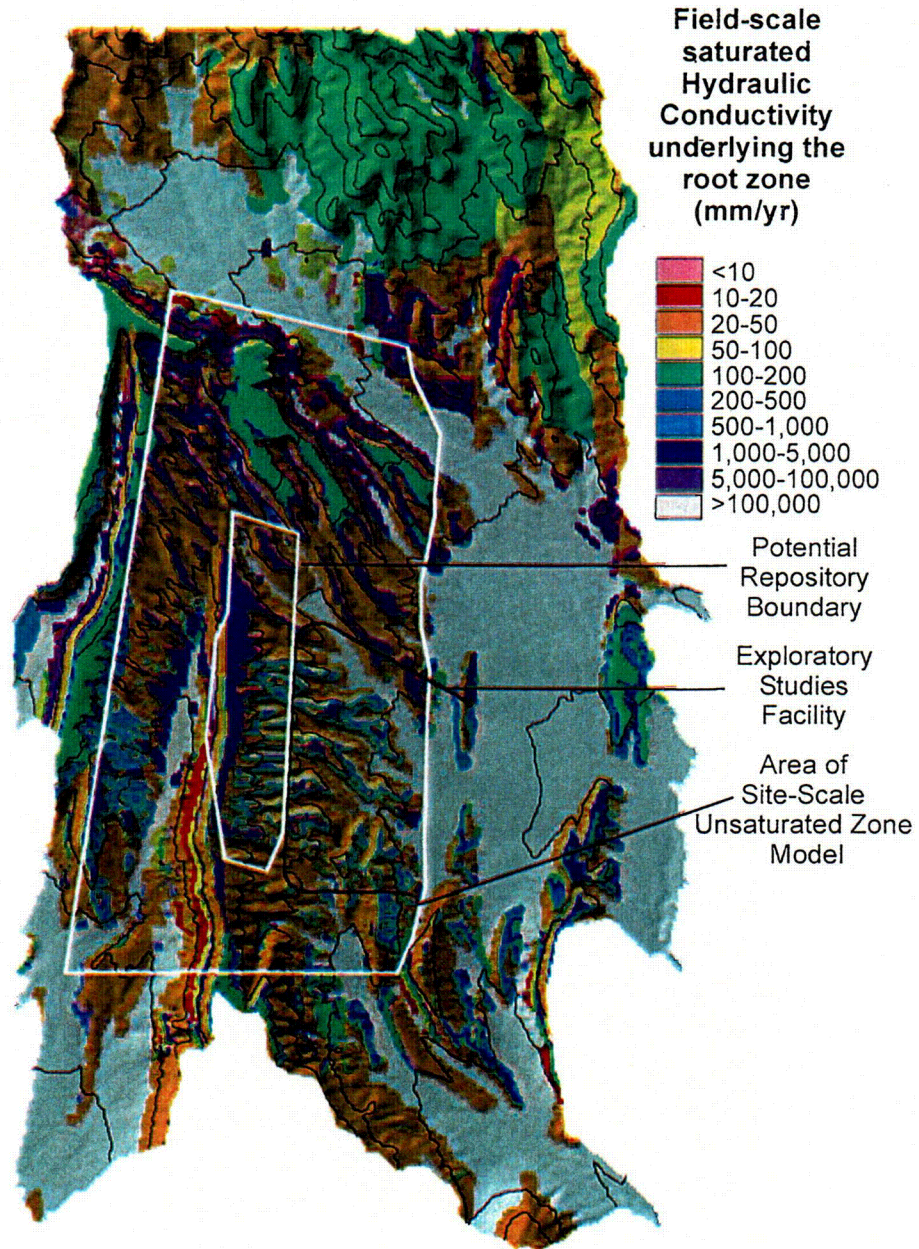
Figure 8.2-24. Domain of the Revised Infiltration Model and Locations of the 10 Watershed Domains



82-25.CDR.SITEDESC-R01

Source: USGS (2000b, Figure 6-14)

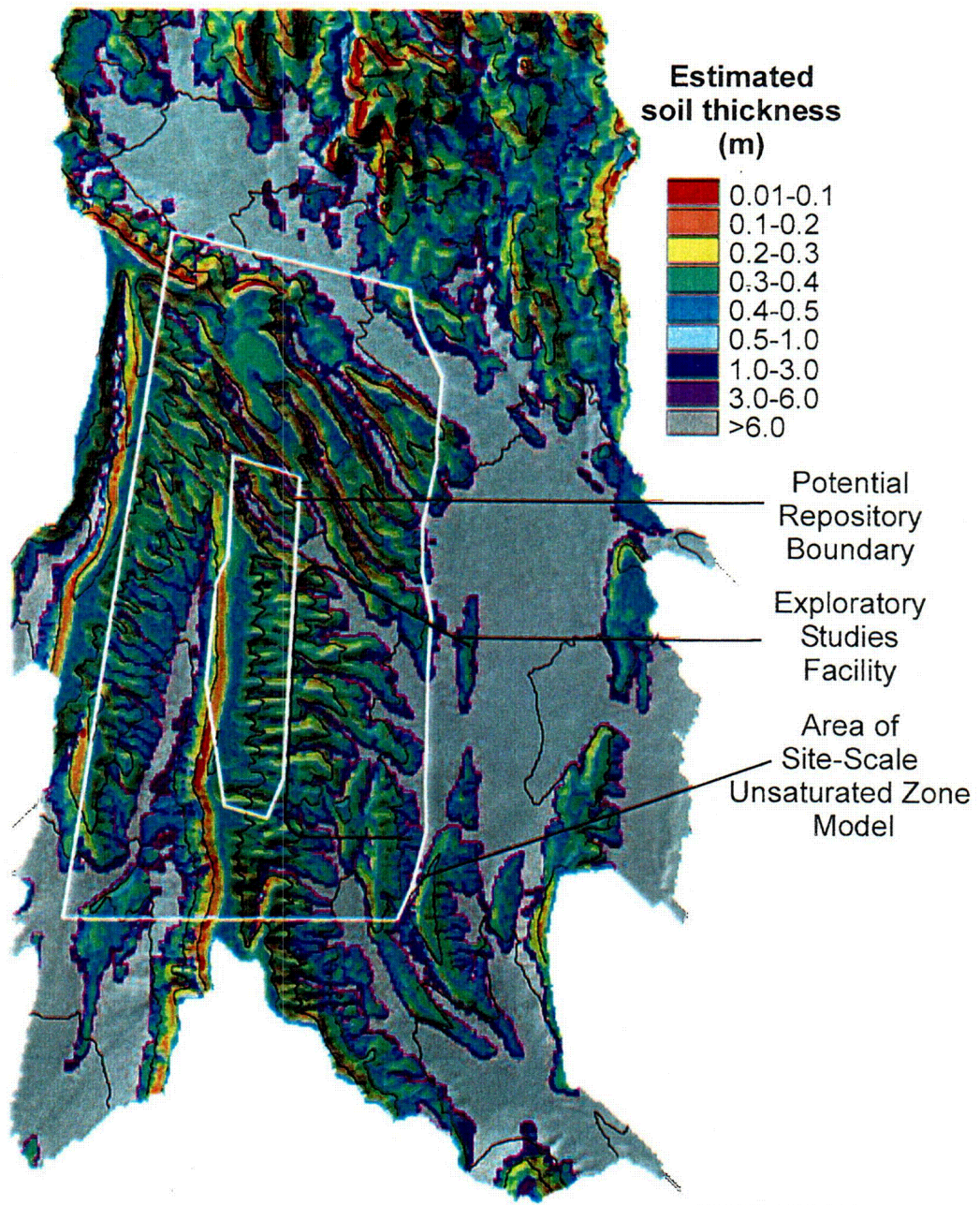
Figure 8.2-25. Overlay of the Three Geologic Maps Used to Define Bedrock Types for the 1999 Infiltration Model



82-26.CDR.SITEDESC-R01

Source: USGS (2000b, Figure 6-15)

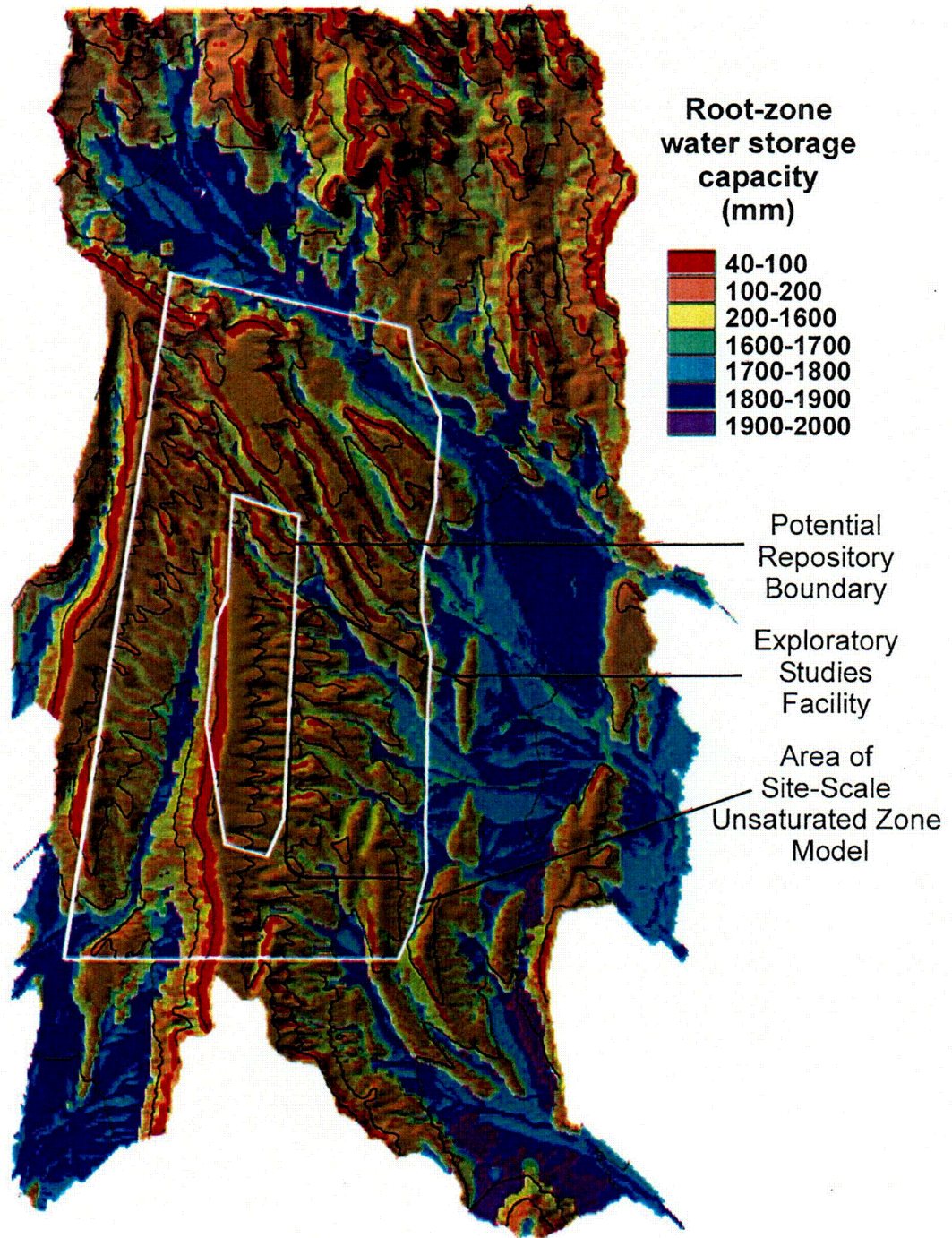
Figure 8.2-26. Estimated Field-Scale Saturated Hydraulic Conductivity of Bedrock and Alluvium Underlying the Root Zone



82-27.CDR.SITEDESC-R01

Source: USGS (2000b, Figure 6-16)

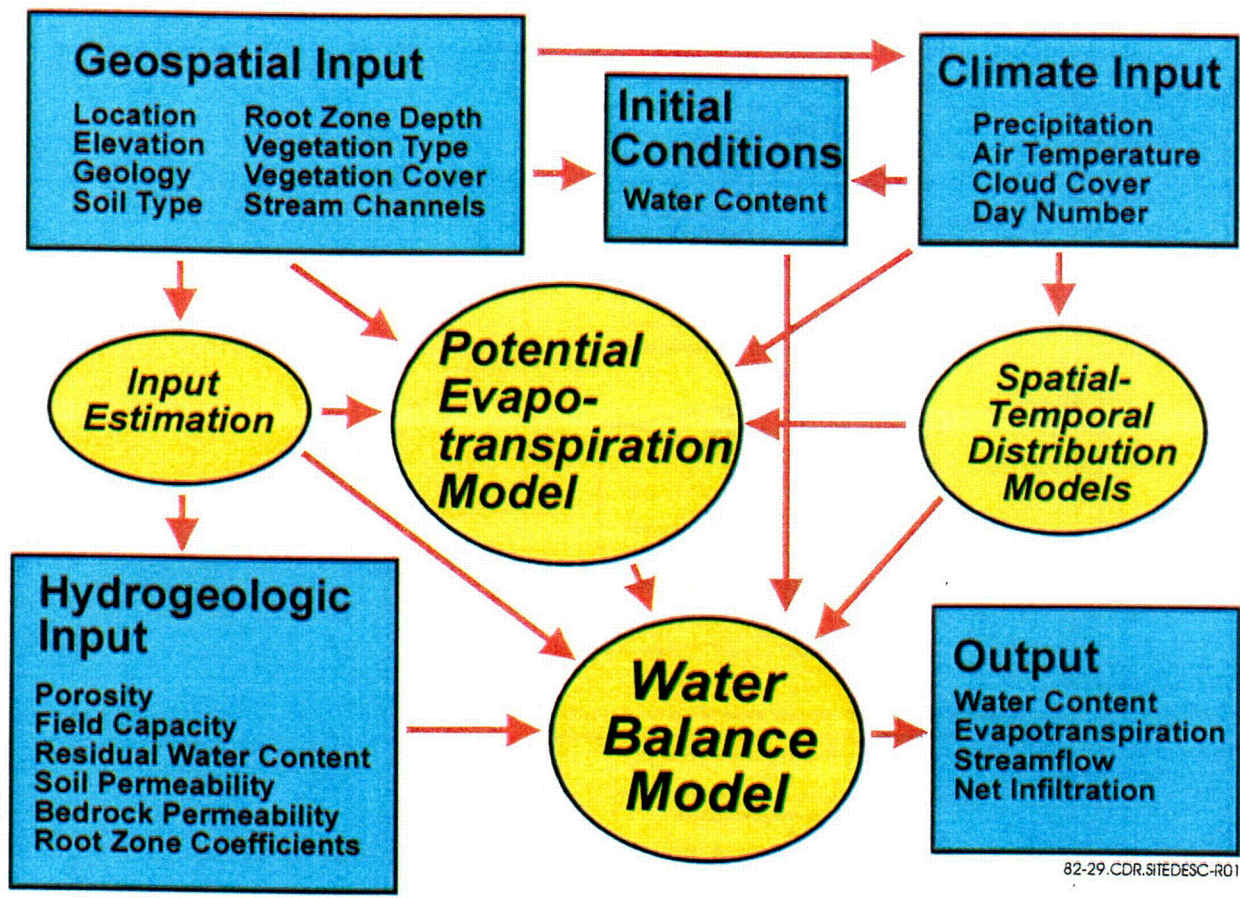
Figure 8.2-27. Estimated Soil Thickness Using the 1996 Soil-Thickness Class Map and Calculated Ground-Surface Slope



82-28.CDR.SITEDESC-R01

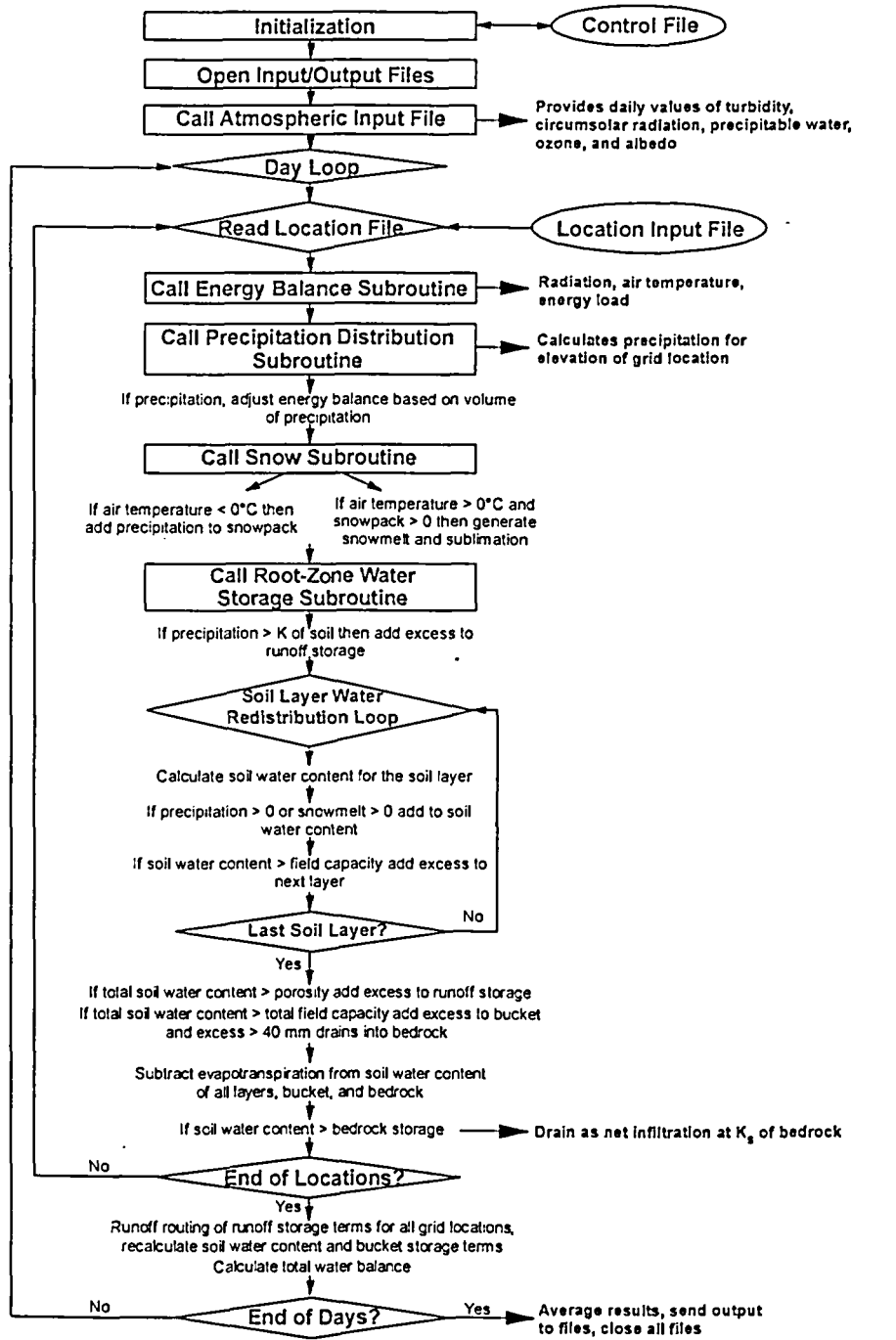
Source: USGS (2000b, Figure 6-17)

Figure 8.2-28. Total Water Storage Capacity of the Modeled Root Zone, Including Both Bedrock and Soil Layers



Source: USGS (2000b, Figure 6-3)

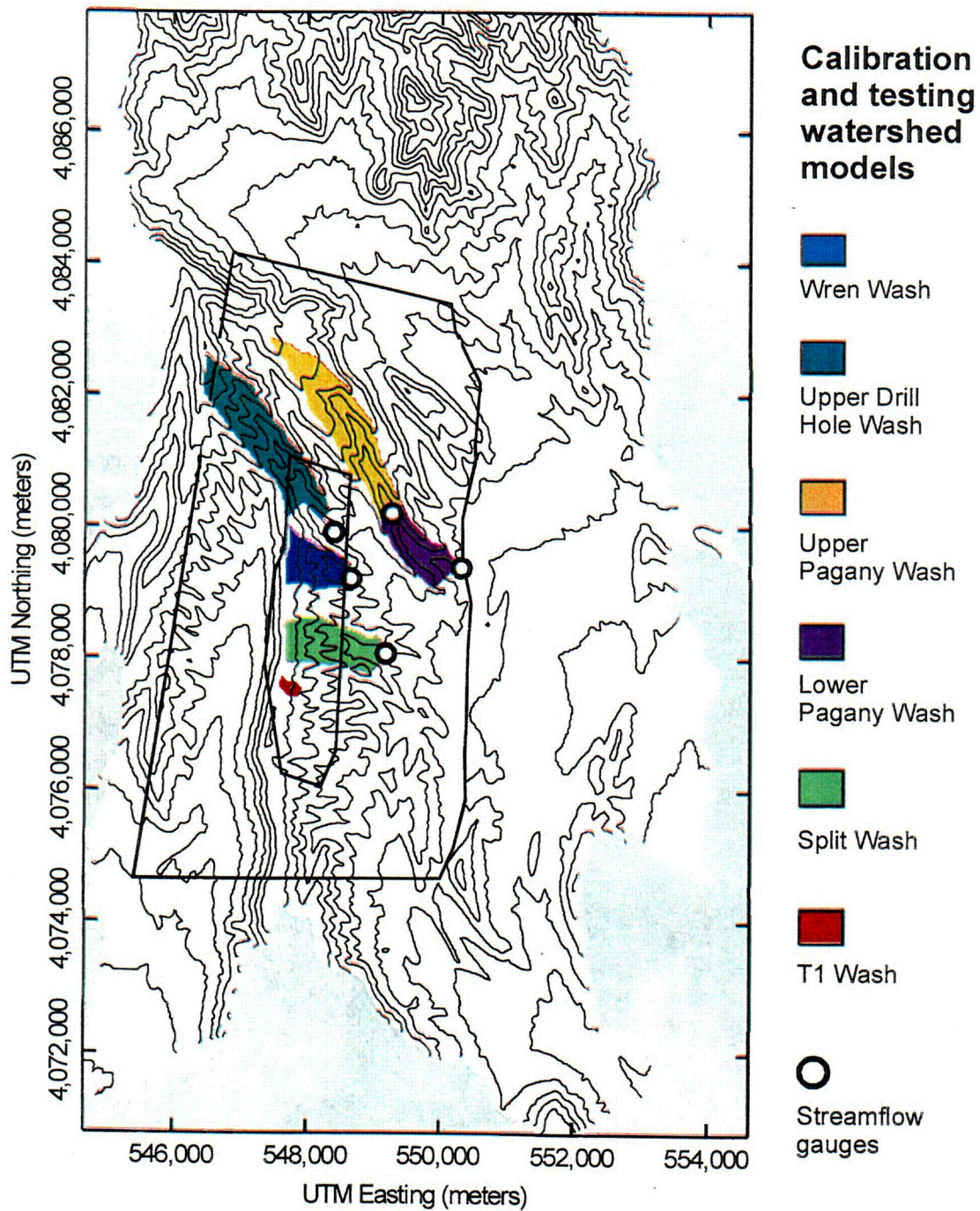
Figure 8.2-29. Major Components of the Net-Infiltration Modeling System



82-30.CDR.SIETDESC-R01

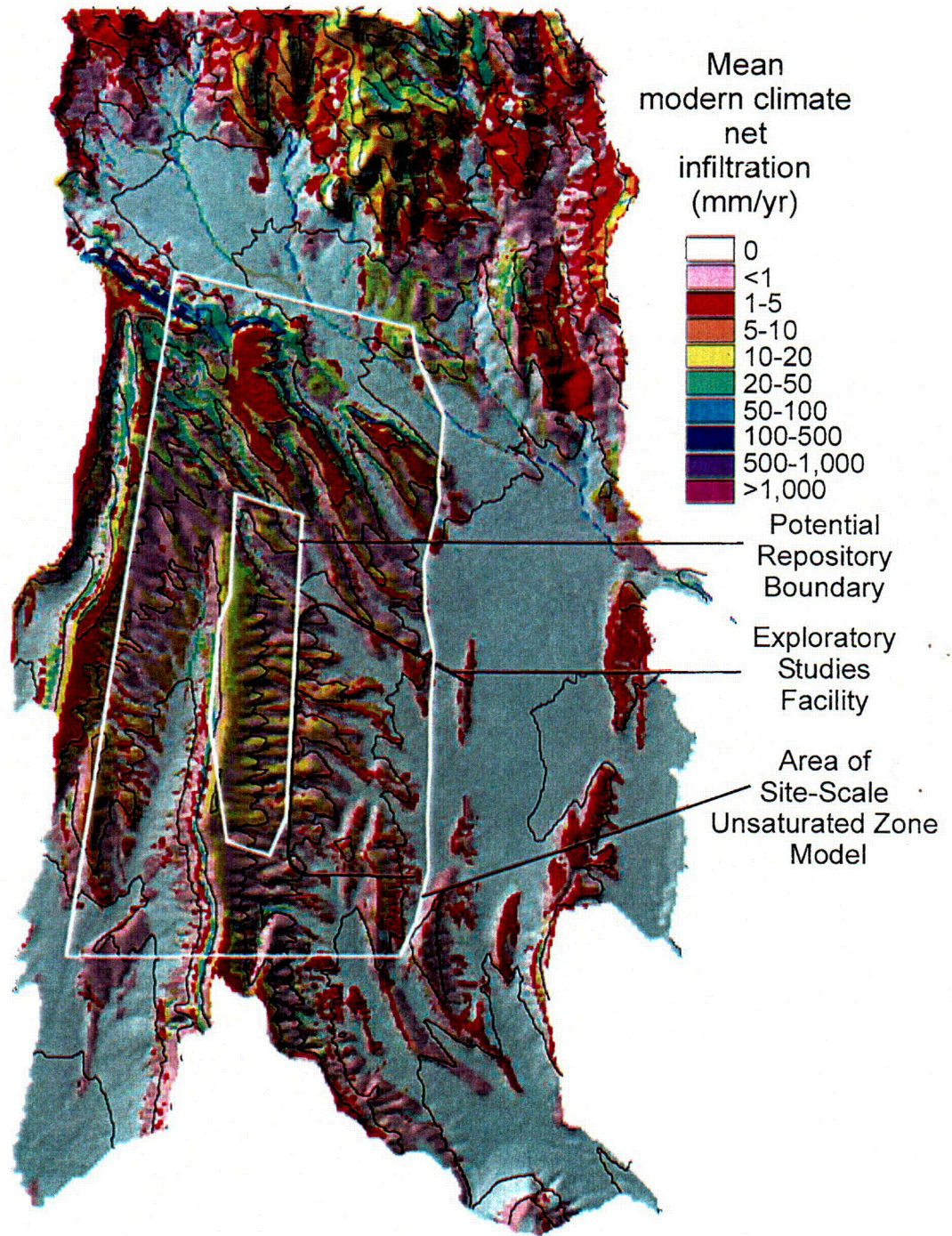
Source: USGS (2000b, Figure 6-7)

Figure 8.2-30. Flow Chart of the INFIL Version 2.0 Model Algorithm for Simulating Net Infiltration



Source: USGS (2000b, Figure 6-19)

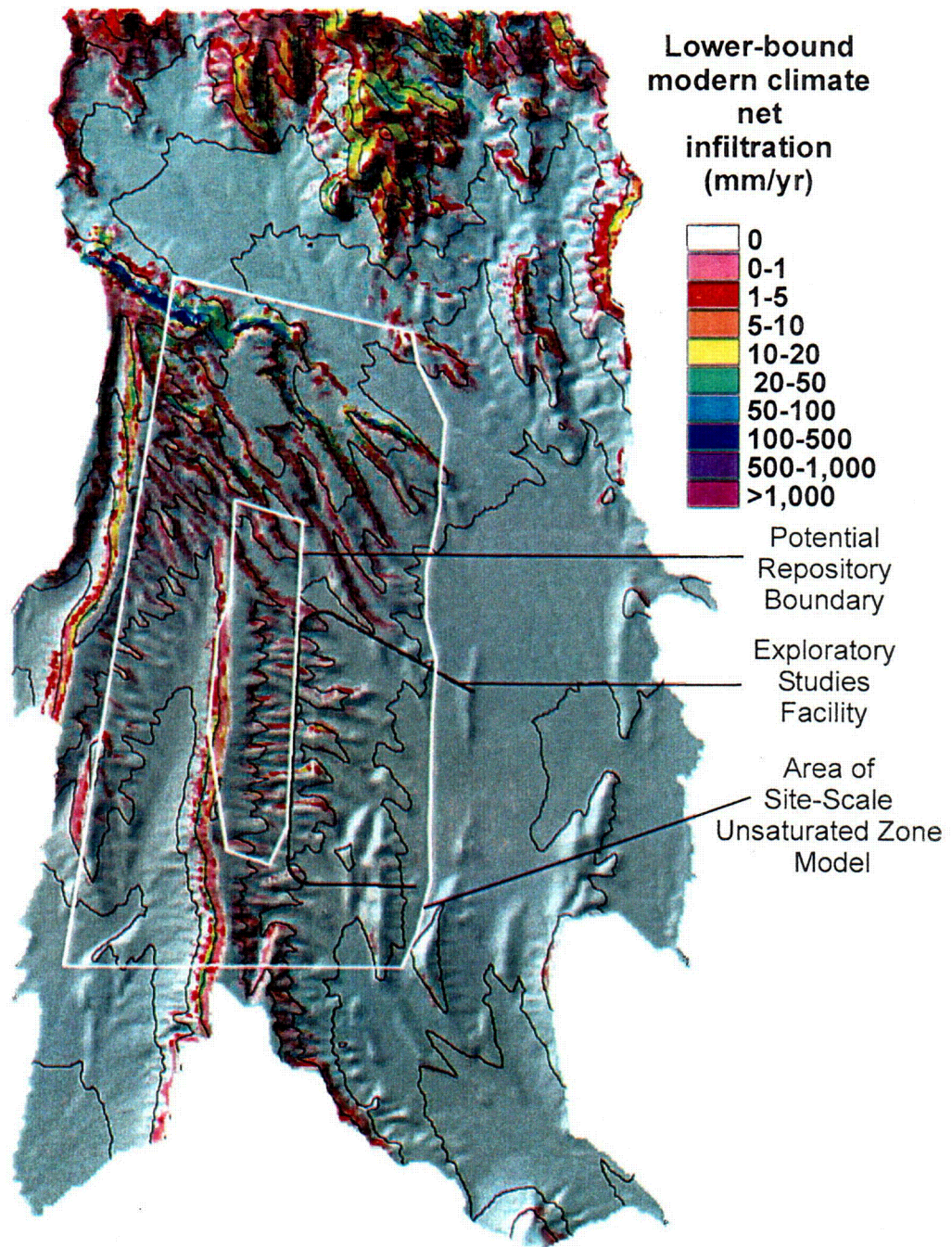
Figure 8.2-31. Location of Stream Gauging Sites and Watersheds Used for Model Calibration



82-32.CDR.SITEDESC-R01

Source: USGS (2000b, Figure 6-26)

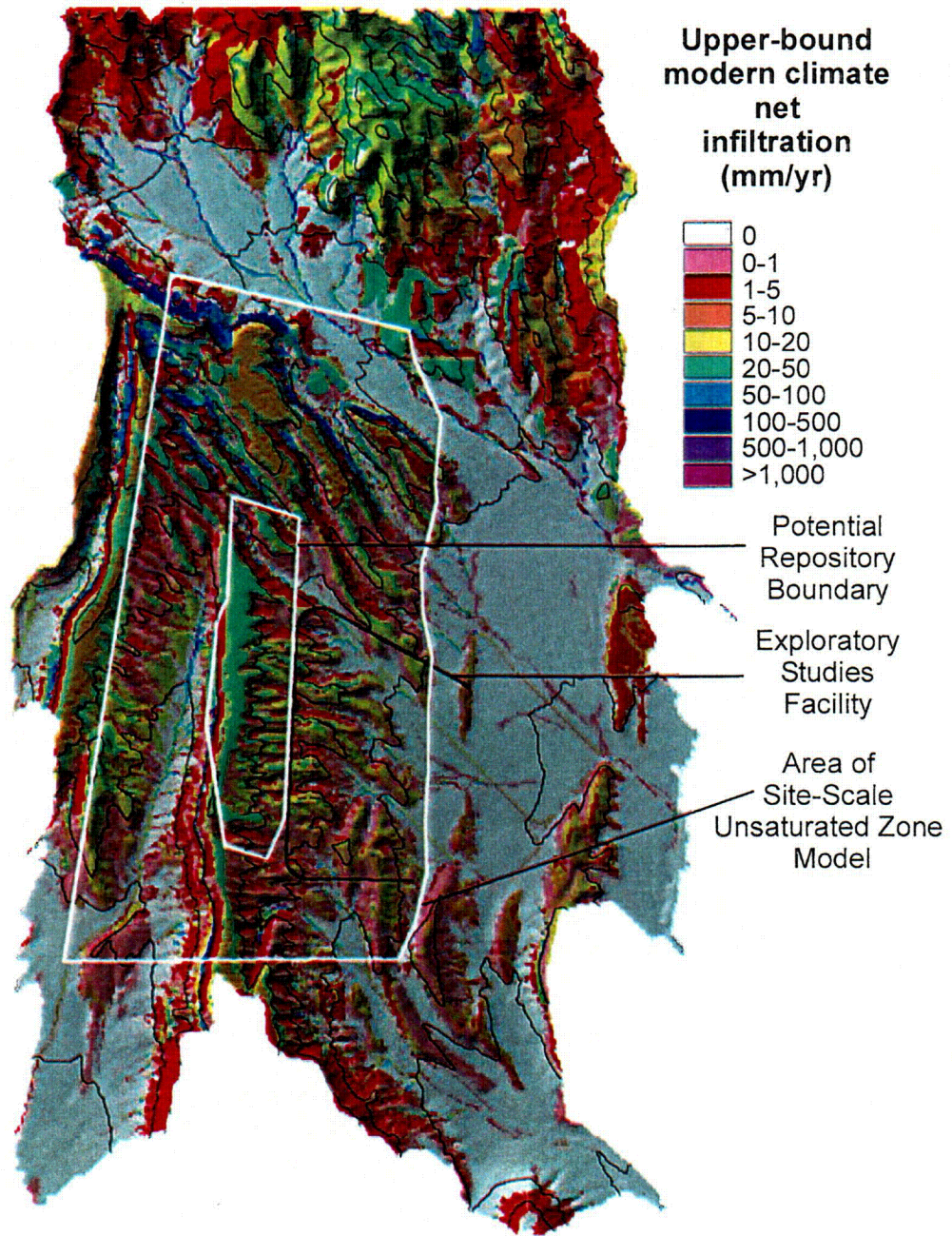
Figure 8.2-32. Net Infiltration for the Mean Modern Climate Scenario



82-33.CDR.SITEDESC-R01

Source: USGS (2000b, Figure 6-27)

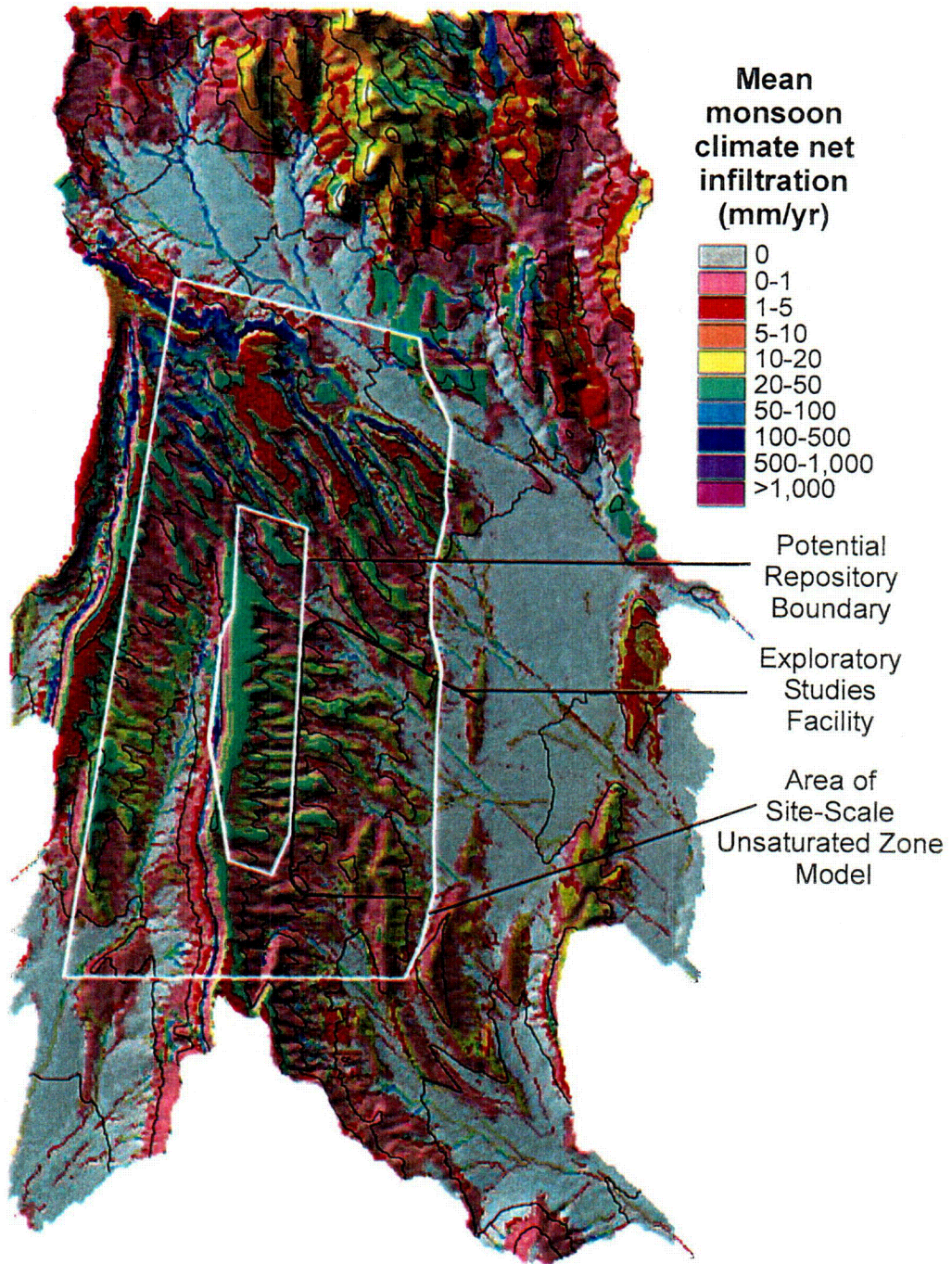
Figure 8.2-33. Net Infiltration for the Lower-Bound Modern Climate Scenario



82-34.CDR.SITEDESC-R01

Source: USGS (2000b, Figure 6-28)

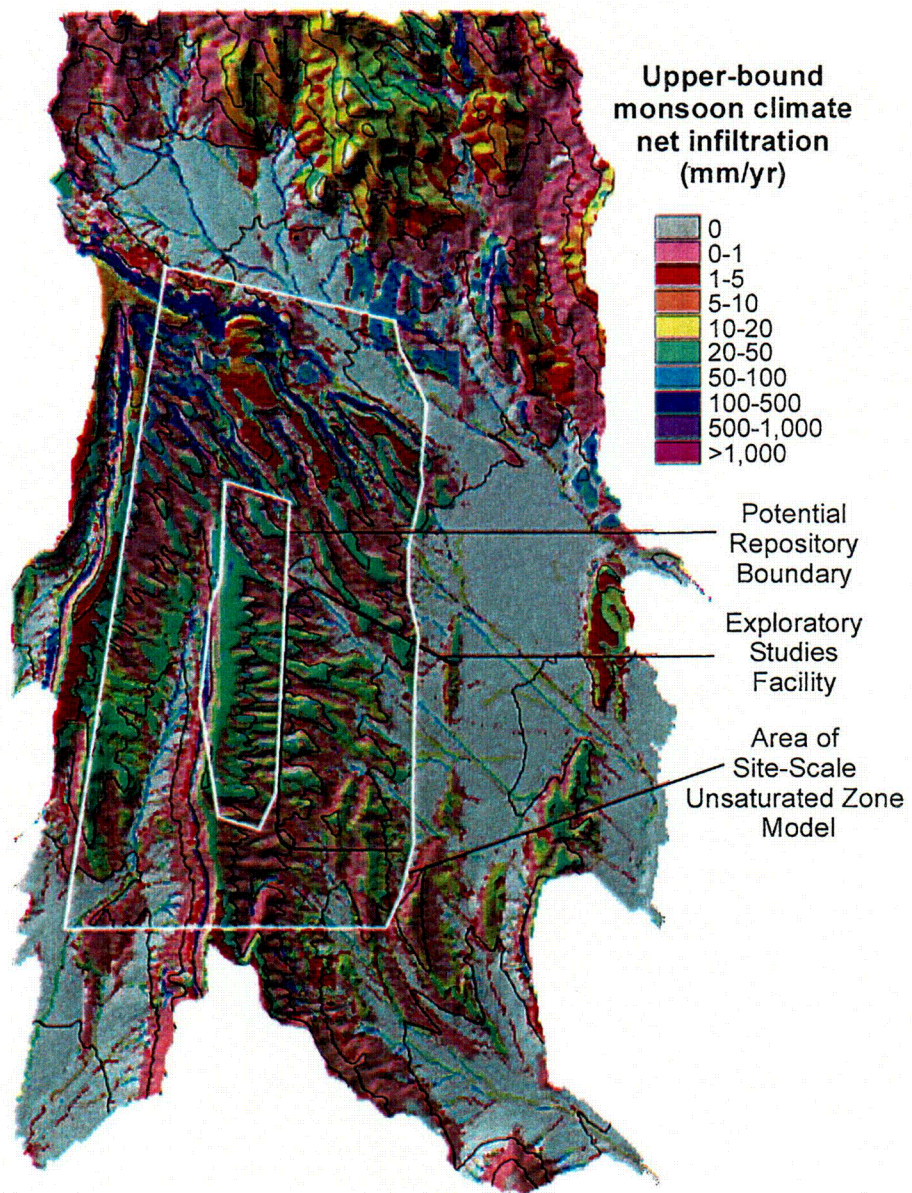
Figure 8.2-34. Net Infiltration for the Upper-Bound Modern Climate Scenario



82-35.CDR.SITEDESC-R01

Source: USGS (2000b, Figure 6-29)

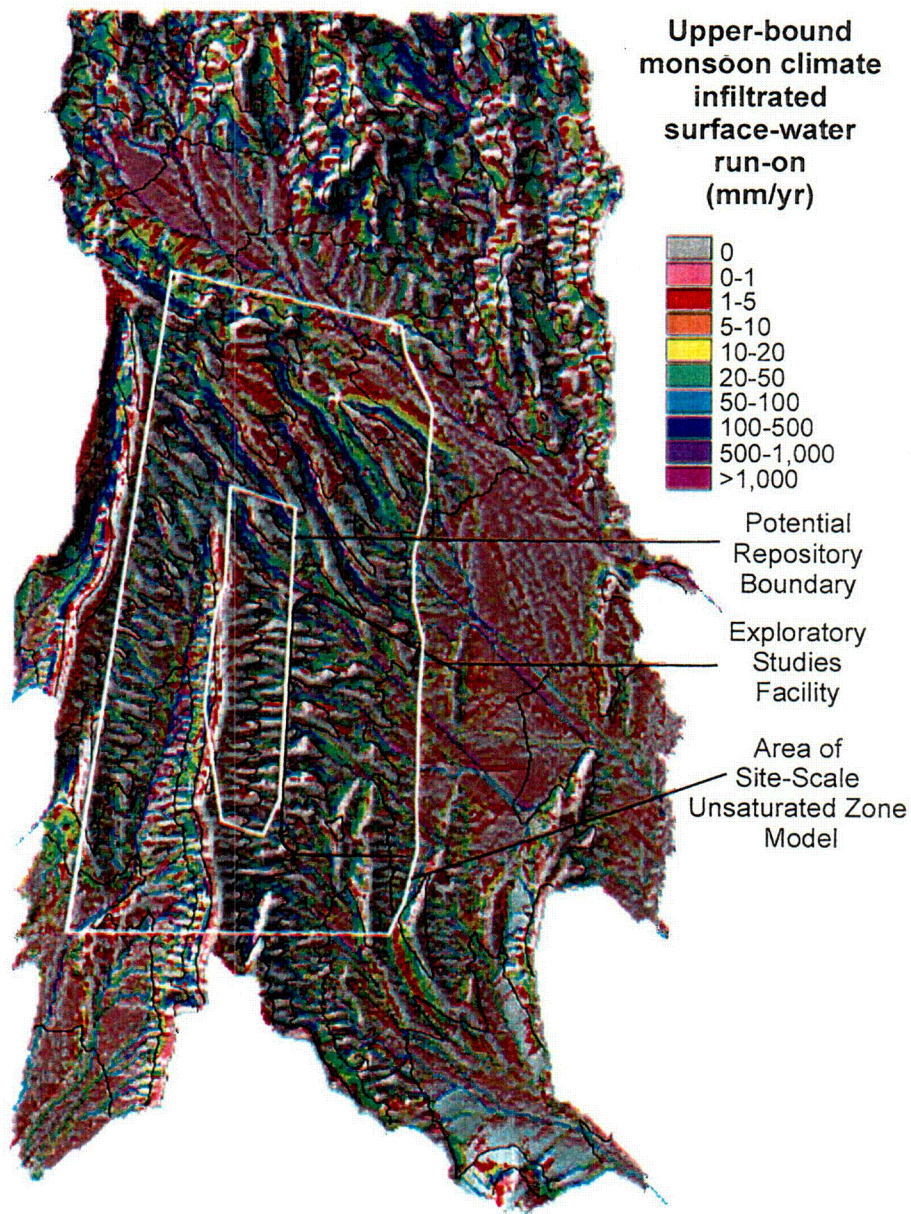
Figure 8.2-35. Net Infiltration for the Mean Monsoon Climate Scenario



82-36.CDR.SITEDESC-R01

Source: USGS (2000b, Figure 6-30)

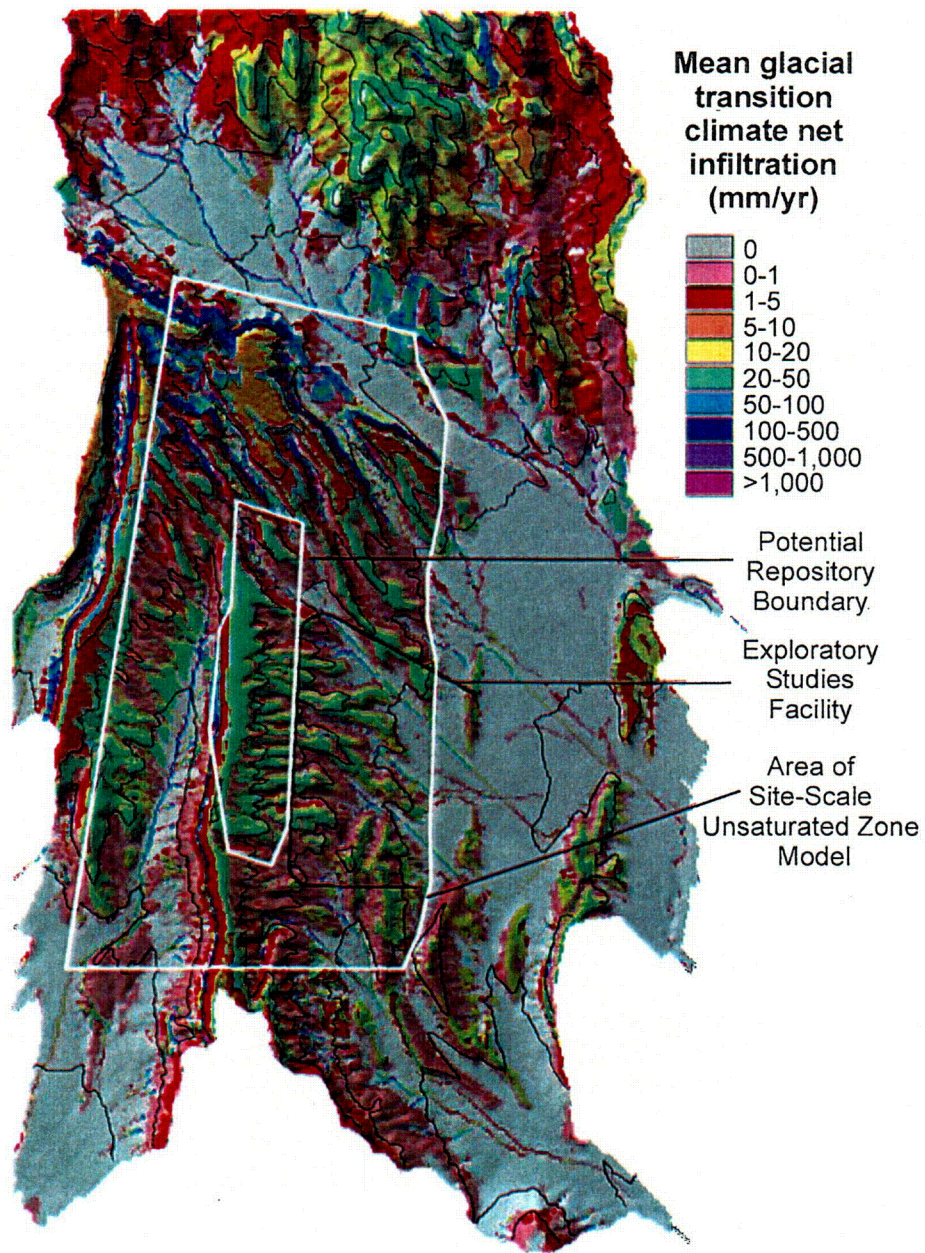
Figure 8.2-36. Net Infiltration for the Upper-Bound Monsoon Climate Scenario



82-37.CDR.SITEDESC-R01

Source: USGS (2000b, Figure 6-31)

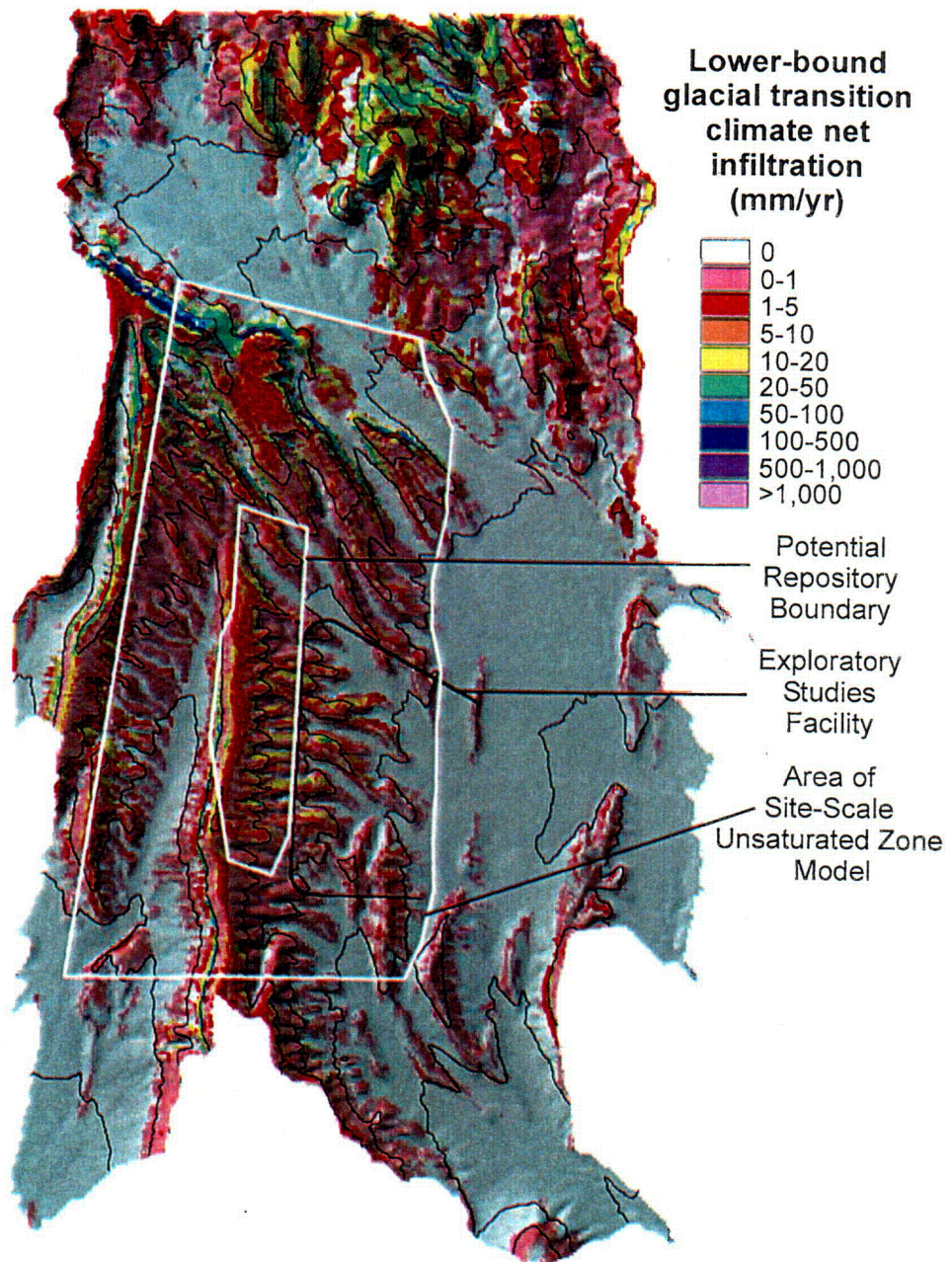
Figure 8.2-37. Infiltrated Surface-Water Run-On Depth for the Upper-Bound Monsoon Climate Scenario



82-38.CDR.SITEDESC-R01

Source: USGS (2000b, Figure 6-36)

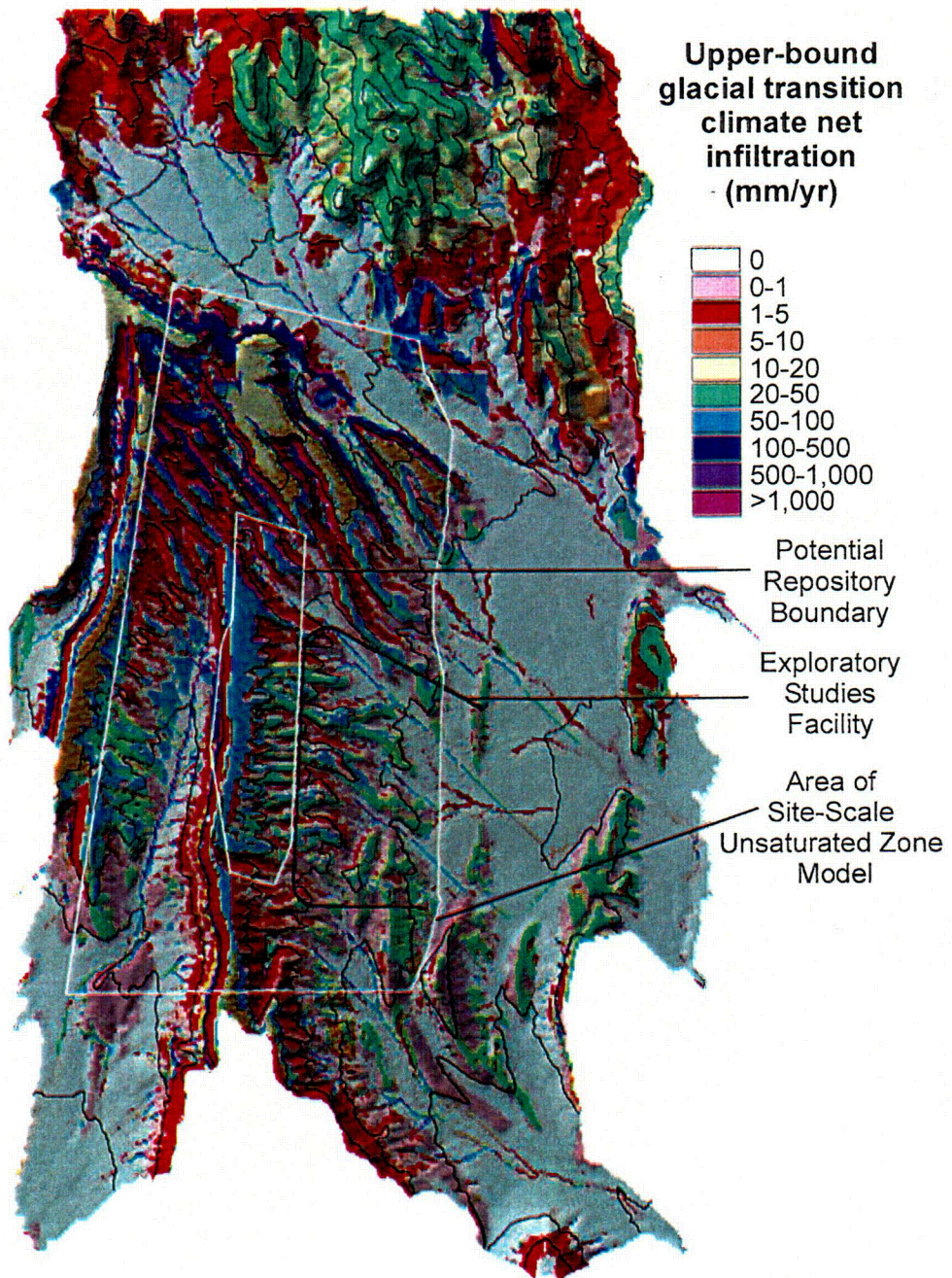
Figure 8.2-38. Net Infiltration for the Mean Glacial Transition Climate Scenario



82-39.CDR.SITEDESC-R01

Source: USGS (2000b, Figure 6-37)

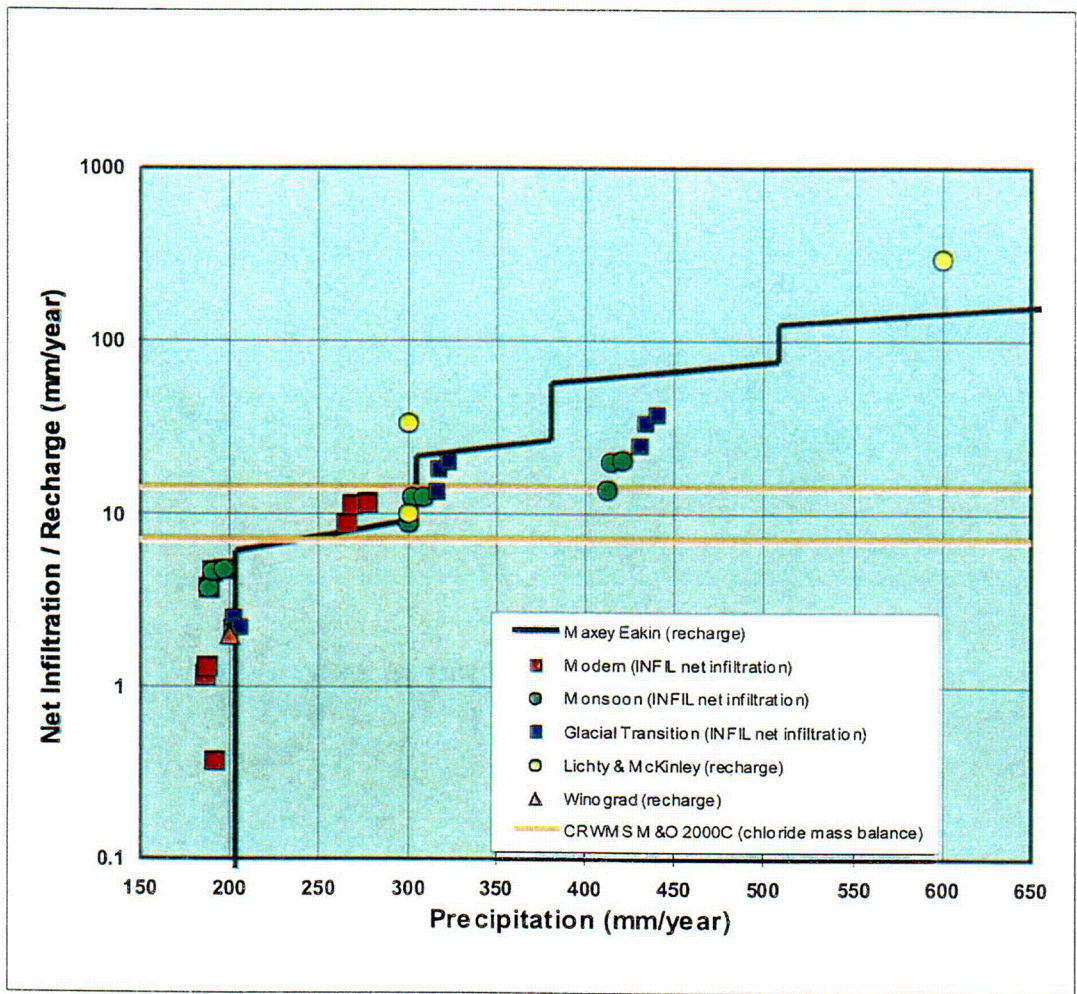
Figure 8.2-39. Net Infiltration for the Lower-Bound Glacial Transition Climate Scenario



82-40.CDR.STEDESC-R01

Source: USGS (2000b, Figure 6-39)

Figure 8.2-40. Net Infiltration for the Upper-Bound Glacial Transition Climate Scenario



82-41.CDR.SITEDESC-RO1

Source: USGS (2000b, Figure 6-41); Lichy and McKinley (1995); Winograd (1981); CRWMS M&O (2000c)

Figure 8.2-41. Comparison of Model-Calculated Net Infiltration (INFIL) with Estimates of Recharge in the Southern Great Basin

INTENTIONALLY LEFT BLANK